



THE UNIVERSITY *of* EDINBURGH

This thesis has been submitted in fulfilment of the requirements for a postgraduate degree (e.g. PhD, MPhil, DClinPsychol) at the University of Edinburgh. Please note the following terms and conditions of use:

This work is protected by copyright and other intellectual property rights, which are retained by the thesis author, unless otherwise stated.

A copy can be downloaded for personal non-commercial research or study, without prior permission or charge.

This thesis cannot be reproduced or quoted extensively from without first obtaining permission in writing from the author.

The content must not be changed in any way or sold commercially in any format or medium without the formal permission of the author.

When referring to this work, full bibliographic details including the author, title, awarding institution and date of the thesis must be given.

Electrospun piezoelectric polymer 3D structures for wearable energy harvesters.

Francisco Javier Diaz Sanchez



A thesis presented for the degree of

Doctor of Philosophy

University of Edinburgh

School of Engineering

August 2022

Title

Electrospun piezoelectric polymer 3D structures for wearable energy harvesters.

© August 2022

Author

Francisco Javier Diaz Sanchez

Supervisors

Dr Norbert Radacsi (School of Engineering, The University of Edinburgh, UK)

Dr Stewart Smith (School of Engineering, The University of Edinburgh, UK)

Location

Edinburgh, UK

The author would like thank the Mexican Science and Technology Council (CONACyT) for funding this PhD studentship.

Abstract

Wearable devices have emerged as one of the most rapidly growing branches of the consumer electronics industry in recent years. Having a wide breadth of applications, ranging from leisure and fitness tracking to therapeutics and diagnostics, their development has become a critical driving force in the field of personalised medicine and point-of-care technologies. With the availability of more powerful processing techniques, efficient design approaches, and the miniaturisation of the basic building blocks that conform them, the capabilities of wearable devices have great potential for growth.

Energy sources are one of the critical challenges associated with the design of wearable electronics. Renewable sources such as piezoelectric energy harvesters are of great interest, offering a viable alternative that can help tackle the problem of e-waste by enhancing the lifespan of a primary power source or as an independent power source. The piezoelectric active core materials of energy harvesters are the elements that allow for the conversion of mechanical energy to electrical energy. Contrary to the case of using piezoelectric ceramics, polymer based active cores offer superior flexibility, low manufacturing costs, and are non-toxic. However, their piezoelectric properties are comparatively lower than those of ceramics. Micro and nanofabrication methods for the manufacture of polymer based piezoelectric structures are of great interest in the field of energy harvesting because they allow for the tuning of specific morphological properties of these materials, offering the possibility of tailoring the material to the intended application and for the enhancement of the piezoelectric properties of the manufactured structures in some cases, which can bring the piezoelectric performance of polymer based materials closer to that of ceramics

Electrospinning is a technique for the fabrication of nano and microfibrinous structures based on the principles of electrohydrodynamics. This versatile manufacturing method not only allows for the fabrication of diverse morphologies of a material depending on the working parameters, ambient conditions and reagents, but can also intrinsically enhance the properties of the product.

In this thesis, electrospinning will be used for the fabrication of polymer based piezoelectric materials. The work presented in the following chapters will focus firstly on the optimisation of the working parameters and on the composition of the polymer solutions for the fabrication of morphologically stable fibres and consequently will deal with improving the electrical response of these structures when they are used as the active core of a piezoelectric generator.

Initial experimental work deals with the optimisation of polymer solutions containing the ferroelectric polymer poly(vinylidene fluoride) (PVDF). Favourable conditions for the fabrication of PVDF nanofibres were identified, and the resulting 2D fibrous mats were used for assembling a first iteration of piezoelectric generators. The findings indicated that the electrospun PVDF product had a favourable electrical response in spite of the morphology of the fibrous product not being ideal. Thus, improving the quality of the electrospun products would certainly allow for the fabrication of better performing generators.

The use of chemical additives, solvent systems, and the combination of polymers for electrospinning can heavily influence the quality of the product. This thesis proceeds with the exploration of this premise, using combinations of PVDF with poly(ethylene oxide) (PEO) and lithium chloride (LiCl) for improving the quality of the material. Fibre morphology improved dramatically with the use of these additives, and it was observed that the fabricated fibrous structures could now transition to 3D materials under specific conditions, with variants ranging from a cloud-like structure to thick sponge-like fibrous mats. The conditions required for the production of 3D structures were found to be compatible with poly(vinylidene fluoride-co-trifluoroethylene) (PVDF-TrFE), a copolymer known to have intrinsically superior piezoelectric properties than PVDF. The fabricated structures were used for assembling piezoelectric generators, and their electrical properties were shown to be comparable or to outperform similar state-of-the-art devices.

Design opportunities were identified while working on the proposed piezoelectric generator architecture and the interfacing methods used for bonding the active core to the electrode materials. The thesis finalises with an exploration of additional methods that can be used to further increase the electrical response of generators with thick sponge-like fibrous PVDF-TrFE/PEO active cores. The findings of this final study revealed that electrode placement and design that conforms to the characteristics of the electrospun fibrous core and the use of electrode materials that can interface with both the surface of the active core and the fibrous network within the core material can improve the electrical output of the generators dramatically.

The multidisciplinary work presented in this thesis explored fields ranging from chemistry and materials science to electronics and electrical engineering, laying the ground work upon which new research opportunities for the development of portable renewable energy sources can develop.

Lay Summary

In recent years, wearable devices have become more readily available, being commonly used for keeping track of parameters such as heart rate, counting steps, tracking sleep, among other uses. The market for these types of devices is expected to keep growing steadily; however, so is the demand for batteries which in turn will eventually reflect in the amount of e-waste being generated globally. Renewable energy sources are an attractive clean alternative that has the potential to extend the lifespan of the batteries used in these systems, and might even be able to independently power up devices with more simplistic designs.

Throughout the day, a person will move as they go through their daily activities. Piezoelectric energy harvesters can harness the residual mechanical energy associated with these activities and convert it into electrical energy, which can then be stored and used for powering up electronic devices. Piezoelectric active materials lie at the core of these type of energy harvesters. The type of material determines how effective the generator will be for harvesting energy, with some materials allowing for more electrical energy to be extracted than others. The most effective piezoelectric materials are ceramics, which are known to be hard and brittle. Polymer based piezoelectric materials offer flexibility and are non-toxic, but their piezoelectric properties are not as potent as those of ceramics. Micro and nanofabrication techniques can help to manufacture polymer based piezoelectrics with enhanced properties, bringing their piezoelectric properties closer to ceramics while conserving their flexibility and biocompatibility.

Electrospinning is one of those fabrication methods, and is typically used for the creation of fibrous structures that range from micrometre thin membranes to thicker non-woven fabrics. This method uses a very high voltage to eject liquid jets from a polymer solution towards a charged collector. As the jets travel to the collector, the material elongates and twists around, resulting in an assortment of micron-sized or even finer fibres depositing on the surface of the collector.

The work presented in this thesis explores how electrospinning can be used to create piezoelectric polymer based materials with enhanced properties and demonstrates how effective the resulting materials are as part of a piezoelectric generator by testing various energy harvester designs under different types of mechanical excitation.

Initially, it was necessary to evaluate the conditions, both those related to the ambient and the controllable ones, which facilitate the fabrication of piezoelectric nanofibrous structures. The study then moved forward, continuing with the evaluation of more complex conditions which would ultimately allow for the fabrication of better quality materials. It was during this step that the favourable conditions for fabricating electrospun 3D piezoelectric fibrous structures were identified. Tweaking a few controllable conditions allowed for the resulting product to become either cloud-like structures or thick, sponge like fibrous mats. The thick sponge-like mats were used as the active core of an energy harvester, and were found to perform comparably better or similarly to other state-of-the-art generators based on the same type of base materials.

The final part of this study deals with the exploration of design choices that would further enhance the performance of the previously built generators. Not only was it found that improving the interfacing materials used in the generator and the type of electrodes resulted in a dramatic increase in the power generated by the device, but it was demonstrated that the complex 3D morphology of the core material has the potential for achieving even higher output figures if the designer can figure out more effective methods for interfacing with both the surface and the complex inner network within the core material.

The work presented in this thesis shows that electrospinning allows for the fabrication of piezoelectric polymer based materials which can be successfully used as energy harvester components, and offers new generator design paths to explore by the introduction of piezoelectric polymer based electrospun 3D fibrous structures.

Declaration of Originality

I hereby declare that this thesis and the work contained presented throughout this document has been made by myself, including those sections deriving from an article under review for which I am the first-author. I confirm that this work has not been previously submitted for any other degree or professional qualification.

Francisco Javier Diaz Sanchez

August 2022

Acknowledgements

First and foremost, I would like to thank my family for their love and support. To my parents, thank you for being there for me and for believing in me. To my brother Aldo, thank you as well for your support. You all kept me going even when things got difficult.

A big thanks as well for Allana Lewis, Ammara Akram, Antonios Keirouz, Atika Al Hasaini, Faraz Fazal, Fergus Dingwall, Mei Zhang, Michael Chung, Michel Vong, Muhammad Waqas, Sakshika Raghav, Ting Chen, and Xiuming Wei. Big thanks as well for Yu “Pat”, Ricardo, and all my previous flatmates. Big thanks to my friends back home, Rodrigo and Luis the Homunculus. To Mei and Ammara, thank you very much for your emotional support and for encouraging me to keep going. To Michael, thank you very much for your encouragement, I learned so much from you, thanks very much. To all of you, thank you for your friendship and for the time we got to spend together, it was a pleasure meeting you all.

During my time as a PhD student, I had the opportunity to assist other students and researchers with their work. I would like to express my gratitude to Dr. Colin Robert, Dr. Wiwat Nuansing, Dr. Antonios Keirouz, Dr. Michel Vong, Faraz Fazal, Michael Chung, Muhammad Waqas, Sakshika Raghav, and Niklas Hartikainen for allowing me to assist and participate in your projects. I firmly believe that working with all of you allowed me to learn a great deal about other disciplines and gave me plenty of opportunities to continue developing as an electrical and electronics engineer and a researcher.

My gratitude as well for Dr. Norbert Radacsi and Dr. Stewart Smith. Thank you very much for being my supervisors and making this work possible.

Publications & Conference Contributions

Research articles

Tsiamis, A.; **Diaz-Sanchez, F.**; Hartikainen, N.; Chung, M.; Mitra, S.; Lim, Y.; Tan, H.; Radacsi, N. Graphene Wrapping of Electrospun Nanofibers for Enhanced Electrochemical Sensing. ACS Omega, 2021, 6, 16, 10568–10577.

DOI: 10.1021/acsomega.0c05823

Waqas, M.; Keirouz, A.; Kana, M.; Fazal, F.; **Diaz-Sanchez, F.**; Roy, D.; Koutsos, V.; Radacsi, N. Nozzle-free electrospinning setup for low cost and high yield production of nanofibers. Medical Engineering & Physics, 2021, 92, 80-87.

DOI: 10.1016/j.medengphy.2021.04.007

Fazal, F.; **Diaz-Sanchez, F.**; Waqas, M.; Koutsos, V.; Callanan, A.; Radacsi, N. A modified 3D printer as a hybrid bioprinting-electrospinning system for use in vascular tissue engineering applications. Medical Engineering & Physics, 2021, 94, 52-60.

DOI: 10.1016/j.medengphy.2021.06.005

Vong, M.; **Diaz-Sanchez, F.**; Keirouz, A.; Nuansing, W.; Radacsi, N. 3D electrospinning: A technology for the facile and precise fabrication of 3d macrostructures with microfibrinous features. Materials & Design, 2021, 208, 109916.

DOI: 10.1016/j.matdes.2021.109916

Muenwacha T., Weeranantanapan, O., Nuannoi, C., **Diaz Sanchez, F.**, Maensiri, S., Radacsi, N., Nuansing, W. Fabrication of Piezoelectric Electrospun Termite Nest-like 3D Scaffolds for Tissue Engineering. Materials. 2021, 14(24), 7684.

DOI: 10.3390/ma14247684

Diaz Sanchez, F.J., Chung, M., Waqas, M., Koutsos, V., Smith, S., Radacsi, N.: ‘Sponge-like piezoelectric micro- and nanofiber structures for mechanical energy harvesting’ Nano Energy, 2022, 98, p. 107286.

DOI: 10.1016/j.nanoen.2022.107286

Conferences

Diaz-Sanchez, F.; Smith, S.; Radacsi, N. Hybrid Energy Harvesters for Wearable Devices. **The University of Edinburgh, School of Engineering Conference, April 18, 2019, Edinburgh, United Kingdom.**

Heat and Decentralised Energy 2021: Green Skills and Jobs. **Virtual Conference.**
The Association for Decentralised Energy (ADE). 29th September, 1st October.

Table of Contents

Abstract	iii
Lay Summary	v
Declaration of Originality.....	vii
Acknowledgements	viii
Publications & Conference Contributions	ix
Table of Contents	xi
List of Figures	xv
List of Tables	xx
Acronyms.....	xxiii
1. Introduction.....	2
1.1 Problem statement and motivation	2
1.2 Thesis aims and objectives	7
1.3 Thesis outline	8
1.4 References	10
2. Literature Review	16
2.1 Energy harvesting overview	16
2.1.1 Energy demands of implantable and wearable electronics	16
2.1.2 Enzymatic biofuel cells	18
2.1.3 Triboelectric generators	19
2.1.4 Piezoelectric generators	20
2.1.5 Thermoelectric generators.....	20
2.1.6 Hybrid energy harvesters.....	21
2.1.7 Comparing the different energy harvesting techniques	22
2.1.8 The case for mechanical energy harvesting.....	30
2.2 Piezoelectricity	32
2.2.1 The piezoelectric effect.....	32
2.2.2 Implications of using 2D or 3D structures for mechanical energy harvesting....	37
2.2.3 Piezoelectric polymers	38

2.2.3.1 Polymers: an overview	39
2.2.3.2 Piezoelectric polymers	41
2.2.3.3 PVDF	49
2.2.3.4 PVDF-TrFE	53
2.3 Electrospinning	57
2.3.1 Principles of electrospinning	57
2.3.1.1 The formation of the Taylor cone.....	58
2.3.1.2 Straight jet region	60
2.3.1.3 The whipping jet region	61
2.3.1.4 Fibre deposition on the collector.....	62
2.3.2 Electrospinning parameters and their effect on the resulting products	63
2.3.2.1 Voltage.....	63
2.3.2.2 Flow rate	65
2.3.2.3 Working distance.....	66
2.3.2.4 Temperature	66
2.3.2.5 Relative Humidity	67
2.3.2.6 Electrode geometry	68
2.3.2.7 Solution dependent parameters and the role of additives	71
2.3.2.8 Specialised emitter electrode topologies	73
2.3.3 Electrospinning setup selection	74
2.4 Harvesting energy from a piezoelectric generator	77
2.4.1 Piezoelectric device as electromechanical systems and equivalent electrical models.....	77
2.4.2 AC signals	79
2.4.3 Maximum power transfer theorem	84
2.5 Interim summary	87
2.6 References	88
3. General Materials & Methods	106
3.1 Introduction	106
3.2 Materials and devices	106
3.2.1 Reagents.....	106
3.2.2 Electronic components and electrical devices.....	108
3.2.3 Equipment	110

3.2.4 Software	110
3.3. Active core material fabrication by electrospinning	112
3.3.1 Nozzle-based electrospinning	112
3.3.1.1 Nitrogen flow adapter for the nozzle-based electrospinner	113
3.3.2 Nozzle-free electrospinning	113
3.3.3. Relative humidity and temperature measurements	114
3.4. Mechanical testing device design and manufacture	115
3.5. Mechanical energy harvester assembly	117
3.6. Polymer solutions and electrospun material characterisation	121
3.6.1 Scanning electron microscopy (SEM)	121
3.6.2 Digital photography	121
3.6.3 X-ray diffraction (XRD)	121
3.6.4 Polymer solution conductivity measurement	121
3.7. Electrical response characterisation of the mechanical energy harvesters	123
3.7.1 Mechanical stimuli	123
3.7.1.1 Dropping a 100 g weight	123
3.7.1.2 Automated impacts	124
3.7.1.3 Test subject mediated impact	124
3.7.1.4 Impact force monitoring	124
3.7.2 Electrochemical impedance spectroscopy	126
3.7.3 Variable load resistance conditions	126
3.7.4 Capacitor charging test	128
3.8 Statistical analysis	130
3.9 References	131
4. A preliminary study on electrospun PVDF fibres and methods for enhancing their piezoelectric properties	132
4.1 Introduction	132
4.2 Results and discussion	133
4.2.1 Electrospinning PVDF: parameter variation effect on fibre morphology	133
4.2.2 A preliminary assessment of 2D PVDF fibre mat core generators	141
4.2.3 Generator equivalent impedance and behaviour	143
4.3 Interim summary	147

4.4 References	148
5. 3D sponge-like PVDF micro and nanofibrous structures for mechanical energy harvesting.....	151
5.1 Introduction	151
5.2 Results and discussion	152
5.2.1 Electrospun materials morphology.....	152
5.2.2 Electrospun 3D structures as active cores for the generators	164
.....	170
5.2.3 Extended cyclic mechanical impact test.....	171
5.2.4 Testing under real world conditions with a live test subject	174
5.3 Interim summary	177
5.4 References	179
6. Electrode-core interface optimisation for enhanced mechanical energy harvester performance ..	182
6.1 Introduction	182
6.2 Results and discussion	183
6.2.1 Effect of electrode placement and active core surface modifications on generator response	183
6.2.2 Conductive thread and fabric electrodes.....	190
6.3 Interim summary	198
6.4 References	199
7. Conclusions & Recommendations for future work	200
7.1 Conclusions	200
7.1.1 Conclusions related to the fabrication of electrospun PVDF active core materials.	201
7.1.2 Conclusions related to the mechanical energy harvesters.....	203
7.1.3 Limitations of the work presented in this thesis	207
7.2 Thesis contributions	210
7.3 Recommendations for future work.....	212
7.4 References	216
Appendix A: Publications	218
Appendix B: Morphological effects of using other salt additives for electrospinning PVDF/PEO ..	223

List of Figures

Chapter 2:

Figure 2-1: Simplified architecture of a wearable system	16
Figure 2-2: Three-dimensional space notation for piezoelectric tensors	34
Figure 2-3: Crystal to tensor matrix correspondence	34
Figure 2-4: Poling a ferroelectric material.....	35
Figure 2-5: Hysteresis loop of a ferroelectric material.....	36
Figure 2-6: Polymer crystallisation	41
Figure 2-7: Semi-crystalline polymer structure	42
Figure 2-8: Processing of a bulk semi-crystalline polymer.....	43
Figure 2-9: Tensor matrices associated to certain polymer processing techniques	44
Figure 2-10: Chemical structure of PVDF	49
Figure 2-11: PVDF molecule and crystalline unit models	50
Figure 2-12: Processing techniques for PVDF crystalline region transformation.....	51
Figure 2-13: Hysteresis loop of PVDF	52
Figure 2-14: Chemical structure of PVDF-TrFE.....	53
Figure 2-15: PVDF-TrFE molecule and crystalline unit models.....	54
Figure 2-16 Hysteresis loop of PVDF-TrFE	55
Figure 2-17: Electrospinning process overview for a nozzle-based system	59
Figure 2-18: Net forces acting on the electrospun jet	62
Figure 2-19: Voltage variation effect on electrospun fibres	64
Figure 2-20: Net forces acting on the electrospun jet, DC vs. AC biasing.....	65
Figure 2-21: Working distance variation effect on electrospun fibres.....	66
Figure 2-22: Relative humidity variation effect on fibre diameter	67

Figure 2-23: Relative humidity variation effect on fibre surface porosity	68
Figure 2-24: Emitter electrode topologies.....	70
Figure 2-25: Collector topologies.....	71
Figure 2-26: Mechanical model of a compression piezoelectric generator.....	78
Figure 2-27: Generalised electrical circuit equivalent of a piezoelectric generator	78
Figure 2-28: Generic sinusoidal signal	79
Figure 2-29: Voltage observed across individual components for a series LCR circuit	82
Figure 2-30: AC apparent power	83
Figure 2-31: AC to DC conversion.....	84
Figure 2-32: Equivalent circuit for a power source.....	85

Chapter 3:

Figure 3-1: Nozzle-based electrospinning setup.....	112
Figure 3-2: Gas flow accessory for the nozzle-based setup	113
Figure 3-3: Schematic diagram of the nozzle-free electrospinning setup.....	114
Figure 3-4: Digital thermometer hygrometer	114
Figure 3-5: Cyclic mechanical impact device.....	115
Figure 3-6: 3D model of a heel obtained with a 3D scanner	116
Figure 3-7: Method for placing the copper foil electrodes for generator assembly	117
Figure 3-8: Method for coating areas of the thick sponge-like materials with gold	118
Figure 3-9: Thick sponge-like core generator assembly method	118
Figure 3-10: Weight drop mechanical excitation test for measuring generator output.....	123
Figure 3-11: FSR and a 15k Ω in a voltage divider configuration.....	125
Figure 3-12: Calibration curves relating force for output voltage.....	125
Figure 3-13: Circuit used for measuring the output power of the piezoelectric generators when connected to several different resistive loads	127
Figure 3-14: Circuit used for recording the charging of different capacitors	128

Figure 3-15: Circuit used for monitoring the voltage of a capacitor as it was charged by a user stepping on a compound generator	129
--	-----

Chapter 4:

Figure 4-1: SEM images of the fibre mats obtained from electrospinning 20 wt% PVDF in DMF/acetone solutions under different working conditions.....	136
Figure 4-2: SEM images of the fibre mats obtained from electrospinning 20 wt% PVDF in DMF solutions with nitrogen flow, $7 \mu\text{L}\cdot\text{min}^{-1}$ FR, 18 kV, and varying WD.....	138
Figure 4-3: SEM images of the fibre mats obtained from electrospinning 20 wt% PVDF in DMF solutions with nitrogen flow, $15 \mu\text{L}\cdot\text{min}^{-1}$ FR, and varying WD and voltage	140
Figure 4-4: SEM images of the fibre mats obtained from electrospinning 15 wt% PVDF in DMF solutions with nitrogen flow, $25 \mu\text{L}\cdot\text{min}^{-1}$ FR, 21 kV and varying WD.....	141
Figure 4-5 Schematic diagram of the two generator designs used for testing the electrical output of the electrospun products	143
Figure 4-6: Test circuit for evaluating the impedance and behaviour of the generators	144
Figure 4-7: Nyquist plot of the EIS test.....	145

Chapter 5:

Figure 5-1: Electrospinning setups used for the fabrication of the active core material for piezoelectric generators	152
Figure 5-2: SEM images of the fibre mats obtained from electrospinning 10 wt% PVDF/PEO in DMF/water (50:3 ratios for both solvents and polymers) solutions.....	154
Figure 5-3: SEM images of the fibre mats obtained from electrospinning 10 wt% PVDF/PEO in DMF/water (50:3 ratios for both solvents and polymers) solutions. Temperature and WD were kept constant at 21.8°C and 35 cm respectively	155
Figure 5-4: 3D structure obtained from electrospinning a 10 wt% PVDF/PEO in DMF/water (50:3 ratios) with 1 wt% added LiCl solution.....	158
Figure 5-5: Cloud-like structures obtained from electrospinning PVDF/PEO in DMF/water (50:3 ratio) solutions.....	159
Figure 5-6: SEM images of the 3D cloud-like structures obtained from electrospinning the 10 wt% PVDF/PEO in DMF/water (50:3 ratios) with added 0.75 wt% LiCl.....	159

Figure 5-7: Thick sponge-like sample obtained from electrospinning a 12 wt% PVDF/PEO in DMF/water with added 0.75 wt% LiCl solution.....	160
Figure 5-8: SEM images for the thick sponge-like PVDF/PEO fibre mats.....	162
Figure 5-9: XRD pattern obtained from scanning two PVDF/PEO sponge like samples	162
Figure 5-10: Schematic diagram showing the method used for assembling the piezoelectric generators used for evaluating the electrical response of various PVDF fibrous mats.....	165
Figure 5-11: The output voltage and current figures obtained when recording the electrical response of 3 different types of generators when subjected to a 4 Hz impact	169
Figure 5-12: Detailed view of the output voltage signals obtained for PVDF/PEO and PVDF-TrFE core generators	170
Figure 5-13: Response of the best performing PVDF/PEO and PVDF-TrFE/PEO generators under a constant mechanical impacts (4Hz) over a window of 500 seconds	173
Figure 5-14: Experimental setup used to evaluate the performance of a compound PVDF-TrFE/PEO generator	175
Chapter 6:	
Figure 6-1: Thick sponge-like fibrous PVDF-TrFE/PEO non-woven mats model	184
Figure 6-2: Histograms showing the distribution of the standardised output V_{PP} values recorded for each of the tested generators	187
Figure 6-3: Empirical cumulative distribution function plots of the normalised responses obtained from the generators with different surface modifications	188
Figure 6-4: Box plots for the data recorded when subjecting the three generators with different active core material surface treatments to cyclic mechanical impacts	189
Figure 6-5: Histogram showing the recorded V_{PP} values for the PVDF-TrFE/PEO generator with conductive fabric electrodes	191
Figure 6-6: Detailed output voltage waveform obtained from the conductive fabric and thread electrode PVDF-TrFE generator	193
Figure 6-7: Power waveforms obtained when multiplying the voltage and current recorded for each type of generator under	194
Figure 6-8: Capacitor charging curves obtained from the generators used in the previous experiments	196

Chapter 7:

Figure 7-1: True 3D PVDF/PEO generator..... 214

Figure 7-2: Prototype fabric only compound generator..... 215

List of Tables

Chapter 2:

Table 2-1: A list of energy harvesters belonging to each of the four families discussed in this text	24
Table 2-2: List of piezoelectric polymers and their characteristics	47
Table 2-3: List of different types of electrospun products	76

Chapter 3:

Table 3-1: List of chemicals	106
Table 3-2: List of electronic components and other materials	108
Table 3-3: List of equipment	110
Table 3-4: List of software	110

Chapter 4:

Table 4-1: Working parameters for the electrospinning a 20wt% PVDF in DMF/Acetone solution	135
Table 4-2: Working parameters used for evaluating product variation when electrospinning a 20 wt% PVDF in DMF solution under nitrogen gas flow	137
Table 4-3: Working parameters used for evaluating the effect of an increased flow rate when electrospinning 20 wt% PVDF in DMF solutions under nitrogen gas flow	137
Table 4-4: Working parameters used for electrospinning a 15 wt% PVDF in DMF solution under a nitrogen flow with a $25 \mu\text{L} \cdot \text{min}^{-1}$ flow rate	139
Table 4-5: Comparison of the differences in the average output V_{PP} recorded for vigorous finger tapping on an electrospun PVDF core piezoelectric generator for two different generator designs	142

Chapter 5:

Table 5-1: Electrospinning parameters used for fabricating 10 wt% PVDF/PEO fibre mats using the nozzle-based setup. $T=22^\circ\text{C}$, $\text{RH}\% = 42$	153
---	-----

Table 5-2: Electrospinning parameters used for fabricating 10 wt% PVDF/PEO fibre mats using the nozzle-based setup. T=21.8 °C, WD 35 cm	154
Table 5-3: Average fibre diameter measured for the thick and thin regions for the electrospun 10 wt% PVDF/PEO in DMF/water (50:3 solvent and polymer ratio) fibre mats	156
Table 5-4: Average fibre diameter for the PVDF/PEO samples obtained from the nozzle-free electrospinner	160
Table 5-5: Thickness measurements of the electrospun thick sponge-like product obtained with the nozzle-free setup.	162
Table 5-6: Measured solution conductivity changes under different polymer and added LiCl concentrations.....	163
Table 5-7: Electrical response of the best performing generators per core material family when subjected to continuous mechanical impacts. 15.1 MΩ load conditions.....	165
Table 5-8: Average electrical response of the generators as a response to repeated mechanical impacts for all 3 generator families	166
Table 5-9: Summary of the data gathered from recordings obtained from the best performing generators under continuous mechanical impacts.....	172
Table 5-10: Output power figures of a broad spectrum of state-of-the-art piezoelectric energy harvesters with PVDF-based cores and those produced for this thesis	177

Chapter 6:

Table 6-1: Output V_{PP} figures obtained when regular and L-shaped electrode generators were subjected to 100 seconds of continuous mechanical impacts.....	185
Table 6-2: Output V_{PP} figures obtained when generators with different interface surface modifications were subjected to 100 seconds of continuous mechanical impacts	185
Table 6-3: Results of running a one way ANOVA on the data recorded for the generators with different active core surface modifications.....	187
Table 6-4: Results of running a Tukey's HSD test on the data recorded for the three different generators.....	189
Table 6-5: Output V_{PP} figures obtained when generators with different interface modifications or electrodes were subjected to 100 seconds of continuous mechanical impacts.....	190

Table 6-6: Summary of the output characteristics of the generator with conductive fabric electrodes and the impact forces recorded when powering up various resistive loads	191
Table 6-7: Summary of the output characteristics and recorded impact forces for the best performing unmodified PVDF, PVDF/PEO or PVDF/TrFE/PEO and a PVDF-TrFE/PEO generator with conductive fabric electrodes	192
Table 6-8: RMS values calculated for pairs of voltage and current signals recorded for each type of generator	194
Table 6-9: Estimated PVDF based active core generator area required for powering up a low-power wireless transmission module in one of several available modes.....	195

Acronyms

Symbol	Defined as:
2D	Two-dimensional
3D	Three-dimensional
A	Ampere
AC	Alternating Current
a_0	Average value (Fourier series)
a_n	n^{th} harmonic cosine coefficient (Fourier series)
b_n	n^{th} harmonic sine coefficient (Fourier series)
C	Capacitance
CE	Counter electrode
d_{xy}	Piezoelectric coefficient or tensor
D	Electric displacement
DC	Direct Current
DI	De-ionised (water)
DMF	N, N-dimethylformamide
E	Electric field
E_0	Electric field strength
EBFC	Enzymatic biofuel cell
EIS	Electrochemical impedance spectroscopy
f	Frequency
F	Farads
FR	Flow rate
g	Grams
H	Nozzle to collector distance
HMTA	Hexamethylenetetramine
hr	Hour
Hz	Hertz
HV	High voltage
I	Current
I_{SC}	Short-circuit current
I_{PP}	Peak-to-peak current

j	$\sqrt{-1}$ (Electrical engineering notation)
K	Jet curvature or wave number
L	Litre, inductance or capillary length
LiCl	Lithium chloride
LTI	Linear time invariant
m	Metre
M	Molarity
MW	Molecular weight
N	Newtons
P	Power
Pa	Pascals
PBS	Phosphate-buffered saline solution
PDMS	poly(dimethylsiloxane)
PEG	Piezoelectric generator
PEO	poly(ethylene oxide)
PLLA	Poly(L-Lactic acid)
PVDF	poly(vinylidene fluoride)
PVDF-TrFE	poly(vinylidene fluoride-co-trifluoroethylene)
Q	Reactive power
Q_s	Solution flow rate
R	Resistance
R_0	Droplet radius
RE	Reference electrode
RF	Radiofrequency
RH%	Relative humidity
RMS	Root mean square
RPM	Revolutions per minute
s	Seconds or strain
S	Apparent power or cross-sectional area
SE	Sense electrode
SEM	Scanning electron microscopy
T	Temperature, period or stress
TEG	Triboelectric generator
ThEG	Thermoelectric generator
V	Voltage
V_0	Amplitude (AC signals)

V_C	Critical voltage
VA	Volt-ampere
VAR	Reactive volt-ampere
V_{oc}	Open circuit voltage
V_{PP}	Peak-to-peak voltage
W	Watt
WD	Working distance
WE	Working electrode
wt%	Weight percentage
X_C	Capacitive reactance
X_L	Inductive reactance
XRD	X-Ray diffraction
Z	Impedance
γ	Surface tension
ρ	Density
θ	Phase shift
Φ_0	Electric potential
σ	Surface tension
σ_s	Surface charge
ξ	Reference axis
ω	Angular frequency
Ω	Ohms

Chapter 1

Introduction

1.1 Problem statement and motivation

The field of implantable electronics and wearable medical devices has grown at a considerably fast pace over the course of the last century. The availability of new technologies for the fabrication of solid-state electronic components and a better understanding of the physiological and biochemical aspects of health and disease are some of the main motivations behind the rapid growth of this field. With the implementation of the first self-powered cardiac pacemaker in the late 1950's [1], technological and clinical research and development activities have allowed for the continuous development of more effective interfacing materials and electrode designs, signal processing techniques, and biocompatible design, among others. Initial iterations of implantable medical devices often required complicated surgical procedures and carried great risk to the users, primarily because of the lack of biocompatible materials and the limitations posed by the energy sources available to the designers in those days [2].

During the early 1960s, several studies were conducted to evaluate the condition of patients who had received the earlier cardiac pacemaker implants, allowing both engineers and scientists to identify the areas of opportunity in which the application of new technologies and methodologies would provide critical improvements for patients [1, 3]. The applications of the implants started to diversify as well, with other devices now being used to treat hypertension or used as implanted defibrillators [4, 5]. The rapid development of solid-state devices and integrated microelectronics were critical for the proposal of more complex devices. For instance, an automatic implantable defibrillator was presented in 1980. This device was designed to be fully biocompatible, fitted with lithium batteries which would allow it to deliver a total of 100 shocks and operate for at most 3 years. The device had the processing power to monitor the electrical activity of the heart, detect atypical patterns in the input signals being monitored, and deliver a shock. It also had the capability of identifying if the application of a shock had not been successful and consequently would deliver another one [5].

Progressively smaller, denser, and more powerful integrated circuits (ICs) and advances in the implementation of Very Large-Scale Integrated circuits (VLSI) allowed for the design and

implementation of systems capable of performing tasks such as supplying a drug as a response to the current condition of the patient. At times, the ideas coming out of the collaboration between medical professionals and engineers could not be realised mainly because of technological limitations. For instance, the development of application-specific systems (ASIC) for performing individual tasks such as controlling micron-sized pumps for the handling of biological fluid samples, and the availability of low-power memory and input/output modules, allowed for the creation of a fully programmable implantable drug delivery system. This system was first conceived by its inventor in the 1970s, but was only realisable well into the 1980s, highlighting how this field is highly dependent on advances in other fields such as consumer electronics, and materials science, among others [6, 7]. During these decades, various techniques and approaches for the design of implantable and wearable electronics involving the development of specialised biomedical ICs and VLSI systems were developed and became easily accessible to the wider research community, allowing designers and engineers to create systems that were tailored for medical applications. These guidelines and adopted techniques would be useful to tackle common challenges such as the presence of interference in the form of external electromagnetic signals or internally in the form of sensor drift [6, 8–13].

As stated previously, technological progress related to processing power and miniaturisation was not the only aspect that allowed for the design of more complex and powerful devices; the development of energy sources was a critical factor around which designers needed to work around. The batteries used in the first implantable cardiac pacemakers had mercuric oxide cathode and zinc anodes, battery chemistry which was in principle not adequate for implantable devices because gaseous hydrogen would be released as a by-product of the half-cell reactions [2]. This would be problematic for the implementation of sealed devices, as the release of gases would compromise the structural integrity of the implanted device. Additionally, the energy density of these types of batteries would only allow the implanted devices to operate for a few hours or days for the earliest designs and up to 1 or 2 years for more advanced ones [1, 2].

Lithium-based batteries became commercially available to the general public in the 1970s. This type of battery had a much higher energy density, did not produce gases, and offered higher stability, which was very attractive for designers and proved to be very beneficial for the transition from concept to product for many implantable devices [2, 6]. The fabrication of specialised batteries for medical applications has seen a very substantial development as well, with very rigorous testing procedures being carried out spanning from the discharge characteristics to the assembly and mechanical properties of the casing [14]. Additionally, as

technologies such as the fabrication of nanostructured devices emerge, more efficient and durable lithium batteries are expected to become available in the near future [15].

In more recent times, as communication among devices and approaches such as that of Internet-of-things (IoT) and telemetry become more commonplace, specialised devices such as those employed for point of care (PoC) applications and wearables have also become ubiquitous in daily life, enabling healthcare professionals to monitor vulnerable people or for consumers to keep a record of their own parameters of interest [16–23]. As rechargeable batteries with higher energy density became more widely available, and electronics became more efficient and were capable of operating at low-power conditions, the idea of battery replacement might not appear to be of much concern. However, the mass production of wearable devices and consumer electronics, in general, is inevitably associated with the production of e-waste at the end of life for these products.

The generation of e-waste is of great concern for public health institutions and environmental agencies worldwide. As emergent economies develop, so does the annual consumption of consumer electronics and thus the generation of e-waste. E-waste is a term coined for encompassing all the parts associated with an electronic device such as printed circuit boards (PCBs), discrete components, batteries, and casings, among others. Recycling approaches target specific components such as electrode materials, heavy metals, and electrolytes, to name a few examples. The implementation of legislation and policies for the correct management of e-waste allows for the sustainable recovery of materials and for the safe disposal of those that cannot be recovered [24]. Emerging technologies for more efficient recovery processes are also helping to tackle the challenges associated with the sustainable disposal of e-waste [25]. However, an estimate of around 82.6% of the total e-waste disposal is informal, disorganised, and unregulated according to some studies. The unregulated methods often involve the use of toxic mediators, incineration or incorrectly dumping the devices into landfills, all of which have a severe impact on the environment and human health [24, 26–28]. As pointed out in the Intergovernmental Panel on Climate Change (ICPP) reports, while batteries can play a crucial role in diminishing losses and reducing fuel-production emissions in sectors such as transport [29], legislation and policies for the processing of these devices at the end of their life is also necessary for minimising their environmental impact.

The use of energy harvesters constitutes an alternative that not only offers the possibility of slowing down the production of e-waste by extending the battery life of devices but may also one day provide the means to fully power up implantable and wearable devices on their own. Emerging self-powered devices and sensors, which are defined as those that are autonomous

and supply their own energy, allow relatively simple sensing systems, wearables, implants and wireless sensor networks to operate without the need for a primary power source [30–37].

Energy harvesting devices rely on active materials, which convert mechanical, chemical, thermal, and biological energy to electrical power. Recent advances in nanofabrication techniques for the production of active materials used for energy harvesting have resulted in the production of materials, with emerging methods being capable of further enhancing the efficiency of energy harvesters [38–43]. For instance, in the case of mechanical energy harvesters, it has been observed that the fabrication of piezoelectric structures with very high length to diameter aspect ratios exhibit a more powerful electrical response than those of lower aspect ratios [44].

Piezoelectric ceramics and polymers are typically used to fabricate mechanical energy harvesters [45]. Ceramic based energy harvesters can reach output power figures of up to the range of milliwatts per square centimeter (mW cm^{-2}), while those constituted of polymers or of combinations of ceramics and polymers can achieve outputs in the range of single nanowatts per square centimeter (nW cm^{-2}) to the tens of microwatts per centimeter square ($\mu\text{W cm}^{-2}$) [46–48]. While ceramics have higher output power figures, they are brittle and often contain toxic materials such as lead.

Unlike ceramics, polymer-based piezoelectric elements are biocompatible, non-toxic, and offer superior flexibility at low manufacturing costs [35]. A biocompatible material can be generally defined as those which do not affect the biological and physical nature of living beings or living tissue [49, 50]. More specific definitions of this term are highly dependent on the context and scope of the project. In regards to the design of a wearable or an implantable device, a biocompatible material is that which minimises the appearance of an inflammatory response by having mechanical and chemical properties that closely match those of living tissue, besides not being toxic [51, 52]. However, the definition of biocompatible materials will be more restrictive for implantable devices, since it is necessary to understand how severe an inflammatory response would be and how the body will react to an implanted foreign body on a local and a systemic level [49]. In the case of wearable devices, using flexible and stretchable materials that conform to the shape of a stationary and moving body part can minimise the chance of triggering an allergic reaction since friction between the skin and the material can be minimized [51, 53, 54]. Since the scope of the work presented in this thesis is focused on wearable devices, biocompatible materials will be defined as those that do not cause an allergic reaction simply by touching the skin, and have properties such as flexibility and stretchability that allow them to be manufactured in forms that will reduce the likelihood of damaging the skin of the end user. Additionally, in regards to the power output associated with

polymers, the work presented in this thesis will deal with mechanical energy harvesters with only polymer based cores. Thus, in the scope of the project, the output power range of interest will be defined between the hundreds of nW cm^{-2} to the tens of $\mu\text{W cm}^{-2}$.

Electrospinning is a micro and nanofabrication technique that allows the user to create polymer-based fibre mats with individual fibre tuneable properties such as dimension, porosity, mechanical properties, among other characteristics. Typically, the most fundamental type of structure that can be obtained from electrospinning consists of a single fibre, whether it has a diameter in the nano or micrometric scale. A single fibre produced via electrospinning is often categorised as a 1D structure [55–57]. A collection of electrospun fibres is known as a fibre mat, and is often referred as a 2D structure [58, 59]. Given that the fabrication of 3D electrospun structures has emerged only recently and there exist different approaches for the production of this type of structures such as near-field techniques or those using liquid collectors [60–62], the definition of a 3D structure in the context of the work presented in this thesis will refer to those electrospun structures or fibre mats which have thicknesses greater than $500 \mu\text{m}$ and can acquire this property in less than 30 minutes of continuous electrospinning. Compared to the basic electrospinning method, near-field techniques involving extrusion or others that rely on liquid collectors require additional specialised equipment, accessories or additional processing steps to generate electrospun 3D materials. Alternative methods which can reliably create electrospun 3D structures using the basic electrospinning approaches have yet to be explored.

The electrospinning of ferroelectric polymers for the fabrication of 2D fibre mats for energy harvesting has been studied extensively. Information about the production of different types of structures with different types of polymers, as well as extensive documentation relating to the effects that experimental conditions and additives have on the morphology and properties of the final product [41, 60, 63–67]. However, the advantages that using electrospun 3D ferroelectric polymer structures for fabricating mechanical energy harvesters may have in terms of power output performance and their potential for integration into wearable systems have yet to be studied.

The research work presented in this thesis is motivated by the need to create biocompatible and efficient active core materials for mechanical energy harvesters based on emerging 3D electrospinning technologies, aiming to help bring the transition to a more sustainable battery life cycle closer to reality for wearable devices.

1.2 Thesis aims and objectives

This thesis aims is to explore the usage of ferroelectric polymers for the fabrication of active materials. Outlining a method that allows for the fabrication of structures that can be easily adapted for integration into wearable devices and that may facilitate the formation of complex 3D structures are the core aims of the project. Electrospinning is a fabrication technique that can potentially allow for reaching these goals, and will thus be the primary experimental method for the fabrication of polymer-based active materials. A condensed list of the objectives is as follows:

- Electrospinning ferroelectric polymer fibrous structures
 - Focus on materials and methods that will allow for the manufacture of biocompatible active materials that can be easily adapted to diverse wearable device design approaches such as textile-based wearables or that can be integrated into accessories such as watches or bracelets.
- Characterisation of the resulting fibrous structures
 - Observe which conditions allow for the fabrication of the best fitting morphs of the product. Use those particular fabrication settings and parameters as a basis which can be further improved by controlled tuning, the use of additives or different electrospinning setups.
 - Assess the properties of the manufactured materials and evaluate their suitability as cores for a mechanical energy harvester.
- Use the fabricated fibrous product to design and implement a mechanical energy harvester.
- Demonstrate the properties of the fabricated materials and designed generators by evaluating their electrical response.
 - Evaluate the effects of using different electrode designs and materials. Assess how assembly, placement, and interfacing methods affect the electrical response of the generators.
 - Characterise the electrical response of the generators under different testing conditions. For instance, evaluate under controlled mechanical excitation conditions and when being used by a test subject.
- If any improvements to the designs or material fabrication methods are found, implement and re-evaluate the electrical responses.

1.3 Thesis outline

- **Chapter 1:** This introductory chapter describes the motivations behind the project in the context of the historical and recent developments associated with electronic wearable devices, as well as the challenges that arise from the rapid growth of these technologies. A brief discussion of these aspects leads to the formulation of the aims and objectives of the project, followed by a description of the contents corresponding to each of the chapters presented in this thesis.
- **Chapter 2:** This chapter presents an overview of the concepts, methods, working principles and theory associated with the project. It begins by introducing the reader to the basics of energy harvesting, the different methods that exist for this purpose, and outlines the reasons why a mechanical energy harvesting approach was chosen for this project. This is followed by an introduction to piezoelectric materials, their properties, and a discussion of the differences that exist between 2D and 3D structured materials when used as active cores for mechanical energy harvesting. A variety of ferroelectric polymers and their properties are also discussed in this section. The chapter continues with a section dedicated to electrospinning, including the principles behind the technique and an introduction to the different available techniques. The chapter concludes with the fundamentals of AC signals and the electromechanical characteristics of mechanical energy harvesting devices in general.
- **Chapter 3:** This chapter describes the materials employed in this thesis, as well as the general methods used for fabricating the active cores and generators. The methods used for characterising their mechanical properties, and their electrical response are also outlined, including brief introductions to the working principles of some of the characterisation techniques used. This section also includes information on custom-built devices for mechanical testing.
- **Chapter 4:** In this chapter, the reader will find the experimental work carried out for determining the best fitting electrospinning and solution parameters for the fabrication of ferroelectric polymer polyvinylidene fluoride (PVDF) fibres. A range of favourable parameters for the electrospinning of PVDF polymer solutions is the result of these experimental trials. This data will serve as the basis on which efforts for improving the morphology and adapting the resulting product for wearable integration would be investigated at a later stage. A preliminary overview of the electrospun PVDF as the core of a piezoelectric generator is also presented.
- **Chapter 5:** This chapter presents the experimental work that resulted in the fabrication of electrospun 3D PVDF structures. The use of additives such as lithium chloride (LiCl),

polyethylene glycol oxide (PEO), and carefully controlled ambient and electrospinning conditions allowed for the electrospinning of 3D PVDF structures with tuneable morphologies, which ranged from dense cloud like structures to thick sponge-like non-woven fibre mats. The compatibility of the methods and electrospinning parameters used for obtaining 3D structures for similar copolymers such as PVDF and Trifluoroethylene (TrFE) is demonstrated as well. The electrical response of the resulting materials was characterised by fabricating piezoelectric energy harvesters.

- **Chapter 6:** This chapter describes further work that builds upon the results obtained from the previous chapter. Experimental methods related to improving the active core to electrode interface for the generators presented in the previous chapter. Conductive fabric electrodes and conductive thread, carbon and silver glue, and a combination of copper foils and conductive fabrics were used for exploring methods for further enhancing the response of the proposed generators. This work was inspired by observations done on the experimental work of the previous chapter.
- **Chapter 7:** This chapter provides a conclusion for the research work presented in this thesis. The reader will find a brief presentation of future work, a final reflection on the accomplishment of the goals laid out for the project, and a description of the contributions that this work offers to the field of energy harvesting for wearables.

Keywords: Mechanical energy harvesting, Electrospun materials, 3D electrospinning, Ferroelectric polymers.

1.4 References

- 1 Chardack, W.M., Gage, A.A., Greatbatch, W.: 'Experimental observations and clinical experiences with the correction of complete heart block by an implantable, self-contained pacemaker' *ASAIO J.*, 1961, **7**, (1), p. 286–294.
- 2 Greatbatch, W., Holmes, C.F.: 'History of Implantable Devices: Entrepreneurs, Bioengineers and the Medical Profession, in a Unique Collaboration, Build an Important New Industry' *IEEE Eng. Med. Biol. Mag.*, 1991, **10**, (3), p. 38–41.
- 3 Zoll, P.M., Frank, H.A., Linenthal, A.J.: 'Four-Year Experience with an Implanted Cardiac Pacemaker' *Ann. Surg.*, 1964, **160**, (3), p. 351.
- 4 Bilgutay, A.M., Lillehei, C.W.: 'Treatment of Hypertension With an Implantable Electronic Device' *JAMA*, 1965, **191**, (8), p. 649–653.
- 5 Mirowski, M., Mower, M.M., Reid, P.R.: 'The automatic implantable defibrillator' *Am. Heart J.*, 1980, **100**, (6), p. 1089–1092.
- 6 Fischell, R.E.: 'The Invention of the Programmable Implantable Medication System' *IEEE Eng. Med. Biol. Mag.*, 1989, **8**, (4), p. 65–66.
- 7 Farley, B.E.: 'Medical device industry and the biomedical engineer: Current status and future trends' *Eng. Med. Biol.*, 1989, **8**, (3), p. 27–32.
- 8 Meindl, J.D.: 'Biomedical Implantable Microelectronics' *Science (80-.)*, 1980, **210**, (4467), p. 263–267.
- 9 Stotts, L.J.: 'VLSI applications in implantable medical electronics' *Tech. Dig. - Int. Electron Devices Meet.*, 1989, p. 9–14.
- 10 Stotts, L.J.: 'Introduction to Implantable Biomedical IC Design' *IEEE Circuits Devices Mag.*, 1989, **5**, (1), p. 12–18.
- 11 Sander, C.S., Knutti, J.W., Meindl, J.D.: 'A Monolithic Capacitive Pressure Sensor with Pulse-Period Output' *IEEE Trans. Electron Devices*, 1980, **27**, (5), p. 927–930.
- 12 Manzetti, S., Andersen, O.: 'Toxicological aspects of nanomaterials used in energy harvesting consumer electronics' *Renew. Sustain. Energy Rev.*, 2012, **16**, (4), p. 2102–2110.
- 13 Irnich, W., Bakker, J.M.T. de, Bisping, H.-J.: 'Electromagnetic Interference in Implantable Pacemakers' *Pacing Clin. Electrophysiol.*, 1978, **1**, (1), p. 52–61.

- 14 Eberhard, D.P., Stinebring, R.C.: 'Qualification of high reliability medical grade batteries' *Proc. Annu. Reliab. Maintainab. Symp.*, 1989, p. 356–362.
- 15 Sun, Y., Liu, N., Cui, Y.: 'Promises and challenges of nanomaterials for lithium-based rechargeable batteries' *Nat. Energy* 2016 17, 2016, **1**, (7), p. 1–12.
- 16 Güler, N.F., Übeyli, E.D.: 'Theory and applications of biotelemetry' *J. Med. Syst.*, 2002, **26**, (2), p. 159–178.
- 17 Aileni, R.M., Suciu, G., Suciu, V., Pasca, S., Strungaru, R.: 'Health Monitoring Using Wearable Technologies and Cognitive Radio for IoT' *EAI/Springer Innov. Commun. Comput.*, 2019, p. 143–165.
- 18 Narita, F., Fox, M.: 'A Review on Piezoelectric, Magnetostrictive, and Magnetoelectric Materials and Device Technologies for Energy Harvesting Applications' *Adv. Eng. Mater.*, 2018, **20**, (5).
- 19 Chan, C., Sounderajah, V., Acharya, A., Normahani, P., Bicknell, C., Riga, C.: 'The Role of Wearable Technologies and Telemonitoring in Managing Vascular Disease' *Vasc. Endovasc. Rev.*, 2020, **3**.
- 20 Haghi, M., Thurow, K., Stoll, R.: 'Wearable devices in medical internet of things: Scientific research and commercially available devices' *Healthc. Inform. Res.*, 2017, **23**, (1), p. 4–15.
- 21 Liao, Y., Thompson, C., Peterson, S., Mandrola, J., Beg, M.S.: 'The Future of Wearable Technologies and Remote Monitoring in Health Care' https://doi.org/10.1200/EDBK_238919, 2019, (39), p. 115–121.
- 22 Cheung, C.C., Krahn, A.D., Andrade, J.G.: 'The Emerging Role of Wearable Technologies in Detection of Arrhythmia' *Can. J. Cardiol.*, 2018, **34**, (8), p. 1083–1087.
- 23 Malwade, S., Abdul, S.S., Uddin, M., *et al.*: 'Mobile and wearable technologies in healthcare for the ageing population' *Comput. Methods Programs Biomed.*, 2018, **161**, p. 233–237.
- 24 Ikhlayel, M.: 'Environmental impacts and benefits of state-of-the-art technologies for E-waste management' *Waste Manag.*, 2017, **68**, p. 458–474.
- 25 Abdelbasir, S.M., Hassan, S.S.M., Kamel, A.H., El-Nasr, R.S.: 'Status of electronic waste recycling techniques: a review' *Environ. Sci. Pollut. Res.*, 2018, **25**, (17), p. 16533–16547.
- 26 Rautela, R., Arya, S., Vishwakarma, S., Lee, J., Kim, K.H., Kumar, S.: 'E-waste

- management and its effects on the environment and human health' *Sci. Total Environ.*, 2021, **773**, p. 145623.
- 27 Shittu, O.S., Williams, I.D., Shaw, P.J.: 'Global E-waste management: Can WEEE make a difference? A review of e-waste trends, legislation, contemporary issues and future challenges' *Waste Manag.*, 2021, **120**, p. 549–563.
 - 28 Gollakota, A.R.K., Gautam, S., Shu, C.M.: 'Inconsistencies of e-waste management in developing nations – Facts and plausible solutions' *J. Environ. Manage.*, 2020, **261**, p. 110234.
 - 29 'AR5 Synthesis Report: Climate Change 2014 — IPCC', <https://www.ipcc.ch/report/ar5/syr/>
 - 30 Pi, Z., Zhang, J., Wen, C., Zhang, Z. bin, Wu, D.: 'Flexible piezoelectric nanogenerator made of poly(vinylidene fluoride-co-trifluoroethylene) (PVDF-TrFE) thin film' *Nano Energy*, 2014, **7**, p. 33–41.
 - 31 Hu, P., Yan, L., Zhao, C., Zhang, Y., Niu, J.: 'Double-layer structured PVDF nanocomposite film designed for flexible nanogenerator exhibiting enhanced piezoelectric output and mechanical property' *Compos. Sci. Technol.*, 2018, **168**, p. 327–335.
 - 32 Mahmud, A., Khan, A.A., Voss, P., Das, T., Abdel-Rahman, E., Ban, D.: 'A High Performance and Consolidated Piezoelectric Energy Harvester Based on 1D/2D Hybrid Zinc Oxide Nanostructures' *Adv. Mater. Interfaces*, 2018, **5**, (23), p. 1801167.
 - 33 Li, N., Yi, Z., Ma, Y., *et al.*: 'Direct Powering a Real Cardiac Pacemaker by Natural Energy of a Heartbeat' *ACS Nano*, 2019, **13**, (3), p. 2822–2830.
 - 34 Nozariasbmarz, A., Collins, H., Dsouza, K., *et al.*: 'Review of wearable thermoelectric energy harvesting: From body temperature to electronic systems' *Appl. Energy*, 2020, **258**, p. 114069.
 - 35 Yu, Y., Sun, H., Orbay, H., *et al.*: 'Biocompatibility and in vivo operation of implantable mesoporous PVDF-based nanogenerators' *Nano Energy*, 2016, **27**, p. 275–281.
 - 36 Park, J., Bhat, G., NK, A., Geyik, C.S., Ogras, U.Y., Lee, H.G.: 'Energy per Operation Optimization for Energy-Harvesting Wearable IoT Devices' *Sensors 2020, Vol. 20, Page 764*, 2020, **20**, (3), p. 764.
 - 37 Wang, S., Jiang, Y., Tai, H., *et al.*: 'An integrated flexible self-powered wearable respiration sensor' *Nano Energy*, 2019, **63**, p. 103829.

- 38 Sun, H., Zhang, Y., Zhang, J., Sun, X., Peng, H.: 'Energy harvesting and storage in 1D devices' *Nat. Rev. Mater.* 2017 26, 2017, **2**, (6), p. 1–12.
- 39 Hyeon, D.Y., Park, K.-I.: 'Vertically Aligned Piezoelectric Perovskite Nanowire Array on Flexible Conducting Substrate for Energy Harvesting Applications' *Adv. Mater. Technol.*, 2019, **4**, (8), p. 1900228.
- 40 Aleksandrova, M.: 'Polymeric seed layer as a simple approach for nanostructuring of Ga-doped ZnO films for flexible piezoelectric energy harvesting' *Microelectron. Eng.*, 2020, **233**, p. 111434.
- 41 Jing, Q., Kar-Narayan, S.: 'Nanostructured polymer-based piezoelectric and triboelectric materials and devices for energy harvesting applications' *J. Phys. D. Appl. Phys.*, 2018, **51**, (30), p. 303001.
- 42 Chowdhury, A.R., Jaksik, J., Hussain, I., *et al.*: 'Multicomponent nanostructured materials and interfaces for efficient piezoelectricity' *Nano-Structures & Nano-Objects*, 2019, **17**, p. 148–184.
- 43 Mokhtari, F., Spinks, G.M., Fay, C., *et al.*: 'Wearable Electronic Textiles from Nanostructured Piezoelectric Fibers' *Adv. Mater. Technol.*, 2020, **5**, (4), p. 1900900.
- 44 Kammel, R.S., Sabry, R.S.: 'Effects of the aspect ratio of ZnO nanorods on the performance of piezoelectric nanogenerators' *J. Sci. Adv. Mater. Devices*, 2019, **4**, (3), p. 420–424.
- 45 Briscoe, J., Jalali, N., Woolliams, P., *et al.*: 'Measurement techniques for piezoelectric nanogenerators' *Energy Environ. Sci.*, 2013, **6**, (10), p. 3035–3045.
- 46 Mishra, S., Unnikrishnan, L., Nayak, S.K., Mohanty, S.: 'Advances in Piezoelectric Polymer Composites for Energy Harvesting Applications: A Systematic Review' *Macromol. Mater. Eng.*, 2019, **304**, (1), p. 1800463.
- 47 Eltouby, P., Shyha, I., Li, C., Khaliq, J.: 'Factors affecting the piezoelectric performance of ceramic-polymer composites: A comprehensive review' *Ceram. Int.*, 2021, **47**, (13), p. 17813–17825.
- 48 Sezer, N., Koç, M.: 'A comprehensive review on the state-of-the-art of piezoelectric energy harvesting' *Nano Energy*, 2021, **80**, p. 105567.
- 49 Onuki, Y., Bhardwaj, U., Papadimitrakopoulos, F., Burgess, D.J.: 'A Review of the Biocompatibility of Implantable Devices: Current Challenges to Overcome Foreign Body Response' *J. Diabetes Sci. Technol.*, 2008, **2**, (6), p. 1003–1015.

- 50 Saroia, J., Yanen, W., Wei, Q., Zhang, K., Lu, T., Zhang, B.: 'A review on biocompatibility nature of hydrogels with 3D printing techniques, tissue engineering application and its future prospective' *Bio-Design Manuf.*, 2018, **1**, (4), p. 265–279.
- 51 Sunwoo, S.-H., Ha, K.-H., Lee, S., Lu, N., Kim, D.-H.: 'Wearable and Implantable Soft Bioelectronics: Device Designs and Material Strategies' *Annu. Rev. Chem. Biomol. Eng.*, 2021, **12**, (1), p. 359–391.
- 52 Chen, Z., Chen, Y., Hedenqvist, M.S., *et al.*: 'Multifunctional conductive hydrogels and their applications as smart wearable devices' *J. Mater. Chem. B*, 2021, **9**, (11), p. 2561–2583.
- 53 Todaro, M.T., Guido, F., Algieri, L., *et al.*: 'Biocompatible, Flexible, and Compliant Energy Harvesters Based on Piezoelectric Thin Films' *IEEE Trans. Nanotechnol.*, 2018, **17**, (2), p. 220–230.
- 54 Jin, H., Abu-Raya, Y.S., Haick, H.: 'Advanced Materials for Health Monitoring with Skin-Based Wearable Devices' *Adv. Healthc. Mater.*, 2017, **6**, (11), p. 1700024.
- 55 Huang, W., Tong, Z., Wang, R., *et al.*: 'A review on electrospinning nanofibers in the field of microwave absorption' *Ceram. Int.*, 2020, **46**, (17), p. 26441–26453.
- 56 Garnett, E., Mai, L., Yang, P.: 'Introduction: 1D Nanomaterials/Nanowires' *Chem. Rev.*, 2019, **119**, (15), p. 8955–8957.
- 57 Zhong, H., Huang, J., Wu, J., Du, J.: 'Electrospinning nanofibers to 1D, 2D, and 3D scaffolds and their biomedical applications' *Nano Res.*, 2022, **15**, (2), p. 787–804.
- 58 Ding, B., Li, C., Miyauchi, Y., Kuwaki, O., Shiratori, S.: 'Formation of novel 2D polymer nanowebs via electrospinning' *Nanotechnology*, 2006, **17**, (15), p. 3685–3691.
- 59 Lin, W., Chen, M., Qu, T., Li, J., Man, Y.: 'Three-dimensional electrospun nanofibrous scaffolds for bone tissue engineering' *J. Biomed. Mater. Res. Part B Appl. Biomater.*, 2020, **108**, (4), p. 1311–1321.
- 60 Fuh, Y.K., Wang, B.S.: 'Near field sequentially electrospun three-dimensional piezoelectric fibers arrays for self-powered sensors of human gesture recognition' *Nano Energy*, 2016, **30**, p. 677–683.
- 61 Chen, H., Peng, Y., Wu, S., Tan, L.P.: 'Electrospun 3D Fibrous Scaffolds for Chronic Wound Repair' (2016), 9
- 62 Keirouz, A., Chung, M., Kwon, J., Fortunato, G., Radacsi, N.: '2D and 3D electrospinning technologies for the fabrication of nanofibrous scaffolds for skin tissue

- engineering: A review' *WIREs Nanomedicine and Nanobiotechnology*, 2020, **12**, (4), p. e1626.
- 63 Duan, Y., Ding, Y., Bian, J., *et al.*: 'Ultra-Stretchable Piezoelectric Nanogenerators via Large-Scale Aligned Fractal Inspired Micro/Nanofibers' *Polymers (Basel)*., 2017, **9**, (12), p. 714.
- 64 Persano, L., Dagdeviren, C., Su, Y., *et al.*: 'High performance piezoelectric devices based on aligned arrays of nanofibers of poly(vinylidene fluoride-co-trifluoroethylene)' *Nat. Commun.*, 2013, **4**, (1), p. 1633.
- 65 Vong, M., Diaz Sanchez, F.J., Keirouz, A., Nuansing, W., Radacsi, N.: 'Ultrafast fabrication of Nanofiber-based 3D Macrostructures by 3D electrospinning' *Mater. Des.*, 2021, **208**, p. 109916.
- 66 Arrigoni, A., Brambilla, L., Bertarelli, C., Serra, G., Tommasini, M., Castiglioni, C.: 'P(VDF-TrFE) nanofibers: Structure of the ferroelectric and paraelectric phases through IR and Raman spectroscopies' *RSC Adv.*, 2020, **10**, (62), p. 37779–37796.
- 67 Kim, M., Wu, Y., Kan, E., Fan, J.: 'Breathable and Flexible Piezoelectric ZnO@PVDF Fibrous Nanogenerator for Wearable Applications' *Polymers (Basel)*., 2018, **10**, (7), p. 745.

Chapter 2

Literature Review

2.1 Energy harvesting overview

2.1.1 Energy demands of implantable and wearable electronics

The concept of wearable and implantable sensing systems has evolved from describing those that integrate additional functions such as self-diagnosis [1] into the inclusion of more advanced features such as self-calibration and self-compensation [2]. Some examples of desirable features are improved accuracy, precision and sensitivity while minimizing the effects of drift, noise, interference from cross-reactants and other artefacts. The additional elements that allow sensing systems to perform such tasks can be implemented on software as compensation algorithms [3] or additional on-chip analogue or mixed signal processing blocks [4], just to mention a few of the possible techniques available.

Typically, along with the previously discussed added features, wearable devices often require additional data storage, transmission and energy management modules tailored for the intended application. Figure 2-1 shows the general architecture of a wearable system [5].

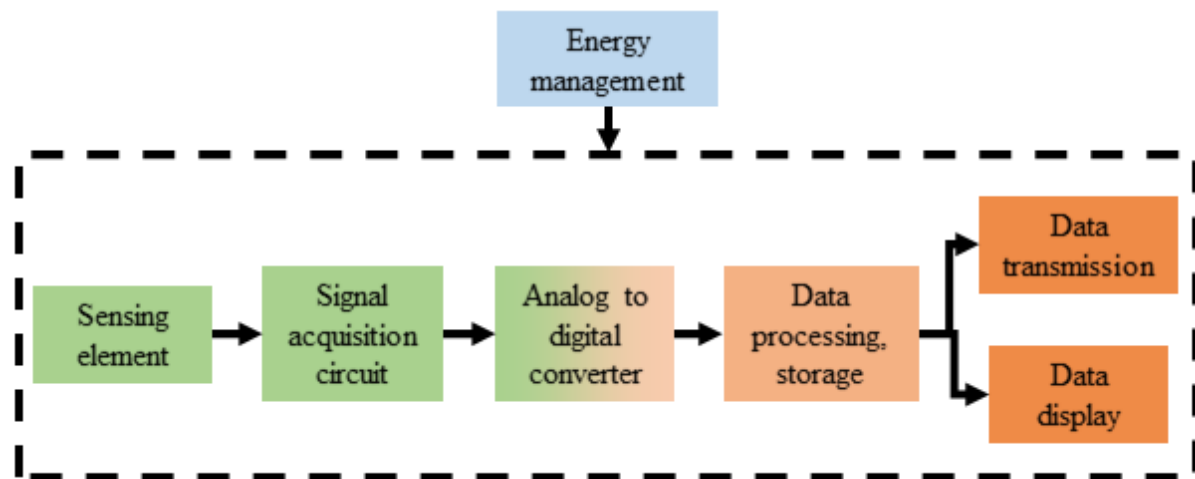


Figure 2-1: Simplified architecture of a wearable system.

System design that allows for added features that improve device performance and its capabilities will demand more processing power and additional or improved instrumentation

when compared with a simplistic one. Currently, blocks that are often found in wearable devices such as voltage regulators, amplifiers and radio frequency (RF) transmitters have been shown to consume power in the order of tens of microwatts (μW) up to tens or hundreds of milliwatts (mW) individually [6–8]. Using combinations of these building blocks, some designs may adopt a fully on-chip integrated approach or rely on discrete components to build the system. Some applications will require continuous-sampling approaches while, for others, sample recording only after long time intervals have elapsed may suffice; these fundamental differences will determine the energy needs of the device. Considering current power consumption figure estimates, the energy needs of a system would range from the tens of μW for very simple devices to possibly tens or hundreds of mW for the more complex ones. A low-power design approach both in terms of hardware and algorithms running the device can further prolong battery life for these systems [9]. However, the most demanding would still require frequent recharging or would need to accommodate for larger batteries to satisfy their power needs. Energy harvesting elements offer an alternative power source that may be successfully integrated into any design as a complementary or main power source.

Energy harvesters are often regarded as secondary power sources that extend and maximise the lifespan of primary power sources. However, whether powering up the simplest or the more complex systems, energy harvesters have shown the potential to become reliable and independent power sources. For instance, a very low voltage, fully integrated continuous-sampling device was built with both the sensor and the energy harvester being implemented as a single functional module [10]. Devices that solely depend on energy harvesters are often referred to as self-powered, independently of it being a device that obtains its energy from the very same process it is intended to sense or from scavenging from another energy source.

Considering all current developments, energy harvesters can complement other power sources and, in some instances, provide sufficient power to drive wearable sensing devices independently. However, several energy harvester iterations still have output power figures that would not fully cover the energy needs of the more complex designs. Literature often shows promising output power figures which have been obtained under carefully controlled experimental conditions; actual performance in vivo will most likely be afflicted severely due to variations in the environment and the condition of the end user. For instance, the presence of an analyte in a bodily fluid required by a biofuel cell will change depending on the current time and what kinds of activities the end-user has been doing. Still, energy harvesters have been observed to be compatible with low-power designs and self-powered schemes. With new implementations and improvements on existing schemes being under development, the outlook for energy harvesters as an alternative source for providing power for a broad range

of wearable devices is promising. The following sections will present a general description of the most common energy harvesting techniques.

2.1.2 Enzymatic biofuel cells

An enzymatic biofuel cell (EBFC) can be defined as a device that obtains electrical energy from biochemical reactions, using enzymes as the catalysts that convert biological fuels into electrical energy, typically relying on a pair of functionalized bio-electrodes or a bio-anode paired with a non-biological cathode [11]. At a fundamental level, EBFCs rely on redox reactions for supplying an electrical current for a load. The power density performance of these cells is a function of parameters associated with the selected biofuel, electrode geometry and structure, additives, and substrate material selection.

Initial implementations of these devices required membranes for isolating the reactions occurring at each electrode. By selecting bio-cathode/bio-anode pairs functionalized with carefully selected enzymes, newer generations of EBFCs architectures no longer need a membrane or separate compartments. Enzyme selectivity can be used to effectively avoid crossover between the reactions occurring at each electrode, thus allowing the setup to be dimensionally compact while preventing the shorting of the electrodes [12].

The addition of mediators that can facilitate electron transfer, the fabrication of micro or nanostructures on the electrodes or the fabrication of artificial enzyme mimic structures is directly linked to power density figure enhancement. The inclusion of micro and nanostructures aids electron transfer by physically reducing the distance between the electrode and the active sites of the enzymes, which are often hidden deep within the structure of the protein. Since the rate of electron transfer between enzymatic active sites and electrodes decays exponentially as a function of the distance between them [13], bringing the active site as close as possible to the electrode via nanoscale structures would increase the efficiency of the electron capture process. The fabrication of artificial enzymes that are more stable, easier to immobilize and possibly more active would result in functionalized electrodes with a longer lifespan and thus more reliable power density figures [12]. Additionally, since protein electron transfer rates are closely linked to the distance between donor and acceptor sites, modifying or creating structures that bring these sites closer together may increment the rate of electron transfer [14].

EBFCs have the potential to power up complex, fully integrated wearable systems as well as being suitable for implementing self-powered biosensors. As long as the biofuel concentration remains within an optimal level and other essential analytes such as oxygen are not depleted in the probed fluid, EBFCs are capable of providing a constant figure of power density within

a range of physiological concentrations of the target analyte. However, EBFCs have relatively low open circuit voltage (V_{OC}), which may require stacking many functional units to rise the voltage and will require additional instrumentation for conditioning the harvested energy. Typical V_{OC} values for a single unit can reach up to hundreds of mV under controlled conditions, which often deviate significantly from those found in vivo. However, they do have the potential to offer a relatively high current density as long as the enzymatic loading density is enhanced [15]

2.1.3 Triboelectric generators

Kinetic energy harvesting has attracted much attention given the presence of residual mechanical vibrations and friction present in the environment and living organisms [16]. When two different materials come into frictional contact and separate, the resulting charge separation and distribution in the materials can be harnessed as a power source [17]. The tendency of a material to either accumulate positive or negative charges, as well as how easily it can achieve that, is illustrated on a scale known as the triboelectric series. Although materials are ordered relative to their interactions with others, it is claimed that the series remains consistent across a wide spectrum of material families [18].

The working principle of triboelectric generators (TEGs) can be described as a four-stage process. The first stage corresponds to when the surfaces of two materials that are on opposite sides of the triboelectric series come into contact with each other. Charge transfer between them is promoted, often resulting in charge accumulation along the contact area. The second stage occurs when the surfaces are being separated. The opposite ends of the surfaces that were in contact will experience charge build up due to electrostatic induction. When this occurs, if the external surfaces are connected to a load, it is possible to induce a current flow on it. The third stage happens as, after separation, charges recombine, thus polarization will be neutralized on the materials. The last stage occurs as the materials are brought together again, resulting in charge induction and a current will flow through the load, but the direction will be reversed relative to that observed in the second stage. It is the cyclic separation and union of the surfaces that results in energy generation [19].

TEGs can deliver V_{OC} values in the range of hundreds of volts and, depending on the design and post-processing done on the surfaces, and can be implemented in forms such as fabrics due to their flexibility. However, the short circuit current (I_{SC}) figures are lower than those obtained from EBFCs. The output voltage and current of TEGs are not a DC waveform, thus requiring additional instrumentation for rectifying and conditioning the obtained signals.

However, they do offer flexible solutions that can be easily adapted for wearables such as wristbands or clothing.

2.1.4 Piezoelectric generators

The piezoelectric effect can be defined as the generation of a voltage across a material that is exposed to a mechanical stimulus [16]. Crystalline materials with specific structures exhibit piezoelectric properties. Under no strain, crystal subunits are electrically neutral. When subjected to a mechanical deformation, dipole charges align, resulting in a net electric polarization on the material [20]. Taking zinc oxide crystals as an example, the undisturbed tetrahedral crystal subunits of the material will exhibit a neutral polarity given that both charge centres for their respective positive and negative charges are coincident. When an external force is applied to the material, the mechanical deformation will cause those charge centres to separate, causing the formation of a dipole [21]. Polymers and ceramics exhibit piezoelectric properties, with the former having the advantage of being flexible and less brittle than ceramics. However, their electromechanical coupling constants, generally used as a measure of performance for piezoelectric materials, are comparatively low to those found in ceramics [22].

While recent examples will show that both ceramics and polymers have been successfully employed for developing PEGs, device architecture and the approach used for their implementation can vary significantly, with some proposals being flexible enough to be easily integrated into textiles while others would be limited to rigid structures [23–25]. In general terms, the performance of PEGs depends on the piezoelectric strain coefficient d_{ij} , a parameter that measures the electric polarisation generated in the material in direction i as a response to a mechanical stress applied to the material in direction j [26].

Piezoelectric generators (PEGs) can have an output of tens to hundreds of Volts. However, their output currents are in the nA to μ A range. Similar to what was discussed for TEGs, the output of these devices is in the form of an AC signal. Thus, additional instrumentation for rectifying and converting these signals to DC values will be required. Several examples of the integration of PEGs into wearable systems have been documented, with applications ranging from smart textiles, shoe pads, and backpack straps, among others [23, 26, 27].

2.1.5 Thermoelectric generators

The thermoelectric effects were first described by Seebeck, Peltier and Thomson. These refer to electrical and thermal effects that occur when a material is exposed to a temperature gradient, to an electrical current or both. The Seebeck effect consists of the generation of an

electric potential difference when two surfaces with different temperatures come into contact. A thermoelectric generator (ThEG) converts a portion of the thermal energy into electrical energy using an arrangement of thermoelectric materials thermally in parallel and electrically in series [28]. The output of a ThEG is a function of the temperature difference ΔT and the figure of merit of the thermoelectric materials employed ZT [28–30].

ThEG layout design plays an important role for determining the observed surface power density figures of the device. For instance, using flexible materials for manufacturing the layers that surround the thermoelectric couples enhances the power density figure because it facilitates contact with the heat source, which would help reduce the thermal interface resistance between that surface and the device [31]. Another important consideration is that, while this family of generators is capable of outputting a constant power figure given that, physiologically, the temperature of the human body surface is relatively stable, ambient conditions do have a critical effect on their efficiency. For example, the power figure obtained from a person at rest will be much lower than that observed from someone who is on the move. The reason is that incident airflow on the ‘cool’ surface increments the temperature differential across the device, resulting in an increased electron-hole pair production [31].

ThEGs provide a constant power output figure under steady-state conditions, which is one of its greatest advantages since it is not limited by variations in analyte concentration or lack of mechanical stimulus. However, this figure tends to stabilize at an equilibrium point which is often well below the estimated temperature differential for a system mainly because of poor insulation and heatsink design.

2.1.6 Hybrid energy harvesters

Individually, the previously discussed energy harvesting families have limitations that would affect their feasibility as an individual power source of a wearable device. Hybrid energy harvesters, which could be defined as devices that combine different harvester families in a single system, address those limitations by increasing the situational coverage of power generation.

The integration of two or more different types of energy harvesters can increase the likelihood of an energy harvesting system to work in practical situations by allowing for the extraction of energy from more than a single source. For instance, the combination of a ThEG with a TEG would allow for a system to obtain a constant output from the ThEG when no motion is occurring and an enhanced output when the user starts to move. Another advantage of hybrid systems is that they may also be able to operate over an enhanced range of electrical loads. For PEGs and TEGs, power extraction is maximised when the electrical load has a high

impedance value, typically over 1 M Ω . For ThEGs, the most efficient extraction occurs at comparatively very low loads, often below 10 Ω . Combining these two energy harvesting approaches would result in a system that can adapt to two different ranges of electrical loads, which could be advantageous for smart, adaptable systems that can switch and match loads depending on the situation.

2.1.7 Comparing the different energy harvesting techniques

The idea of having a complex system being reliant entirely on energy harvesters as a power source gets increasingly difficult as the implementation scenario gets closer to what can be found in practice. The selection of the type of energy harvester to use is also of great importance, mainly because of the situational limitations associated with the implementation of the system.

EBFCs offer the greatest current densities with V_{OC} s in the order of tens of millivolts. As outlined previously, this family of generators is heavily dependent on the concentration of an analyte, which is most likely variable due to multiple factors related to metabolic differences between users [32]. The encapsulation of the device would also add another layer of difficulty to the implementation of EBFCs. The designer would have to consider the best scheme for maximizing the exposition of the EBFC to the analyte, keeping the effect of cross-reactants at a minimum and possibly dealing with diffusion rates for chemicals which might take some time for being replenished in the probed medium. In terms of energy conversion and management, EBFCs have an advantage in being a DC power source. The instrumentation required for power conditioning, typically a DC-DC converter that adjusts the EBFC output into a higher voltage but lower current, offers relatively better efficiency with less complex designs when compared with AC to DC conversion. Basic AC to DC conversion techniques typically require a secondary DC-DC converter to condition the intermediate stage DC-like power into true DC, as seen from works that discuss on the efficiency of the converters used for mechanical energy harvesters [33].

Mechanical energy harvesters offer higher V_{OC} figures and arguably offer the most flexible formats that are capable of being integrated into clothing and other accessories that are compatible with wearable design. However, the current output is typically low and the instrumentation needed for conditioning the raw output power of the generator can be complicated, often requiring more processing stages. This can be addressed by tailoring the instrumentation to the needs of the device; the inclusion of an advanced AC-DC conversion module with a feedback control architecture can potentially increase the conversion efficiency figure by having power scavenging occurring only at those moments when the available energy is sensed to be at a maximum. These improvements are often achieved by techniques

that employ switching devices, such as synchronized switch harvesting on inductor or synchronous electric charge extraction [34, 35].

ThEGs provide a constant power output figure under steady state conditions, which is one of its greatest advantages since it is not limited by variations in analyte concentration or lack of mechanical stimulus. However, this figure tends to stabilize at an equilibrium point which is often well below the ideal ΔT because of poor insulation and challenging heatsink design. Typically, the V_{OC} of these devices will be close to tenths of millivolts with current levels closer to the μA level, placing these devices in between EBFCs and mechanical energy harvesters.

Thus far, a general overview of the capabilities of each type of energy harvester has been provided. While the nature of their output signals and fundamental characteristics are shared within each family, the output V_{OC} , I_{SC} and estimated power figures can be enhanced by the introduction of new materials, fabrication methods or architectures. Table 2-1 provides some examples of the measured outputs of different types of energy harvesters belonging to the groups discussed in the previous sections.

Table 2-1: A list of energy harvesters belonging to each of the four families discussed in this text.

Architecture or Materials	Maximum Open Circuit Voltage (mV)	Maximum Short Circuit Current (μA)	Maximum Current Density ($\mu\text{A} \cdot \text{cm}^{-2}$)	Maximum Power Density Figure ($\mu\text{W} \cdot \text{cm}^{-2}$)	Conditions	Reference
EBFCs						
Hybrid EBFC	459.6		28.9	1.3 at 90mV	Oxygen bubbled Phosphate Buffer solution (PBS) with 20mM Glucose	[36]
Graphite electrodes with pyranose dehydrogenase.	650		410	275 at 300mV	5mM Glucose in PBS	[37]
Paper based glucose EBFC	570		148	46 at 310mV	1M PBS with 100mM glucose	[38]
Gas/Liquid porous diaphragm EBFC	700		285	70.7 at 300mV	5mM glucose	[39]

EBFC based on a 3D gold coated nickel foam	580	9040	2320 at 350mV	PBS with 100mM glucose	[15]
Carbon cloth electrode with hydrogel containing cholesterol oxidase	109		11.4 at 53mV	0.5mM cholesterol solution	[40]
Gold nanoparticles on bacterial cellulose EBFC, glucose oxidase and laccase	500	2800 (per cm^3)	345.14 at 247mV (per cm^3)	50mM glucose	[41]
Compressed carbon nanotube electrodes with glucose dehydrogenase and laccase.	681.8	202.2	67.86 at 335mV	45mM glucose	[42]

Stretchable skin EBFC, silver and lactate	500	1100		1200 at 200mV	20mM lactate	[43]
Lactate Oxidase and dehydrogenase EBFC	800	1600	760	380	14mM lactate, 0.1mM glucose, 17mM urea and 0.8mM table salt	[44]
Triboelectric						
Hydrogel based generator, PDMS, aluminium and nickel fabric	200k peak-to- peak	22.5 peak-to- peak		31.25	Bending frequency of 2Hz	[45]
Rotating disk scheme, copper stator/rotor	240k peak-to- peak	2200 peak-to- peak			500rpm	[46]
3D orthogonal woven textile, PDMS and steel yarn	45k peak-to-peak	2.2 peak-to-peak	0.55	26.33	Tapping at 3Hz	[47]
Generator formed from multiple silicone	200k peak-to- peak	200 peak-to-peak		76	Excitation at 5Hz	[48]

coated steel threads.						
Aluminium and kapton half generator with several contact materials						
	300k peak-to-peak	610 peak-to-peak		0.013	Excitation at 1 Hz	[49]
Thin, on-skin generator, made of 2 elastomer films and carbon grease.						
	115k peak-to-peak	5 peak-to-peak		10		[50]
Copper electrode covered in kapton, mercury acts as a tribocouple.						
	800k peak-to-peak	16 peak-to-peak		670	Excited at 2.5Hz	[51]
Piezoelectric						
Self-powered cardiac pacemaker						
	8k peak-to-peak	145 peak-to-peak			Excited at 0.3Hz	[52]

ZnO nanorod array between silver paste and nylon fabric substrates	8k peak-to-peak	0.035 peak-to-peak		Excited at roughly 1Hz	[24]
Boron Nitride nanowires encased within PDMS	50k peak-to-peak	0.280 peak-to-peak		Excited at 11Hz	[53]
Fibre-based generators, PVDF and low density PE.	3k peak-to-peak	0.0012 peak-to-peak		Single fibre tested, 83mHz	[54]
Barium titanate nanoparticles, silver and alginate 'worm' generator	5.5k peak after rectification	0.590 peak after rectification		Excited at 20Hz	[55]
Sponge-Like Piezoelectric Polymer Films	11.1 k peak-to-peak	9.7 peak-to-peak		Operated at 40 Hz	[56]
Bioinspired elastic	25k peak-to-peak	0.55 peak-to-peak	2.6	Maximum output power recorded	[57]

piezoelectric composite		at a load value of 400 MΩ			
Flexible piezoelectric nanogenerator made of PVDF-TrFE thin film					[58]
Double-layer structured PVDF nanocomposite film					[59]
Thermoelectric					
Stretchable inorganic-organic generator	18		0.017	ΔT of 75 °C	[60]
Silk fabric-based generator	10		0.015	ΔT of 35 °C	[61]
Woven yarn thermoelectric textiles	14.8		0.21	ΔT of 55 °C	[62]

2.1.8 The case for mechanical energy harvesting

In the previous section, the characteristics of each family harvesting technique were discussed. In the context of energy harvesting for wearable devices, some of the previously mentioned families would have more favourable working conditions than others. For example, EBFCs have the advantage of generating power in the form of a DC signal. However, their output depends on the concentration of particular analytes; thus, the available output power would vary over time and at different rates depending on what activity levels the end-user is having. Perhaps the most challenging aspect of designing an EBFC for a wearable device would be devising a strategy for the non-invasive collection of the bodily fluids. Instances of self-powered systems based on EBFCs with such collections systems have been demonstrated, with the most advanced ones integrating microfluidic devices for sample collection and flexible electrodes, substrates, and interfaces for constructing the system. However, the use of such collection techniques is still in a developmental stage and the implementation of low-cost and flexible electrodes and substrates has yet to be achieved [63].

ThEGs offer the possibility of a relatively constant DC power output. However, similar to what has been mentioned about EBFCs, the design of ThEGs for wearable devices is still limited by elevated costs and reduced flexibility; the cost of the active materials and electrodes, the lack of cheap, flexible, and high ZT materials, and the relatively low ΔT that exists between the ambient and the human body are some of the main challenges to address when designing a wearable ThEG [30].

Both PEGs and TEGs have the advantage of being compatible with a wide range of low-cost fabrication techniques and of being highly flexible depending on material selection [64]. Approaches such as screen printing, spin coating, mould casting, electrospinning, and extrusion can be used for fabricating functional materials for mechanical energy harvesting and for developing the interfaces needed for harnessing their output power [64, 65]. For both of these types of devices, the maximum output power that can be extracted from the device occurs at a higher resistive load value than that observed for ThEGs or EBFCs, with average figures for both types of mechanical energy harvesting approaches being on the range of single digits to hundreds of $M\Omega$ [66–68]. The output power density that can be obtained from both these kind of devices is in the order of 100 nW to 100 $\mu W\ cm^{-2}$; while it is true that this figure is relatively lower than those observed for EBFCs operating in ideal conditions [30, 63], the low-cost of implementation and the diverse types of flexible materials that can be used to design a mechanical energy harvesting device coupled with the range of obtainable output power density figures were the aspects that led to the decision of exploring mechanical energy harvesting for the work presented in this project.

Piezoelectric energy harvesting was selected over triboelectric energy harvesting mainly due to the relatively higher output current that these type of generators can source when compared to triboelectric generators [66, 69]. TEGs tend to have higher peak-to-peak output voltage figures, generally one order of magnitude greater than those observed for PEGs [64, 69]. However, when considering the output power of both devices, TEGs have slightly higher figures.

From the perspective of the electronic design for the interfacing circuits and other instrumentation needed for harvesting the energy, dealing with inputs signals in the range of hundreds of volts would require additional functional blocks for component protection [70]. The instrumentation needed for harvesting the AC waveforms produced by both these types of generators is very similar otherwise.

Taking into consideration the differences between PEGs and TEGs discussed previously, the focus of this project will be directed to PEGs. However, the work undertaken for this thesis should be open to the development of a hybrid system considering how advantageous that would be for the performance of an energy harvesting device.

2.2 Piezoelectricity

A very brief overview of piezoelectricity was covered in section 2.1.4. This section presents a more detailed of piezoelectric effect theory, types of materials and the behaviour of polymer-based piezoelectric structures.

2.2.1 The piezoelectric effect

As described in the previous sections, the piezoelectric effect can be defined as a property of some materials for becoming electrically polarised when under mechanical stress, or vice versa [71]. Not every type of material has this property; only some crystalline materials are piezoelectric. Crystalline materials are classified into one of 32 crystallographic classes depending on their symmetry. Only 20 out of 32 groups do not have a defined centre of symmetry and can exhibit polarisation, thus, allowing these materials to show separate, opposite charge centres when the material is deformed mechanically [72]. Of these 20 groups, some will only get polarised when subjected to mechanical stress while others will be inherently polarised. These groups are classified under the category of pyroelectrics, since they not only get polarised under mechanical stress but also by changes in temperature. Among the group of pyroelectrics, there is one more subset for which the axis of polarisation can be modified when exposing the material to a very high electric field. These materials are known as ferroelectrics [73]. These will be discussed at a later stage in this section.

Crystals are highly ordered materials composed of repeating units of a fundamental entity known as the unit cell [74]. The atoms constituting a unit cell can be described within an arbitrary three-dimensional coordinate system, with the lengths and angles describing the unit cell relative to a three-dimensional Cartesian coordinate system being defined as the lattice constants of the unit cell. Considering operations such as rotations, inversions, reflections, among others, it is possible to reduce the whole universe of possible structures into the 32 general symmetry groups mentioned previously [74]. Thus, any unit cell can be described in a three-dimensional space as belonging to one of those crystallographic classes groups. Some of these classes are grouped into six systems depending on the number of mirror planes, inversion axes, among other characteristics that are common to them [75].

The polarisation of a material as a response to mechanical stress is referred to as the direct piezoelectric effect, with the opposite being referred to as the indirect piezoelectric effect [71, 76]. Equation 2.1 shows an simplified expression for the direct piezoelectric effect, and Equation 2.2 shows one for the indirect effect [77]. D represents the electric displacement, T_m is the stress, s_m is the strain, E is electric field, the subscripts i represent a three-dimensional

coordinate plane system and m represents a direction parallel to one of the axis or a rotation relative to one of the axis [77].

$$\text{Equation 2.1} \quad D_i = d_{im}T_m$$

$$\text{Equation 2.2} \quad s_m = d_{im}E_i$$

The d_{im} term represents a piezoelectric tensor, and has units of coulombs per Newton. In rough terms, a tensor is a mathematical object that allows for proportionally relating a set of conditions with others. In the case of the direct piezoelectric effect, a piezoelectric tensor or coefficient relates the change in net polarisation arising from the deformation of the material to the applied stress mediating that deformation. The net polarisation is a vector and can be described relative to the planes of the three-dimensional Cartesian coordinate system, and thus can be indexed as 1, 2, and 3. The applied stress is also a vector, and describes stress exerted along the three axis of the coordinate system and also for rotations occurring along these, thus being indexed 1 to 3 for stress applied along an axis and 4 to 6 for shear stress [77–79]. It is of interest to note that the applied stress vector would in reality involve not just six possible states but nine. However, given that stress and strain are symmetrical, three pairs can be reduced [75]. The group of piezoelectric tensors is thus a 3·6 matrix. The vector and matrix representation of equation 2.1 is shown in Equation 2.3.

$$\text{Equation 2.3} \quad \begin{bmatrix} D_1 \\ D_2 \\ D_3 \end{bmatrix} = \begin{bmatrix} d_{11} & d_{12} & d_{13} & d_{14} & d_{15} & d_{16} \\ d_{21} & d_{22} & d_{23} & d_{24} & d_{25} & d_{26} \\ d_{31} & d_{32} & d_{33} & d_{34} & d_{35} & d_{36} \end{bmatrix} \cdot \begin{bmatrix} T_1 \\ T_2 \\ T_3 \\ T_4 \\ T_5 \\ T_6 \end{bmatrix}$$

Each piezoelectric tensor represents the change in polarisation occurring on the surface of the material relative to a reference direction as a response to stress applied to the surface of the material. This is more easily explained in Figure 2-2. Figure 2-2a shows a solid in a three-dimensional space. In figure 2-2b, polarisation along axis 3 occurs when applying a compressive stress on the surfaces of the object lying in the 1-2 plane can be described by the piezoelectric tensor d_{33} . Applying a shear stress on the surface of the object along the 1-3 plane, as shown in figure 2-2c and observing a polarisation oriented along the positive axis labelled 1 can be described by the piezoelectric tensor d_{15} .

Depending on the type of crystal being considered, an applied stress might not result in a net electrical polarisation, thus, the corresponding piezoelectric tensor is effectively zero in that case. Thus, the responses of individual crystal classes depend on their particular symmetry can be associated to a specific piezoelectric tensor matrix [80, 81]. Figure 2-3 illustrates this by showing the piezoelectric tensor matrix associated with a polar crystal belonging to the

tetragonal system category [80, 82]. It is important to note that the previous discussion mostly applies to a single crystal unit cell.

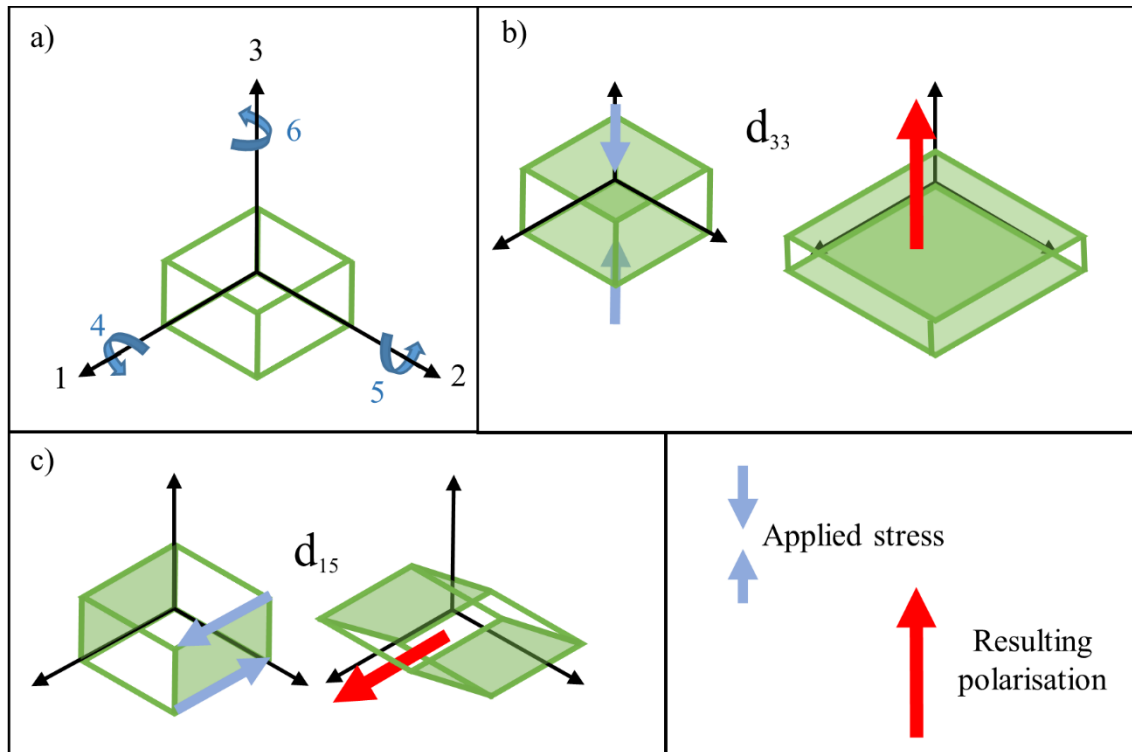
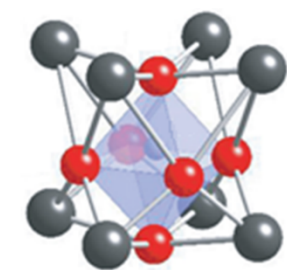


Figure 2-2: (a) Reference three-dimensional place notation used for describing piezoelectric tensors. (b) Tensor d_{33} describes polarisation observed along axis 3 when compressive stress is applied relative to axis 3. (c) Tensor d_{15} describes polarisation observed along axis 1 when shear stress is applied relative to the rotation labelled as 5. Adapted from [79].



Ditetragonal-pyramidal
class crystal

$$\begin{bmatrix} 0 & 0 & 0 & 0 & d_{15} & 0 \\ 0 & 0 & 0 & d_{15} & 0 & 0 \\ d_{31} & d_{31} & d_{33} & 0 & 0 & 0 \end{bmatrix}$$

Associated piezoelectric
tensor matrix

Figure 2-3: Each crystal class can be related to a specific tensor matrix depending on its symmetry. Adapted from [80] and [82].

As mentioned previously, ferroelectrics are a subtype of piezoelectric materials characterised by having spontaneous electric polarisation, and the observed polarisation can be

manipulated by the application of a very strong external electric field [76, 83, 84]. The procedure of reorienting the dipoles in a material by means of applying a strong, external electric field is known as poling. Ferroelectric materials can be considered to be systems with memory, since the dipole orientation acquired after poling will remain, ideally until the material is exposed once again to an external electric field [76, 83, 84]. A representation of the process of poling is illustrated in Figure 2-4. Figure 2-4 a shows discrete ferroelectric units immersed in an unspecified medium that won't react to an external electric field. Figure 2-4b shows how the discrete units are reoriented after poling.

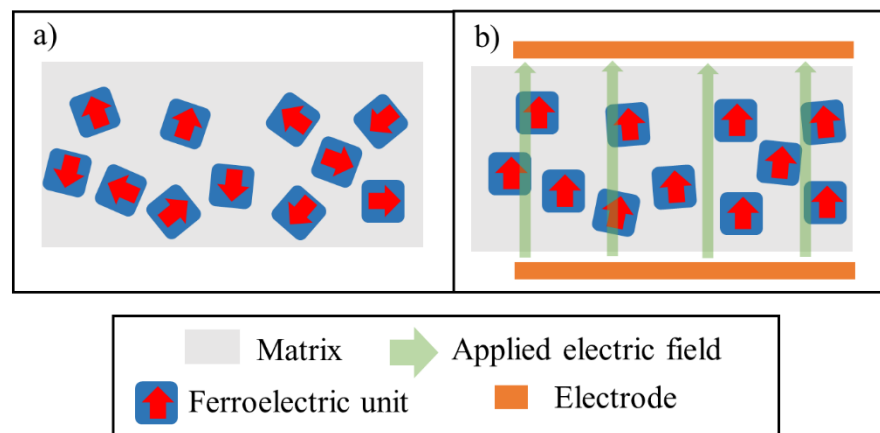


Figure 2-4: Reorientation of the dipoles of discrete ferroelectric particles. (a) Before poling, the dipoles are oriented at random directions. (b) The application of the external electric field causes the dipoles to be reoriented.

Observing the response of material as it is poled with a variable electric field can be used to identify whether the material is ferroelectric. If varying the strength of the electric field causes a remnant net polarisation on the material, showing that the current state depends on the previous conditions, then it can be confirmed that it is a ferroelectric material. This is also known as hysteresis, and curves showing the measured polarisation P or displacement D as a function of the applied electric field E are referred to as hysteresis P - E or D - E loops. An example of such curve is shown in Figure 2-5.

Piezoelectric materials are often classified in four main categories, which are ceramics, single crystals such as some minerals, polymers, and composites [85]. Each of the families have unique properties, such as magnitude of the piezoelectric response, stiffness, brittleness, among others.

Single crystal piezoelectric materials are often found in nature, but are often grown synthetically for fine-tuning the material and improving its properties. This is commonly done with crystals such as quartz [85, 86]. These materials are characterised by strong piezoelectric

coefficients, but their brittleness and hardness can make it difficult to process and reshape them [87].

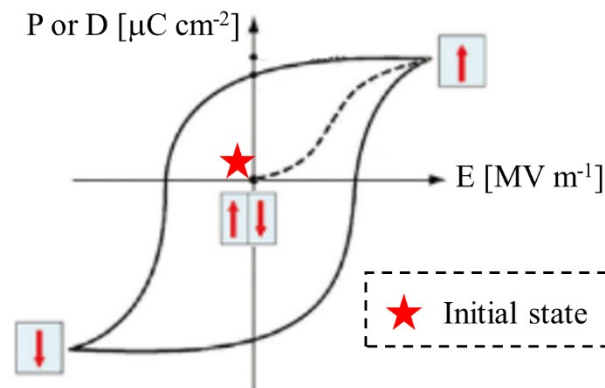


Figure 2-5: Hysteresis loop of a ferroelectric material. The electric field is varied while the polarisation is recorded. Figure adapted from [84].

Piezoelectric ceramics are polycrystalline, inorganic, non-metallic processed materials with a perovskite structure [83, 85]. Perovskites are crystals that follow the form ABX_3 , which is a type of ternary structure consisting of two different ions typically linked by oxygen, represented by the X [88]. Ceramics are hard and brittle, but can be easily be manufactured in complex shapes, and may be processed and structured with different intermediate layers or post-processing steps for fine-tuning its properties [88]. Piezoelectric ceramics in general can have high piezoelectric coefficients; for instance, lead zirconate titanate (PZT), which is a widely used ceramic with excellent piezoelectric properties, boast d_{33} values of up to 593 pC N^{-1} [83]. However, piezoelectric ceramics may contain elements that are toxic to living beings, such as lead. The study of lead-free ceramics has gained much interest, and has shown potential for the development of ceramics that can be used in implantable or wearable devices [89].

Polymers are materials composed of long chains of repeating units called monomers. In contrast to ceramics, polymers are commonly biocompatible, may be biodegradable, are flexible, can endure higher strain before breaking, and, depending on the manufacturing method, have the potential to be less expensive and easier to manufacture than ceramics [79, 85]. In contrast with ceramics, the main disadvantage of piezoelectric polymers are the comparatively low piezoelectric coefficients. However, diverse methods for increasing the piezoelectric potential of these materials have been identified and are being continuously developed [26, 79].

Composite piezoelectric materials consisting of a mixture of fillers and polymers have been developed, offering an alternative that bridges the disparities between these two groups. A filler can be a ceramic, an organic piezoelectric structure, and carbon nanotubes, among other

materials. Composite piezoelectric materials can be tailored for specific applications and targeted for achieving particular properties. For example, PZT particles embedded in a polymeric matrix may offer the chance of using this ceramic for implantable or wearable devices without exposing the user to dangerous substances. As an example, a composite PZT and ferroelectric polymer Poly(Vinylidene fluoride) (PVDF) film was measured to have a d_{33} of 84 pC N^{-1} after increasing the volume fraction of PZT to 30%. This is in contrast with the d_{33} of -30 pC N^{-1} measured for a PZT-free PVDF film [85].

While ceramics clearly offer the highest piezoelectric potential out of all the materials discussed previously, they are also known for being hard and brittle, and generally not being biocompatible. Composite piezoelectric materials offer an intermediate alternative in terms of performance, mechanical properties, and compatibility with wearable applications. However, these still carry the risk of exposing a user to harmful substances in the event that the encapsulating materials were damaged. Piezoelectric polymers have very attractive properties in relation to the design of portable energy harvesters for wearable devices. Their flexibility, biocompatibility, and the potential of manufacturing at lower costs, as well as the potential of finding alternative manufacturing methods that would allow for the conservation of these characteristics while offering an improved piezoelectric response, are all promising characteristics that align with the aims of the project. For this reason, piezoelectric polymers have been selected as the materials that will be explored in the work presented in this thesis.

2.2.2 Implications of using 2D or 3D structures for mechanical energy harvesting

As discussed in the previous section, the most fundamental piezoelectric element consists of a crystalline unit. In the context of nanostructures, a single piezoelectric crystal is considered to be zero-dimensional. Structures such as nanowires or single fibres are 1D, while thin-films are considered to be 2D piezoelectric materials [90]. According to some authors, collections of 1D and 2D materials in close contact with each other can be considered as 3D piezoelectric structures [90, 91].

The formation of 3D piezoelectric structures can be achieved using diverse methods, and is not limited to structures constituted purely of piezoelectric materials. For instance, additive manufacturing methods can be used to 3D print structures consisting of stacked layers of the active material while approaches using moulds can use chemical processes such as dip-casting a template in a solution containing the active material and then proceeding with the calcination of the structure for crystallising it, yielding structures consisting of a complex interconnected network of the active material in the shape of the mould [57, 92]. Several of

these 3D manufacturing methods allow the user to maximise the piezoelectric potential of their products by being compatible with or integrating a poling technique. For instance, extrusion-based methods can be adapted for integrating the poling process by the installation of an electrode on the printing bed and having the printing head of the device house another electrode [91–94]. Other methods rely on pre or post-processing techniques.

Independent of the approach used for creating the 3D piezoelectric structures and whether they contain purely piezoelectric materials or not, the use of 3D over 2D structures provides several advantages. From the point of view of the manufacturing process, 3D techniques have the potential to create structures that conform to complex architectures without the need to resort to the use of adhesives or other interfacing elements, effectively limiting the generated power that is lost at those interfaces [93]. Additionally, the mechanical properties of brittle materials such as ceramics can be dramatically enhanced for some 3D manufacturing methods, in which the nanostructured material can be taken beyond its elastic limit, up to the point where it can be deformed plastically [95, 96].

Another advantageous aspect is the potential for the materials to have an enhanced electromechanical response. This is mainly attributed to the increased effect that out-of-plane strain has on the structure, as well as the more effective distribution of the incident force on the material in cases where it is embedded within a flexible elastomer [57]. Studies in which the performance of 3D and 2D structures were compared revealed that the output voltage can increase by a factor of 10 in some cases, and that the efficiency of strain to voltage conversion can increase dramatically, with some examples achieving 30 times the figures observed for 2D devices made with thin films of the same material [57, 93]. The potential for obtaining more sensitive responses or obtaining comparatively greater power out of 3D structures rather than from 2Ds with identical incident forces offer the possibility of fabricating more efficient sensors/actuators and generators [57, 97].

The experimental work presented in this thesis will focus on the use of piezoelectric polymers. While composites and ceramics have higher piezoelectric coefficients than polymers, they lack the biocompatibility, flexibility and ease of manufacturing that are characteristic of polymers. Additionally, as discussed in this section, successfully achieving the fabrication of 3D polymer structures can potentially compensate for their low piezoelectric coefficients by allowing for greater efficiency and a net increase in the electrical outputs of the resulting structures. The following section will discuss the properties of polymers in general and provide an overview of some of the existing types of piezoelectric polymers.

2.2.3 Piezoelectric polymers

2.2.3.1 Polymers: an overview

Polymers have several key characteristics, such as elasticity, that make them very attractive for developing unique products for specialized environments and conditions. By definition, a polymer is a molecule that is comprised of one or more types of atoms or functional groups linked together. The simplest units are typically known as monomers, and the chemical process of linking these elements together is known as polymerisation [98, 99]. If the polymer is formed only by identical monomers, it may be referred to as a homopolymer. A copolymer is defined a chain of repeating groups comprised of complex combinations of two or more different unique single units. Both polymers and copolymers can exist as linear, branched or more complex structures such as three-dimensional networks or combinations of linear, branched and cyclic sections [98]. The process of polymerisation may require complex chemical processes, and determines the degree of branching and cross-linking, among other properties. For instance, careful control of the time of polymerisation is what allows manufacturers to create elastic and strong materials instead of an amorphous, brittle product [100].

The physical properties of polymers are heavily dependent on characteristics such as the individual interaction among each monomer link within the chain and the overall interaction between individual polymer chains, for example. The electrostatic interaction of individual functional groups may influence the orientation of the molecules in the chain, resulting in the formation of dipoles, which can be induced or permanent [98, 100]. Conformational changes in the spatial or steric configuration of the individual molecules relative to each other can occur due to the electrostatic interaction between functional groups, which results in the rotation and reorientation of the elements within the chain. While there might exist several possible rotational states for a given molecule, the electronic charge of a functional group and how bulky the adjacent molecules are will determine which is the most favourable or stable configuration. Thus, the shape and the size of a polymer chain is determined by the local spatial or steric restrictions arising from the interactions occurring between each part of the chain [101, 102]. For instance, a polymer for which the most stable configuration at a given temperature consists of mostly all-*trans* chemical bonds will have a linear configuration. A *trans* bond configuration is defined in the context of a single molecule having a double covalent bond. If both carbons are each bonded to a specific functional group, the bond is said to be *trans* if the specific functional groups are across each other relative to the double bond. If two or more conformational states are favourable, then the overall configuration of the molecule will be a random combination of segments with these favourable segments [101].

Additionally, depending on how the chains that constitute them are arranged, groups of polymeric chains can exist in either an amorphous or a crystalline state [100]. Crystallinity in polymers is observed when individual chains become aligned. Steric restrictions, electrostatic interactions, and the formation of hydrogen bonds among adjacent chains are some of the aspects that influence the crystallinity of a bulk polymer structure and the form that it acquires [101]. Independent of the fabrication method used, bulk polymer structures will acquire a degree of crystallinity. The degree of crystallinity and the proportion of specific crystal configurations acquired by the bulk material can be fine-tuned by carefully controlling the fabrication conditions. The proportion of crystalline regions within the bulk material relative to the amorphous regions and boundaries surrounding them is used to quantify the degree of crystallinity [101, 103].

Temperature is one of the critical parameters that influences the degree of crystallinity and the existing proportion of specific configurations or domains in a bulk structure. As discussed in the previous paragraphs, the overall polymer chain size is determined by steric restrictions, electrostatic interactions, and other aspects. Individual molecules in the chain will try to adopt the most energetically favourable configuration, corresponding to the one that has the least potential energy. However, if the temperature of the system is increased, then none of all the possible configurations is favoured, thus resulting in all of them being viable. Under these conditions, the bulk material is said to exist in an amorphous state. Reducing the temperature of the system will result in the material once again adopting the most energetically favourable configuration, which will in turn affect the shape and properties of the polymer chain and of how it interacts with others in the bulk material, ultimately affecting the degree of crystallinity of the material [101, 103]. If the bulk polymer is exposed to a temperature high enough for it to transition from a rubbery solid to a viscous liquid comprised of randomly distributed polymer chains, known as the crystalline melting temperature (T_M), and then brought back to a lower temperature, the bulk polymer will begin to crystallise again. This lower temperature, which a user is able to control, is typically known as crystallisation temperature (T_{CR}). Selecting a specific crystallisation temperature determines how fast the bulk material will crystallise, influences which crystalline configurations will be formed and how much individual crystallising regions will grow. Additionally, applying a temperature gradient or a uniform temperature determines the growth direction of the crystalline regions. Figure 2-6 shows an example of radially growing crystal structures in a molten bulk polymer sample being held at a T_{CR} of 165 °C. At this particular temperature, this type of polymer can crystallise into two different configurations or phases. The larger sphere represents the most common crystalline phase on which the material would exist if a lower T_{CR} had been used. Having the higher T_{CR} value allows for the likelihood of one of the other possible yet not the most energetically favourable

spatial configurations of the individual molecules in the polymer chains to increase. This change reflects in the configuration of the overall polymer chain structure, which in turn changes how this chain interacts with others on its vicinity. This results in the formation of a different crystalline phase [103]. Another important property associated with temperature is the glass transition temperature T_G . While T_M represents the temperature at which the bulk polymer transitions from a rubber solid to a viscous liquid state, T_G corresponds to the temperature at which an amorphous polymer transitions from a rubbery state to a glass-like brittle, rigid and stiff state. Materials for which T_G is well below 0 °C exist as flexible and stretchable solids at room temperature [99, 104].

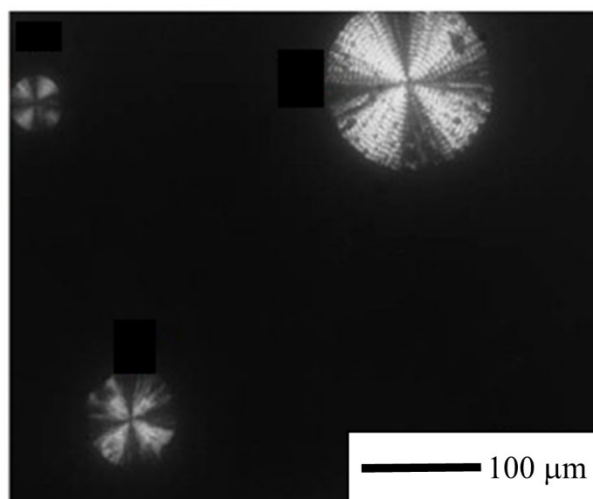


Figure 2-6: Holding a material at a particular T_{CR} after having melted it by going above its T_M promotes crystallisation. The circles represent radially growing crystal regions, while the black background represents the amorphous phase of the material that has yet to crystallise. Adapted from [103].

Other methods and parameters can be used to influence the crystallisation of polymers. Applied strain can be used to mediate the transition from an amorphous state into a particular crystalline structure [105, 106]. The elongation of a piece of bulk polymer material can be used to orient the individual chains in the direction of pulling. In the case of polymer melts or polymer solution, shear flow of the material can induce the flowing material to crystallise [106].

2.2.3.2 Piezoelectric polymers

The theory of piezoelectricity discussed in previous sections has been historically built around crystalline solids [107, 108]; for this reason, it is necessary to discuss how these principles extend to polymers and which additional conditions should be considered for evaluating their properties in comparable terms to those other solid materials. The discussion presented in this section will exclude the group of composite piezoelectric polymers, which consist of a

polymeric matrix and ceramic particles, since some piezoelectric ceramics are not biocompatible.

The piezoelectric effect has been observed in different types of polymers, whether these are naturally occurring or synthetic [85, 109]. Biologically occurring polymers such as cellulose [110, 111], collagen [112, 113], silk fibroins [114, 115], polymers artificially synthesised from naturally occurring substances such as poly(lactic acid) [116, 117], and organic polymers such as some polyamides [118–120] and fluoropolymers [117, 121] all have the potential to exhibit some degree of piezoelectric activity [73, 122–124]. Although all of the previously mentioned polymers and many others can exhibit piezoelectric properties, the underlying mechanism responsible for this effect will differ depending on the particular characteristics of each material [125]. One common characteristic that piezoelectric polymers have with other piezoelectric materials is that the strength of the response is heavily dependent on the symmetry of the material [77, 109, 110, 126].

Piezoelectric bulk polymers are often classified as semi-crystalline or amorphous depending on their degree of crystallinity [109, 125]. In the previous section, it is mentioned that bulk polymers exist as a combination of piezoelectric phase embedded within a non-piezoelectric phase [110]. The piezoelectric phase can be either a crystalline regions or highly-ordered, uniaxially-oriented domains, while the non-piezoelectric phase is usually an amorphous matrix [110]. The degree of crystallinity and dominance of a particular type of crystalline domain depending on the processing conditions [26, 109]. Figure 2-7 shows an example of the composition of a semi-crystalline piezoelectric polymer.

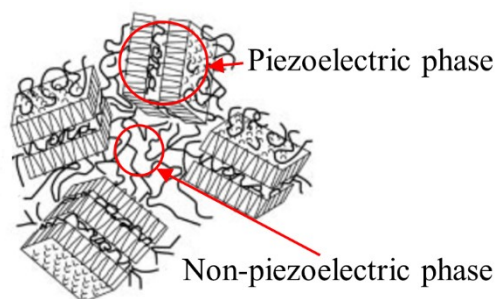


Figure 2-7: Representation of a semi-crystalline polymer, formed by an amorphous region or non-piezoelectric phase and crystallised regions or piezoelectric phases. Adapted from [109].

In general, the critical characteristics that define a piezoelectric polymer are permanent molecular dipoles that susceptible to reorientation, and they should be capable of conserve the orientation of the dipoles [109]. While these characteristics can explain piezoelectricity in, for instance, individual crystalline or highly-oriented domains existing within an amorphous matrix in a bulk polymer, this is not necessarily the case for the bulk semi-crystalline polymer

as a whole; it is possible for a multiple piezoelectric domains to exist as discrete domains within a matrix, but the material as a whole may exhibit poor macroscopic piezoelectric properties [77, 109]. This could be because, for instance, the individual crystalline domains are non-polar or the dipole orientation distribution is random.

Some processing methods are very effective for modifying the properties of the material, allowing the users to effectively influence properties of the material such as the net macroscopic dipole orientation and the degree of alignment of the chains constituting the amorphous phase of the bulk material [109]. As discussed in the previous section, annealing a bulk polymer and varying the T_{CR} allow users to promote the formation of a specific crystalline phase. Mechanically stretching a bulk polymer promotes the alignment of the amorphous phase of a bulk material [109]. Poling the material, which consists in exposing the bulk material to an external electric field, can effectively reorient the piezoelectric phases within the bulk polymer as long as the material is ferroelectric [109, 122]. Poling ferroelectric polymer structures have been exhaustively studied for thin films and membranes [127–129]. Combinations of these techniques, as shown in Figure 2-8, are often used for processing bulk polymers and can successfully result in piezoelectric films and structures.

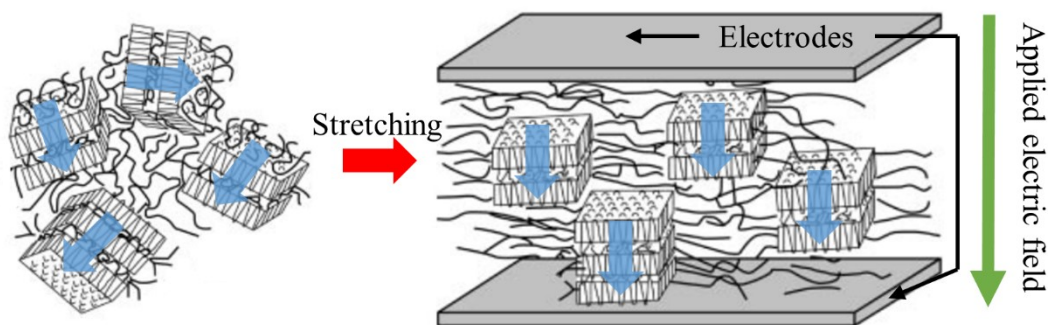


Figure 2-8: Processing a bulk polymer allows for the material to gain a bulk piezoelectric response. Mechanically stretching and electrically poling the material allow for the reorientation of the dipoles of the piezoelectric phase of the sample and the alignment of the non-piezoelectric phase. Adapted from [109]

Depending on the processing method used, the resulting material may show a shear and/or longitudinal/transverse piezoelectric response(s) [77, 110, 130]. Recalling the discussion on tensors from a previous section, the piezoelectric tensor matrix for piezoelectric polymers with both shear and longitudinal/transverse responses is shown in Figure 2-9a and that for a material with only shear response is shown in figure 2-9b. The effect that these processing techniques have in the bulk polymer is ensuring the macroscopic asymmetry of the material, thus resulting in piezoelectric structures [77]. Both the processing method and characteristics of the polymer are of critical importance in determining the types of response. In the case

piezoelectric polymers in which the piezoelectric phase consists of crystalline regions, poling and combined poling and stretching result in a material with both longitudinal/transverse and shear responses [77]. In the case of polymers in which there is chirality, drawing alone results in a shear piezoelectric response [77]. Biologically occurring polymers typically exhibit this type of behaviour [110, 111, 114, 131].

$$\begin{array}{c} \text{a)} \\ \left[\begin{array}{cccccc} 0 & 0 & 0 & 0 & d_{15} & 0 \\ 0 & 0 & 0 & d_{24} & 0 & 0 \\ d_{31} & d_{32} & d_{33} & 0 & 0 & 0 \end{array} \right] \\ \hline \text{b)} \\ \left[\begin{array}{cccccc} 0 & 0 & 0 & d_{14} & 0 & 0 \\ 0 & 0 & 0 & 0 & d_{25} & 0 \\ 0 & 0 & 0 & 0 & 0 & 0 \end{array} \right] \end{array}$$

Figure 2-9: Piezoelectric tensor matrices associated to certain processing methods. (a) Matrix describing the tensors for a sample that was mechanically stretched and poled. It shown both longitudinal/transverse and shear responses (b) Matric associated with a sample that was mechanically stretched, showing only a shear response. Adapted from [110].

The properties of cellulose as a piezoelectric material were first studied in wood [111], with further analysis being carried out in nanocrystals or nanofibres that may be obtained by different processing methods [131]. This naturally occurring polymer is biocompatible, biodegradable, has be proven to have tuneable physical and chemical properties, and has been used in combination with other materials for producing state-of-the-art energy harvesting devices. The shear piezoelectric coefficient d_{14} for cellulose films has been measured as 0.41 pC N^{-1} , and has been observed to increase up to 7.3 pC N^{-1} when stretched using a one-to-two ratio [111, 131].

Silk fibroin is another type of naturally occurring piezoelectric polymer. This material is formed by repeating chains of aminoacids, forming α -helixes and β -sheets which in turn may form semi-crystalline regions out of which that known as silk II represents the most electroactive [114]. Silk fibroin is biocompatible, biodegradable, and can potentially reach d_{14} values of -1.5 pC N^{-1} when subjected to stretching with a one-to-2.7 ratio [114]. Thin films of collagen have also been shown to have a shear piezoelectric response, with measured d_{14} values between 2 and 3 pC N^{-1} [112].

Lactic acid (LA) is a chiral molecule obtained from processing naturally occurring materials. LA polymerisation methods can be selected depending on the desired L or D form content, allowing the manufacturer to produce materials with specific properties; for instance, L-LA chains are known for their piezoelectric potential [116]. Stretching and thermal annealing of

PLLA structures promote the re-orientation of the molecular chains of the material into a piezoelectric crystalline phase. Similar to the biologically occurring polymers mentioned previously, PLLA has a shear piezoelectric response, which has been measured to from 6 to 12 pC N⁻¹ for this processing method [79, 132]. PLLA is biocompatible, biodegradable, flexible, and non-toxic [116].

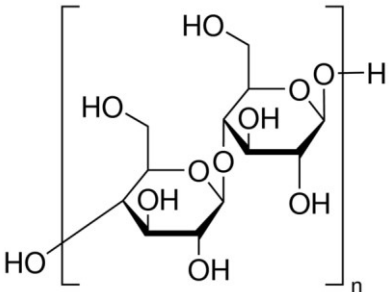
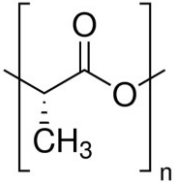
The fluoropolymer Poly(Vinylidene fluoride) (PVDF) has been extensively studied, being one of the earlier polymers to be identified not only as piezoelectric but as ferroelectric as well [121]. This semi-crystalline polymer has four different crystalline phases, with the one known as the β form having the greatest piezoelectric potential. PVDF is known for being biocompatible, flexible, non-toxic, being resistant to chemicals and harsh environmental conditions [133]. An example of measured d_{31} and d_{33} values for PVDF samples that have been stretched and poled are 17.9 and -27.1 pC N⁻¹ respectively [121]. Copolymers of VDF and other fluoropolymers such as trifluoroethylene (TrFE) or Hexafluoropropylene (HFP) have been shown to have enhanced piezoelectric coefficients; for PVDF-TrFE, measured d_{31} and d_{33} values are 25 and -30 to -40 respectively [58].

Polyamides, most commonly known as nylons, were one of the first commercially available synthetic materials, becoming an important component in the manufacture of clothing and for other industries [118]. Nylon monomers typically consist of either a continuous chain of methyl groups terminated in an amine and a carboxyl functional group, or a chain of methyl groups terminated in carboxyl groups and a chain of methyl groups terminated in amino groups linked by an amide bond formed by a reaction involving the terminal groups of both chains. The polymer is labelled depending on the number of methyl groups contained in the chain(s) [134]. Only odd-numbered polyamides have been observed to have piezoelectric responses, with these arising from their polar structure [85]. For an odd-numbered polyamides, the negative charge associated with the carboxyl groups exist on one side of the polymer chain while the positive one associated with the amino groups are on the opposite one, considering the carbon chain as the symmetry axis. In the case of odd-numbered nylon, the terminal functional groups alternate, resulting in the polymer chain being non-polar. For nylon 11,11, measured d_{33} values of -3.9 pC N⁻¹ have been reported in the literature [119]. As a material, nylon is known to be flexible and biocompatible, well suited for medical applications [135].

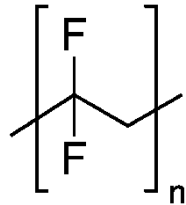
Table 2-2 summarises the properties of the piezoelectric polymers discussed previously. Out of all the polymers explored in this section, PVDF and its copolymers have the most promising piezoelectric properties. Additionally, these materials are non-toxic, flexible, and have strong chemical and abrasion resistance. These characteristics are favourable for the development of a generator intended for wearable devices, and are compatible with the aims and

requirements of the project presented in this thesis. Thus, these polymers were selected as the materials to be explored. The following sections will provide a more detailed description of PVDF and PVDF-TrFE.

Table2-2: List of some piezoelectric polymers and their characteristics.

Polymer	Primary monomer structure	Additional monomers for use as a copolymer	Processing method	Piezoelectric modulus (pC N ⁻¹)	Reference
Cellulose		---	Mechanical stretching	$d_{14} = 7.3$	[111, 131]
Silk fibroin	Repeating units of these amino acids: Glycine-Serine-Glycine-Alanine- Glycine Alanine	---	Mechanical stretching	$d_{14} = -1.4$	[114, 115]
Collagen	Repeating units of these amino acids (most common variation): Proline-Hydroxyproline-Glycine	---	Electrodeposited films	$d_{14} = 2 \text{ to } 3$	[112, 114]
Poly(L-lactic acid) (PLLA)		---	Electrical poling, mechanical stretching	$d_{14} = -10$	[132]

**Poly(vinylidene
fluoride) (PVDF)
and its
copolymers**



- TrFE
(Trifluoroethylene)
- HFP
(Hexafluoropropylene)
- CTFE
(Chlorotrifluoroethylene)

Electrical poling,
mechanical
stretching

PVDF:

$$d_{31} = 17.9$$

$$d_{33} = -29.1$$

PVDF-TrFE:

$$d_{31} = 25$$

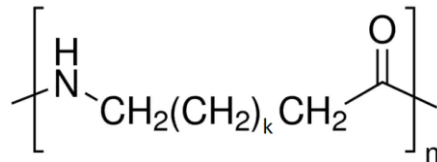
$$d_{33} = -30 \text{ to } -40$$

[58, 85,
136]

Polyamides

(Nylon)

$$k \geq 2m + 1$$



Electrical poling,
mechanical
stretching

$$d_{33} = -3.9$$

[119, 120]

2.2.3.3 PVDF

Poly(vinylidene fluoride) (PVDF) is a semi-crystalline fluoro-homopolymer that typically exists at a 35 to 70% crystallinity in its bulk form depending on the processing method that was used to fabricate it. The VDF monomer is formed from carbon (C), fluorine (F) and hydrogen (H) atoms, with the backbone of the molecule being C-C bonds, and the pendant functional groups of the monomer being C-F or C-H bonds [133, 136]. The polymerisation process of PVDF is often achieved by techniques such as emulsion or suspension mediated by persulfates or peroxides as the initiators of the reaction [136]. The chemical structure of PVDF is shown in Figure 2-10.

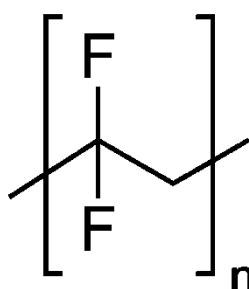


Figure 2-10-Chemical structure of PVDF.

PVDF has a linear backbone, and is non-centrosymmetric. Being a dielectric material, PVDF exhibits electric, ionic, and dipole orientation polarisation. Dipole orientation polarisation arises from the spatial configuration of the pendant functional groups. In the case of PVDF, the orientation of the two F and H atoms determine the net dipole polarisation, with a strong dipole moment that is perpendicular to the backbone of the molecule [136].

PVDF has a T_G of $-35\text{ }^{\circ}\text{C}$, a T_M ranging from 140 to $170\text{ }^{\circ}\text{C}$, and has a density of 1.76 g cm^3 . The Curie temperature (T_C), which can be defined as that beyond which the magnetic and ferroelectric properties of a material are lost, is estimated to be close to $170\text{ }^{\circ}\text{C}$ for PVDF. Processed forms of this polymer have favourable mechanical properties such as resistance to deformation, damage from abrasion, and to repeated bending. It is resistant to several organic solvents with the exception of polar solvents. It also resists a variety of acids and bases, alcohols, halogens, among other substances. These properties make PVDF a material with attractive chemical resistance properties that has been widely used as an electrical insulator and a coating to protect tools or structures [133].

PVDF is known to exist in 4 different crystalline phases, which are commonly named α , β , γ , and δ , with each one of these being determined by the orientation of the C-F and C-H bonds. Figure 2-11a and b shows the ball-and-stick model and crystalline unit-cell for some of these crystalline phases respectively. The α -phase has an orientation defined as an alternating trans-gauche configuration, often shortened as TGTG', and exists as a combination of a helical and planar structure. A gauche configuration can be described as a stable conformational state for a molecule in which the electronic interactions have a stronger effect than steric or spatial restrictions. The electronegativity of the F atoms in PVDF and how this influences the electronic interaction between elements in the chain plays a role in determining the most favourable spatial conformation for the molecule, and thus, the crystal phase of PVDF. The α -phase is the most common for bulk PVDF produced by melt crystallisation using a T_{CR} of 160°C or less [136, 137]. Individually, each TGTG' segment has a net dipole moment. However, the α -phase crystalline unit has no net polarity because of antiparallel dipole moments, as can be seen in Figure 2-11 [133, 136, 138].

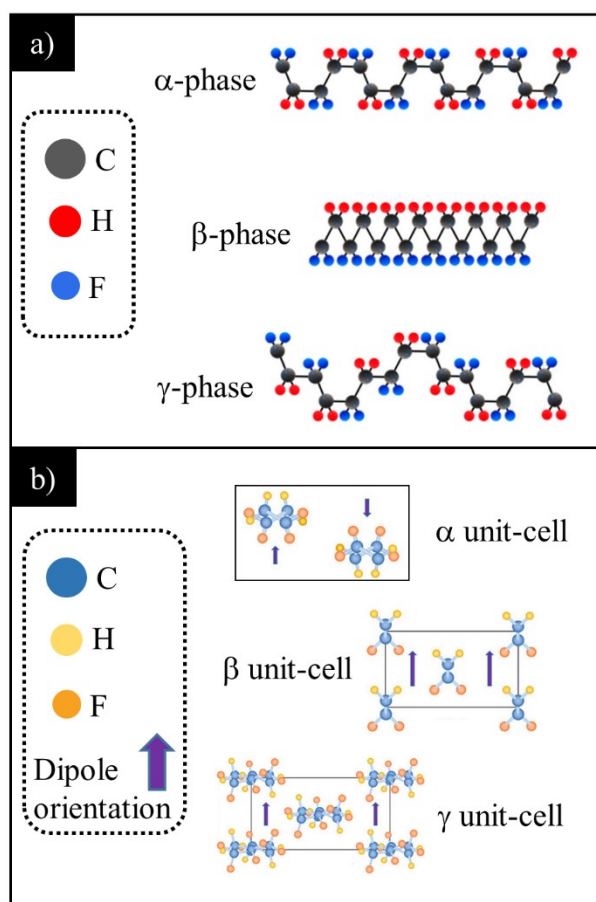


Figure 2-11: (a) Ball-and-stick model of α , β , and γ PVDF. (b) Crystalline unit cells of α , β , and γ PVDF.

Adapted from [138].

The β -phase consists of VDF linked in an all-*trans* configuration, thus resulting in planar zigzag conformation. Since all the F atoms are positioned on one side of the chain, this crystalline

phase has the highest net dipole moment of all PVDF phases. For a β unit-cell, all dipoles are coincident in direction and aligned along a single axis, forming an orthorhombic unit-cell with lattice constants of $a = 8.58$, $b = 4.91$ and $c = 2.56$ Å [136–138]. Another feature exhibited by the β -phase of PVDF is that it is permanently polarised and the net polarisation can be switched between two stable states by exposing the material to high electric fields [139]. Thus, β -phase PVDF is a ferroelectric material. Some sources indicate that β -phase PVDF has a d_{33} of -27.1 pC N $^{-1}$ and a d_{31} of 17.9 pC N $^{-1}$ [121]. Both ball-and-stick model and unit-cell representation for this phase are shown in Figure 2-11.

The γ -phase has VDF monomers linked in a TTTGTTTG' configuration. This crystalline phase has a net dipole orientation, although this is not as strong as that observed for β -phase PVDF [136, 137]. Some sources mention that this crystalline phase has a d_{33} of -13.3 pC N $^{-1}$ and a d_{31} of 4.9 pC N $^{-1}$ [121]. The δ -phase is thought to occur as a distortion of all previous crystalline phases [136].

Previously, it was mentioned that the α -phase is the most commonly found in bulk PVDF processed by melt crystallisation. However, as mentioned in the previous section, it is possible to transform the crystalline phases present in a sample by using methods such as electrical poling, stretching or drawing, and annealing. Some of these techniques in combination with other conditions such as temperature and the magnitude of the mechanism driving the transformation result in different crystalline phases [136, 137]. A diagram illustrating the methods that can be used to transform from different phases into β -phase is shown in Figure 2-12.

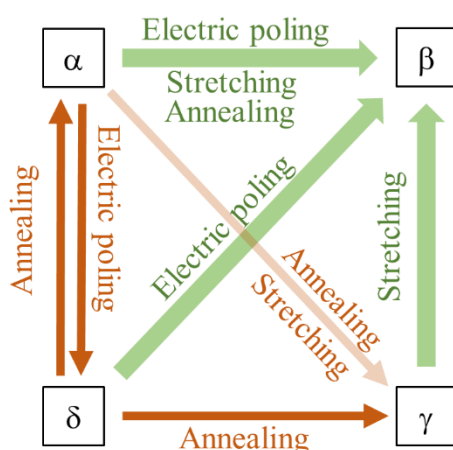


Figure 2-12: Diagram showing the different methods that can be employed for transforming PVDF crystalline phases. Adapted from [136].

While some PVDF phases have been shown to have a net dipole orientation that confers its piezoelectric properties, the β -phase offers the most promising piezoelectric properties. Out

of all the crystalline phases, β -phase also exhibits the strongest ferroelectric behaviour. This is illustrated in Figure 2-13, in which the electric field vs dielectric displacement hysteresis loops for different PVDF crystalline phases are shown [136]. Common methods for producing bulk PVDF often result in a material that is 35 to 70% crystalline and the α -phase will be the most common of them all. This is a consequence of the TGTG' configuration being favoured over others because of the highly electronegative F atoms in the chain. The electronic interaction of these atoms with the opposite charged functional groups tends to be stronger than the effect imposed by the steric restrictions that would normally favour a TT rather than a TG or TG' form [136–138].

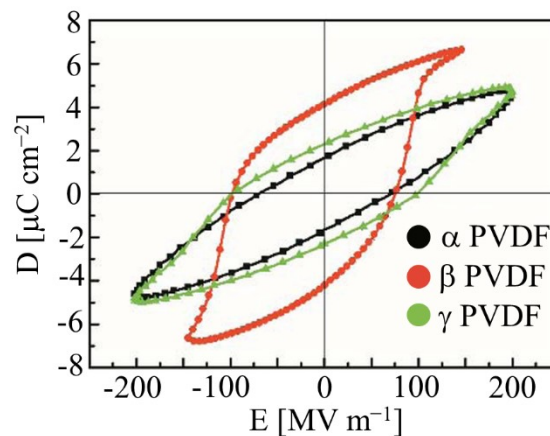


Figure 2-13: Hysteresis loop of α , β , and γ PVDF. Adapted from [136].

Mechanical means such as compression, shearing and tensile forces can be used to mediate the transition of the bulk material into having predominantly β -phase. Methods such as electrospinning, on which an electric field is used to create fibres from a polymer solution and on which the manufactured product is being exposed to a high electric field and stretching forces arising from perturbations due to the influence of this field can be used to subject the material to both electrical poling and mechanical stretching. It is possible to obtain samples with up to 82% β -phase content with this method [138].

In summary, PVDF is a flexible, resistant material with dielectric properties that are dependent on its crystalline structure. The properties of the can be fine-tuned by diverse techniques, which allow for the transformation of the existing phases into the preferred one. In terms of its cost, it is relatively cheap if compared to other piezoelectric polymers [136]. Since PVDF is also a ferroelectric polymer, processing techniques which employ very high electric fields for creating structures with it have the potential to enable the user to obtain PVDF optimised for applications such as mechanical energy harvesting based on piezoelectrics. Compared to PLLA, odd-numbered polyamides, and biopolymers such as silk fibroin, PVDF can be easily processed to have relatively high d_{33} and d_{31} indexes without having to rely on the use of

additives that would make the material a composite rather than being purely polymer-based. Based on these characteristics, PVDF was chosen as one of the materials that would be explored for the work presented in this thesis.

2.2.3.4 PVDF-TrFE

In a previous section, copolymers of VDF and other fluoropolymer monomers such as trifluoroethylene (TrFE) were mentioned as one of the other existing types of piezoelectric polymers.

TrFE is a monomer very similar to VDF, with the exception that instead of having two C-F and C-H bonds it has three C-F bonds and a single C-H. PVDF-TrFE is typically classified by the molar percentage for each type of monomer used for producing it. Copolymers for which the amount of TrFE constitutes between 20 and 50% of the total composition tend to favour crystallisation in the β -phase rather than in the α -phase. The reason for this is that a larger steric restriction is imposed in the molecule by substituting one C-H bond with a C-F bond. Therefore, contrary to what occurs with PVDF, it is possible to tip the balance so that an all-*trans* configuration is favoured over the TGTG' because the compressive forces exerted by the steric hindrance have a stronger influence than the electronic effects of the individual atoms. This causes bulk PVDF-TrFE to crystallise predominantly in the β -phase if processed from solutions or from melt crystallisation [138, 140]. The chemical structure for PVDF-TrFE is shown in Figure 2-14.

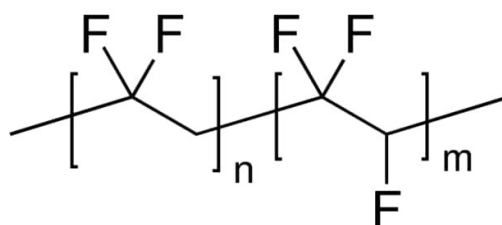


Figure 2-14: Chemical structure of PVDF-TrFE.

The T_C value of PVDF-TrFE is estimated to be around 100 °C. The T_M value is close to 148 °C. These values correspond to a molar percentage of 70% VDF and 30% VDF [136]. The lower Curie temperature is a consequence of the introduction of TrFE; adding this molecule to the mix causes the crystal unit cell to increase in size, with the same happening for the relative distance between dipoles. Since the interaction between dipoles is reduced, less thermal energy is required to promote the random shift of dipoles, thus facilitating the loss of dipole alignment for the material [141]. In contrast with the crystalline structure of PVDF, the lattice constants for PVDF-TrFE depend on the molar percentage of the copolymer. For an 80% VDF 20% TrFE copolymer, these are $a = 8.9$, $b = 5.05$, and $c = 2.55$ Å. For a 70% VDF 30% TrFE,

these would be $a = 9.05$, $b = 5.23$, and $c = 2.55$ Å [142]. The PVDF-TrFE ball-and-stick model and its crystal unit cell are shown in Figure 2-15.

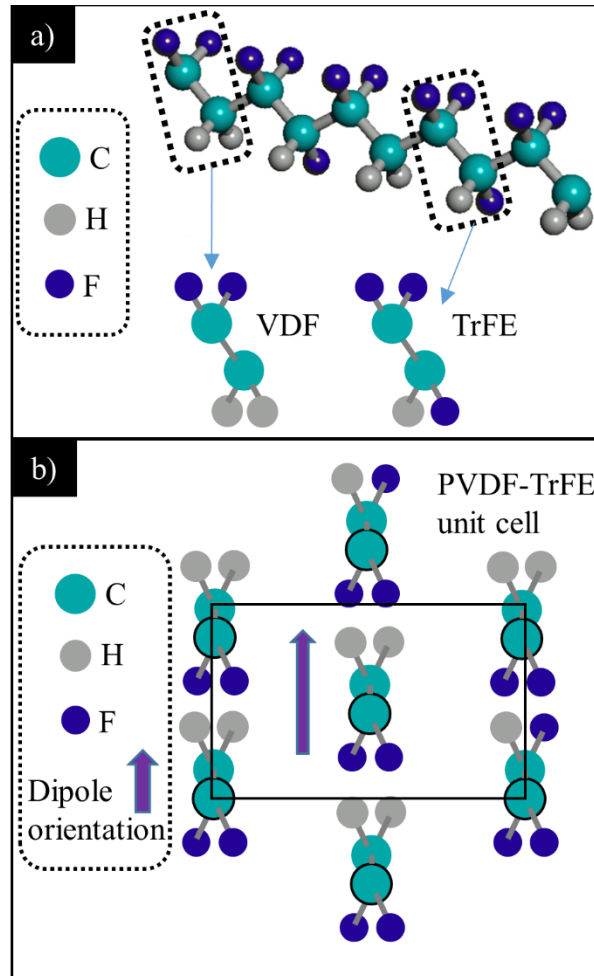


Figure 2-15: (a) Ball-and-stick model of PVDF-TrFE. (b) Crystalline unit cell of PVDF-TrFE. Adapted from [141].

The lower T_C of PVDF-TrFE affects its performance in higher temperature conditions. While the material itself will not melt when exposed to temperatures higher than 100 °C, it will lose its ferroelectric properties and behave as a paraelectric material, which is defined as the materials that does not preserve the net polarisation it has been exposed to [138].

Compared to PVDF, PVDF-TrFE has been reported to have a d_{33} of -30 pC N $^{-1}$ and a d_{31} of 25 pC N $^{-1}$ [58]. The electric field vs dielectric displacement hysteresis loop for various molar percentages of PVDF-TrFE are shown in Figure 2-16. In contrast with that shown in the previous section for β -phase PVDF, 65:35 PVDF-TrFE has a remnant polarisation value closer to saturation [143]. For this reason, PVDF-TrFE is often for developing ferroelectric memory devices [138, 139].

In summary, PVDF-TrFE is a ferroelectric polymer with properties that depend heavily on its molar ratio of VDF and TrFE. It is similar to PVDF in that it is a flexible material that can be processed by relatively simple methods and can be fine-tuned to acquire excellent piezoelectric properties. The addition of TrFE results in the crystalline β -phase being more favourable than the α -phase, thus allowing for the bulk polymer to acquire favourable properties for piezoelectric applications even by processing it by melt crystallisation [58]. This copolymer has piezoelectric constants values of -30 pC N^{-1} for d_{33} and of 25 pC N^{-1} for d_{31} , values which are greater than those reported for PVDF. The fact that the β -phase is the most likely crystalline phase to form when the material is being processed from a solution or melt crystallisation, this copolymer is often used for applications related to mechanical energy harvesting since further processing might not be required for optimising its properties. However, in contrast with PVDF, its use in high-temperature applications is limited.

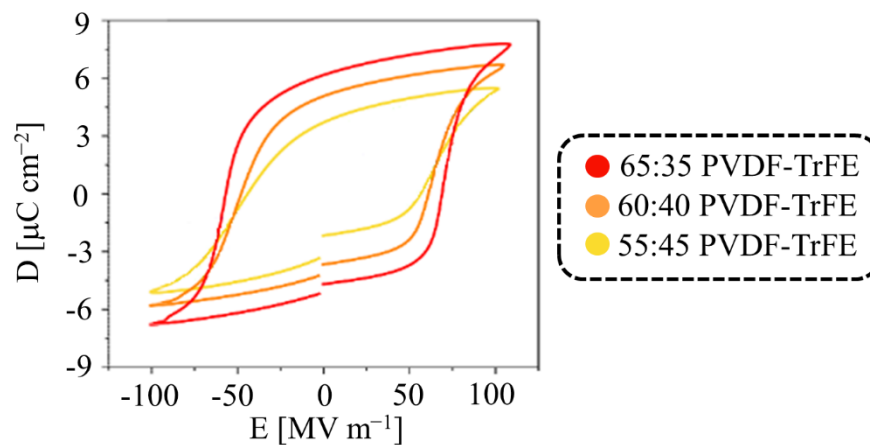


Figure 2-16: Hysteresis loop of PVDF-TrFE, for three different molar ratios of the substance. Adapted from [144]

In the context of the scope of the project, the temperature conditions will be close to ambient and possibly body temperature. Therefore, the limitations of a lower T_C will be of no concern. The prospect of using a material that will tend to crystallise in a phase favourable for mechanical energy harvesting and its greater piezoelectric properties when compared to other piezoelectric polymers are the main reasons why this material has been chosen for being explored in this thesis, along with PVDF.

In this section, it has been discussed how processing methods such as stretching and poling can enhance the piezoelectric properties of a material. The piezoelectric polymer PVDF and its copolymer PVDF-TrFE have been selected as the materials to explore in the experimental work outlined in this thesis because of their high piezoelectric properties in comparison with other polymers, and their suitability for being included in wearable devices. One material manufacturing method that can provide both stretching and poling to a bulk polymer solution

is electrospinning. In the following section, the principles of electrospinning and diverse variations of this technique will be explored.

2.3 Electrospinning

Electrospinning as a fabrication method was first observed several centuries ago, with an early description of how bringing a charged object close to a droplet deposited on a flat surface would result in the droplet acquiring a cone-like shape that grew towards the charged object having been recorded in the early 1600s [144]. It was until the early 1900s, after equipment for producing high-voltages had become more readily available, that patents describing the earliest electrospinning apparatus began to be filed [144, 145]. In recent years, this method has evolved rapidly, allowing for the scaling of the method to industrial levels and the manufacture of complex fibrous structures [146, 147].

Electrospinning is a fabrication method that uses electrostatic forces to mediate the formation and stretching of a jet from a viscoelastic solution, such as polymer solutions or melts, yielding fibres that can have diameters ranging from micrometres to nanometres. The fabricated electrospun materials are characterised by a very high surface area, which can be advantageous in applications such as catalysis and electrode design [148–150]. This versatile fabrication technique has been used extensively in applications including biomedical science, electronics, and renewable energy, among others [145].

The following sections will describe the principles of this fabrication method in detail, discussing the effect that the working parameters and environment have on the morphology of the resulting products.

2.3.1 Principles of electrospinning

The electrospinning process consists of biasing a pair of electrodes with a very high electromagnetic field, typically in the order of kilovolts, and placing a polymer solution in direct contact with one of the charged electrodes to force the solution to become charged and to create jets of liquid that travel towards the opposite electrode, producing fibres in the process [145, 149, 150]. An electrospinning setup will typically have a high voltage (HV) power supply, which can be either an AC or a DC source [151], a collector electrode, an emitter electrode, and a mechanism for continuously supplying the polymer solution or melt to the system [150, 152].

The process of electrospinning occurs as follows. When the polymer solution that is in contact with the emitter electrode becomes charged as a result of applying the HV to the system, point charges on the solution separate, with those having the same polarity as the electrode accumulating on the surface of the solution. The surface tension of the solution tends to keep the liquid in even, spherical or curved shapes. However, the electrostatic forces acting on the charged surface of the solution attempt to reshape the surface of the liquid into spike-shaped

protuberances since this type of shapes tend to attenuate the repulsion of the charges accumulated in the solution by increasing its surface area [144, 145, 149]. If the electric field is strong enough to cause the electrostatic repulsion to surpass the surface tension, the spike-shaped protuberances will continue to develop into a cone-like structure, known as Taylor cone, out of which a jet of liquid will be expelled [150, 153, 154].

The liquid jet expelled from the tip of the Taylor cone travels towards the collector, attracted by the opposite polarity of the latter. As the jet travels towards the collector, in the immediate vicinity of the electrode and Taylor cone, it keeps a relatively stable, straight shape and trajectory. As it keeps travelling further away from the electrode, the jet becomes unstable, resulting in it being stretched as it whips around and accelerates towards the collector. The point at which this transition occurs is known as the first critical point. As the whipping jet keeps traveling towards the collector, it starts thinning and branching as further bending instabilities occur [145, 150]. The solvent starts to evaporate during this stage, thus resulting, most of the time, in a dry product depositing on the collector [155]. For a nozzle-based system with a simple stationary collector, the fibres being formed in the process deposit as a collection of randomly oriented and overlapping fibres, a structure known as an electrospun fibre mat [145].

Figure 2-17a shows a schematic diagram of a nozzle-based electrospinning setup, showing the basic elements most electrospinning setups will have. Figure 2-17b shows a schematic diagram of the formation of the Taylor cone. Figure 2-17c shows the stages that the ejected jet goes through as it travels towards the collector.

The electrospinning process can be better understood by exploring the underlying phenomena of its various stages from a first-principles approach. The following subsections discuss some of the principles that govern the formation of the electrospinning jet and its motion as it travels towards the collector, all of this considering that a nozzle-based system with a stationary collector is being employed to electrospin a polymer solution consisting of a polymer dissolved in a solvent system. The nozzle is assumed to be a capillary.

2.3.1.1 The formation of the Taylor cone

For a single nozzle system, a syringe pump will be used to pump the solution or melt into the charged nozzle. Considering the instant at which the pumping of the solution causes a droplet to start forming on the tip of the nozzle, there will be three forces influencing its shape. One of these will be the surface tension; the molecules of the polymer solution that are located at the liquid and external media interface will experience an imbalanced attractive force towards other molecules within the fluid or also at the interface. Since these molecules are right at the edge of the interface, they will experience a net attractive force directed towards the interior

of the solution [156]. The solution-to-external-media interface will tend to acquire a spherical shape since this minimises the surface area of the interfacial region for a specific volume at equilibrium [157].

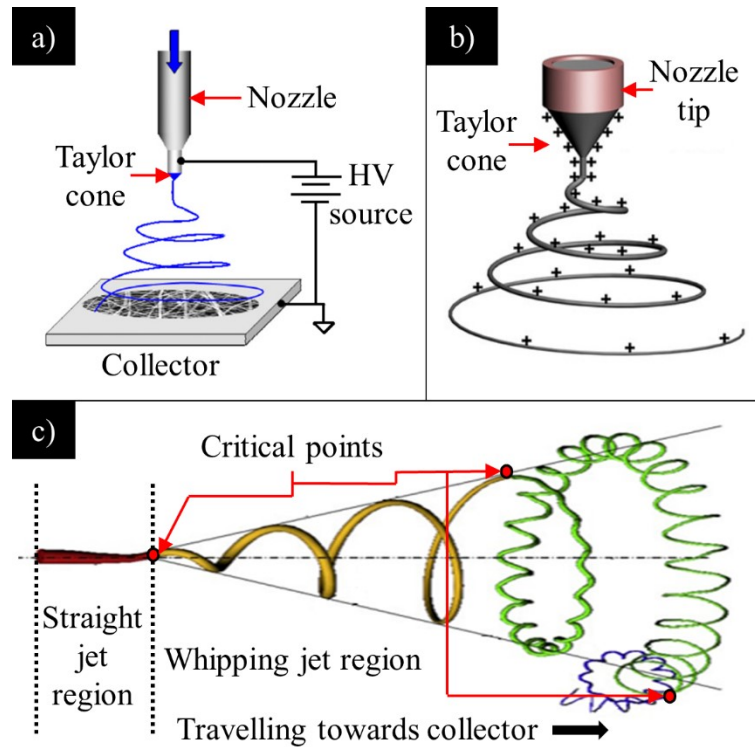


Figure 2-17: (a) Nozzle-based electrospinning apparatus. (b) Formation of the Taylor cone in a nozzle-based device. (c) Regions of the electrospinning jet. Adapted from [145], [149], and [158].

The other two forces acting on the droplet are those related to the electric field that is being applied to the system. One of them is the electrostatic attraction/repulsion force arising from the interaction between two molecules, in this case point charges within the solution. The other is the electrostatic force exerted on each individual molecule within the solution by the electric field being applied to the system [153, 156, 158]. The combined effect of these two electrostatic forces will result in a net outbound force that opposes the surface tension. Equation 2.4 corresponds to the Rayleigh condition, an expression that describes up to which point a droplet will retain its shape in relation to its surface tension and an applied electric potential [153].

Equation 2.4
$$\Phi_0(\pi R_0 \sigma)^{-\frac{1}{2}} < 4$$

Φ_0 corresponds to the applied electric potential, R_0 describes the volume-equivalent radius of the droplet and σ is the surface tension coefficient. Increasing the magnitude of the electric field being applied to the system causes the droplet to deform since the net charge accumulated at the surface of the droplet increases. In relation to equation 2.4, this means

that the applied electric field approaches critical values for which the Rayleigh condition is disrupted [153, 156, 158]. Beyond a critical applied field value, the droplet tends to deform and might transition to a cone-like shape if the magnitude of the field is great enough. Taylor, the person after which this cone-like shape has been named after, described the critical voltage that needs to be applied for ejecting a jet of liquid from a droplet formed on the tip of a capillary as shown in equation 2.5 [159].

Equation 2.5
$$V_C^2 = 4 \frac{H^2}{L^2} \left(\ln \frac{2L}{R} - 1.5 \right) (0.117\pi\gamma R)$$

V_C is the critical voltage needed to form the jet, H is the effective distance between the nozzle and collector, L is the length of the nozzle capillary, R is the radius of the capillary, and γ is the surface tension. As long as a voltage equal or greater than V_C is applied, a jet will be ejected from the tip of the Taylor cone.

2.3.1.2 Straight jet region

The jet that is being ejected from the nozzle is charged and will tend to travel towards the collector. For distances that are relatively close to the nozzle, the jet is relatively stable. For this reason, it is known as the straight region or segment [158].

At this stage, jet properties such as diameter, velocity, length of the stable region, and others can be modelled by taking some considerations into account. For instance, the diameter of the straight segment can be estimated by taking into consideration the flow rate of the solution, the velocity of the jet, and the time elapsed [160]. For a section of the straight segment for which the cross-sectional area is S_1 , the speed is v_1 and the elapsed time is t , the amount of solution consumed, Q_s can be estimated as shown in equation 2.6.

Equation 2.6
$$Q_s = S_1 v_1 t$$

Using Q_s , Ding et.al derived an expression of the initial diameter, d_1 , of the jet as it is ejected from the Taylor cone [160]. This is shown in equation 2.7.

Equation 2.7
$$d_1 = \left(\frac{4Q_s t}{\pi v_1} \right)^{\frac{1}{2}}$$

The authors observed that the diameter of the straight segment was larger at the beginning and decreases as it travels away from the tip of the Taylor cone; thus, the velocity of the jet as it thins will increase dramatically. For instance, a study in which the jet velocity in this region was measured by Doppler velocimetry revealed that the increase went from 1 to 15 m s⁻¹ [156, 160].

The electric field also influences the behaviour and characteristics of this region of the electrospinning jet. The effect that the electric field has on the jet is opposed by the viscoelastic forces and the air drag forces. At some point, the air drag force overcomes the electric stretching force due to the applied electric field, which may cause the jet to bend [156, 161, 162]. Additionally, other instabilities attributed to perturbations arising from self-repulsion of point charges within the jet as they start to overcome the viscoelastic forces keeping the jet from deforming contribute to the bending of the jet [153, 156]. The point at which the bending is observed is known as a critical point, and marks the region after which the electrospinning jet starts whipping.

2.3.1.3 The whipping jet region

The whipping motion that starts to occur as the jet travels further away from the collector can be mainly attributed to the combined effect of instabilities occurring in the jet. These are the axisymmetric instability and the whipping instability [156].

The axisymmetric instability consists of two different effects, the Rayleigh-Plateau instability related to the electric field and the oscillatory conducting mode of the jet [163]. The Rayleigh-Plateau instability is related to the degree of molecular interaction within the electrospun solution. It can be modulated by changing the polymer concentration or by changing the viscosity. For solutions with low degrees of molecular interactions, the surface tension of the solution will amplify small perturbations occurring on the fluid column, something that could eventually build up and result in the jet being broken into droplets [153, 156, 164, 165]. When factoring in the presence of an external electric field, the Rayleigh-Plateau instability can be further suppressed [163]. The conducting mode instability relates to how the charge density of the surface of the jet is not stably coupled to the external electric field. Thus, this instability is being driven by an electric potential dependent component [163].

The bending instability, also known as Earnshaw's instability, describes how the jet experiences self-repulsion in the regions that deviate slightly from the axis of travel. When a deviation occurs, a net force perpendicular to the axis of travel is exerted on the jet. The viscoelastic properties of the jet resist the pull of this force, but the pull will eventually be stronger, contributing to the whipping motion of the jet and on its stretching [144, 156, 158]. Figure 2-18 shows a schematic diagram of the net force driving the bending instability. This net force causes the jet to stretch, which in turn increases the surface area of the jet but reduces the charge density of the surface [156, 164, 166]. The net force responsible for causing the bending instability can be expressed as indicated by Equation 2.8 [156].

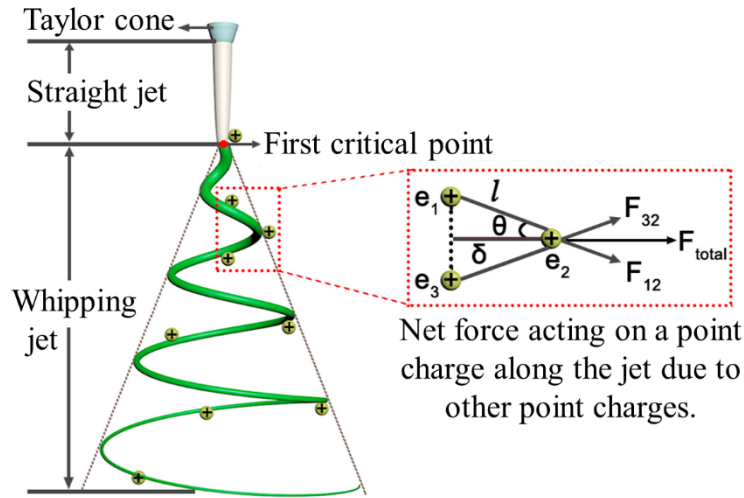


Figure 2-18: Net force driving the bending instability in the whipping jet region of an electrospinning jet. Adapted from [166].

Equation 2.8
$$F = -\sigma_s^2 \ln \frac{L}{a} |k| d\xi$$

F represents the net force, σ_s is the surface charge of the jet, L is the radius of the jet, and k is the curvature of the jet. This is relative to changes for the reference axis ξ [156]. At this point, the jet starts to move in loops and continues to stretch as it travels towards the collector. Depending on the conditions, it is possible that other critical points appear in the jet.

At this stage, the electrospun fibres are subjected to a very high ratio of stretching; depending on the conditions, this would be comparable to that used for uniaxial mechanical stretching [167, 168]. For certain types of polymers, this may be a determining factor for the crystallinity of the fibrous products. For some ferroelectric polymers such as PVDF, a combination of exposure to a high electric field and the net forces mediating the stretching of the material while in the whipping jet region can promote the resulting fibrous mat to have a higher content of one crystalline phase when compared to those that are predominant when other manufacturing methods such as spin-coating or casting [168].

2.3.1.4 Fibre deposition on the collector

Further travelling of the jet in a whipping motion causes it to stretch and thin even more, which in turn also causes the loss of solvent, eventually resulting in the jet transitioning into a solid state [156]. This mostly or completely dried product is what would ideally be deposited on the collector. Different sources indicate that the drying process contributes to some properties such as the degree of crystallinity of the material, the tensile strength of the fibres, among others [152, 156, 158].

2.3.2 Electrospinning parameters and their effect on the resulting products

The stages of the electrospinning process discussed in the previous section have components dependent on the electric field, the viscoelastic properties of the solution, the geometry of the nozzle, the distance between the nozzle and the collector, and other aspects. While the working principles behind electrospinning remain relatively the same irrespective of the type of device being used, there are a series of conditions that will affect the properties of the fibres being produced.

2.3.2.1 Voltage

As discussed in the previous section, the role of applied voltage is of great importance for electrospinning. In accordance to equation 2.5, the applied voltage must overcome a critical value for the electrospinning process to take place. Furthermore, it is also a determining factor affecting the time of flight of the jet being emitted from the Taylor cone and contributes to the disturbances that influence the whipping motion of the jet as it travels towards the collector [156, 159, 164, 166]. Thus, the applied voltage is one of the main contributing factors to the stability of the Taylor cone and the electrospinning process in general [169].

While the effect that the applied voltage has on the morphology of the electrospun product has been observed to vary depending on the properties of the polymer solution being employed, parametric studies have revealed that, in some cases, its magnitude directly affects the diameter of the fibres being produced [169–171]. Increasing the applied voltage means that also the electric field is being increased, which will result in greater electrostatic forces acting on the jet. Since the electrostatic repulsion is being amplified by applying an electric field of a higher magnitude, the disturbances driving the whipping motion become stronger, which leads to the narrowing of the jet [152, 170, 172]. However, the opposite has been reported from other parametric studies. For instance, varying the voltage from 16 kV to 35 kV while keeping parameters such as distance or flow rate constant has resulted in a net diameter increase from 860 nm to 1.18 μm for fibres obtained from a polyvinylpyrrolidone (PVP) solution [171]. Figure 2-19 shows one instance for which fibre diameter increased as a result of an increase in the applied voltage.

The uniformity of the electrospun product has also been identified as one of the characteristics being influenced by the voltage. High voltage magnitudes relative to the critical value needed for the formation of the Taylor cone have been observed to cause the electrospun product to acquire shapes that appear as beads connected by strings [152, 169]. It is theorised that the

instability of the electrospinning jet as the electric field is increased is responsible for the formation of beaded structures [152]. However, it is also necessary to consider the viscoelastic properties of the solution being used. The formation of beads in relation to the properties of the solution will be further explored in section 2.3.2.7.

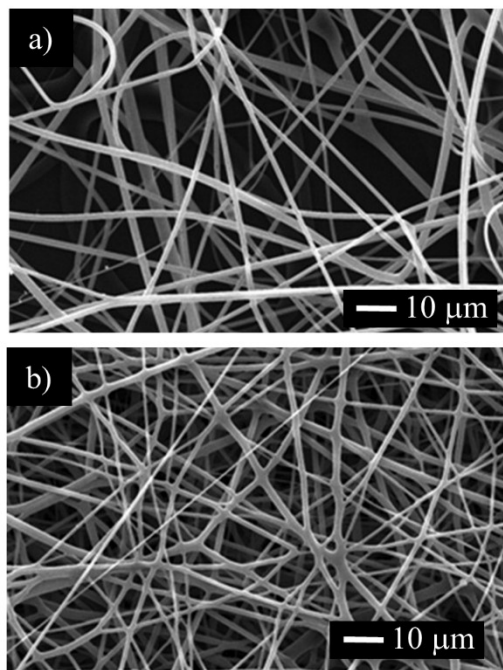


Figure 2-19: PVP fibers from 36 wt % solutions of PVP in a mixture of pure alcohol/distilled water (9:1, w/w) at applied voltages of 16 and 35 kV. Adapted from [171]

The effects discussed previously apply to electrospinning setups that use a direct current (DC) high-voltage (HV) power sources. Alternate current (AC) sources differ from DC sources in that the voltage measured to ground or reference is not constant, instead having a varying magnitude that follows a time dependent sinusoidal waveform. AC sources have been tested as alternative power sources for electrospinning setups, with some proponents of this alternative stating that the changing polarity of an AC source can add further control to the electrospinning process.

Considering that in electrospinning with DC sources the charged jet can be modelled as a series of similar point charges, just as previously mentioned when describing the regions of the electrospinning jet, in the case of AC electrospinning this is instead thought to be a series of point charges with alternating polarities, as shown in figure 2-18. Thus, the net force that causes the bending instability in the electrospinning jet would be reduced since the balance of individual electrostatic interactions is now constituted by both event of repulsion and attraction [151]. Figure 2-20 shows a schematic diagram of the net forces driving the bending instability in a jet for a DC and an AC source.

An analysis of the stages of fibre formation during AC electrospinning with a high-speed camera revealed that for both the positive and negative half-cycles of the AC wave, the formation of the Taylor cone remains the same as in DC electrospinning as long as the effective voltage value is higher than the critical value calculated from equation 2.5. If this condition is not met, no Taylor cone will be formed [173].

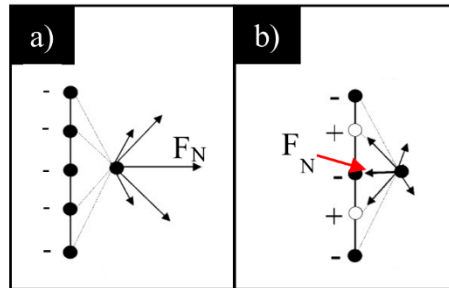


Figure 2-20: Differences in the forces driving the bending instability of the electrospinning jet in the whipping jet region for DC and AC electrospinning setups. Adapted from [151].

When using DC HV sources, it is possible to obtain fibres if using a negative DC source. The effect this would have on the morphology of the obtained product will depend on the characteristics of the polymer solutions. In some instances, studies have shown that reversing the polarity of the electrodes causes the electrospun fibres to be slightly thicker and for the yield to be reduced [174, 175]. However, other parametric studies have demonstrated that, for certain solutions, increasing the magnitude of applied positive DC voltages results in increasing fibre diameter while increasing the magnitude of applied negative DC voltages promote a reduction of the diameter of the final product [176].

2.3.2.2 Flow rate

Flow rate is defined as the rate at which the polymer solution is being fed to the electrospinning system. While this parameter can be controlled in electrospinning setups that depend on a syringe pump to feed the solution to a nozzle, this will not be the case for free surface methods [177]. These will be discussed in section 2.3.2.6.

The flow rate will influence the speed of the fluid as it leaves from the tip of the needle. Recalling equations 2.6 and 2.7, it can be appreciated how this parameter will be determining the velocity of the jet on the straight segment region [160]. If the time it takes for the electrospinning jet to travel from the tip of the Taylor cone to the collector is too short, the morphology of the fibres depositing on the collector tend to be non-uniform, with a heavy presence of beads. Thus, a low flow rate is associated with more uniform fibres because the travel time of the product is increased as well, which in turn allows for more time for solvent evaporation to occur on the whipping jet region [170]. Additionally, flow rate influences the

degree of polarisation of the jet, with lower rates allowing for the fluid to be more uniformly polarised [172].

2.3.2.3 Working distance

The working distance also affects the thickness of the fibres, and can be adjusted to elongate or shorten the time of flight of the electrospinning jet. While it has been discussed how the applied voltage influences the increase or decrease of the fibre diameter, the role of the working distance has been unequivocally identified. The greater the distance between the collector and the emitter electrode, the smaller the average fibre diameter will become [178]. Figure 2-21 shows an example of the effect of varying the working distance. Additionally, as the distance required for the product to reach the collector has increased, the solvent may have more time for evaporating fully [156, 170, 178].

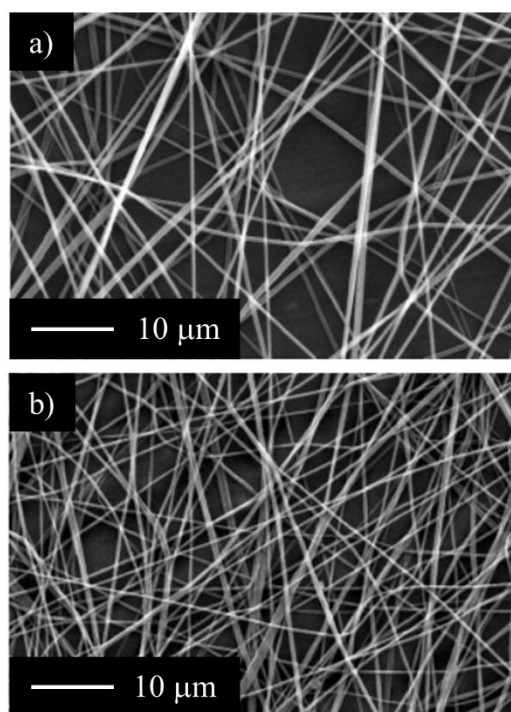


Figure 2-21: 20% polysulfone in acetone and N,N-dimethylacetamide solution, the applied voltage was 10 kV. (a) 10 cm working distance. (b) 15 cm working distance. Adapted from [178].]

2.3.2.4 Temperature

The effects that ambient temperature has on the morphology of the electrospun product are very closely related to other parameters, mainly to those related to the properties of the polymer solution being used. For instance, temperature (T) has an effect on the evaporation of the solvent and on the viscosity of the solution [179], which influences the diameter of the fibres [180].

Studies evaluating the role of temperature in electrospinning have revealed that an increase in the ambient temperature decreases the viscosity of the solution and increases the evaporation rate of the solvent [144, 170].

2.3.2.5 Relative Humidity

The relative humidity (RH%) can have a big impact on an electrospinning setup. If the RH% is too high, water condensation on the Taylor cone can affect charge density on the surface of the solution, disrupting the formation of the jet. A high RH% may also affect the evaporation rate of the solvent as the fibre jet travels to the collector, which in turn may produce thinner fibres as the jet may take longer time to solidify before depositing on the collector [181]. However, in some cases, an increase to fibre diameter has been observed for increasing RH% values [182]. This is shown in Figure 2-22.

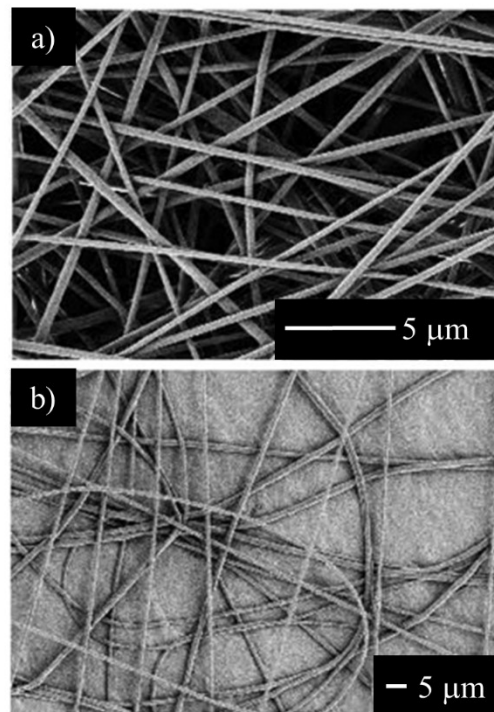


Figure 2-22: Effect of relative humidity in the diameter of electrospun fibres. (a) 23% (b) 43% Adapted from [182].

The relative humidity also plays a role in the formation of pores in the surface or within the electrospun fibres. [183, 184]. These pores arise from phase separation that occurred in the early stages of the electrospinning jet, namely, the straight segment and early whipping jet region [183]. As the jet is travelling towards the collector, water molecules that interact with it may deposit and remain on the surface or might penetrate into the jet. Once the jet starts to stretch and both solvents and sequestered water evaporate, only pores will remain [183]. Images of fibres electrospun at different RH% conditions are shown in Figure 2-23.

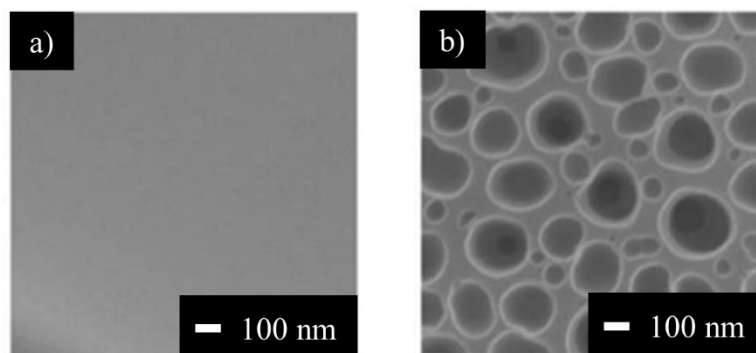


Figure 2-23: Image of the surface of fibres that were obtained from electrospinning a polymer solution of polystyrene in tetrahydrofuran electrospun at different RH% conditions. (a) 2% (b) 42%. Adapted from [183].

2.3.2.6 Electrode geometry

The contents of the sections discussed previously refer to single needle-nozzle systems. However, other electrode geometries, both for the collector and for the emitter, are compatible with the fabrication process, and each has the potential to create fibrous products with unique properties. This section will first describe the different types of emitters based on nozzle emitter electrodes.

One of the main limitations of using a single nozzle-based system is the production rate of the device. While the yield of the process depends on the solutions and parameters being used, common figures range from 0.1 to 1 grams of product per hour [185, 186]. One type of methods that have been proposed for potentially increasing the yield of nozzle-based systems is the use of emitters that can produce multiple electrospinning jets [185, 187–189]. One approach employs arrangements of multiple nozzles [188, 189], and is illustrated in Figure 2-24a. Multiple-nozzle systems consist of a series of nozzles carefully spaced out and all biased at the same voltage. One of the main limitations of using multiple-nozzle systems is that adjacent nozzles and jets interfere with each other, causing the trajectory of the fibres as they travel towards the collector to be deflected up to some degree as a result of coulombic and electric field dependent forces. Another limitation is that nozzle-based systems in general may become clogged, interrupting the process. Spacing out the needles can be used to prevent the nozzles and jets from interfering with each other [185, 187].

Another emitter geometry that is often grouped with other the nozzle-based systems are known as porous electrodes. The porous emitter electrode may be stationary or rotating; if rotating, the likelihood of the pores clogging is reduced since the solution is continuously being

pushed out by the centrifugal force. If stationary, feeding a gas into the system can also be used to facilitate the outward flow of the solutions [186]. The use of these kind of electrodes can reduce the influence each individual Taylor cone and jet exert on the neighbouring structures [188]. An example of a porous, rotating emitter is shown in figure 2-24a.

Free-surface electrodes do not rely on nozzles or capillaries for facilitating the formation of the electrospinning jets; instead, the solutions are unconfined, left to flow freely over surfaces such as spheres, cylinders, baths or wires [177, 190, 191]. These surfaces can be stationary or they may move [188]. Some examples of these types of collector are shown in figure 2-24b. The principles governing the formation of the Taylor cone and of the electrospinning jet that were described earlier are still valid for free-surface electrospinning. However, since this technique lacks a nozzle or capillary, the electric field exerted on the system is comparatively weaker. For this reason, free-surface techniques often require greater applied voltage magnitudes for promoting the formation of the Taylor cones [152, 187, 189, 191].

The mechanism mediating the formation of the Taylor cones in these kind of emitter electrodes can be described as an effect of waves forming on the freely flowing surface of the solution arising from disturbances mediated by the effect of the electric field, gravity, and capillary effects [190, 191]. The angular frequency ω of the waves being formed is described by the expression shown as equation 2.9 [190, 191].

Equation 2.9
$$\omega^2 = (\rho g + \gamma k^2 - \epsilon E_0^2 k) \frac{k}{\rho}$$

The acceleration due to gravity is g , ρ is the density of the solution, k is the wave number, E_0 is the field strength, and γ is the surface tension. Since the motion of a wave can be described by a sinusoidal function, and the electric field strength E_0 can be adjusted by the user, varying the applied voltage will determine the stability of the system. If the angular frequency remains positive, the waves on the surface of the solution will have either constant or damped amplitudes. However, if E_0 goes beyond a critical value, E_C , then the angular frequency term becomes negative, thus resulting in the system becoming unstable [190, 191]. An expression for the critical value E_C is shown as equation 2.10.

Equation 2.10
$$E_C = \sqrt[4]{\frac{4\rho\gamma g}{\epsilon^2}}$$

The formation and growth of unstable wave crests favours the formation of a Taylor cone and electrospinning jet at those locations. Furthermore, crests are forming one wavelength apart from each other; thus, using a free-surface electrode also results in the self-organised formation of Taylor cones [190, 191].

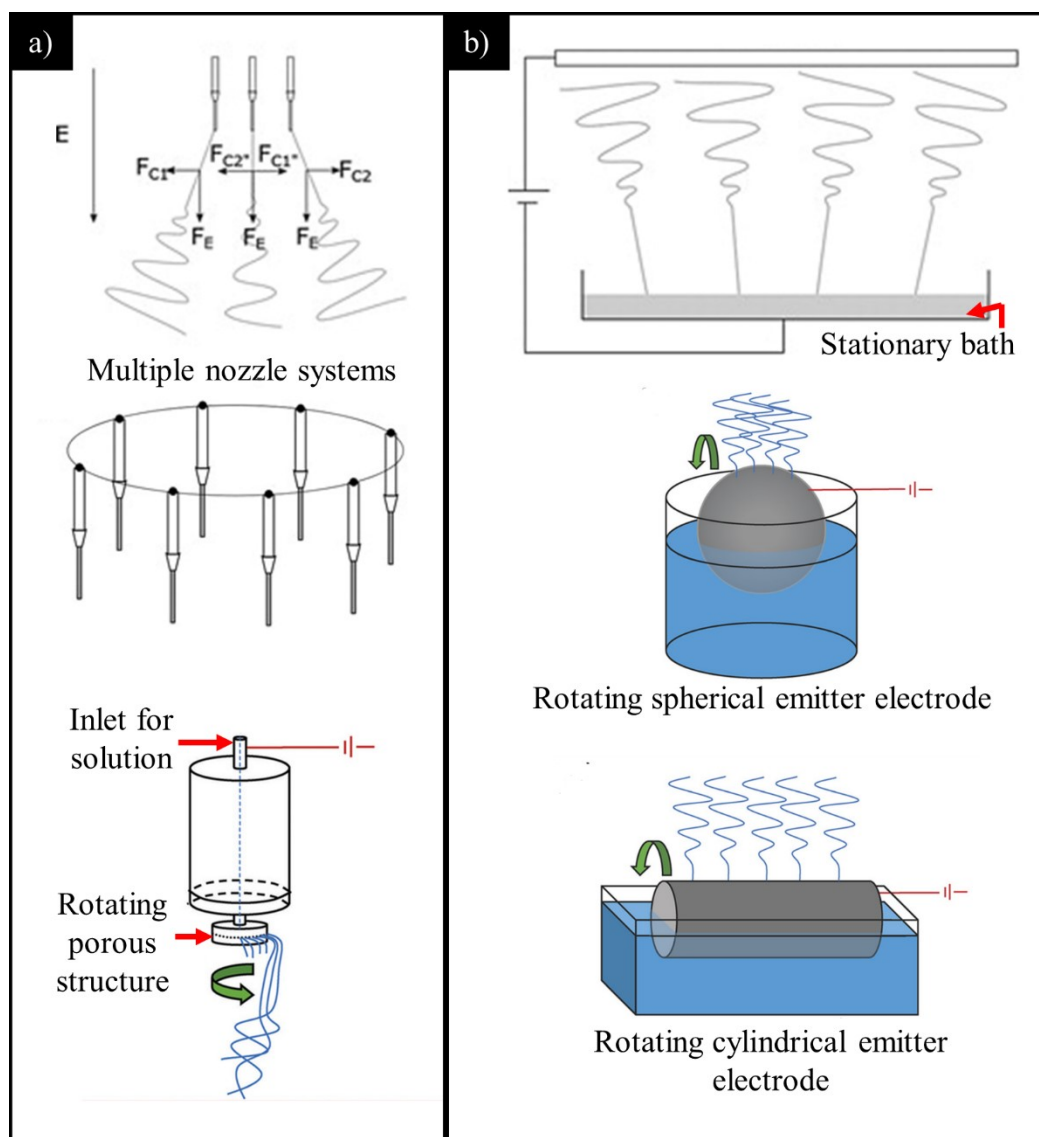


Figure 2-24: Different emitter electrode geometries. (a) Multiple nozzle electrodes. (b) Free surface electrodes. Adapted from [188] and [199].

Collector [188, 189] electrode geometry also plays an important role on the properties of the electrospun product. In general terms, these can be classified in two categories, stationary and dynamic [189]. The most basic stationary collector geometry consists of a flat, continuous plate, and allows for the collection of a single mat of randomly aligned fibres. Modifying the shape so that the electrode becomes a continuous curved or ridged structure greatly influences the distribution of the electric field on the system; these kind of surfaces can mediate the formation of multiple Taylor cones from one single droplet for nozzle emitter systems, allowing for the collection of multiple fibre mats [152, 189]. Discontinuous surfaces can also be used as alternatives. Arrays of physically separated plates or wires can mediate the deposition of highly aligned fibres [152, 192]. Examples of stationary collectors are shown in Figure 2-25a.

Rotating collectors can also be used to obtain highly aligned fibres. These are typically cylindrical or disc-shaped continuous structures, although discontinuous rotating structures have also been proposed [149, 152, 189]. Systems employing rotating collectors fitted with speed control modules can be used to modulate the degree of alignment of the product. While low rotating speeds still result in the deposition of randomly oriented fibres, operating the device at more than a thousand revolutions per minute (RPM) will result in the fibres deposited on the collector to become aligned [193]. Examples of rotating collectors are shown in figure 2-25b. [149, 152, 192]

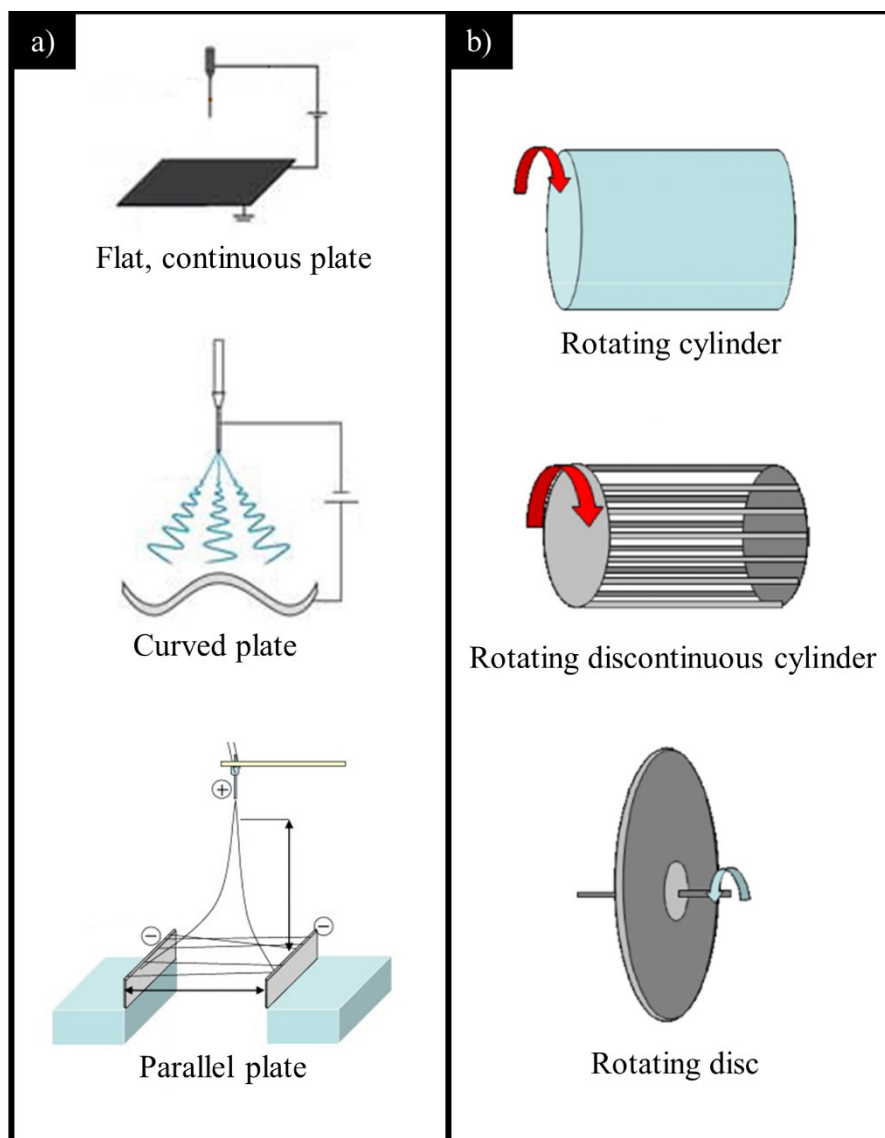


Figure 2-25: Different collector geometries. (a) Stationary collectors. (b) Rotating collectors Adapted from [149], [152], and [192].

2.3.2.7 Solution dependent parameters and the role of additives

Among the parameters that a user can control, there are those related to the properties of the solvents being used for preparing the polymer solutions. The choice of solvent depends on

the type of polymer being used, with some of them being water soluble while others would require organic solvents such as dimethylformamide (DMF) or dimethyl sulfoxide. Solvents can be used on their own or combined in complex mixtures. The boiling point, volatility and surface tension of the solvent influence the properties of the fibres obtained from the process [170].

Using a solvent with a high boiling point prevents the solution from drying on the emitter electrode allowing for continuous electrospinning to take place. However, a very high boiling point may cause the fibres that deposit on the collector not to be completely dry. This would cause the collected fibres to dissolve and fuse on the collector since the remaining solvent may dissolve some of the fibres [144, 170].

Recalling how the perturbations that drive the motion of the electrospinning jet in the whipping jet region, the role that the viscoelastic properties of the fluid has on the stability of the jet and thus on preventing it from breaking into a spray, are crucial for determining the viability of the process [156, 164, 165].

The surface tension of the solvent affects the uniformity of the individual fibres. A high surface tension causes the polymer jet being ejected from the Taylor cone to become a chain of beads and thin thread-like regions instead of a straight jet. This occurs since the high surface tension of the solvent prevents some regions of the jet from stretching. The combination of solvents can be used to modulate these effects on a polymer solution .[172, 194, 195].

Having a solution with low viscosity causes surface tension to be dominant, thus resulting in the production of beaded fibres or could even cause the process to transition into electrospraying. Increasing the polymer concentration results in the production of more uniform fibres. Solvent composition of the solution, polymer concentration and molecular weight (MW) all influence the viscosity of the solution. Polymer MW and its concentration in the solution are often regarded as a figure of merit for how likely it is that a solution can be used for electrospinning. If the viscoelasticity or extensional viscosity of the polymer solution jet is low, it will break or lead to the formation of beaded fibres. The viscoelasticity depends on the concentration of the polymer and the MW; the higher the concentration of the polymer and the higher its MW, the likelihood of polymeric chains overlapping will increase. Overlapping polymer chains cause entanglement, which provides enough viscoelasticity to the solution for the formation of a jet at the tip of the Taylor cone instead of causing it to break into droplets. Only solutions with a polymer concentration above a critical value will be compatible with the electrospinning method. Thus, tuning the polymer MW and solvent viscosity can be used to make a solution more compatible with the electrospinning process [145, 150, 196]. An expression for the critical value of polymer concentration for a solution to be “electrospinnable” is shown in equation 2.11 [197].

Equation 2.11
$$C^* = \frac{3 MW}{4\pi R_g^3 N_A}$$

The critical polymer concentration C^* can be estimated from the MW of the polymer, the radius of gyration of an individual polymer molecule R_g , and Avogadro's number. The term R_g is related to the effective volume that is occupied by each polymer molecule in the solution, and can be modelled as a sphere occupied by an individual polymer chain [197].

Other chemicals such as salts and acids can be added to the electrospinning solutions to modify the properties of the final products being fabricated; these are often referred to as additives in the literature [198]. The addition of minute amounts of acids or salts can effectively alter the conductivity of a solution. Increasing the conductivity of the solution may result in a reduced fibre diameter as the jet will carry more charges, ultimately affecting the balance of the disturbances that govern the motion of the jet in the whipping region [152, 198].

In some instances, additives can be used to improve the uniformity of the fibres being produced and to reduce the fibre diameter. For instance, the addition of 0.5 μL per mL of a 18% weight to volume solution of thermoplastic polyester-polyurethane resulted in the fibre diameter of an electrospun product being reduced from 1.048 μm to 231 nm [199].

Inorganic salts have also been extensively studied as additives for electrospinning. In general, salts help to increase the conductivity of the solutions, which can influence the diameter of the produced fibres and can also prevent the formation of a beaded product. The use of salts as additives has also been associated with an increasingly unstable jet that is more susceptible to develop more critical points in the whipping jet region [170, 200, 201].

Lithium chloride (LiCl) is a low toxicity metal chloride salt with a colourless, crystal-like appearance [202]. While other salts such as sodium chloride or nickel chloride have been used as additives for the electrospinning of the ferroelectric polymer PVDF [203–205], a study on which different inorganic salts were used as additives for electrospinning identical solutions indicated that Lithium Chloride achieved the greatest solution conductivity increase for unit of added weight per volume of solution, as well as the second best reduction of solution viscosity [200]. Considering that, as discussed previously in section 2.2.3.3, an increase in the conductivity of PVDF solutions can potentially increase the likelihood that the material will crystallise in the β -phase during polling, and taking into account the claims that LiCl mediates the greatest solution conductivity increase relative to the performance of other salts, it was selected as the additive that would be explored in the experimental work presented in this thesis.

2.3.2.8 Specialised emitter electrode topologies

The previous sections have provided an overview of the many parameters that affect the properties of the electrospun fibres; thickness, uniformity, degree of alignment, and other properties can be fine-tuned by the careful selection of the electrospinning setup and conditions. Specialised modifications to the emitter electrodes can allow for the production of more complex fibrous products. Co-axial electrospinning is defined as the technique that allows for the formation of layered fibrous structures out of two or more solutions [197]. The nozzles used for this electrospinning technique consist of an arrangement of concentric capillaries, with each compartment being dedicated to one of the solutions to be used. The selection of solvents and polymers allows for the fabrication of fibres with several interesting properties, such as structures with conductive cores but inert shells, or cores loaded with bioactive elements coated in a biodegradable shell for drug delivery applications [197, 206]. Additionally, using other fluids such as mineral oils as the core material can result in the formation of completely hollow fibrous structures.

The various types of emitter and collector electrodes can be mixed and matched for creating fibrous structures with unique characteristics. A visual summary of the various product morphologies that can be obtained from different electrode combinations is shown in Table 2-3.

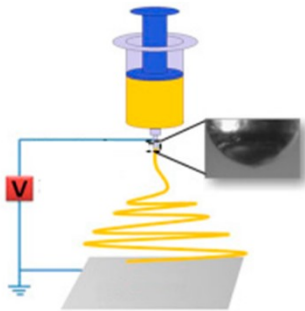
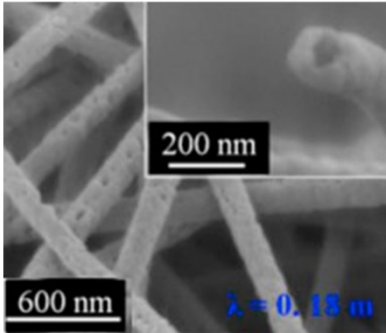
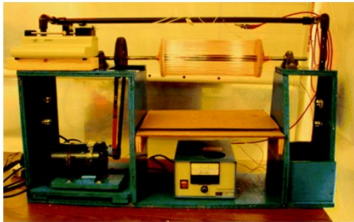
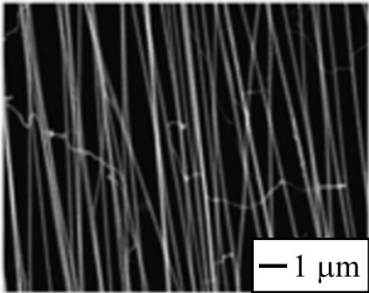
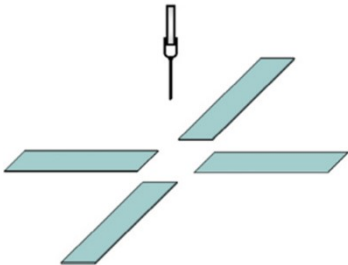
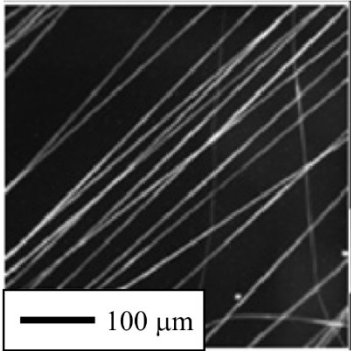
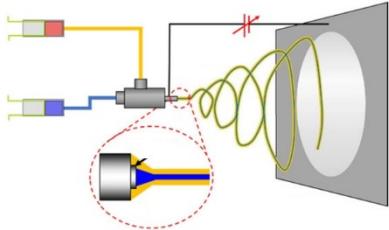
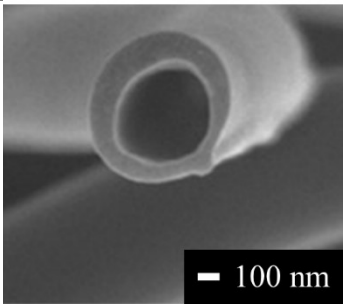
2.3.3 Electrospinning setup selection

The experimental work presented in this thesis focuses on the use of two different electrospinning setups. The first one consists of a single nozzle setup with a stationary collector and a pumping system for feeding the solution to the nozzle. The aim of choosing this setup was that the solution and working parameter optimisation process would be easily carried out since critical parameters such as working distance, voltage and flow rate can be easily controlled and varied. A free-surface method consisting of a rotating cylindrical emitter similar to that shown in figure 2-24b and a rotating cylindrical collector similar to that from figure 2-25b was also employed in the experimental work that will be explored in further chapters. The reasons for choosing this method were mainly related to the advantages that a nozzle-free setup has in terms of product formation rate. Compared to the 0.1 to 1 g hr⁻¹ produced by single-nozzle systems, free-surface methods can produce figures such as 50 g hr⁻¹ [188] or even in the range of g min⁻¹. The use of this type of emitter electrode would allow the upscaling of the production of the active core materials, which is one of the main objectives of this thesis.

Up to this point, a selection of piezoelectric polymers and the methods that will be used to process them have been discussed. One of the main goals of the project is the fabrication of

piezoelectric energy harvesting devices. As discussed in a previous section, piezoelectric generators and mechanical energy harvesters in general have electrical outputs in the form of AC signals. In the following section, basic and advanced concepts of AC circuits are presented, offering an overview of the theoretical knowledge required for understanding the fundamentals and the complexities of AC signals, which will be essential for designing the electronic instrumentation needed for extracting the output power from the generators.

Table 2-3: Different types of products can be obtained from using different kinds of emitter and collector electrodes.

Type	Setup image	Product image	Reference
Stationary plate collector, single needle-nozzle emitter electrode			[207]
Rotating discontinuous cylinder collector, high RPM, single nozzle emitter electrode			[208]
Array of parallel plate collectors, single needle-nozzle emitter electrode			[149]
Coaxial nozzle emitter electrode			[197]

2.4 Harvesting energy from a piezoelectric generator

The output signals that can be obtained from a piezoelectric generator have specific characteristics that depend on the mechanical excitation being imparted on the generator and the internal properties of the generator itself. This section provides the basic theoretical background for understanding the output response of these generators, showing how the circuit equivalents of these devices are modelled and outlining the analytic tools that will allow for the characterisation of their electrical response. Methods for conditioning the harvested energy are also discussed in detail.

2.4.1 Piezoelectric device as electromechanical systems and equivalent electrical models

Piezoelectric devices are electromechanical systems that can be modelled as circuit elements depending on the implemented design. For instance, a piezoelectric crystal oscillator is often used in certain circuits for generating an electrical signal with a constant frequency. These can be modelled as a capacitance, which arises from the crystal being a dielectric material sandwiched between two electrical plates, in parallel with an inductance-capacitance-resistance (LCR) branch that represents the mechanical properties of the crystal such as stiffness and friction in the system [209, 210].

The equivalent circuit for a piezoelectric generator depends on how the device was assembled, the geometry of the design, types of materials used, among other aspects. For instance, generators built in a plate configuration that have been mounted as a cantilever beam fixed on one end and fitted with a mass on its other end is mechanically equivalent to a spring-mass-damper system [211–215]. In the case of compression piezoelectric generators, an equivalent mechanical model is shown in Figure 2-26 [214].

The complexity of the model and how it can be described as an electrical circuit equivalent depends on considerations pertaining to the degrees of freedom of the system, adoption of a lumped parameter or distributed parameter model, taking into account the effect that the electrodes have on the piezoelectric material, among others. However, a simplistic lumped model can be taken as an approximation [215, 216]. A generalised electric circuit equivalent model for a piezoelectric generator is shown in Figure 2-27 [217]. In this ideal model, the generator is shown as a current source in parallel with the capacitance C_P , which depends on the geometry of the device and the piezoelectric properties of the material. Under mechanical excitation conditions, a current will be produced and will be distributed between the electrical load and C_P . In practice, the branch with C_P will include a resistive element that represents the

internal loss of the generator. Thus, the generator is equivalent to a current source in parallel with passive elements representing the characteristics of its construction, materials and the losses that would occur because of contact resistance issues, mechanical damping, etc [214, 216].

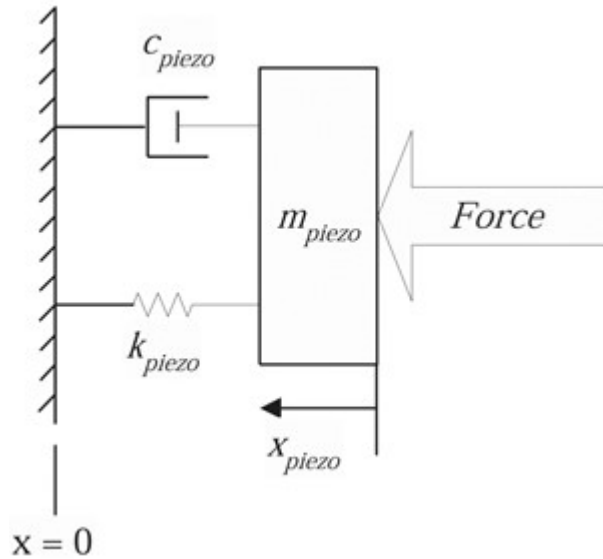


Figure 2-26: Mechanical model of a compression piezoelectric generator. Adapted with permission from [214]. Copyright 2003 IEEE.

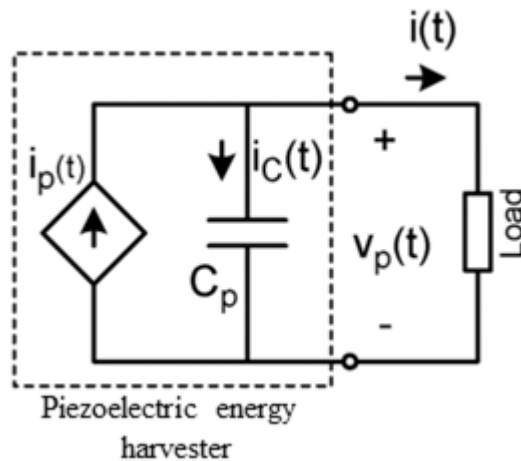


Figure 2-27: Generalised electrical circuit equivalent of a piezoelectric generator. Adapted with permission from [217]. Copyright 2010 IEEE.

Following the assumption that a generator can be modelled as a spring-mass-damper system, the expected impulse response for these are in the form of a damped sinusoidal waveform [218]. Sinusoidal signals are a class of alternating current (AC) signals. The following section will discuss the AC signal fundamentals required for understanding this class of output responses.

2.4.2 AC signals

AC signals are defined as any electrical signal with a magnitude that varies as a function of time. The instantaneous magnitude value can be either positive or negative, thus indicating that the current flow is reversed at certain times. Sinusoidal signals are regarded as the most general and fundamental type of AC signal. The general equation that describes such a signal is shown as equation 2.12.

Equation 2.12
$$f(t) = V_o \cdot \sin(\omega t \pm \theta)$$

V_o is the peak value or amplitude, ω is the angular frequency, which is equivalent to $2\pi f$, and θ is a phase shift in degrees for this example. An example of a sinusoidal signal is shown in Figure 2-28.

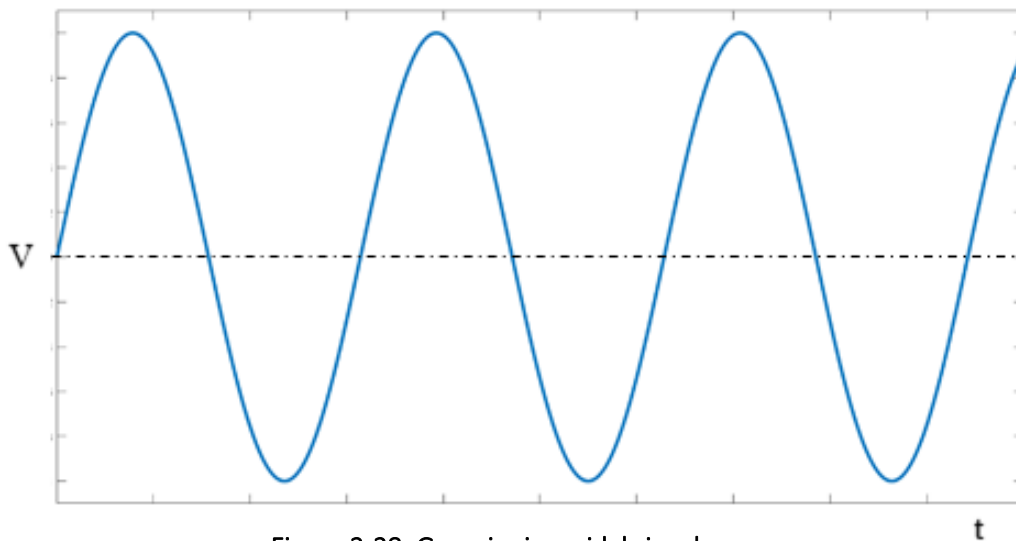


Figure 2-28: Generic sinusoidal signal

The analysis of AC circuits is often simplified by the use of phasors. A phasor is the representation of a sinusoidal function as a vector which rotates counter-clockwise in the complex plane. Phasors are represented in polar form, which consists of a magnitude and an angle. The polar form of the signal from figure 2-28 is shown in equation 2.13.

Equation 2.13
$$V \angle \theta$$

While the magnitude V of a phasor can be the amplitude value seen on the sinusoidal representation equation, V_o , it is more common for the root mean square (RMS) value (V_{RMS}) to be used instead. The RMS voltage or current can be defined as an AC value that can deliver the same power to a constant resistive load as a DC source. Equation 2.14 can be used to calculate the RMS value of a periodic signal, in which T represents the period of the signal.

Equation 2.14
$$V_{RMS} = \left(\frac{1}{T} \int_0^T (f(t))^2 dt \right)^{\frac{1}{2}}$$

The derivation of V_{RMS} for sine wave relative to its amplitude V_o is shown in equation 2.15.

Equation 2.15
$$V_{RMS} = \frac{V_o}{\sqrt{2}}$$

Adhering to the principles of linear, time-invariant (LTI) systems, it is understood that feeding an electrical load with a specific type of input signal results in a known output behaviour which depends on the characteristics of the load and the previous state of the system in some cases. Similarly to what is observed in DC circuits, having an input voltage in the passive element results in a particular electrical current being observed in the load. The electrical load of an AC circuit is known as impedance (Z), which is defined as the ratio of the observed voltage to the measured current on a circuit element, or, alternatively, as the ratio of the voltage to current phasors. The currents observed for capacitive (C), resistive (R) and inductive (L) loads when excited by a sinusoidal voltage can be described as follows.

For an ideal resistor, Ohm's law states that the voltage V observed across a resistor is equal to the current I multiplied times R . If the voltage is a function of time instead of a constant value, it follows that the current is also a function of time. The current observed for an input sinusoidal voltage is shown in equation 2.16, and the impedance constant and equal to R , as shown in equation 2.17.

Equation 2.16
$$\frac{V_o}{R} \cdot \sin(\omega t) = I(t)$$

Equation 2.17
$$\frac{\frac{V_o \cdot \sin(\omega t)}{\frac{V_o}{R} \cdot \sin(\omega t)}}{R} = R = \frac{V_{RMS} \angle 0^\circ}{\frac{V_{RMS}}{R} \angle 0^\circ} = R \angle 0^\circ$$

In the case of an ideal capacitor, the general form of its current to voltage relation is shown in equation 2.18. The expression shown in equation 2.19 corresponds to the current observed for the ideal capacitor when the input voltage is a sinusoid. The current has a different phase than that of the input voltage signal; this is why, for ideal capacitors, the voltage is said to lag 90° behind the current.

Equation 2.18
$$I(t) = C \cdot \frac{dV(t)}{dt}$$

Equation 2.19
$$I(t) = \omega C \cdot \cos(\omega t) = \omega C V_o \cdot \sin(\omega t + 90^\circ)$$

The impedance for a capacitive load is shown in equation 2.20. Contrary to the case of the ideal resistor, the impedance of a capacitor is a function of the frequency of the sinusoidal excitation input, and is associated with a phase shift of -90° when compared to R . This parameter is called capacitive reactance, X_C .

Equation 2.20
$$\frac{V_o \cdot \sin(\omega t)}{\omega C V_o \cdot \sin(\omega t + 90^\circ)} = \frac{V_{RMS} \angle 0^\circ}{\omega C V_{RMS} \angle 90^\circ} = \frac{1}{\omega C} \angle -90^\circ = X_C$$

For an inductor, for which the voltage to current relation is defined as shown in equation 2.21, the observed current would be equal to what is shown in equation 2.22. For the inductor, the current waveform has a different phase than that of the input voltage signal as well, with the voltage signal leading the current by 90° .

Equation 2.21
$$V(t) = L \cdot \frac{dI(t)}{dt}$$

Equation 2.22
$$I(t) = \frac{1}{L} \int V(t) dt = -\frac{1}{\omega L} V_o \cdot \cos(\omega t) = \frac{1}{\omega L} V_o \cdot \sin(\omega t - 90^\circ)$$

The impedance of an inductor is shown in equation 2.23. Its value is also a function of frequency, and is associated with a 90° phase shift when compared to R. This parameter is known as the inductive reactance, X_L .

Equation 2.23
$$\frac{V_o \cdot \sin(\omega t)}{\frac{1}{\omega L} V_o \cdot \sin(\omega t - 90^\circ)} = \frac{V_{RMS} \angle 0^\circ}{\frac{1}{\omega L} V_{RMS} \angle -90^\circ} = \omega L \angle 90^\circ = X_L$$

Figure 2-29 shows a series LCR circuit, a plot of the individual V for each element as both sine waves, and a phasor diagram of the same signals. As it can be observed from both the plot and the phasor diagram, the voltages for reactances X_L and X_C are 180° out of phase with each other. Depending on the values of L, C and ω , it is possible for these to cancel each other out completely and thus have input V being in phase with I or for either one of them to dominate, which would result in V lagging or leading I by an angle that is a function of L, C and ω . This is reflected in the total impedance of the network, which exists as a linear combination of an active and reactive component. The active component is that for which the V to I ratio has an angle of 0° and is associated with resistive elements. The reactive component has a $\pm 90^\circ$, depending on which is more dominant, either X_L or X_C . The equivalent impedance Z can be expressed as the complex number shown in equation 2.24. Any complex load network consisting of LCR elements in series, parallel or combinations of these can ultimately be reduced to a single equivalent impedance that can be expressed in that form.

Equation 2.24
$$Z = R + j(X_L - X_C)$$

The concepts discussed above can be extended to any periodic signal, allowing the use of AC circuit analysis techniques for signals such as those obtained from a heart rate monitor or a microphone. Any periodic signal can be described as an infinite weighted sum of sine and cosine functions; this description is known as the Fourier series. The general form for the Fourier series is shown in equation 2.25. The value a_0 represents the DC offset of the signal, a_n and b_n are the amplitudes for the sines and cosines, ω_0 represents the fundamental angular

frequency and n is the multiplier for the fundamental frequency, which indicates that for $n > 1$ we are now dealing with harmonics. The a_0 , a_n and b_n terms can be calculated from equations 2.26, 2.27 and 2.28 respectively.

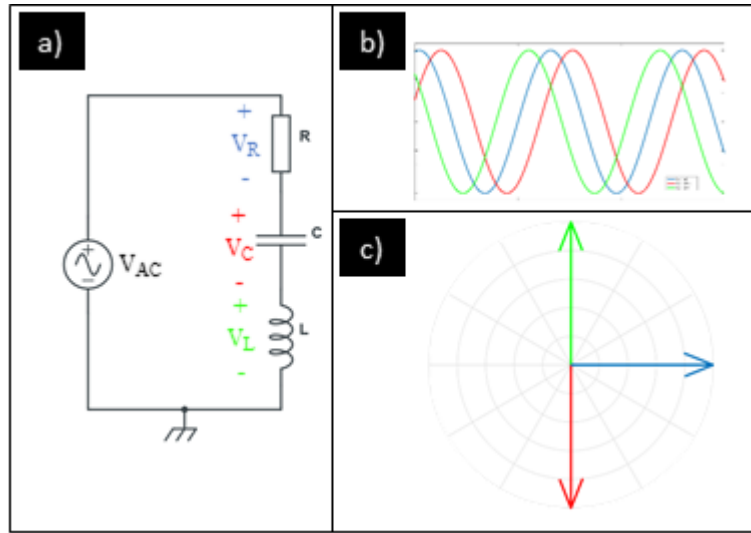


Figure 2-29: Voltage observed across individual components for a series LCR circuit. (a) Circuit diagram (b) Sinusoidal voltages observed across each element. (c) Phasor representation of each element's voltage.

Equation 2.25
$$f(t) = a_0 + \sum_{n=1}^{\infty} a_n \cdot \cos(n\omega_0 t) + \sum_{n=1}^{\infty} b_n \cdot \sin(n\omega_0 t)$$

Equation 2.26
$$a_0 = \frac{1}{T} \int_{-\frac{T}{2}}^{\frac{T}{2}} f(t) dt$$

Equation 2.27
$$a_n = \frac{2}{T} \int_{-\frac{T}{2}}^{\frac{T}{2}} f(t) \cdot \cos(n\omega_0 t) dt$$

Equation 2.28
$$b_n = \frac{2}{T} \int_{-\frac{T}{2}}^{\frac{T}{2}} f(t) \cdot \sin(n\omega_0 t) dt$$

The power consumed by an electrical load is simply the multiplication of the voltage observed across its terminals and the current flowing through its ports. The instantaneous output power figure is defined as the product of the current and voltage values at a specific moment. This value is often used to express maximum instantaneous power figures. Obtaining the average power figure for a load in an AC circuit introduces a slight degree of complexity, requiring careful consideration of the active and reactive components of the load. The power consumed by the active component of the load impedance is simply known as the active power (P), its unit being Watts (W). This value represents the power that is actually being converted to productive work and is often used to easily compare AC power to DC power (only if RMS

values have been used for calculating it). The power consumed by the reactive elements is known as the reactive power (Q), which has reactive volt-ampere (VAR) as its units and represents the power that is being lost to the network. The combination of the active and reactive power is known as apparent power (S), and has volt-ampere (VA) as its units. S is calculated by calculating the vector addition of P and Q .

Considering the voltage and current signals for an ideal capacitor, at the instant when the current is at its maximum or minimum, the voltage is zero given the 90° phase difference between these waveforms. When the voltage is at its maximum and minimum values, the current is zero. Mathematically, this implies that the instantaneous power is zero at those specific moments. Practically, this means that the energy stored in the capacitor is being lost in the network. The same occurs for the ideal inductor, only at complementary instants due to phase differences. The efficiency of powering up an AC load can be measured by comparing the angle of S relative to P . The closer this angle is to 0, the more efficient the system is since power is only being used to perform a task rather than being lost in the network. A diagram showing how S is constructed from Q and P is shown in Figure 2-30.

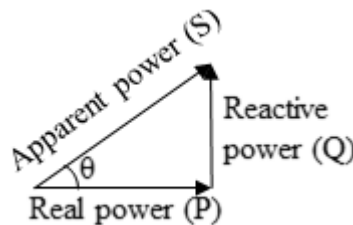


Figure 2-30: The apparent power is equal to the vector sum of the real power and the reactive power.

One method for enhancing the efficiency of the system is to calculate the reactive impedance component of the load and add an additional reactive load that has the same magnitude but an opposing nature (adding X_L to compensate for a dominant X_C or the other way around). These concepts can be extended to the evaluation of the conditions required to maximise the output power for an AC source, which can be critical for designing the circuit blocks used for energy conversion and storage for energy harvesting systems.

On an additional note about energy conversion and storage, portable electronics are typically DC systems. Thus, methods for transforming the AC output of a piezoelectric generator into a DC output will be necessary. One way for converting an AC signal to a DC signal is to use a full-wave rectifier, which is a functional block composed of 4 diodes that allow for both the negative and positive peaks of an AC signal to be delivered to a load, each with the same polarity/direction of current flow. A diode is a circuit element that allows current to flow through only in one direction [219]. A schematic diagram of a generic full-wave rectifier is shown in

Figure 2-31a. Figure 2-31b shows the AC input waveform. Figure 2-31c shows the converted waveform on the load.

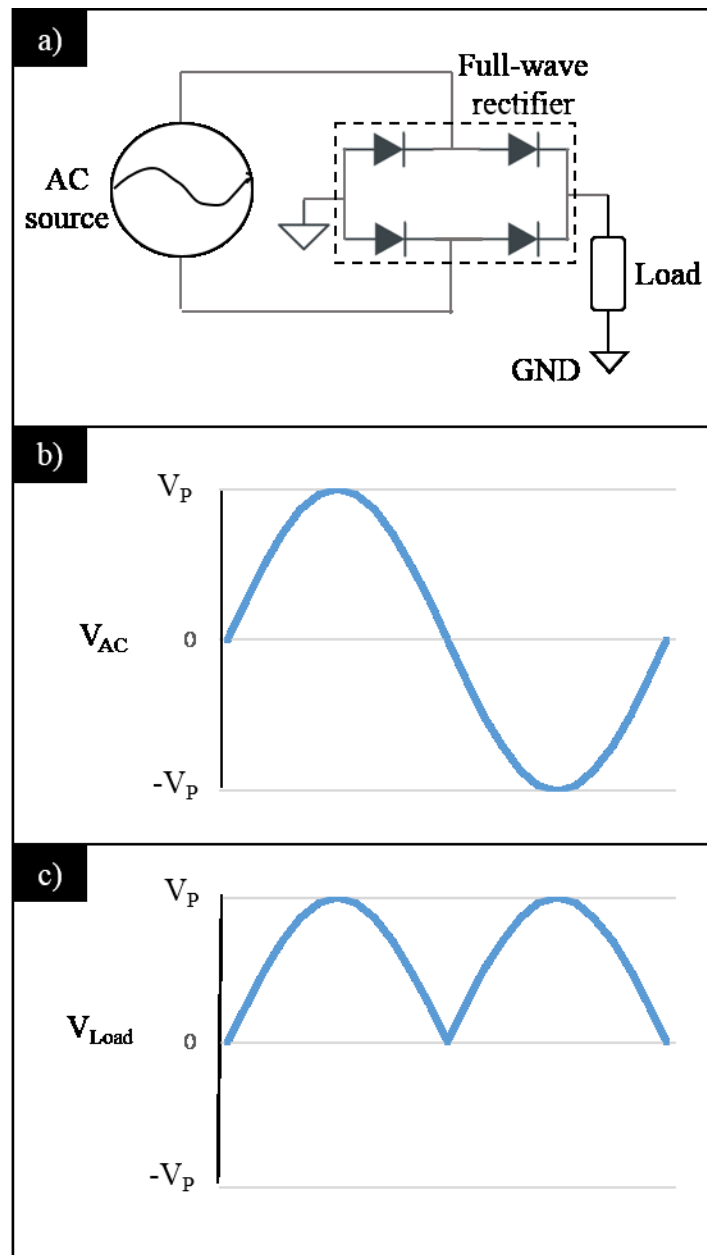


Figure 2-31: AC to DC conversion. (a) Circuit diagram of a full-wave rectifier. (b) Input sinusoidal waveform. (c) Output waveform.

2.4.3 Maximum power transfer theorem

In practical situations, any power source has an internal impedance. Independent of the type of electrical load that this source is powering up, there will inevitably be a power loss since the internal impedance of the source itself is also consuming part of the supplied energy.

Similarly to what happens in DC circuits, it is possible to derive an expression for the maximum power that can be transferred to a load. A power source can be modelled as a Thévenin (voltage source in series with a source impedance) or a Norton (current source in parallel with a source admittance, which is the reciprocal of impedance) equivalent circuit. These are shown in Figure 2-32 [220].

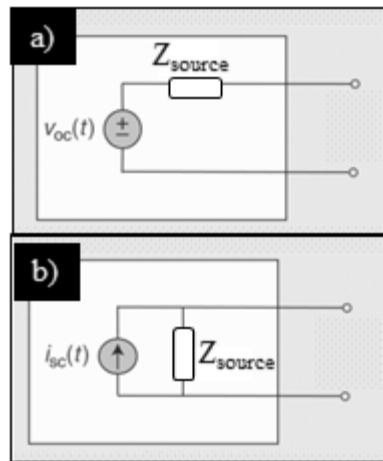


Figure 2-32: Equivalent circuit for a power source (a) Thévenin equivalent. (b) Norton equivalent. Adapted with permission from [220]. Copyright 2018 IEEE.

The following analysis uses the Norton equivalent. Connecting a load impedance to the Norton equivalent results in a series circuit for which the source and load impedance share the same current. For calculating the power supplied to the load impedance, it is possible to derive an expression based on the product of the voltage and current of the load. Equation 2.29 shows the current, and equation 2.30 the voltage for the load impedance.

$$\text{Equation 2.29} \quad V_{Load} = \frac{V_{in} \cdot Z_{Load}}{Z_{Load} + Z_{Source}} = \frac{V_{in} \cdot (R_{Load} + jX_{Load})}{Z_{Load} + Z_{Source}}$$

$$\text{Equation 2.30} \quad I_L = \frac{V_{in}}{Z_{Load} + Z_{Source}}$$

Since, as discussed previously in section 2.3.1, the power value of interest when analysing AC circuits is the active power P , the expression of interest in regards to power should then be in relation to the active component of the load impedance, R_{Load} . Assuming that the load impedance is composed of a real component R_{Load} and a reactive component X_{Load} , the previous equations can be combined to obtain an expression for the power. The real component of this expression is shown in equation 2.31.

$$\text{Equation 2.31} \quad P_{Real} = \frac{V_{in}}{Z_{Load} + Z_{Source}} \cdot \frac{V_{in} \cdot R_{Load}}{Z_{Load} + Z_{Source}} = \frac{(V_{in})^2 \cdot R_{Load}}{(Z_{Load} + Z_{Source})^2}$$

Working with this equation will show that for the maximum power delivered to the delivered it is necessary for R_{Load} to be equal to R_{Source} and for the reactive component X_{Load} to be equal

in magnitude but opposite in nature to X_{Source} . In other words, the real components should have identical magnitudes, just as in DC circuits, and the reactive components should cancel each other out. In mathematical terms, when the load impedance is the complex conjugate of the source impedance, maximum AC power transfer is achieved. This is shown in equation 2.32, in which the asterisk operator signifies the complex conjugate.

Equation 2.32 $Z_{Load} = Z_{Source}^*$

2.5 Interim summary

This chapter provided a summary of the essential theory and concepts relevant to the experimental work covered in this thesis. It begins with an overview of the existing energy harvesting methods that can be considered when designing wearable devices. Comparing features such as their working principles, output type, additional elements required for their operation, and their limitations is essential for selecting the one that fits best the target application. Additionally, depending on the type of materials and generator design, it might be possible to implement a hybrid design that can potentially allow for a more efficient and effective solution.

This section is followed by a detailed introduction to the piezoelectric effect. The different types of materials that show piezoelectric behaviour are discussed, with particular focus on polymers, followed by a detailed discussion of the properties of those chosen for the project. The following section deals with electrospinning, which is the main fabrication technique that will be employed in this thesis. Two of the electrospinning methods discussed, nozzle-based and nozzle-free, will allow first for the development of an optimised polymer solution and for the identification of the favourable conditions that facilitates the fabrication of quality fibrous products. Once these have been achieved, the two different electrospinning setups can be used for further developing novel structures and for the extrapolation of the previous conditions to the high-throughput setup, potentially allowing for upscaling of the process.

The final section of this chapter describes the theory related to extracting energy from piezoelectric generators. The concepts presented in this explain the equivalent models and electrical output characteristics that make it possible to implement the appropriate auxiliary instrumentation that will guarantee that a piezoelectric generator is being used to its maximum potential.

The contents of this chapter discussed the fundamental knowledge that allowed for the work presented in this thesis to progress from an initial exploration of material fabrication to the application of the obtained products in the form of functioning piezoelectric energy harvesters. The following chapter will describe the general materials and methods employed in the project, outlining the approaches that were followed for the fabrication of materials and their characterisation, generator design and assembly, and the implementation of testing fixtures.

2.6 References

- 1 Favenneec, J.-M.: 'Smart sensors in industry' *J. Phys. E.*, 1987, **20**, (9), p. 1087.
- 2 Nihtianov, S., Luque, A.: 'Smart Sensors and MEMS: Intelligent Sensing Devices and Microsystems for Industrial Applications' (Elsevier Science, 2018)
- 3 Munivel, K.V., Samraj, T., Kandasamy, V., Chilamkurti, N.: 'Improving the Lifetime of an Out-Patient Implanted Medical Device Using a Novel Flower Pollination-Based Optimization Algorithm in WBAN Systems' *Math. 2020*, 2020, **8**, (12), p. 2189.
- 4 Guney, M.G., Chung, V.P.J., Mukherjee, T., Fedder, G.K.: 'On-chip environmental sensors for bias drift compensation' *Proc. IEEE Sensors*, 2017, **2017-Decem**, p. 1–3.
- 5 Imani, S., Mercier, P.P., Bandodkar, A.J., Kim, J., Wang, J.: 'Wearable chemical sensors: Opportunities and challenges' *Proc. - IEEE Int. Symp. Circuits Syst.*, 2016, **2016-July**, p. 1122–1125.
- 6 Kargaran, E., Manstretta, D., Castello, R.: 'A Sub-1V, 220 μ w Receiver Frontend for Wearable Wireless Sensor Network Applications' *Proc. - IEEE Int. Symp. Circuits Syst.*, 2018, **2018-May**, p. 1–5.
- 7 Kargaran, E., Manstretta, D., Castello, R.: 'Design and Analysis of 2.4 GHz 30 μ w CMOS LNAs for Wearable WSN Applications' *IEEE Trans. Circuits Syst. I Regul. Pap.*, 2018, **65**, (3), p. 891–903.
- 8 Magod, R., Bakaloglu, B., Manandhar, S.: 'A 1.24 μ A quiescent current NMOS low dropout regulator with integrated low-power oscillator-driven charge-pump and switched-capacitor pole tracking compensation' *IEEE J. Solid-State Circuits*, 2018, **53**, (8), p. 2356–2367.
- 9 Wang, C., Lu, W., Narayanan, M.R., Redmond, S.J., Lovell, N.H.: 'Low-power technologies for wearable telecare and telehealth systems: A review' *Biomed. Eng. Lett.* 2015 51, 2015, **5**, (1), p. 1–9.
- 10 Niitsu, K., Kobayashi, A., Nishio, Y., *et al.*: 'A Self-Powered Supply-Sensing Biosensor Platform Using Bio Fuel Cell and Low-Voltage, Low-Cost CMOS Supply-Controlled Ring Oscillator With Inductive-Coupling Transmitter for Healthcare IoT' *IEEE Trans. Circuits Syst. I Regul. Pap.*, 2018, **65**, (9), p. 2784–2796.
- 11 Bandodkar, A.J., Wang, J.: 'Wearable Biofuel Cells: A Review' *Electroanalysis*, 2016, **28**, (6), p. 1188–1200.

- 12 Rasmussen, M., Abdellaoui, S., Minter, S.D.: 'Enzymatic biofuel cells: 30 years of critical advancements' *Biosens. Bioelectron.*, 2016, **76**, p. 91–102.
- 13 Schuhmann, W., Ohara, T.J., Schmidt, H.-L., Heller, A.: 'Electron Transfer between Glucose Oxidase and Electrodes via Redox Mediators Bound with Flexible Chains to the Enzyme Surface' *J. Am. Chem. Soc.*, 1991, **113**, p. 1394–1397.
- 14 Moser, C.C., Keske, J.M., Warncke, K., Farid, R.S., Dutton, P.L.: 'Nature of biological electron transfer' *Nature*, 1992, **355**, (6363), p. 796–802.
- 15 Hui, Y., Ma, X., Qu, F.: 'Flexible glucose/oxygen enzymatic biofuel cells based on three-dimensional gold-coated nickel foam' *J. Solid State Electrochem.*, 2018, p. 1–10.
- 16 Zhu, D., Beeby, S.: 'Kinetic energy harvesting', in 'Energy Harvesting Systems: Principles, Modeling and Applications' (Springer New York, 2011), p. 1–77
- 17 Fan, F.-R., Tian, Z.-Q., Lin Wang, Z.: 'Flexible triboelectric generator' *Nano Energy*, 2012, **1**, (2), p. 328–334.
- 18 Gooding, D.M., Kaufman, G.K.: 'Tribocharging and the Triboelectric Series', in 'Encyclopedia of Inorganic and Bioinorganic Chemistry' (John Wiley & Sons, Ltd, 2014), p. 1–9
- 19 Ha, M., Park, J., Lee, Y., Ko, H.: 'Triboelectric generators and sensors for self-powered wearable electronics' *ACS Nano*, 2015, **9**, (4), p. 3421–3427.
- 20 Howells, C.A.: 'Piezoelectric energy harvesting' *Energy Convers. Manag.*, 2009, **50**, (7), p. 1847–1850.
- 21 Fan, F.R., Tang, W., Wang, Z.L.: 'Flexible Nanogenerators for Energy Harvesting and Self-Powered Electronics' *Adv. Mater.*, 2016, **28**, (22), p. 4283–4305.
- 22 Kim, H.S., Kim, J.H., Kim, J.: 'A Review of Piezoelectric Energy Harvesting based on Vibration' *Int. J. Precis. Eng. Manuf.*, 2011, **12**, p. 1129–1141.
- 23 Mokhtari, F., Spinks, G.M., Fay, C., *et al.*: 'Wearable Electronic Textiles from Nanostructured Piezoelectric Fibers' *Adv. Mater. Technol.*, 2020, **5**, (4), p. 1900900.
- 24 Zhang, Z., Chen, Y., Guo, J.: 'ZnO nanorods patterned-textile using a novel hydrothermal method for sandwich structured-piezoelectric nanogenerator for human energy harvesting' *Phys. E Low-dimensional Syst. Nanostructures*, 2019, **105**, p. 212–218.
- 25 Zaarour, B., Zhu, L., Huang, C., *et al.*: 'A review on piezoelectric fibers and nanowires

- for energy harvesting' *J. Ind. Text.*, 2021, **51**, (2), p. 297–340.
- 26 Ramadan, K.S., Sameoto, D., Evoy, S.: 'A review of piezoelectric polymers as functional materials for electromechanical transducers' *Smart Mater. Struct.*, 2014, **23**, (3), p. 33001.
 - 27 Lu, X., Qu, H., Skorobogatiy, M.: 'Piezoelectric Micro- and Nanostructured Fibers Fabricated from Thermoplastic Nanocomposites Using a Fiber Drawing Technique: Comparative Study and Potential Applications' *ACS Nano*, 2017, **11**, (2), p. 2103–2114.
 - 28 Champier, D.: 'Thermoelectric generators: A review of applications' *Energy Convers. Manag.*, 2017, **140**, p. 167–181.
 - 29 Yan, J., Liao, X., Yan, D., Chen, Y.: 'Review of Micro Thermoelectric Generator' *J. Microelectromechanical Syst.*, 2018, **27**, (1), p. 1–18.
 - 30 Siddique, A.R.M., Mahmud, S., Heyst, B. Van: 'A review of the state of the science on wearable thermoelectric power generators (TEGs) and their existing challenges' *Renew. Sustain. Energy Rev.*, 2017, **73**, p. 730–744.
 - 31 Hyland, M., Hunter, H., Liu, J., Veety, E., Vashaee, D.: 'Wearable thermoelectric generators for human body heat harvesting' *Appl. Energy*, 2016, **182**, p. 518–524.
 - 32 Green, J.M., Bishop, P.A., Muir, I.H., Lomax, R.G.: 'Gender differences in sweat lactate' *Eur. J. Appl. Physiol.*, 2000, **82**, (3), p. 230.
 - 33 Guan, M.J., Liao, W.H.: 'On the efficiencies of piezoelectric energy harvesting circuits towards storage device voltages' *Smart Mater. Struct.*, 2007, **16**, (2), p. 498–505.
 - 34 Liu, W.Q., Badel, A., Formosa, F., Wu, Y.P., Agbossou, A.: 'Wideband energy harvesting using a combination of an optimized synchronous electric charge extraction circuit and a bistable harvester' *Smart Mater. Struct.*, 2013, **22**, (12), p. 125038.
 - 35 Shu, Y.C., Lien, I.C., Wu, W.J.: 'An improved analysis of the SSHI interface in piezoelectric energy harvesting' *Smart Mater. Struct.*, 2007, **16**, (6), p. 2253–2264.
 - 36 Xiao, X., Conghaile, P.Ó., Leech, D., Ludwig, R., Magner, E.: 'A symmetric supercapacitor/biofuel cell hybrid device based on enzyme-modified nanoporous gold: An autonomous pulse generator' *Biosens. Bioelectron.*, 2017, **90**, p. 96–102.
 - 37 Ó Conghaile, P., Falk, M., MacAodha, D., *et al.*: 'Fully Enzymatic Membraneless Glucose|Oxygen Fuel Cell That Provides 0.275 mA cm⁻² in 5 mM Glucose, Operates in Human Physiological Solutions, and Powers Transmission of Sensing Data' *Anal. Chem.*, 2016, **88**, (4), p. 2156–2163.

- 38 Shitanda, I., Nohara, S., Hoshi, Y., Itagaki, M., Tsujimura, S.: 'A screen-printed circular-type paper-based glucose/O₂ biofuel cell' *J. Power Sources*, 2017, **360**, p. 516–519.
- 39 Arakawa, T., Xie, R., Seshima, F., Toma, K., Mitsubayashi, K.: 'Air bio-battery with a gas/liquid porous diaphragm cell for medical and health care devices' *Biosens. Bioelectron.*, 2018, **103**, p. 171–175.
- 40 Sekretaryova, A.N., Beni, V., Eriksson, M., Karyakin, A.A., Turner, A.P.F., Vagin, M.Y.: 'Cholesterol self-powered biosensor' *Anal. Chem.*, 2014, **86**, (19), p. 9540–9547.
- 41 Lv, P., Zhou, H., Mensah, A., *et al.*: 'A highly flexible self-powered biosensor for glucose detection by epitaxial deposition of gold nanoparticles on conductive bacterial cellulose' *Chem. Eng. J.*, 2018, **351**, p. 177–188.
- 42 Slaughter, G., Kulkarni, T.: 'A self-powered glucose biosensing system' *Biosens. Bioelectron.*, 2016, **78**, p. 45–50.
- 43 Bandodkar, A.J., You, J.-M., Kim, N.-H., *et al.*: 'Soft, stretchable, high power density electronic skin-based biofuel cells for scavenging energy from human sweat' *Energy Environ. Sci.*, 2017, **10**, (7), p. 1581–1589.
- 44 Koushanpour, A., Gamella, M., Katz, E.: 'A Biofuel Cell Based on Biocatalytic Reactions of Lactate on Both Anode and Cathode Electrodes-Extracting Electrical Power from Human Sweat' *Electroanalysis*, 2017, **29**, p. 1602.
- 45 Xu, W., Huang, L.-B., Wong, M.-C., Chen, L., Bai, G., Hao, J.: 'Environmentally Friendly Hydrogel-Based Triboelectric Nanogenerators for Versatile Energy Harvesting and Self-Powered Sensors' *Adv. Energy Mater.*, 2017, **7**, (1), p. 1601529.
- 46 Song, P., Kuang, S., Panwar, N., *et al.*: 'A Self-Powered Implantable Drug-Delivery System Using Biokinetic Energy' *Adv. Mater.*, 2017, **29**, (11), p. 1605668.
- 47 Dong, K., Deng, J., Zi, Y., *et al.*: '3D Orthogonal Woven Triboelectric Nanogenerator for Effective Biomechanical Energy Harvesting and as Self-Powered Active Motion Sensors' *Adv. Mater.*, 2017, **29**, (38), p. 1702648.
- 48 Lai, Y.-C., Deng, J., Zhang, S.L., Niu, S., Guo, H., Wang, Z.L.: 'Single-Thread-Based Wearable and Highly Stretchable Triboelectric Nanogenerators and Their Applications in Cloth-Based Self-Powered Human-Interactive and Biomedical Sensing' *Adv. Funct. Mater.*, 2017, **27**, (1), p. 1604462.
- 49 Chandrasekhar, A., Alluri, N.R., Sudhakaran, M.S.P., Mok, Y.S., Kim, S.-J.: 'A smart mobile pouch as a biomechanical energy harvester towards self-powered smart

- wireless power transfer applications' *Nanoscale*, 2017, **9**, (28), p. 9818–9824.
- 50 Chen, X., Wu, Y., Shao, J., *et al.*: 'On-Skin Triboelectric Nanogenerator and Self-Powered Sensor with Ultrathin Thickness and High Stretchability' *Small*, 2017, **13**, (47), p. 1702929.
 - 51 Tang, W., Jiang, T., Fan, F.R., *et al.*: 'Liquid-Metal Electrode for High-Performance Triboelectric Nanogenerator at an Instantaneous Energy Conversion Efficiency of 70.6%' *Adv. Funct. Mater.*, 2015, **25**, (24), p. 3718–3725.
 - 52 Hwang, G.-T., Park, H., Lee, J.-H., *et al.*: 'Self-Powered Cardiac Pacemaker Enabled by Flexible Single Crystalline PMN-PT Piezoelectric Energy Harvester' *Adv. Mater.*, 2014, **26**, (28), p. 4880–4887.
 - 53 Kim, K.-B., Cho, J.Y., Jeon, D.H., *et al.*: 'A biocompatible and flexible piezoelectric generator with high-quality boron nitride nanotubes from human running' *Nano Energy*, 2018.
 - 54 Lu, X., Qu, H., Skorobogatiy, M.: 'Piezoelectric Microstructured Fibers via Drawing of Multimaterial Preforms' *Sci. Rep.*, 2017, **7**, (1), p. 2907.
 - 55 Alluri, N.R., Selvarajan, S., Chandrasekhar, A., *et al.*: 'Worm structure piezoelectric energy harvester using ionotropic gelation of barium titanate-calcium alginate composite' *Energy*, 2017, **118**, p. 1146–1155.
 - 56 Mao, Y., Zhao, P., McConohy, G., Yang, H., Tong, Y., Wang, X.: 'Sponge-Like Piezoelectric Polymer Films for Scalable and Integratable Nanogenerators and Self-Powered Electronic Systems' *Adv. Energy Mater.*, 2014, **4**, (7), p. 1301624.
 - 57 Zhang, Y., Jeong, C.K., Yang, T., *et al.*: 'Bioinspired elastic piezoelectric composites for high-performance mechanical energy harvesting' *J. Mater. Chem. A*, 2018, **6**, (30), p. 14546–14552.
 - 58 Pi, Z., Zhang, J., Wen, C., Zhang, Z. bin, Wu, D.: 'Flexible piezoelectric nanogenerator made of poly(vinylidene fluoride-co-trifluoroethylene) (PVDF-TrFE) thin film' *Nano Energy*, 2014, **7**, p. 33–41.
 - 59 Hu, P., Yan, L., Zhao, C., Zhang, Y., Niu, J.: 'Double-layer structured PVDF nanocomposite film designed for flexible nanogenerator exhibiting enhanced piezoelectric output and mechanical property' *Compos. Sci. Technol.*, 2018, **168**, p. 327–335.
 - 60 Rojas, J.P., Singh, D., Conchouso, D., Arevalo, A., Foulds, I.G., Hussain, M.M.:

- 'Stretchable helical architecture inorganic-organic hetero thermoelectric generator' *Nano Energy*, 2016, **30**, p. 691–699.
- 61 Lu, Z., Zhang, H., Mao, C., Li, C.M.: 'Silk fabric-based wearable thermoelectric generator for energy harvesting from the human body' *Appl. Energy*, 2016, **164**, p. 57–63.
 - 62 Lee, J.A., Aliev, A.E., Bykova, J.S., *et al.*: 'Woven-Yarn Thermoelectric Textiles' *Adv. Mater.*, 2016, **28**, (25), p. 5038–5044.
 - 63 Sanati, A., Esmaeili, Y., Bidram, E., *et al.*: 'Recent advancement in electrode materials and fabrication, microfluidic designs, and self-powered systems for wearable non-invasive electrochemical glucose monitoring' *Appl. Mater. Today*, 2022, **26**, p. 101350.
 - 64 Chandrasekaran, S., Bowen, C., Roscow, J., *et al.*: 'Micro-scale to nano-scale generators for energy harvesting: Self powered piezoelectric, triboelectric and hybrid devices' *Phys. Rep.*, 2019, **792**, p. 1–33.
 - 65 Smith, M., Kar-Narayan, S.: 'Piezoelectric polymers: theory, challenges and opportunities' *Int. Mater. Rev.*, 2022, **67**, (1), p. 65–88.
 - 66 Dagdeviren, C., Joe, P., Tuzman, O.L., *et al.*: 'Recent progress in flexible and stretchable piezoelectric devices for mechanical energy harvesting, sensing and actuation' *Extrem. Mech. Lett.*, 2016, **9**, p. 269–281.
 - 67 Liang, X., Hu, S., Shen, S.: 'Nanoscale mechanical energy harvesting using piezoelectricity and flexoelectricity' *Smart Mater. Struct.*, 2017, **26**, (3), p. 35050.
 - 68 Zhou, M., Al-Furjan, M.S.H., Zou, J., Liu, W.: 'A review on heat and mechanical energy harvesting from human – Principles, prototypes and perspectives' *Renew. Sustain. Energy Rev.*, 2018, **82**, p. 3582–3609.
 - 69 Thainirarnit, P., Yingyong, P., Isarakorn, D.: 'Impact-Driven Energy Harvesting: Piezoelectric Versus Triboelectric Energy Harvesters' (2020), 20
 - 70 Luo, L.-C., Bao, D.-C., Yu, W.-Q., Zhang, Z.-H., Ren, T.-L.: 'A Low Input Current and Wide Conversion Ratio Buck Regulator with 75% Efficiency for High-Voltage Triboelectric Nanogenerators' *Sci. Rep.*, 2016, **6**, (1), p. 19246.
 - 71 Yang, J.: 'An Introduction to the Theory of Piezoelectricity', in 'An Introduction to the Theory of Piezoelectricity' (Springer US, 2006), p. 1–28
 - 72 Kakimoto, K.I.: 'Ferroelectric Materials and Their Applications' (Elsevier Science, 2021)

- 73 J., L.A.: 'Ferroelectric Polymers' *Science* (80-.), 1983, **220**, (4602), p. 1115–1121.
- 74 Ameh, E.S.: 'A review of basic crystallography and x-ray diffraction applications' *Int. J. Adv. Manuf. Technol.*, 2019, **105**, (7), p. 3289–3302.
- 75 Kholkin, A.L., Pertsev, N.A., Goltsev, A. V: 'Piezoelectricity and crystal symmetry', in 'Piezoelectric and Acoustic Materials for Transducer Applications' (Springer US, 2008), p. 17–38
- 76 Brown, C., Kell, R., Taylor, R., Thomas, L.: 'Piezoelectric Materials, A Review of Progress' *IRE Trans. Compon. Parts*, 1962, **9**, (4), p. 193–211.
- 77 Tajitsu, Y.: 'Piezoelectric Polymers BT - Soft Actuators: Materials, Modeling, Applications, and Future Perspectives', in Asaka, K., Okuzaki, H. (Eds.): 'Soft Actuators' (Springer Japan, 2014), p. 203–215
- 78 Shahinpoor, M.: 'Review of piezoelectric materials', in 'Fundamentals of Smart Materials' (Royal Society of Chemistry, 2020), p. 13–22
- 79 Chorsi, M.T., Curry, E.J., Chorsi, H.T., *et al.*: 'Piezoelectric Biomaterials for Sensors and Actuators' *Adv. Mater.*, 2019, **31**, (1), p. 1802084.
- 80 de Jong, M., Chen, W., Geerlings, H., Asta, M., Persson, K.A.: 'A database to enable discovery and design of piezoelectric materials' *Sci. Data*, 2015, **2**, (1), p. 150053.
- 81 Zou, W.-N., Tang, C.-X., Pan, E.: 'Symmetry types of the piezoelectric tensor and their identification' *Proc. R. Soc. A Math. Phys. Eng. Sci.*, 2013, **469**, (2155), p. 20120755.
- 82 Henriques, A., Graham, J.T., Landsberger, S., *et al.*: 'Crystallographic changes in lead zirconate titanate due to neutron irradiation' *AIP Adv.*, 2014, **4**, (11), p. 117125.
- 83 Tressler, J.F., Alkoy, S., Newnham, R.E.: 'Piezoelectric Sensors and Sensor Materials' *J. Electroceramics*, 1998, **2**, (4), p. 257–272.
- 84 Sun, Y., Zeng, K., Li, T.: 'Piezo-/ferroelectric phenomena in biomaterials: A brief review of recent progress and perspectives' *Sci. China Physics, Mech. Astron.*, 2020, **63**, (7), p. 278701.
- 85 Mishra, S., Unnikrishnan, L., Nayak, S.K., Mohanty, S.: 'Advances in Piezoelectric Polymer Composites for Energy Harvesting Applications: A Systematic Review' *Macromol. Mater. Eng.*, 2019, **304**, (1), p. 1800463.
- 86 Jaffe, H., Berlincourt, D.A.: 'Piezoelectric transducer materials' *Proc. IEEE*, 1965, **53**, (10), p. 1372–1386.

- 87 Guzzo, P.L., Raslan, A.A., De Mello, J.D.B.: 'Ultrasonic abrasion of quartz crystals' *Wear*, 2003, **255**, (1), p. 67–77.
- 88 Bhalla, A.S., Guo, R., Roy, R.: 'The perovskite structure—a review of its role in ceramic science and technology' *Mater. Res. Innov.*, 2000, **4**, (1), p. 3–26.
- 89 Wu, Y., Ma, Y., Zheng, H., Ramakrishna, S.: 'Piezoelectric materials for flexible and wearable electronics: A review' *Mater. Des.*, 2021, **211**, p. 110164.
- 90 Fang, X.-Q., Liu, J.-X., Gupta, V.: 'Fundamental formulations and recent achievements in piezoelectric nano-structures: a review' *Nanoscale*, 2013, **5**, (5), p. 1716–1726.
- 91 Cholleti, E.R.: 'A Review on 3D printing of piezoelectric materials' *IOP Conf. Ser. Mater. Sci. Eng.*, 2018, **455**, p. 12046.
- 92 Chen, C., Wang, X., Wang, Y., *et al.*: 'Additive Manufacturing of Piezoelectric Materials' *Adv. Funct. Mater.*, 2020, **30**, (52), p. 2005141.
- 93 Bodkhe, S., Ermanni, P.: 'Challenges in 3D printing of piezoelectric materials' *Multifunct. Mater.*, 2019, **2**, (2), p. 22001.
- 94 Mahmud, M.A.P., Adhikary, P., Zolfagharian, A., Adams, S., Kaynak, A., Kouzani, A.Z.: 'Advanced Design, Fabrication, and Applications of 3D-Printable Piezoelectric Nanogenerators' *Electron. Mater. Lett.*, 2022, **18**, (2), p. 129–144.
- 95 Kim, K., Tiwari, A.P., Novak, T.G., Jeon, S.: '3D ordered nanoelectrodes for energy conversion applications: thermoelectric, piezoelectric, and electrocatalytic applications' *J. Korean Ceram. Soc.*, 2021, **58**, (4), p. 379–398.
- 96 Kim, H., Yun, S., Kim, K., *et al.*: 'Breaking the elastic limit of piezoelectric ceramics using nanostructures: A case study using ZnO' *Nano Energy*, 2020, **78**, p. 105259.
- 97 Pan, M., Yuan, C., Liang, X., Zou, J., Zhang, Y., Bowen, C.: 'Trieoelectric and Piezoelectric Nanogenerators for Future Soft Robots and Machines' *iScience*, 2020, **23**, (11), p. 101682.
- 98 Ravve, A.: 'Principles of Polymer Chemistry' (Springer New York, 2012)
- 99 Young, R.J., Lovell, P.A.: 'Introduction to Polymers, Third Edition' (Taylor & Francis, 2011)
- 100 Peppas, N.A.: 'Fundamentals of polymer science: an introductory text' (CRC Press, 1996)
- 101 Chanda, M.: 'Introduction to Polymer Science and Chemistry: A Problem-Solving

- Approach' (Taylor & Francis, 2006)
- 102 Phillips, P.J.: 'Polymer crystals' *Reports Prog. Phys.*, 1990, **53**, (5), p. 549–604.
 - 103 Silva, M.P., Sencadas, V., Botelho, G., *et al.*: 'α- and γ-PVDF: Crystallization kinetics, microstructural variations and thermal behaviour' *Mater. Chem. Phys.*, 2010, **122**, (1), p. 87–92.
 - 104 Wang, A.C., Wu, C., Pisignano, D., Wang, Z.L., Persano, L.: 'Polymer nanogenerators: Opportunities and challenges for large-scale applications' *J. Appl. Polym. Sci.*, 2018, **135**, (24), p. 45674.
 - 105 Rao, I.J., Rajagopal, K.R.: 'A study of strain-induced crystallization of polymers' *Int. J. Solids Struct.*, 2001, **38**, (6), p. 1149–1167.
 - 106 Eder, G., Janeschitz-Kriegl, H.: 'Theory of shear-induced crystallization of polymer melts' *Colloid Polym. Sci.*, 1988, **266**, (12), p. 1087–1094.
 - 107 Jaffe, B., Cook, W.R., Jaffe, H.: 'Chapter I - HISTORICAL INTRODUCTION', in Jaffe, B., Cook, W.R., Jaffe, H.B.T.-P.C. (Eds.): 'Piezoelectric ceramics' (Academic Press, 1971), p. 1–5
 - 108 Mason, W.P.: 'Piezoelectricity, its history and applications' *J. Acoust. Soc. Am.*, 1981, **70**, (6), p. 1561–1566.
 - 109 Harrison, J.S., Ounaies, Z.: 'Piezoelectric Polymers', in 'Encyclopedia of Polymer Science and Technology' (2002), p. 475–493
 - 110 Fukada, E.: 'Piezoelectric properties of biological polymers' *Q. Rev. Biophys.*, 1983, **16**, (1), p. 59–87.
 - 111 Fukada, E.: 'Piezoelectricity as a fundamental property of wood' *Wood Sci. Technol.*, 1968, **2**, (4), p. 299–307.
 - 112 Marino, A.A., Spadaro, J.A., Fukada, E., Kahn, L.D., Becker, R.O.: 'Piezoelectricity in collagen films' *Calcif. Tissue Int.*, 1980, **31**, (1), p. 257–259.
 - 113 Kaczmarek, H., Królikowski, B., Klimiec, E., Chylińska, M., Bajer, D.: 'Advances in the study of piezoelectric polymers' *Russ. Chem. Rev.*, 2019, **88**, (7), p. 749–774.
 - 114 Yucel, T., Cebce, P., Kaplan, D.L.: 'Structural Origins of Silk Piezoelectricity' *Adv. Funct. Mater.*, 2011, **21**, (4), p. 779–785.
 - 115 Sencadas, V., Garvey, C., Mudie, S., Kirkensgaard, J.J.K., Gouadec, G., Hauser, S.: 'Electroactive properties of electrospun silk fibroin for energy harvesting applications'

- Nano Energy*, 2019, **66**, p. 104106.
- 116 Sencadas, V., Ribeiro, C., Heredia, A., Bdikin, I.K., Kholkin, A.L., Lanceros-Mendez, S.: 'Local piezoelectric activity of single poly(L-lactic acid) (PLLA) microfibers' *Appl. Phys. A*, 2012, **109**, (1), p. 51–55.
- 117 Fukada, E.: 'New Piezoelectric Polymers' *Jpn. J. Appl. Phys.*, 1998, **37**, (Part 1, No. 5B), p. 2775–2780.
- 118 Anwar, S., Hassanpour Amiri, M., Jiang, S., Abolhasani, M.M., Rocha, P.R.F., Asadi, K.: 'Piezoelectric Nylon-11 Fibers for Electronic Textiles, Energy Harvesting and Sensing' *Adv. Funct. Mater.*, 2021, **31**, (4), p. 2004326.
- 119 Liu, S., Cui, Z., Fu, P., *et al.*: 'Ferroelectric behavior and polarization mechanism in odd-odd polyamide 11,11' *J. Polym. Sci. Part B Polym. Phys.*, 2014, **52**, (16), p. 1094–1099.
- 120 Newman, B.A., Scheinbeim, J.I., Lee, J.W., Takase, Y.: 'A new class of ferroelectric polymers, the odd-numbered nylons' *Ferroelectrics*, 1992, **127**, (1), p. 229–234.
- 121 Sessler, G.M.: 'Piezoelectricity in polyvinylidene fluoride' *J. Acoust. Soc. Am.*, 1981, **70**, (6), p. 1596–1608.
- 122 Furukawa, T.: 'Piezoelectricity and pyroelectricity in polymers' *IEEE Trans. Electr. Insul.*, 1989, **24**, (3), p. 375–394.
- 123 Furukawa, T.: 'Structure and functional properties of ferroelectric polymers' *Adv. Colloid Interface Sci.*, 1997, **71–72**, p. 183–208.
- 124 Scheinbeim, J.I., Newman, B.A., Mei, B.Z., Lee, J.W.: 'New ferroelectric and piezoelectric polymers', in 'ISAF '92: Proceedings of the Eighth IEEE International Symposium on Applications of Ferroelectrics' (1992), p. 248–249
- 125 Maksimkin, A. V, Dayyoub, T., Telyshev, D. V, Gerasimenko, A.Y.: 'Electroactive Polymer-Based Composites for Artificial Muscle-like Actuators: A Review' (2022), 12
- 126 Wada, Y., Hayakawa, R.: 'Piezoelectricity and Pyroelectricity of Polymers' *Jpn. J. Appl. Phys.*, 1976, **15**, (11), p. 2041–2057.
- 127 Su, Y.P., Sim, L.N., Coster, H.G.L., Chong, T.H.: 'Incorporation of barium titanate nanoparticles in piezoelectric PVDF membrane' *J. Memb. Sci.*, 2021, **640**, p. 119861.
- 128 Cao, P., Shi, J., Zhang, J., *et al.*: 'Piezoelectric PVDF membranes for use in anaerobic membrane bioreactor (AnMBR) and their antifouling performance' *J. Memb. Sci.*, 2020, **603**, p. 118037.

- 129 Kim, Y.-S., Xie, Y., Wen, X., *et al.*: 'Highly porous piezoelectric PVDF membrane as effective lithium ion transfer channels for enhanced self-charging power cell' *Nano Energy*, 2015, **14**, p. 77–86.
- 130 Fukada, E.: 'History and recent progress in piezoelectric polymers' *IEEE Trans. Ultrason. Ferroelectr. Freq. Control*, 2000, **47**, (6), p. 1277–1290.
- 131 Annamalai, P.K., Nanjundan, A.K., Dubal, D.P., Baek, J.-B.: 'An Overview of Cellulose-Based Nanogenerators' *Adv. Mater. Technol.*, 2021, **6**, (3), p. 2001164.
- 132 Takarada, J., Kataoka, T., Yamamoto, K., *et al.*: 'Fundamental Study on Vibration in Edge Face of Piezoelectric Chiral Polymer Film' *Jpn. J. Appl. Phys.*, 2013, **52**, (9S1), p. 09KE01.
- 133 Saxena, P., Shukla, P.: 'A comprehensive review on fundamental properties and applications of poly(vinylidene fluoride) (PVDF)' *Adv. Compos. Hybrid Mater.*, 2021, **4**, (1), p. 8–26.
- 134 Reimschuessel, H.K.: 'Nylon 6. Chemistry and mechanisms' *J. Polym. Sci. Macromol. Rev.*, 1977, **12**, (1), p. 65–139.
- 135 Shakiba, M., Rezvani Ghomi, E., Khosravi, F., *et al.*: 'Nylon—A material introduction and overview for biomedical applications' *Polym. Adv. Technol.*, 2021, **32**, (9), p. 3368–3383.
- 136 Xia, W., Zhang, Z.: 'PVDF-based dielectric polymers and their applications in electronic materials' *IET Nanodielectrics*, 2018, **1**, (1), p. 17–31.
- 137 Gregorio, R., Ueno, E.M.: 'Effect of crystalline phase, orientation and temperature on the dielectric properties of poly (vinylidene fluoride) (PVDF)' *J. Mater. Sci.*, 1999, **34**, (18), p. 4489–4500.
- 138 Li, Q., Zhao, J., He, B., Hu, Z.: 'Solution processable poly(vinylidene fluoride)-based ferroelectric polymers for flexible electronics' *APL Mater.*, 2021, **9**, (1), p. 10902.
- 139 Chen, X., Han, X., Shen, Q.-D.: 'PVDF-Based Ferroelectric Polymers in Modern Flexible Electronics' *Adv. Electron. Mater.*, 2017, **3**, (5), p. 1600460.
- 140 Poulsen, M., Ducharme, S.: 'Why ferroelectric polyvinylidene fluoride is special' *IEEE Trans. Dielectr. Electr. Insul.*, 2010, **17**, (4), p. 1028–1035.
- 141 Mao, D., Gnade, B.E., Quevedo-Lopez, M.A.: 'Ferroelectric Properties and Polarization Switching Kinetic of Poly (vinylidene fluoride-trifluoroethylene) Copolymer', in Lallart, M. (Ed.): 'Ferroelectrics' (IntechOpen, 2011)

- 142 Bellet-Amalric, E., Legrand, J.F.: 'Crystalline structures and phase transition of the ferroelectric P(VDF-TrFE) copolymers, a neutron diffraction study' *Eur. Phys. J. B - Condens. Matter Complex Syst.*, 1998, **3**, (2), p. 225–236.
- 143 Ullah, A., ur Rahman, A., Won Ahn, C., *et al.*: 'Enhancement of dielectric and energy density properties in the PVDF-based copolymer/terpolymer blends' *Polym. Eng. Sci.*, 2015, **55**, (6), p. 1396–1402.
- 144 Lukáš, D., Sarkar, A., Martinová, L., *et al.*: 'Physical principles of electrospinning (Electrospinning as a nano-scale technology of the twenty-first century)' *Text. Prog.*, 2009, **41**, (2), p. 59–140.
- 145 Xue, J., Wu, T., Dai, Y., Xia, Y.: 'Electrospinning and electrospun nanofibers: Methods, materials, and applications' (American Chemical Society, 2019), 119, p. 5298–5415
- 146 Persano, L., Camposeo, A., Tekmen, C., Pisignano, D.: 'Industrial Upscaling of Electrospinning and Applications of Polymer Nanofibers: A Review' *Macromol. Mater. Eng.*, 2013, **298**, (5), p. 504–520.
- 147 Shepa, I., Mudra, E., Dusza, J.: 'Electrospinning through the prism of time' *Mater. Today Chem.*, 2021, **21**, p. 100543.
- 148 Schiffman, J.D., Schauer, C.L.: 'A Review: Electrospinning of Biopolymer Nanofibers and their Applications' *Polym. Rev.*, 2008, **48**, (2), p. 317–352.
- 149 Teo, W.E., Ramakrishna, S.: 'A review on electrospinning design and nanofibre assemblies' *Nanotechnology*, 2006, **17**, (14), p. R89–R106.
- 150 Rutledge, G.C., Fridrikh, S. V.: 'Formation of fibers by electrospinning' *Adv. Drug Deliv. Rev.*, 2007, **59**, (14), p. 1384–1391.
- 151 Sarkar, S., Deevi, S., Tepper, G.: 'Biased AC Electrospinning of Aligned Polymer Nanofibers' *Macromol. Rapid Commun.*, 2007, **28**, (9), p. 1034–1039.
- 152 Angammana, C.J., Jayaram, S.H.: 'Fundamentals of electrospinning and processing technologies' *Part. Sci. Technol.*, 2016, **34**, (1), p. 72–82.
- 153 Yarin, A.L., Koombhongse, S., Reneker, D.H.: 'Taylor cone and jetting from liquid droplets in electrospinning of nanofibers' *J. Appl. Phys.*, 2001, **90**, (9), p. 4836–4846.
- 154 Fernández de la Mora, J.: 'The Fluid Dynamics of Taylor Cones' *Annu. Rev. Fluid Mech.*, 2006, **39**, (1), p. 217–243.
- 155 Doshi, J., Reneker, D.H.: 'Electrospinning process and applications of electrospun

- fibers' *J. Electrostat.*, 1995, **35**, (2–3), p. 151–160.
- 156 Yousefzadeh, M.: '12 - Modeling and simulation of the electrospinning process', in Afshari, M.B.T.-E.N. (Ed.): 'Woodhead Publishing Series in Textiles' (Woodhead Publishing, 2017), p. 277–301
 - 157 Syms, R.R.A., Yeatman, E.M., Bright, V.M., Whitesides, G.M.: 'Surface tension-powered self-assembly of microstructures - the state-of-the-art' *J. Microelectromechanical Syst.*, 2003, **12**, (4), p. 387–417.
 - 158 Reneker, D.H., Yarin, A.L.: 'Electrospinning jets and polymer nanofibers' *Polymer (Guildf)*, 2008, **49**, (10), p. 2387–2425.
 - 159 Taylor, G.I.: 'Electrically driven jets' *Proc. R. Soc. London. A. Math. Phys. Sci.*, 1969, **313**, (1515), p. 453–475.
 - 160 Ding, C., Fang, H., Duan, G., Zou, Y., Chen, S., Hou, H.: 'Investigating the draw ratio and velocity of an electrically charged liquid jet during electrospinning' *RSC Adv.*, 2019, **9**, (24), p. 13608–13613.
 - 161 Wang, C., Hashimoto, T., Wang, Y., Lai, H.-Y., Kuo, C.-H.: 'Formation of Dissipative Structures in the Straight Segment of Electrospinning Jets' *Macromolecules*, 2020, **53**, (18), p. 7876–7886.
 - 162 Wang, Y., Wang, C.: 'Extension rate and bending behavior of electrospinning jet: The role of solution conductivity' *Polymer (Guildf)*, 2021, **222**, p. 123672.
 - 163 Deshawar, D., Chokshi, P.: 'Analysis of axisymmetric instability in polymer melt electrospinning jet' *J. Nonnewton. Fluid Mech.*, 2018, **255**, p. 1–12.
 - 164 Reneker, D.H., Yarin, A.L., Fong, H., Koombhongse, S.: 'Bending instability of electrically charged liquid jets of polymer solutions in electrospinning' *J. Appl. Phys.*, 2000, **87**, (9), p. 4531–4547.
 - 165 Hohman, M.M., Shin, M., Rutledge, G., Brenner, M.P.: 'Electrospinning and electrically forced jets. I. Stability theory' *Phys. Fluids*, 2001, **13**, (8), p. 2201–2220.
 - 166 Lei, S., Quan, Z., Qin, X., Yu, J.: 'Asymptotic decay of velocity of whipping jet in electrospinning' *Polymer (Guildf)*, 2021, **217**, p. 123456.
 - 167 Zheng, J., He, A., Li, J., Han, C.C.: 'Polymorphism Control of Poly(vinylidene fluoride) through Electrospinning' *Macromol. Rapid Commun.*, 2007, **28**, (22), p. 2159–2162.
 - 168 Richard-Lacroix, M., Pellerin, C.: 'Molecular Orientation in Electrospun Fibers: From

- Mats to Single Fibers' *Macromolecules*, 2013, **46**, (24), p. 9473–9493.
- 169 Jacobs, V., Anandjiwala, R.D., Maaza, M.: 'The influence of electrospinning parameters on the structural morphology and diameter of electrospun nanofibers' *J. Appl. Polym. Sci.*, 2010, **115**, (5), p. 3130–3136.
- 170 Ibrahim, H.M., Klingner, A.: 'A review on electrospun polymeric nanofibers: Production parameters and potential applications' *Polym. Test.*, 2020, **90**, p. 106647.
- 171 Liu, Y., Dong, L., Fan, J., Wang, R., Yu, J.-Y.: 'Effect of applied voltage on diameter and morphology of ultrafine fibers in bubble electrospinning' *J. Appl. Polym. Sci.*, 2011, **120**, (1), p. 592–598.
- 172 Li, Z., Wang, C.: 'Effects of Working Parameters on Electrospinning', in Li, Z., Wang, C. (Eds.): (Springer Berlin Heidelberg, 2013), p. 15–28
- 173 Pokorny, P., Kostakova, E., Sanetnik, F., *et al.*: 'Effective AC needleless and collectorless electrospinning for yarn production' *Phys. Chem. Chem. Phys.*, 2014, **16**, (48), p. 26816–26822.
- 174 Kilic, A., Oruc, F., Demir, A.: 'Effects of Polarity on Electrospinning Process' *Text. Res. J.*, 2008, **78**, (6), p. 532–539.
- 175 Wu, C.-M., Chiou, H.-G., Lin, S.-L., Lin, J.-M.: 'Effects of electrostatic polarity and the types of electrical charging on electrospinning behavior' *J. Appl. Polym. Sci.*, 2012, **126**, (S2), p. E89–E97.
- 176 Tong, H.-W., Wang, M.: 'Electrospinning of fibrous polymer scaffolds using positive voltage or negative voltage: a comparative study' *Biomed. Mater.*, 2010, **5**, (5), p. 54110.
- 177 Forward, K.M., Rutledge, G.C.: 'Free surface electrospinning from a wire electrode' *Chem. Eng. J.*, 2012, **183**, p. 492–503.
- 178 Yuan, X., Zhang, Y., Dong, C., Sheng, J.: 'Morphology of ultrafine polysulfone fibers prepared by electrospinning' *Polym. Int.*, 2004, **53**, (11), p. 1704–1710.
- 179 Peleg, M.: 'Temperature–viscosity models reassessed' *Crit. Rev. Food Sci. Nutr.*, 2018, **58**, (15), p. 2663–2672.
- 180 De Vrieze, S., Van Camp, T., Nelvig, A., Hagström, B., Westbroek, P., De Clerck, K.: 'The effect of temperature and humidity on electrospinning' *J. Mater. Sci.*, 2009, **44**, (5), p. 1357–1362.

- 181 Reyes, C.G., Lagerwall, J.P.F.: 'Disruption of Electrospinning due to Water Condensation into the Taylor Cone' *ACS Appl. Mater. Interfaces*, 2020, **12**, (23), p. 26566–26576.
- 182 Levitt, A.S., Vallett, R., Dion, G., Schauer, C.L.: 'Effect of electrospinning processing variables on polyacrylonitrile nanoyarns' *J. Appl. Polym. Sci.*, 2018, **135**, (25), p. 46404.
- 183 Szewczyk, P.K., Stachewicz, U.: 'The impact of relative humidity on electrospun polymer fibers: From structural changes to fiber morphology' *Adv. Colloid Interface Sci.*, 2020, **286**, p. 102315.
- 184 Kim, G.-T., Lee, J.-S., Shin, J.-H., *et al.*: 'Investigation of pore formation for polystyrene electrospun fiber: Effect of relative humidity' *Korean J. Chem. Eng.*, 2005, **22**, (5), p. 783–788.
- 185 Khan, W.S., Asmatulu, R., Ceylan, M., Jabbarnia, A.: 'Recent progress on conventional and non-conventional electrospinning processes' *Fibers Polym.*, 2013, **14**, (8), p. 1235–1247.
- 186 Dosunmu, O.O., Chase, G.G., Kataphinan, W., Reneker, D.H.: 'Electrospinning of polymer nanofibres from multiple jets on a porous tubular surface' *Nanotechnology*, 2006, **17**, (4), p. 1123–1127.
- 187 Omer, S., Forgách, L., Zelkó, R., Sebe, I.: 'Scale-up of Electrospinning: Market Overview of Products and Devices for Pharmaceutical and Biomedical Purposes' (2021), 13
- 188 Vass, P., Szabó, E., Domokos, A., *et al.*: 'Scale-up of electrospinning technology: Applications in the pharmaceutical industry' (Wiley-Blackwell, 2020), 12, p. e1611–e1611
- 189 SalehHudin, H.S., Mohamad, E.N., Mahadi, W.N.L., Muhammad Afifi, A.: 'Multiple-jet electrospinning methods for nanofiber processing: A review' *Mater. Manuf. Process.*, 2018, **33**, (5), p. 479–498.
- 190 Li, Y., Zhu, J., Cheng, H., *et al.*: 'Developments of Advanced Electrospinning Techniques: A Critical Review' *Adv. Mater. Technol.*, 2021, **n/a**, (n/a), p. 2100410.
- 191 Lukas, D., Sarkar, A., Pokorny, P.: 'Self-organization of jets in electrospinning from free liquid surface: A generalized approach' *J. Appl. Phys.*, 2008, **103**, (8), p. 84309.
- 192 Beachley, V., Wen, X.: 'Effect of electrospinning parameters on the nanofiber diameter and length' *Mater. Sci. Eng. C*, 2009, **29**, (3), p. 663–668.

- 193 Pan, H., Li, L., Hu, L., Cui, X.: 'Continuous aligned polymer fibers produced by a modified electrospinning method' *Polymer (Guildf)*., 2006, **47**, (14), p. 4901–4904.
- 194 Wannatong, L., Sirivat, A., Supaphol, P.: 'Effects of solvents on electrospun polymeric fibers: preliminary study on polystyrene' *Polym. Int.*, 2004, **53**, (11), p. 1851–1859.
- 195 Jarusuwannapoom, T., Hongrojjanawiwat, W., Jitjaicham, S., *et al.*: 'Effect of solvents on electro-spinnability of polystyrene solutions and morphological appearance of resulting electrospun polystyrene fibers' *Eur. Polym. J.*, 2005, **41**, (3), p. 409–421.
- 196 Regev, O., Vandebriel, S., Zussman, E., Clasen, C.: 'The role of interfacial viscoelasticity in the stabilization of an electrospun jet' *Polymer (Guildf)*., 2010, **51**, (12), p. 2611–2620.
- 197 Han, D., Steckl, A.J.: 'Coaxial Electrospinning Formation of Complex Polymer Fibers and their Applications' *Chempluschem*, 2019, **84**, (1), p. 1453–1497.
- 198 Vong, M., Diaz Sanchez, F.J., Keirouz, A., Nuansing, W., Radacsi, N.: 'Ultrafast fabrication of Nanofiber-based 3D Macrostructures by 3D electrospinning' *Mater. Des.*, 2021, **208**, p. 109916.
- 199 Chung, M., Skinner, W.H., Robert, C., *et al.*: 'Fabrication of a Wearable Flexible Sweat pH Sensor Based on SERS-Active Au/TPU Electrospun Nanofibers' *ACS Appl. Mater. Interfaces*, 2021, **13**, (43), p. 51504–51518.
- 200 Arayanarakul, K., Choktaweasap, N., Aht-ong, D., Meechaisue, C., Supaphol, P.: 'Effects of Poly(ethylene glycol), Inorganic Salt, Sodium Dodecyl Sulfate, and Solvent System on Electrospinning of Poly(ethylene oxide)' *Macromol. Mater. Eng.*, 2006, **291**, (6), p. 581–591.
- 201 Qin, X.-H., Wan, Y.-Q., He, J.-H., Zhang, J., Yu, J.-Y., Wang, S.-Y.: 'Effect of LiCl on electrospinning of PAN polymer solution: theoretical analysis and experimental verification' *Polymer (Guildf)*., 2004, **45**, (18), p. 6409–6413.
- 202 'Lithium chloride | LiCl - PubChem', <https://pubchem.ncbi.nlm.nih.gov/compound/Lithium-chloride>
- 203 Dhakras, D., Borkar, V., Ogale, S., Jog, J.: 'Enhanced piezoresponse of electrospun PVDF mats with a touch of nickel chloride hexahydrate salt' *Nanoscale*, 2012, **4**, (3), p. 752.
- 204 Matabola, K.P., Moutloali, R.M.: 'The influence of electrospinning parameters on the morphology and diameter of poly(vinylidene fluoride) nanofibers- effect of sodium chloride' *J. Mater. Sci.*, 2013, **48**, (16), p. 5475–5482.

- 205 Mokhtari, F., Shamshirsaz, M., Latifi, M.: 'Investigation of β phase formation in piezoelectric response of electrospun polyvinylidene fluoride nanofibers: LiCl additive and increasing fibers tension' *Polym. Eng. Sci.*, 2016, **56**, (1), p. 61–70.
- 206 Naeimirad, M., Zadhoush, A., Kotek, R., Esmaeely Neisiany, R., Nouri Khorasani, S., Ramakrishna, S.: 'Recent advances in core/shell bicomponent fibers and nanofibers: A review' *J. Appl. Polym. Sci.*, 2018, **135**, (21), p. 1–12.
- 207 Zhang, Q., Li, Y., Ren, Z., Ahmad, Z., Li, X., Han, G.: 'Synthesis of porous CaTiO₃ nanotubes with tunable hollow structures via single-nozzle electrospinning' *Mater. Lett.*, 2015, **152**, p. 82–85.
- 208 Katta, P., Alessandro, M., Ramsier, R.D., Chase, G.G.: 'Continuous Electrospinning of Aligned Polymer Nanofibers onto a Wire Drum Collector' *Nano Lett.*, 2004, **4**, (11), p. 2215–2218.
- 209 Vittoz, E.A., Degrauwe, M.G.R., Bitz, S.: 'High-performance crystal oscillator circuits: theory and application' *IEEE J. Solid-State Circuits*, 1988, **23**, (3), p. 774–783.
- 210 Ferriss, L.S.: 'Transimpedance crystal oscillator', in 'Proceedings of the 43rd Annual Symposium on Frequency Control' (1989), p. 37–43
- 211 Yang, Y., Tang, L.: 'Equivalent Circuit Modeling of Piezoelectric Energy Harvesters' *J. Intell. Mater. Syst. Struct.*, 2009, **20**, (18), p. 2223–2235.
- 212 Richter, B., Twiefel, J., Wallaschek, J.: 'Piezoelectric equivalent circuit models', in Priya, S., Inman, D.J. (Eds.): 'Energy Harvesting Technologies' (Springer US, 2009), p. 107–128
- 213 Elvin, N.G., Elvin, A.A.: 'A General Equivalent Circuit Model for Piezoelectric Generators': <http://dx.doi.org/10.1177/1045389X08089957>, 2008, **20**, (1), p. 3–9.
- 214 Keawboonchuay, C., Engel, T.G.: 'Electrical power generation characteristics of piezoelectric generator under quasi-static and dynamic stress conditions' *IEEE Trans. Ultrason. Ferroelectr. Freq. Control*, 2003, **50**, (10), p. 1377–1382.
- 215 De Marqui Junior, C., Erturk, A., Inman, D.J.: 'An electromechanical finite element model for piezoelectric energy harvester plates' *J. Sound Vib.*, 2009, **327**, (1), p. 9–25.
- 216 Roundy, S., Wright, P.K., Rabaey, J.: 'A study of low level vibrations as a power source for wireless sensor nodes' *Comput. Commun.*, 2003, **26**, (11), p. 1131–1144.
- 217 Tabesh, A., Frechette, L.G.: 'A Low-Power Stand-Alone Adaptive Circuit for Harvesting Energy From a Piezoelectric Micropower Generator' *IEEE Trans. Ind. Electron.*, 2010,

- 57**, (3), p. 840–849.
- 218 Sezer, N., Koç, M.: ‘A comprehensive review on the state-of-the-art of piezoelectric energy harvesting’ *Nano Energy*, 2021, **80**, p. 105567.
- 219 Floyd, T.L.: ‘Electronic Devices: Conventional Current Version’ (Pearson, 2017)
- 220 Sheikholeslami, A.: ‘Thevenin and Norton Equivalent Circuits: Part 1 [Circuit Intuitions]’ *IEEE Solid-State Circuits Mag.*, 2018, **10**, (2), p. 8–10.

Chapter 3

General Materials & Methods

3.1 Introduction

This chapter introduces the reagents, devices, characterisation techniques and general methods used in this thesis. Specific materials or methods required by particular experiments are described in the corresponding chapters.

3.2 Materials and devices

3.2.1 Reagents

Table 3-1: The chemicals and other materials used in the thesis

Chemicals		
Product name	Supplier	Description
poly(vinylidene fluoride) (PVDF)	Sigma-Aldrich Ltd., UK	180k MW
poly(vinylidene fluoride-co-trifluoroethylene) (PVDF-TrFE)	Sigma-Aldrich Ltd., UK	Solvane ® 300/P300
poly(ethylene oxide) (PEO)	Sigma-Aldrich Ltd., UK	100k MW
N, N-dimethylformamide (DMF)	Sigma-Aldrich Ltd., UK	≥99% pure
Ethanol	Thermo Fisher Scientific, UK	≥99.8%
Acetone	VWR International, France	≥99%
De-ionised water (DI water)	---	Provided by the laboratory
Lithium chloride (LiCl)	Sigma-Aldrich Ltd., UK	≥99%
Zinc nitrate hexahydrate	Sigma-Aldrich Ltd., UK	≥99%

Zinc acetate dihydrate	Thermo Fisher Scientific, UK	≥97%
Hexamethylenetetramine (HMTA)	Sigma-Aldrich Ltd., UK	≥99.0%
poly(dimethylsiloxane) (PDMS)	Easy Composites Ltd, UK	CS25, temperature vulcanizing, condensation cure, tin-based catalyst. Shore A 25 (hardness)
PDMS	DOW Inc., USA	SYLGARD 184, transparent, room temperature or heat cure compatible. Shore A 43 (hardness)
RS PRO PLA 3D printer filament	RS Components, UK	Ø 2.85 mm

3.2.2 Electronic components and electrical devices

Table 3-2: Electronic components, modules and interfacing materials used in the thesis

Electronic components and other materials		
Product name	Manufacturer/Provider	Description
Aluminium electrolytic capacitors	KEMET/Mouser Electronics UK	100 VDC, 20% tolerance, 1, 4.7 or 10 μ F
Metallised polyester film capacitors	Panasonic/Mouser Electronics UK	250 VDC, 5% tolerance, 1 or 4.7 μ F
Light emitting diode (LED)	Broadcom/Mouser Electronics UK	1.9 V forward voltage, 2 mA forward current, green colour.
Small signal Schottky diode	Vishay/Mouser Electronics UK	BAT82S-TR Schottky diode. Low forward voltage drop, low leakage current
Operational amplifier CA3140 integrated circuit	Renesas/Mouser Electronics UK	1.5 T Ω input impedance, very low input current
Force sensitive resistor (FSR), model 406	Interlink Electronics/Mouser Electronics UK	4 cm wide, 4 cm long active area
Metal film resistors	SIQUK/Amazon UK	1% tolerance, 0.25 W rating, various resistance values
Copper wire	Available in the laboratory	23 AWG, bare copper
Copper foil	Sunhayato/RS Components UK	0.3 mm thickness, adhesive
Copper tape	3M/RS Components UK	Embossed, adhesive
Liquid crystal display (LCD) and keypad shield module	DFRobot/ RS components UK	Includes a 2x16 LCD and 6 push buttons.
A4988 stepper motor driver	Polulu/ RS components UK	Adjustable current limiting, various microstep resolutions.
Stepper motor	Sanyo Electric Co./ RS components UK	2-phase, 56 mm, 1.8° per step

Arduino Mega2560	Arduino/RS components UK	Development board based on the ATmega2560 microcontroller
842AR Silver conductive pen	RS components	Silver based conductive paint, acrylic base.
1168 Woven conductive fabric	Adafruit	Conductive fabric made of nickel, copper and polyester.
641 Stainless medium conductive thread	Adafruit	Conductive thread, rated at $10 \Omega \text{ ft}^{-1}$

3.2.3 Equipment

Table 3-3: The main and auxiliary equipment used for the characterisation of the properties of the materials and generators

Equipment		
Name	Manufacturer	Model
Scanning electron microscopy (SEM)	JEOL Ltd.	JEOL JSM-IT100
Sputter coater	Agar Scientific	AGB7341
Digital photography	Canon	EOS 6D
Conductivity metre	Traceable	4063 CC
Digital thermometer hygrometre	HTC Co Ltd.	HTC-1
X-Ray diffraction (XRD)	Bruker	D2 Phaser
Electrochemical impedance spectroscopy	Princeton Applied Research	Parstat 2273
Oscilloscope	Agilent	MSO6054A
Nozzle-based electrospinner	IME Technologies	EC-DIG
Nozzle-free electrospinner	---	Built in-house
Mechanical testing device	---	Designed and built in the laboratory. Used for exerting controlled cyclic mechanical impacts
3D printer	Ultimaker BV	Ultimaker 3
3D scanner	Shining 3D	EinScan Pro 2X Plus

3.2.4 Software

Table 3-4: List of the software used for various purposes.

Software used		
Name	Developer	Version
Matlab	Mathworks	R2016a
Ultimaker Cura	Ultimaker B.V.	3.4.1

ImageJ	Rasband, W. and contributors, NIH	1.53e
EX Scan Pro	EinScan	3.6.0.5
Meshmaker	Autodesk	3.5.474
FreeCAD	Riegel, J., Mayer, W., van Havre, Y.	0.18

3.3. Active core material fabrication by electrospinning

3.3.1 Nozzle-based electrospinning

The nozzle-based electrospinning setup consists of a stationary collector, a nozzle mounted on a frame that allows for adjustable working distance, and a syringe pump. The collector and nozzle are both contained within an acrylic chamber. Figure 3-1 shows a photograph of the device. The experimental conditions for these trials were varied depending on the type of solution being electrospun. This electrospinning setup was used for fabricating the materials described in sections [4.2.1](#), and [5.2.1](#).

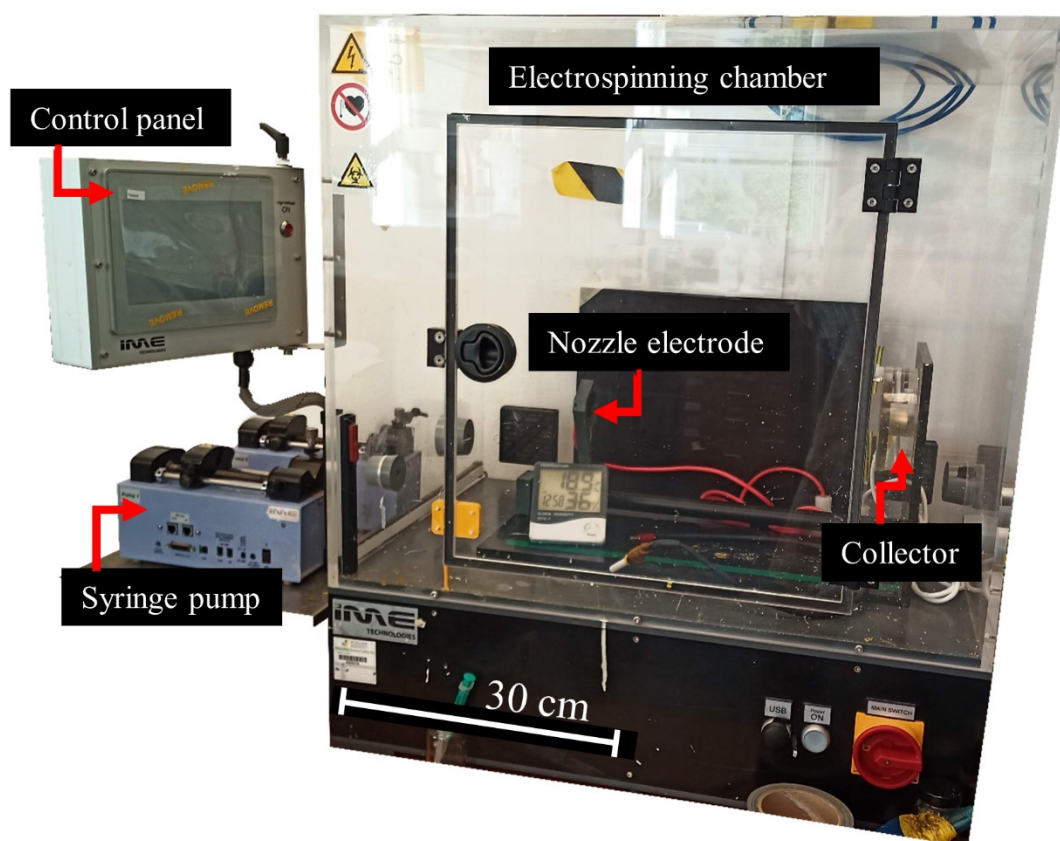


Figure 3-1: Image of the nozzle-based electrospinning setup. The user can select the voltage applied to the system and the flow rate with the control panel. Inlets on the electrospinning chamber allow for the insertion of gas lines that can be attached to other accessories.

3.3.1.1 Nitrogen flow adapter for the nozzle-based electrospinner

The nozzle-based setup includes an accessory that can be used to force gas to flow around the needle electrode. The device consists of an inner disc electrode surrounded by an outer casing that has an input port for the gas. When the needle tip is inserted and secured to the inner electrode, the needle will be positioned within a cylindrical hollow space on the opposite end of the outer casing. The input port injects the gas into the hollow space, forcing a laminar flow along the direction of the length of the needle, surrounding the needle tip as it is ejected. This allows the user to reduce the RH% and control the ambient temperature at the tip of the needle depending on the gas being fed to the system. The adapter is shown in Figure 3-2. This adapter was used for fabricating materials described in section [4.2.1](#).

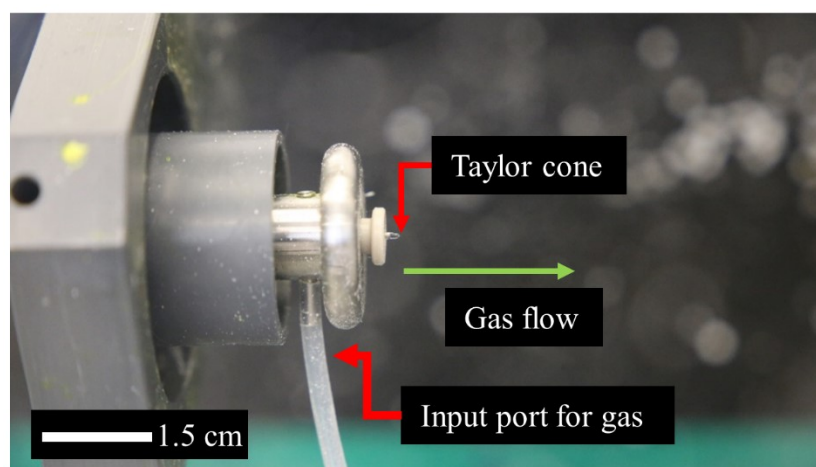


Figure 3-2: Accessory used for nitrogen gas flow for the nozzle-based electrospinning setup.

3.3.2 Nozzle-free electrospinning

The home-built nozzle-free setup had a rotating collector and a rotating drum partially immersed in a Teflon bath containing the polymer solution. Negative and positive high voltage sources are used, each connected to either the drum or collector. A 6 V DC motor is used for keeping the drum rotating at a constant 5 RPM. A brushed 12V DC motor rated at 4500 RPM and a speed controller module is used for rotating the collector and modulating its RPM. The speed controller module allows the user to reliably select the rotating speed of the collector from any value between 100 to the maximum RPM. It is possible to achieve lower RPMs by changing the maximum current and voltage fed to the motor. An adjustable DC power supply that allows for operation in constant current or constant voltage mode is used for powering up the motor that drives the rotating collector. The power source should always be operated in the constant voltage mode at 12 V if the user aims to set the collector speed at 100 RPM or

above. The working parameters such as voltage and RPM of the collector were varied depending on the experiment. These will be outlined individually in their relevant chapter.

An additional feature of this electrospinning setup is that the environmental chamber can be kept at a specific temperature and RH% settings. This can be achieved by using accessories which allow for a conditioned gas to be pumped into the chamber. For the experiments conducted in this thesis, a heat gun was mounted close to the environmental chamber and pointed towards the rotating drum. This would allow preheating of the environmental chamber to a specific temperature value, which would also result in a reduction of the RH%. The setup is illustrated in Figure 3-3. This device was used to fabricate some of the materials described in section [5.2.1](#)

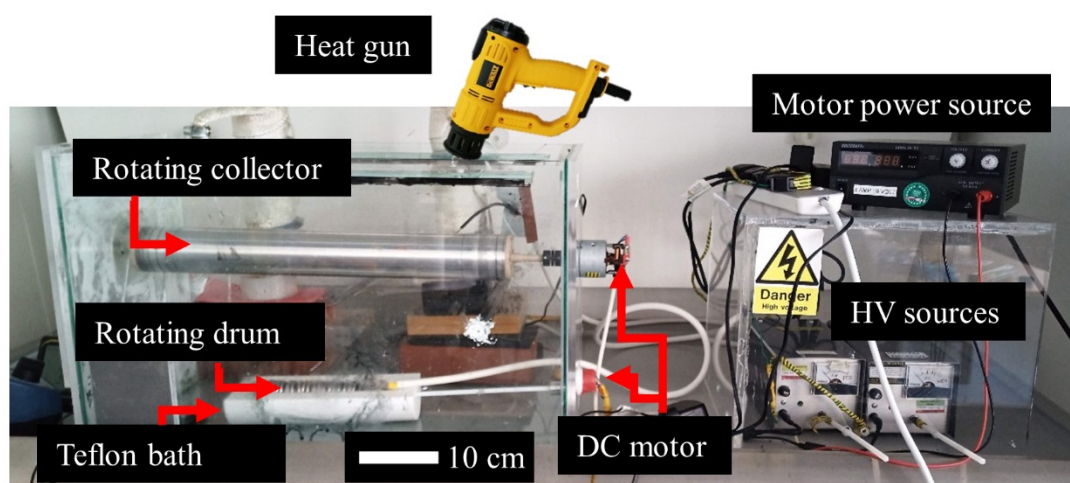


Figure 3-3: Schematic diagram of the nozzle-free electrospinning setup.

3.3.3. Relative humidity and temperature measurements

The temperature and relative humidity conditions during electrospinning were measure with a digital thermometer hygrometer, model HTC-1. This device was kept within the electrospinning chambers. The relative humidity and temperature readings were taken at the start of the electrospinning process. The device is shown in Figure 3-4.



Figure 3-4: Digital thermometer hygrometer HTC-1

3.4. Mechanical testing device design and manufacture

The original idea was to create a device that would allow for repeatedly striking a sample with a constant force and controllable impact frequency. The resultant design resembles a slider and crank mechanism, converting rotational motion into linear motion. A stepper motor, a motor driver shield and an Arduino MEGA 2560 were used for controlling the impact frequency of the device. All parts except for the slider were 3D printed in the nanomaterials laboratory. The critical parts required for the device were a slider, a connecting rod, the crank and a guide block. This device will be referred to as the cyclic mechanical impact device. A photograph of the in-house built device is shown in Figure 3-5. This device was used for the experiments described in sections [5.2.2](#), [5.2.3](#), [6.2.1](#), and [6.2.2](#).

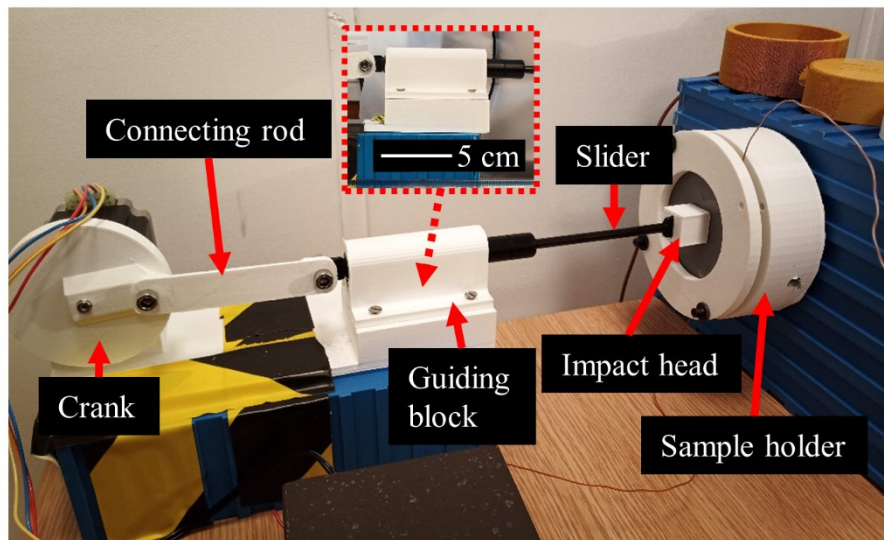


Figure 3-5: Cyclic mechanical impact device.

While the Arduino platform can be convenient for quickly developing a functional system, it is associated to several limitations that need to be taken into account when writing the code for the system. The desired impact frequency range ideally was between 0.5 to 10 Hz. Given that the stepper motor used in the design has a resolution of 1.8° per step, achieving a 1 Hz impact frequency (or 60 RPM) would require the system to send a step trigger signal once every 5 milliseconds. For a 10 Hz impact frequency, the trigger must occur every 500 microseconds. While driving the system at the lower impact frequency range is perfectly possible, driving it at a frequency closer to the upper limit of the desired range was found to be problematic. In fact, in ideal conditions, considering only the effects of integer rounding in the calculations used to set the impact frequency, the highest value that can be reliably reproduced would be 9.42 Hz. This is because both calculations for 565 RPM and 566 RPM return 531 as the number of microseconds required to elapse before triggering a step. Higher RPM values will share identical microsecond values, resulting in the observed frequency deviating from the desired

one. If one took this situation to a more realistic scenario in which other limitations such as those inherent to timings in Arduino are taken into account, the desired impact frequency would start deviating from the observed value at an even lower value. Thus, the custom-built mechanical testing device is only recommended for testing with impact frequencies in the 0.5 to 5 Hz range.

A hollow cylindrical structure and various smaller cylinders that were fitted inside it were used for housing the force sensitive resistor (FSR) and as a sample holder. The interchangeable smaller cylinders and additional thin disks and slides with indentations allowed for positioning the samples depending on how large they were and on their interfacing element type (copper wire or conductive thread). The slider was fitted with one of two different types of impact heads. One of these was a cube with an impact area of 2.6 cm². The other was a model of a human heel. This model is shown in Figure 3-6. This impact head was used for the experimental work described in section [6.2.1](#).

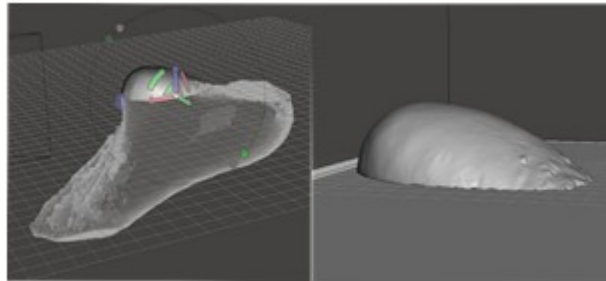


Figure 3-6: 3D model of a heel obtained with a 3D scanner.

All parts were printed using PLA filaments, with the printing settings being a layer height of 0.1 mm and 20% infill. All other settings were left untouched. Printing times ranged from only a few minutes to up to 7 or 8 hours.

3.5. Mechanical energy harvester assembly

Flat PVDF fibre mats, thick sponge-like PVDF/PEO and PVDF-TrFE/PEO mats, and PVDF-TrFE/PEO cloud-like 3D structures were used as the active core material of prototype piezoelectric generators. Differences in active core material morphology required different active core preparation methods. For both the flat fibre mats and the thick sponge-like mats, 1 cm² square-shaped sections were cut. For the cloud-like 3D structure, a medical-grade scalpel was used to obtain a 1 cm³ cube-shaped section from a region close to the core of the the cloud structure to secure a sample with higher fibre density.

Electrode bonding to the active core was achieved using different techniques. An initial approach consisted of using adhesive copper tape and foil, which was simply cut in the required shape and placed directly on the surface of the active core. Copper wire was then soldered to separate cut sections of either the tape or foil and pasted to the electrodes as required to provide interfacing ports. Figure 3-7 illustrates the copper foil electrode bonding process. This technique was used for assembling the generators tested in sections [4.2.2](#), [5.2.2](#), [5.2.3](#), [5.2.4](#), [6.2.1](#), and [6.2.2](#).

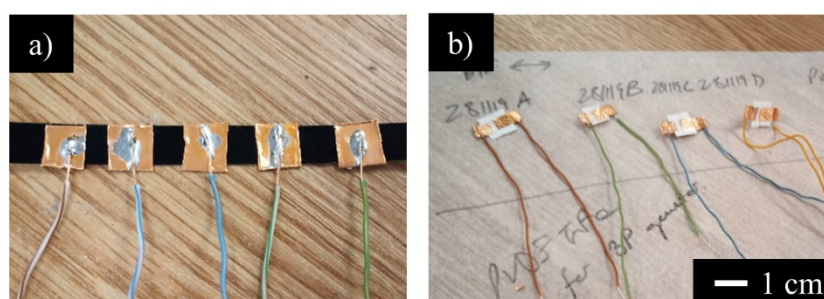


Figure 3-7: Preparation and placement of the copper foil electrodes on the active core materials. (a) Copper wire has been soldered to copper foil pieces. (b) The trimmed foil pieces are then placed on the core material.

A further evaluation of enhancements to this bonding technique involved pre-treating the surface of the active core that would be in contact with the electrodes. One pre-treatment scheme involved coating the required active core surfaces with 15 nm of gold using the sputter coater and masked with waxed paper stencils. The process is shown in Figure 3-8. Conductive silver ink was used for pre-treating the required surfaces as well, with the liquids being brushed on the active core using a size No.1 standard brush and left to dry for a day at room temperature. Copper foil or tape was then placed on the pre-treated surfaces and interfacing

ports attached to the electrodes as described previously. This bonding technique was used for fabricating generators tested in sections [6.2.1](#) and [6.2.2](#).

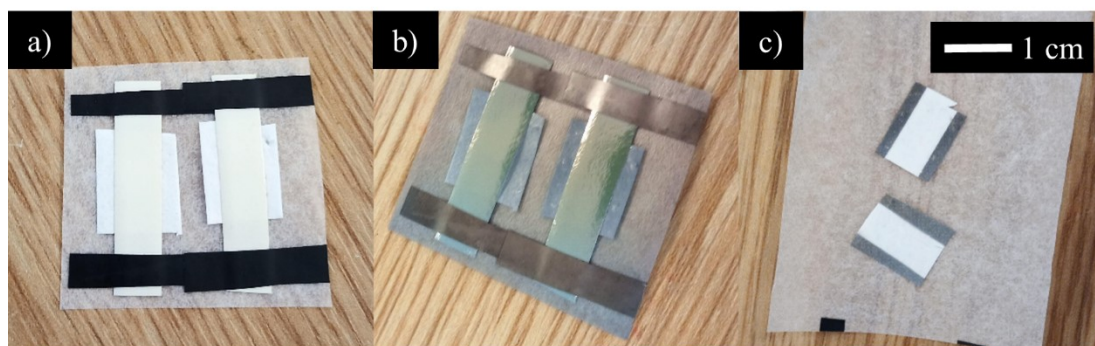


Figure 3-8: Method for coating specific areas of the thick sponge-like materials with gold. (a) The material was fixed in place with tape and waxed paper stencils were used to cover the regions that would remain unmodified. (b) After sputter coating with gold. (c) After removing the stencils.

The thick sponge-like structures resembled a non-woven fabric, an observation which inspired a different approach for electrode placement that would involve conductive threads and fabrics. Sections of the fabrics cut in the desired shape were held in place on the active core with a binder clip. A size 7 embroidery needle was then used to sew the electrode fabric to the active core. 5 cm long pieces of conductive thread were sewn to the electrodes as interfacing ports. The generator assembly process for samples with conductive fabric and thread electrodes is shown in figure 3-9a and 3-9b. This method was used for fabricating the generators tested in sections [6.2.1](#) and [6.2.2](#).

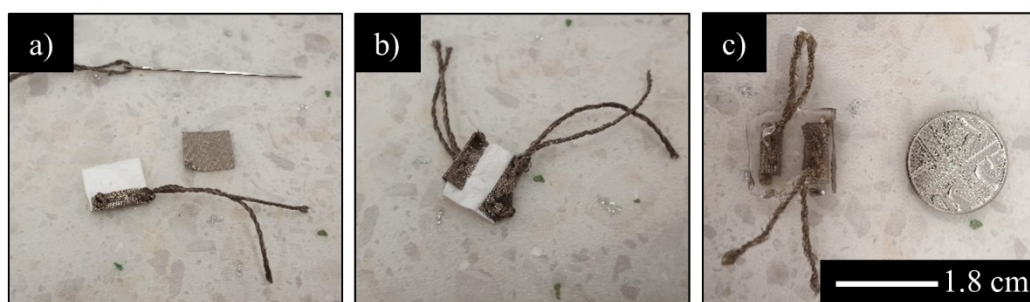


Figure 3-9: Thick sponge-like core generator with conductive fabric and thread electrodes assembly method. (a) One conductive fabric electrode has been sewn to the generator core. (b) Both electrodes have been attached to the core. (c) This generator was encapsulated in clear PDMS to show the layout of the generator.

An active core with electrodes and interfacing ports constituted the fundamental generator subunit. Specifically for the thick sponge-like structures, the implementation of these subunits

allowed for the creation of complex arrangements of multiple subunits in either parallel, series or a combination of these. Copper tape and conductive thread were both used as the interconnecting material, each of these restricted to the type of electrode to connect.

Preparation of the PDMS with a tin-based catalyst used as an encapsulation material for the flat mat or thick sponge-like core generators starts with pouring the required amount of rubber and catalyst into a beaker. The mix ratio indicated by the manufacturer is 100:5 rubber to catalyst. The fluid is thoroughly mixed until it transitions into a uniform grey colour. The mixture is then placed inside a vacuum chamber and exposed to vacuum until all air bubbles have been extracted from the mixture. An initial layer of the mixture is then poured into the empty moulds, which on this case were glass petri dishes. The generator core fitted with electrodes is placed on top of the initial layer, and then more mixture is added to the mould, until it covers the generator. The mould was degassed once more to ensure that no air bubbles would remain within the dense fibrous structure. It is left to cure for a minimum of 12 hours under standard ambient conditions. Excess silicone surrounding the generator may be trimmed after the material has cured. The preparation method for the transparent PDMS is somewhat similar, requiring instead a mix ratio of 1:10 catalyst to rubber. The fluids are placed on a beaker, thoroughly mixed and degassed as indicated for the other PDMS. However, this PDMS allowed for heat curing, thus allowing for speeding up the curing process. An initial layer of PDMS was poured into the mould and placed in an oven at 90°C for 15 minutes. The mould was taken out of the oven, then the generator units were placed on top of the cured PDMS layer and covered with the remaining PDMS mixture until all elements were completely covered. The mould was then placed in the oven again at the same temperature but left for 30 minutes instead to allow for the relatively thicker PDMS layer to cure. The mould was then taken out of the oven and left alone at room temperature for it to cool down. As with the previous PDMS, excess material can then be trimmed safely. Figure 3-9c shows an encapsulated generator after the excess PDMS has been trimmed. This PDMS encapsulation technique was used for fabricating the generators used in sections [5.2.2](#), [5.2.3](#), [6.2.1](#), and [6.2.2](#).

The approach used for bonding an electrode to the 3D cloud-like active material described in section 5.2.1 consisted of attaching adhesive copper tape on two opposite sides of the cube-shaped sample. Copper wire soldered to copper tape was then pasted on top of the electrodes. Encapsulation of the cube-shaped active core was achieved by using a glass test tube as the mould. An initial amount of transparent PDMS was poured into the test tube, which was then placed in an oven at 90°C for 15 minutes for curing. The test tube was to be kept vertical over the whole process and thus was held in this position inside the oven. Once the PDMS was

cured, the sample with electrodes and wires attached was deposited on top of the cured surface. PDMS mixture was then poured on the mould until it had covered the sample. The integrity of the cubic shape was preserved by holding the tips of the interfacing wires to the walls of the mould with binder clips. The mould was degassed one more time before curing to ensure that no air bubbles would remain within the dense fibrous structure. The mould was then placed in the oven at the same temperature for 30 minutes. It was taken out and left to cool down at room temperature, after which the generator was extracted from the mould. This procedure was used to fabricate the prototype generator shown in section 8.3.

3.6. Polymer solutions and electrospun material characterisation

3.6.1 Scanning electron microscopy (SEM)

The fabricated fibre samples were analysed with scanning electron microscopy. Samples were coated with 15 nm of gold using a sputter coater. A probe current of 30 out of 100 and a voltage setting of 15 kV were preferred when operating the device. These particular conditions made it possible to obtain clear images with magnifications of up to 23 000x in some instances.

Further fibre size analysis was done with the ImageJ image processing software. Average fibre size and standard deviations were obtained from measuring 100 individual fibres per SEM image.

The analysis of SEM images was used for the work presented in sections [4.2.1](#), [5.2.1](#), and in [Appendix B](#).

3.6.2 Digital photography

Objects such as the electrospinning apparatus, tools, generators and samples were photographed using a Canon EOS 6D DSLR camera. For instance, the thickness of the sponge-like sample was obtained by measuring the cross-section of each sample using the ImageJ software on digital photographs. A cylindrical SEM stub with a height of 5 mm was used as the reference.

Digital photography was used to capture some of the images shown in chapter 3, 4 5 and 7.

3.6.3 X-ray diffraction (XRD)

X-Ray Powder diffraction (XRD) was used to analyse the crystalline structure of the electrospun products. The performed scans were done over a 2θ range of 5° to 60° , using a scanning rate of 6° per minute. Copper $K\alpha$ radiation was used for the scans. This technique was used for analysing samples that were obtained in the experiments described in sections [4.2.2](#) and [5.2.1](#).

3.6.4 Polymer solution conductivity measurement

The conductivity of the different polymer solutions that were used for creating electrospun fibrous mats and structures was evaluated with a model 4063 CC Traceable portable system. The probe of the device, which is kept immersed in DI water when not in use, was transferred to a flask with DMF and stirred frequently until the reading in the metre stabilised. The probe

was then placed inside the flasks containing one of the polymer solutions, and stirred frequently until a stable reading was obtained. The probe was then taken out of the polymer solution and rinsed with DMF. This process, used mainly for the experiments described in section [5.2.1](#), was repeated for measuring the conductivity of all the other polymer solutions.

3.7. Electrical response characterisation of the mechanical energy harvesters

3.7.1 Mechanical stimuli

The performance of the piezoelectric energy harvesters assembled over the course of this project was evaluated by observing their electrical response to different kinds of mechanical stimuli. The general methods for delivering mechanical impacts were employed.

3.7.1.1 Dropping a 100 g weight

The generators being tested were connected to an oscilloscope probe without employing any interfacing circuits. The oscilloscope probe was set at 10x, thus making the equivalent load resistance of the system 10 M Ω . The output voltage response of the generators was recorded when 100 g weights were dropped on the samples from a height of 10 cm. The electrical response was recorded for a total period of 5 seconds per test. The method is illustrated in Figure 3-10. This technique was used for the experiments described in section [4.2.2](#).



Figure 3-10: Simplified representation of the drop test. The electrical response of the generator as the weight dropped on its surface was recorded with an oscilloscope.

3.7.1.2 Automated impacts

The cyclic mechanical impact device was used to deliver controlled mechanical impacts to a sample. As mentioned previously in this chapter, the system allows for the selection of an impact frequency. The samples were placed on the corresponding holders, with their output terminals attached to wires that were in turn connected to circuits used for varying the electrical load of the system. The device was allowed to strike the sample continuously for different time intervals depending on the type of experiment being conducted, ranging from 2 seconds up to 500 seconds. This method provides controlled mechanical impacts, which is essential for ensuring consistency when comparing the results obtained for different generator types. This method was employed in sections [5.2.2](#), [5.2.3](#), [6.2.1](#) and [6.2.2](#).

3.7.1.3 Test subject mediated impact

A test subject (Male, height of 1.65 m and weight of 63 kg) was asked to march at different speeds wearing a modified flip-flop fitted with a compound generator. As the test subject marched, he would step on the generator, which would result in an electrical response. While this method would not allow for the delivery of controlled mechanical impacts in the sense that the user might at times vary the force with which they step depending on the marching speed, degree of tiredness, among other parameters, it allows for the observation of the electrical response of the generators in practical conditions. This method was used in section [5.2.4](#).

3.7.1.4 Impact force monitoring

The impact force was only monitored when using the cyclic mechanical impact device. An oscilloscope was used to record the electrical output signals obtained from the piezoelectric generators and for the force sensing instrumentation. The force sensitive resistor (FSR) was used to monitor the impact force being exerted on the samples. The squared shaped FSR was placed within the sample holder. A thin, protective PDMS layer was placed on top of the FSR so that the cylinder piece upon which the sample was placed would not damage its surface. As suggested in the datasheet provided by the manufacturer, the FSR was connected in a voltage divider configuration, being in series with a 15 k Ω resistor. An operational amplifier in buffer configuration was connected to the node shared by the 15 k Ω resistor and the FSR. The buffer is supplied with $\pm 9V$. To eliminate the offset voltage observed at the outputs of the amplifiers, the offset nullifying recommendations outlined in the datasheet of the operational

amplifier were followed. A schematic of the circuit is shown in Figure 3-11. This circuit was used when acquiring the signals obtained in sections [5.2.1](#), [5.2.2](#), and [6.2.2](#).

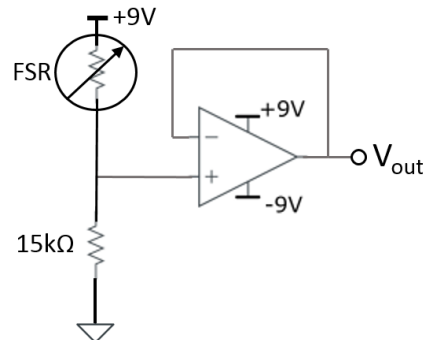


Figure 3-11: Connecting the FSR and a 15kΩ in a voltage divider configuration allows for the monitoring of the impact force on the sample. The resistive value of the FSR changes depending on the force being applied on its surface.

The FSR has an equivalent resistance value of 10 MΩ when not pressed. When pressed, its resistive value drops to almost short-circuit conditions. Using a series of calibration curves provided by the manufacturer as reference, a scaled output voltage to force estimating function was calculated. It was necessary to scale the curve taking into account the original calibration references, the original conditions used for those curves and scaling those values to the ones present in our experiments. For instance, the family of calibration curves provided by the manufacturer correspond to a buffer with a saturation voltage of 5 V. In our circuits, this voltage was 9 V instead. Equation 3-1 shows the equation obtained for the voltage to force conversion. The calibration curves provided by the manufacturer are shown in Figure 3-12.

Equation 3-1:
$$V_{out} = 1.0991 \ln(F) + 3.5657$$

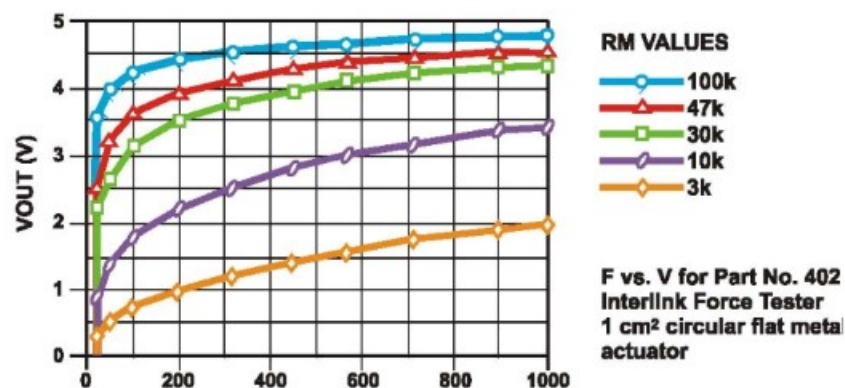


Figure 3-12: Calibration curves relating force for output voltage with the circuit shown in figure 3-6. Provided by the manufacturer.

3.7.2 Electrochemical impedance spectroscopy

The potentiostat (Parstat 2273) was operated in the EIS mode. EIS consists of feeding a small AC current to a sample at different frequencies. The voltages observed on the sample are recorded and used to calculate the impedance of the sample across a broad range of frequencies based on the magnitude and phase of the observed V and I [1]. These devices are often calibrated with a dummy cell, which consists of an arrangement of discrete resistors and capacitors. This method was used for assessing the equivalent impedance of one group of generators for a broad range of frequencies, ranging from 1 Hz to 200 kHz, with a fixed amplitude of 10 mA. The data points collected from this test were used to calculate the equivalent capacitance value of the generators. The samples were connected to the terminals of the generators as follows: Working and sense electrode on one terminal, counter and reference electrode on the other terminal. This device was used in section [4.2.3](#).

3.7.3 Variable load resistance conditions

The circuit diagram shown in Figure 3-13 details the elements used for measuring voltage and current for different resistive load values. This test consists of connecting the piezoelectric generator to a variable resistive load, allowing us to observe changes in the output current and voltage. The instantaneous output power was obtained from multiplying the V and I signals after processing them (offset removal if necessary and filtering out a residual 50Hz signal). As shown in Figure 3-13, the load resistors ranged from 10 Ω up to 15.1 M Ω . For current measurements, the circuit includes an operational amplifier (CA3140) configured as a transimpedance amplifier (TIA). Assuming that the output current was to be in the order of tenths of micro Amperes at most, a 470 k Ω gain resistor was chosen. For stability, a 30 nF capacitor was placed in parallel with the gain resistor; its value was calculated using specifications provided by the supplier in the amplifier's datasheet. Ideally, virtual ground conditions ensure that the voltage signal recorded at the output of the TIA accurately corresponds to the current being delivered by the generator.

The point marked as B in figure 3-8 is the node on which the output voltage of the generator is recorded. For all resistive loads under 100 k Ω inclusive, this node is also directly connected to a generator lead. In other words, if the load resistance is 100 k Ω or less, node A was connected directly to node B. For the higher resistive loads (1.6 M Ω and 15.1 M Ω total), the additional resistive load is connected between this node and a generator lead, resulting in the recorded output voltage having to be multiplied by a factor of 16 or 151 so as to obtain its true value (Node A connected to node C and node B connected to node B'). The operational amplifier connected to node B this node acts as a buffer. Monitoring the voltage signal using a voltage divider was a necessary design consideration required for the observation of the behaviour of the generator when connected to a high impedance load. Piezoelectric generators typically have an equivalent resistance value in the order of M Ω , reaching their maximum output power when connected to loads on a similar level. Given that the oscilloscope/probe circuit has an impedance of up to 10 M Ω , having a buffer with an input impedance in the order of 1.5 T Ω (according to the datasheet) virtually nullifies any loading effects on the output signal. This interfacing circuit was used in section [5.2.2](#), [5.2.3](#), [6.2.1](#), and [6.2.2](#)

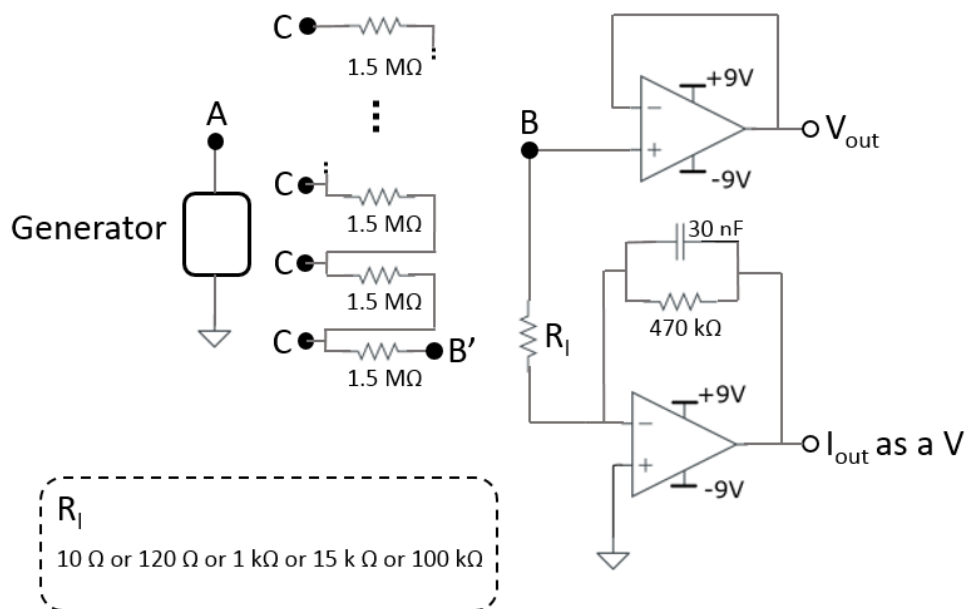


Figure 3-13: Circuit used for measuring the output power of the piezoelectric generators when connected to several different resistive loads. If resistor R_I was 100 k Ω , node A should be connected to B' and node B can be connected to any node marked as C.

3.7.4 Capacitor charging test

A full wave rectifier circuit was built using 4 schottky diodes. The output terminals of the rectifier were connected to 3 different electrolytic capacitors, valued at 1, 4.7 and 10 μF . Since connecting the oscilloscope probe directly to the positive terminal of the capacitor being tested would add a resistive load to the circuit, an operational amplifier in buffer configuration was used to monitor the charging process without draining the charge being stored in the capacitor. The circuit diagram used for this test is shown in Figure 3-14. 100 seconds of charging were recorded for each trial. This circuit was used in section [5.2.3](#) and [6.2.2](#).

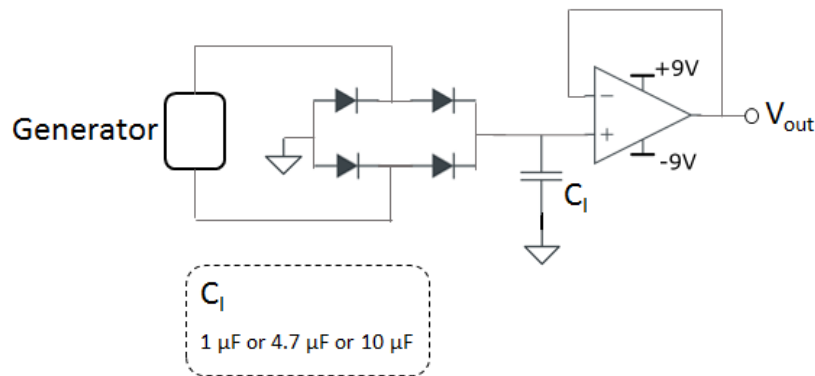


Figure 3-14: Circuit used for recording the charging of different capacitors. The full bridge rectifier was built with discrete schottky diodes. Using a buffer prevents the oscilloscope probe from draining the charge stored in the capacitive load of the rectifier.

For the experimental trial involving the test subject stepping on a generator at different SPM values, a circuit very similar to that shown previously in Figure 3-14 was used. The additional elements added to this version consist of polyester film capacitors instead of electrolytic capacitors, a single pole double throw switch (SPDT) and 40 green LEDs connected in parallel. The switch allows the user to power up the LEDs after a session of charging, which offers an opportunity for applying the energy harvested by the user. Once again, the same type of operational amplifier in buffer configuration was used for monitoring the charge stored in the capacitor without having any loading effects on the circuit. The 40 LEDs are in parallel with the capacitor once the SPDT switch is changed to the 1-3 position. Otherwise, it is connected to the full wave rectifier. The rail-to-rail input voltage for the amplifier was increased to $\pm 15\text{ V}$ to allow for the amplifier to have a greater monitoring range before the signal reaches saturation. This was done as a precaution since the voltage on the capacitor was expected to increase to higher values. The circuit used for this additional experimental trial is shown in Figure 3-15. The experimental trial is described in section [5.2.4](#).

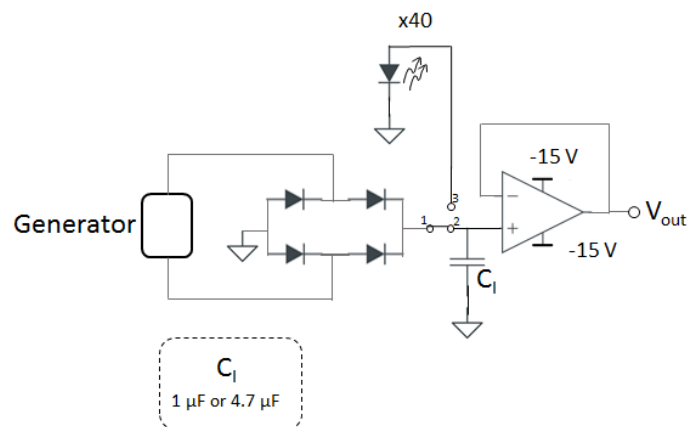


Figure 3-15: Circuit used for monitoring the voltage of a capacitor as it was charged by a user stepping on a compound generator.

3.8 Statistical analysis

The results reported in this thesis are shown as mean values with their associated standard deviations. These were obtained from processed datasets or images, depending on the measurement being conducted. In the case of datasets, these were captured from oscilloscopes in raw binary format and exported to Matlab for analysis. In the case of the values obtained from images, the software ImageJ was used to obtain the measurements, which were then exported to Matlab. Unless otherwise stated, the statistical analysis has been conducted with multiple different samples. This will be further specified in the relevant sections for each experiment.

To assess if a particular dataset followed a normal distribution, empirical cumulative distribution function plots were calculated and compared to a similar curve that had been obtained from a reference normally distributed dataset. One-way analysis of variance (ANOVA) analysis with a confidence level of 95% was performed to evaluate whether there existed a statistically significant difference between the means observed among the output recorded from some samples. In case that a general difference was identified, a post-hoc Tukey HSD test was carried out to evaluate among which specific groups a statistically significant difference would exist, assuming a p-value of 0.001.

3.9 References

- 1 Cesiulis, H., Tsyntsaru, N., Ramanavicius, A., Ragoisha, G.: 'The Study of Thin Films by Electrochemical Impedance Spectroscopy BT - Nanostructures and Thin Films for Multifunctional Applications: Technology, Properties and Devices', in Tiginyanu, I., Topala, P., Ursaki, V. (Eds.): 'Nanostructures and thin-films for multifunctional applications' (Springer International Publishing, 2016), p. 3–42

Chapter 4

A preliminary study on electrospun PVDF fibres and methods for enhancing their piezoelectric properties

4.1 Introduction

The applications of nanostructured materials as sensing and energy harvesting elements have advanced rapidly in recent years. The fabrication of nanostructures on different types of substrates allows for the creation of functionalised materials that can be tailored for specific applications such as biosensing or for developing textile solar cells [1–4]. Methods used for the fabrication of nanostructured materials and functionalised surfaces often involve a series of intermediate steps that allow for the chemical or physical bonding of the sensing elements and coatings. However, the use of additional intermediate functionalisation steps can result in a net increase in production costs and complexity. Additionally, given that each intermediate step might require the use of harmful substances and solvents, the environmental impact of the method will inevitably increase [5–7].

The use of fabrication methods such as electrospinning allows users to manufacture nanostructured, functionalised or enhanced materials in one single step depending on the working parameters and equipment characteristics [8–11]. The work presented in this chapter describe the process of optimisation that was carried out for creating the active materials that would be used as an active core for a mechanical energy harvester based on electrospun PVDF.

4.2 Results and discussion

4.2.1 Electrospinning PVDF: parameter variation effect on fibre morphology

Electrospinning as a fabrication method is often described as versatile, allowing the users to create products with unique properties depending on parameters such as temperature, relative humidity, and distance between electrodes, among others. As discussed in chapter 2, section 3.2, while some parameters have an independent effect on the properties of the obtained product, it is not uncommon for some of them to have an overlapping influence on the properties of the resulting structures. Understanding the relevance of each parameter and how they may influence each other is of critical importance for establishing a set of conditions that will yield the desired result. Electrospinning parametric studies consist of a specific approach in which a set of controllable parameters are systematically varied or held constant, thus allowing the user to observe the effects of using different combinations on the final product [12–14].

As mentioned previously in chapter 2, section 2.2 and 2.3, the ferroelectric polymer PVDF and its copolymers with TrFE have the potential to be used as active materials for mechanical energy harvesting devices based on electrospun fibrous membranes or structures, with the added features of flexibility and being non-toxic. Various case studies showing the successful integration of such materials into wearable and implantable devices is well documented in the literature. Each study offers an overview of different approaches for fabricating the materials, exploring the use of diverse additives and post-processing techniques, as well as showing how the resulting devices perform when exposed to controlled and complex ambient conditions [15–21]. The work presented in this chapter encompasses a parametric study for the electrospinning of PVDF solutions, providing a reference framework upon for the experimental work covered in this thesis.

A study in which electrospun PVDF fibre mats are used as active forward osmosis membranes was selected as the starting point of the experimental work presented in this chapter. The authors outlined a set of conditions used for electrospinning thin PVDF fibre mats using a single-nozzle, stationary collector method [22]. While the purpose of that study was to post-process the fabricated materials for enhancing their filtration properties, the aim of the experimental work presented in this chapter is to explore the effect that varying specific electrospinning parameters has on the resulting electrospun product, taking the parameters outlined by the authors of that study as the initial conditions. Once this has been achieved, it

will be possible to start evaluating the role that specific additives, rather than post-processing techniques, have in the fabrication of structures intended for energy harvesting.

The nozzle-based system was used for these experiments. Using a polymer solution of 20 wt% PVDF in DMF, the working distance of the nozzle-based electrospinner was adjusted to 15 cm, the voltage was set to 18 kV, and the flow rate for the polymer solution was 20 $\mu\text{L min}^{-1}$. The electrospinning setup allows for a rough humidity and temperature control. However, ambient conditions were used for this trial. The recorded temperature was 23 °C and the RH% was 55%. This initial trial did not yield an electrospun product; although the Taylor cone was visible on the tip of the needle, the material depositing on the collector still had solvent, thus resulting in the product dissolving and coagulating. Varying the flow rate from 20 to 5 $\mu\text{L min}^{-1}$ did not solve this issue, although it did help to identify that low flow rates aid in having the most stable Taylor cones.

Solutions with higher polymer concentrations tend to have greater viscosity, which in turn may hinder the formation of the Taylor cone [23]. However, reducing the concentration of the solutions can cause the fabrication process to transition from electrospinning to electrospraying. One method for conserving the polymer solution concentration and reducing the viscosity of the solution is to add an additional solvent [24].

The solution was adjusted for 20 wt% PVDF in a combination of DMF and acetone, with a solvent ratio of 4:1. DMF has a viscosity of 0.92 mPa s^{-1} , while this value is 0.295 mPa s^{-1} for acetone. The combination of these two solvents reduces the viscosity of the system; this, in turn, results in an increased volatility for the solvent system. Similarly to how reducing polymer concentration would result in electrospraying rather than electrospinning, reducing the viscosity of the solvent system has the same impact in the experiment. However, since the concentration of the polymer was kept at 20 wt%, reducing the viscosity of the solvent system carried a low risk, outweighed by the advantage of a higher solvent evaporation rate, which would prevent the collection of wet fibres.

Contrary to what was observed with the solutions that had only DMF as a solvent, a dry product was being depositing on the collector this time, indicating that an electrospun product was possibly being fabricated. Taylor cone formation remained stable to the naked eye. This was true for three experimental runs. The parameters used for each are shown in Table 4-1.

Table 4-1: Working parameters that appear to allow for the electrospinning of a 20wt% PVDF in DMF/Acetone (1:4 solvent ratio).

Sample	Temperature (°C)	RH%	Flow rate ($\mu\text{L min}^{-1}$)	Working distance (cm)	Voltage (kV)
A_0	20	37%	7	20	12
A_1	20.8	39%	7	20	14.5
A_2	20	37%	5	20	14.5

SEM images of the obtained products revealed that the product deposited on the collector were electrospun PVDF fibre mats for all 3 trials. Figure 4-1 shows SEM images of the fabricated materials. The formation of beads was observed for all the resulting nanofibre samples. Bead formation is undesirable as it can cause the fibrous networks to be brittle and stiff, negatively affecting the reproducibility of the final product [25]. The average diameters for the resulting fibres were 388 ± 128 nm, 447 ± 161 nm and 405 ± 139 nm for samples A_0, A_1 and A_2 respectively. As shown in the SEM images, both samples A_1 and A_2 have a lower presence of beads, indicating that having increased the voltage from 12 kV to 14.5 kV resulted in more uniform fibre mats with a slightly reduced presence of beads. There was no observed difference between having a flow rate of 5 or 7 $\mu\text{L min}^{-1}$.

The value of RH% plays an important role in electrospinning. An adapter for feeding nitrogen gas to the system was used to observe the effect of lowering the RH% in the area surrounding the needle electrode of the setup. The solutions used for these experimental trials was adjusted once again to 20 wt% PVDF in DMF. The reason for this change is that lower RH% values and higher polymer concentrations are known to produce relatively thicker fibres and reduce the amount of beads formed during electrospinning [26]. All voltage figures used for the following experimental trials represent the values at which the Taylor cone was observed to be stable. The first experimental trial involved a varying working distance, and constant flow rate and voltage. The parameters used are shown in Table 4.2. An electrospun product was obtained for each one of these sets.

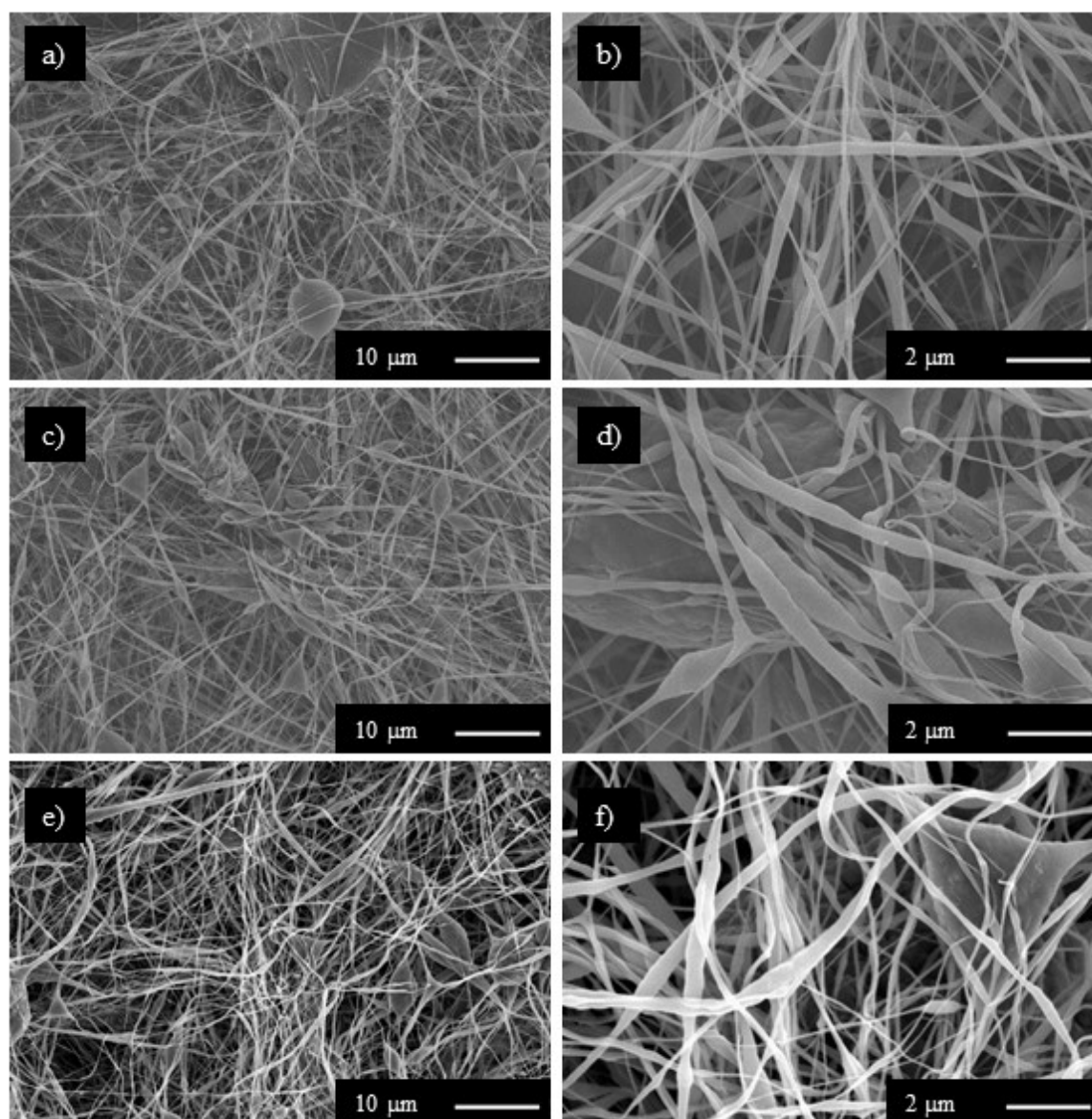


Figure 4-1: SEM images of the fibre mats obtained from electrospinning 20 wt% PVDF in DMF/acetone (4:1 solvent ratio) solutions under different conditions. (a) Sample A_0, electrospun using a $7 \mu\text{L min}^{-1}$ FR, 20 cm WD and 12 kV. (b) Same as (a), magnified image. (c) Sample A_1, electrospun using a $7 \mu\text{L min}^{-1}$ FR, 20 cm WD and 14.5 kV. (d) Same as (c), magnified image. (e) SampleA_2, electrospun using a $5 \mu\text{L min}^{-1}$ FR, 20 cm WD and 14.5 kV. (f) Same as (e), magnified image.

Table 4-2: Working parameters used for evaluating product variation when electrospinning a 20 wt% PVDF in DMF solution under nitrogen gas flow.

Sample	Temperature (°C)	Flow rate (µL min⁻¹)	Working distance (cm)	Voltage (kV)
B_0	20.8	7	20	18
B_1	20.8	7	15	18

SEM images of the resulting products show that beads and coagulated polymer agglomerations were present in the fibre mats. Figure 4-2 shows the SEM images obtained for these samples. A closer inspection of the agglomerates and the distinct patterns that can be observed on their surface indicate that the solvent is not evaporating fast enough, causing the depositing fibres to dissolve and blend into an agglomerate. In order to test this idea, an additional trial was carried out. The flow rate was adjusted to 15 µL min⁻¹, and working distance was the parameter being varied between runs. The parameters used for this trial are shown in Table 4.3.

Table 4-3: Working parameters used for evaluating the effect of an increased flow rate when electrospinning 20 wt% PVDF in DMF solutions under nitrogen gas flow.

Sample	Temperature (°C)	Flow rate (µL min⁻¹)	Working distance (cm)	Voltage (kV)
C_0	19.7	15	25	18
C_1	19.7	15	20	16
C_2	23.1	15	15	11
C_3	23.1	15	10	11

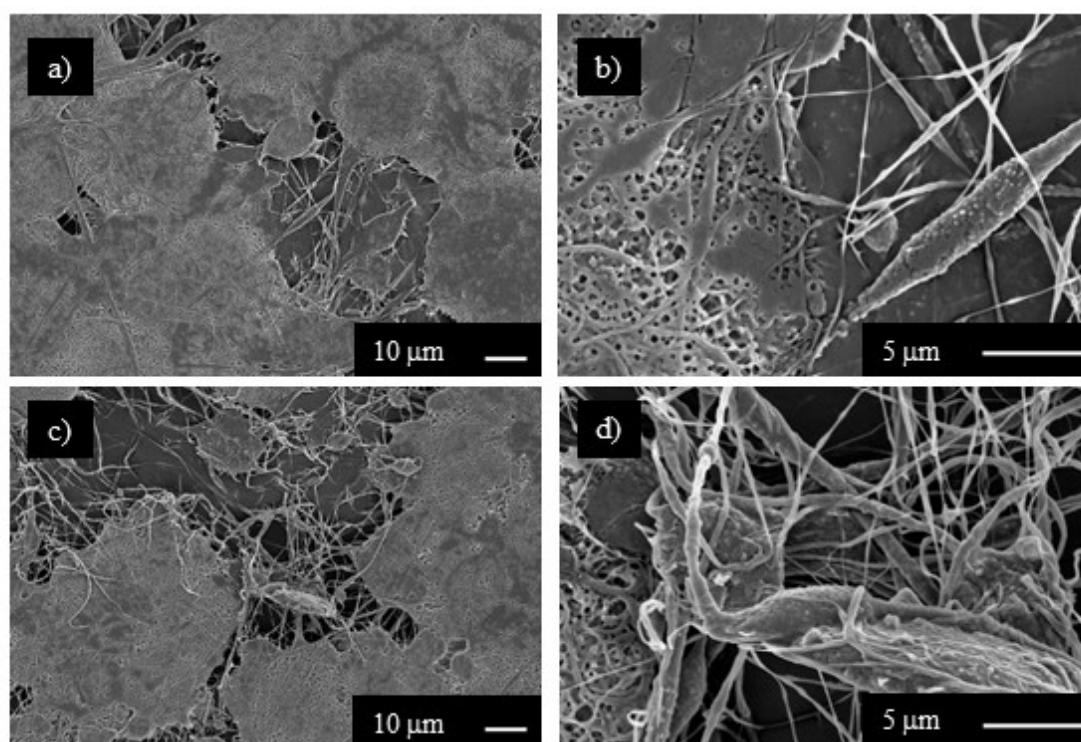


Figure 4-2: SEM images of the fibre mats obtained from electrospinning 20 wt% PVDF in DMF solutions with nitrogen flow, $7 \mu\text{L min}^{-1}$ FR, 18 kV, and varying WD. (a) Sample B_0, electrospun with a 20 cm WD. (b) Same as (a), magnified image. (c) Sample B_1, electrospun with a 15 cm WD. (d) Same as (c), magnified image.

The products obtained from these experiments also had the appearance of an electrospun fibre mat to the naked eye. Once again, SEM images revealed that beads and agglomerations were still present in the samples. The SEM images are shown in Figure 4-3. Having almost doubled the flow rate of the polymer solution, it was expected for the presence of the agglomerates to be dominant. However, as observed from the SEM images, there was a net increase in the amount of fibres in the sample when W.D. was set to 20 cm. For the samples obtained when W.D. was 15 and 10 cm, only a few individual fibres can be observed on top of the agglomerates.

One final trial was carried out to observe how a lower polymer concentration and higher flow rate compare to the samples obtained from the previous trials. A 15 wt% PVDF in DMF solution was electrospun under varying working distance conditions, and constant flow rate and voltage. The parameters used are shown in Table 4.4.

Table 4-4: Working parameters used for electrospinning a 15 wt% PVDF in DMF solution under a nitrogen flow. The flow rate for this trial was $25 \mu\text{L min}^{-1}$.

Sample	Temperature (°C)	Flow rate ($\mu\text{L min}^{-1}$)	Working distance (cm)	Voltage (kV)
D_0	23	25	20	21
D_1	23	25	15	21

SEM images of the resulting products reveal that, for a working distance of 20 cm, an increased flow rate in conjunction with a decreased polymer concentration have a favourable effect on the evaporation of the solvent, thus resulting in a relatively higher amount of independent fibres on the sample. The SEM images are shown in Figure 4-4.

These experimental trials that involved the use of the nitrogen flow for the reduction of the RH% value show that a lower polymer concentration, reduced flow rates, working distances over 15 cm and voltage levels adjusted for facilitating the formation of a stable Taylor cone at the tip of the needle are some of the experimental conditions that favour the formation of electrospun PVDF fibres with our particular experimental setup. Comparing the samples obtained from the trials involving nitrogen flow with those obtained from trials involving ambient RH% conditions, it is clear that the use of a compound solvent system and of ambient RH% conditions close to 35 % allow for the fabrication of PVDF materials on which the presence of individual fibres is dominant. As discussed previously in the chapter 2, micro and nanostructured piezoelectric materials for which the length to width aspect ratio is high will exhibit a greater piezoelectric response. Therefore, the samples obtained from the products electrospun without the nitrogen flow had a greater potential as the active material of a piezoelectric generator.

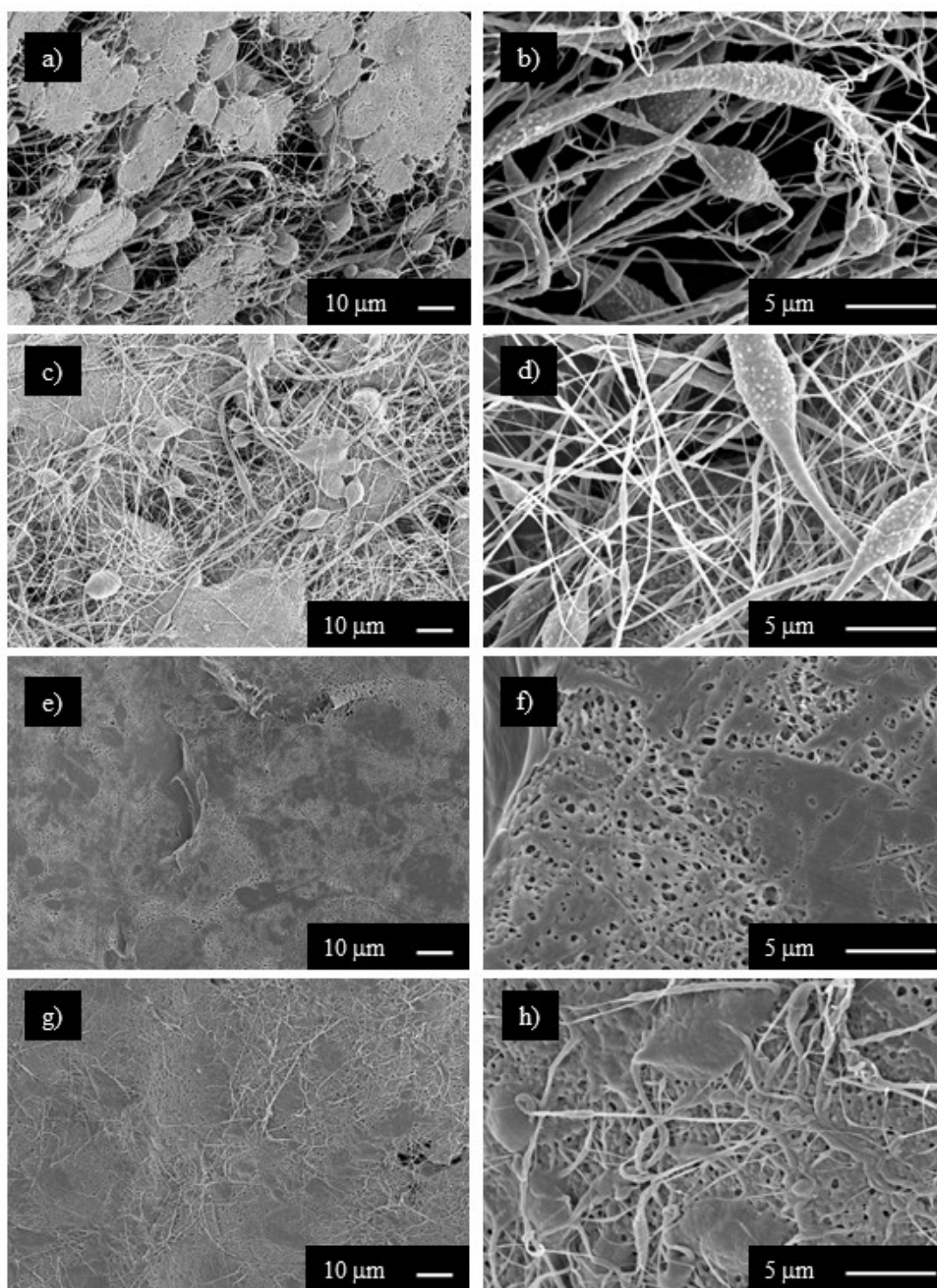


Figure 4-3: SEM images of the fibre mats obtained from electrospinning 20 wt% PVDF in DMF solutions with nitrogen flow, $15 \mu\text{L min}^{-1}$ FR, and varying WD and voltage. (a) Sample C_0, electrospun with a 25 cm WD, 18 kV. (b) Same as (a), magnified image. (c) Sample C_1, electrospun with a 20 cm WD, 16 kV. (d) Same as (c), magnified image. (e) Sample C_2, electrospun with a 15 cm WD, 11 kV. (f) Same as (e), magnified image. (g) Sample C_3, electrospun with a 10 cm WD, 11 kV. (h) Same as (g), magnified image.

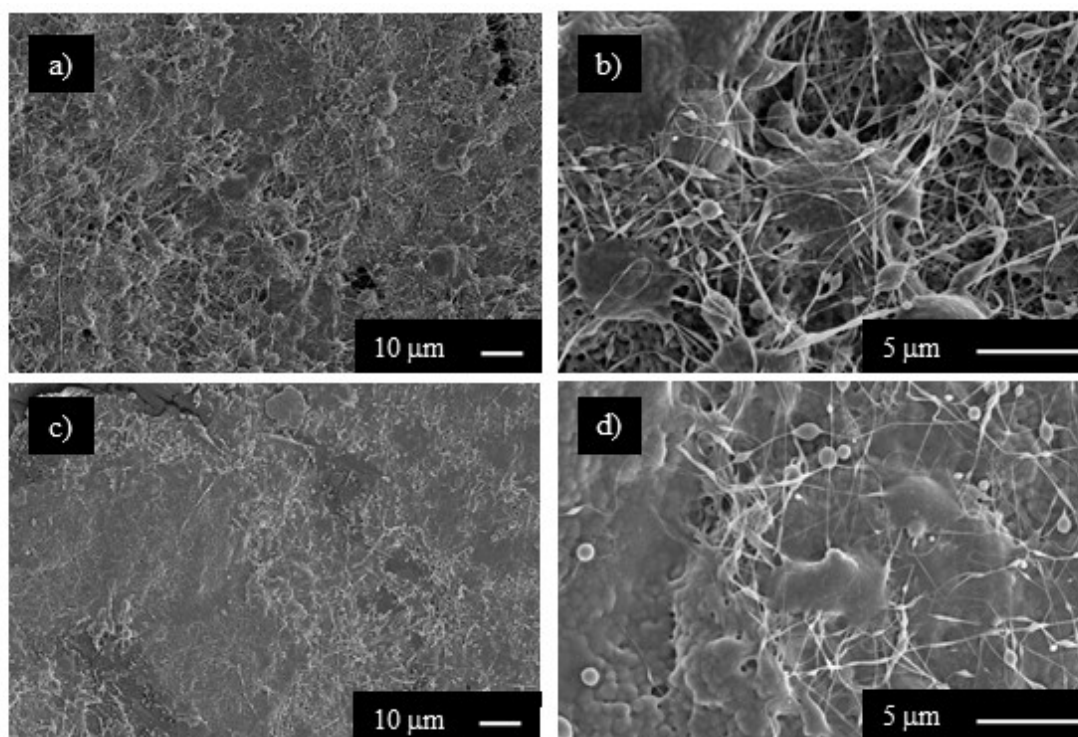


Figure 4-4: SEM images of the fibre mats obtained from electrospinning 15 wt% PVDF in DMF solutions with nitrogen flow, $25 \mu\text{L min}^{-1}$ FR, 21 kV and varying WD. (a) Sample D_0, electrospun with a 20 cm WD. (b) Same as (a), magnified image. (c) Sample D_1, electrospun with a 15 cm WD. (d) Same as (c), magnified image.

4.2.2 A preliminary assessment of 2D PVDF fibre mat core generators

The electrospun fibres obtained when electrospinning 20 wt% PVDF in DMF/Acetone (4:1 solvent ratio) solutions were used as the active core material for a piezoelectric generator. Considering that the fabricated materials were not completely free of beads and agglomerates, a favourable electrical response would indicate that even better results would be obtainable once the solutions and conditions for obtaining bead-free samples are determined.

The first generator design consisted of a 1 cm^2 section of the electrospun material sandwiched between aluminium foil, which would act as the electrode material. The wires were placed directly soldered on top of the aluminium foil and fixed in place with insulating tape. Using the copper wire on top of the active material was the main reason why this generator design failed. Evaluating this prototype required the application of a mechanical stimulus on the surface of the generator, which consisted of a finger tapping strongly on the device. The response would be observed on an oscilloscope, and the equivalent load resistance was 10 M Ω . The

generators were functional only for a few impacts; the electrical response would rapidly decay until no signal could be obtained anymore. Opening the sealed generators revealed the main reason why this occurred. The electrospun fibre mats are frail, and tapping on the surface of the generators caused the wires to scratch away the fibres on the foil. This would result in the wires removing the active core and causing enough damage to short the aluminium foil electrodes.

The response of the generators were recorded for a duration of 5 seconds. Given that the stimulus was not a controlled mechanical impact, these results cannot be used to compare the individual performance of the different types of core material. However, these results are indicative of the potential that the electrospun PVDF fibre mats have for the fabrication of a piezoelectric generator.

An improved generator design was proposed based on the issues that had been identified for the previous iteration. The same electrospun samples were used in the assembly of these generators. Instead of using copper wire, this design used instead copper foil strips. The active material was placed between the two copper foil electrodes, and then sealed with insulating tape. Figure 4-5 shows the differences between the original and improved generator designs.

Similar testing conditions were used for evaluating the voltage response of the generators. The comparison between the V_{PP} figures observed for each type of core for different generator design is shown in Table 4.5.

Table 4-5: Comparison of the differences in the average output V_{PP} recorded for vigorous finger tapping on an electrospun PVDF core piezoelectric generator for two different generator designs.

	Original generator design	Improved design
Sample	Average Peak-to-peak voltage (V)	
A_0	4.11 ± 1.17	10.33 ± 2.22
A_1	2.91 ± 0.68	10.83 ± 2.02
A_2	3.72 ± 1.25	10.93 ± 1.54

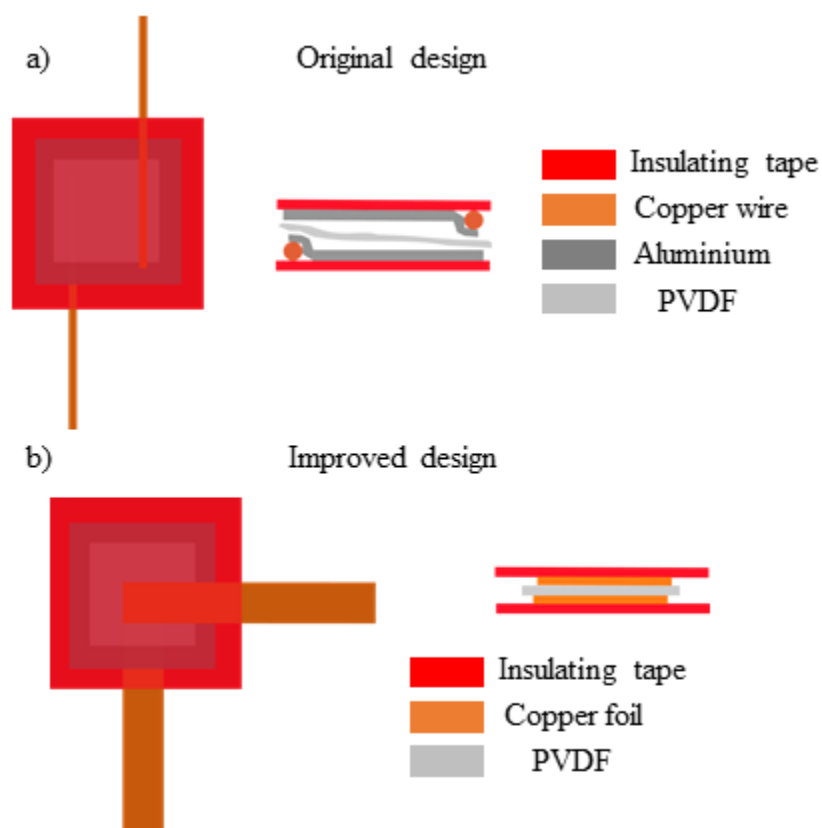


Figure 4-5: Schematic diagram of the two generator designs used for testing the electrical output of the products obtained from electrospinning a 20 wt% PVDF in DMF/acetone solution. (a) Original generator design. (b) Improved generator design.

The results shown in table 4.5 reflect the average V_{PP} values estimated from the waveforms recorded by the oscilloscope. The improved generator design resulted in higher recorded output V_{PP} figures of at least 2.5 times greater than those observed for the original designs for all the 3 different types of core. While the new generator design was more robust, wear and tear damage to the active core still occurred after a few rounds of testing. The differences in the outputs are strong indicators that generator design is critical for maximising the signals that can be obtained from the core materials.

4.2.3 Generator equivalent impedance and behaviour

The responses recorded in the previous section were obtained when the equivalent resistive load of the system was 10 M Ω . This value is not necessarily the optimal for ensuring maximum power transfer from the generator; recalling some of the theories discussed in chapter 2, maximum power transfer for an AC load is achieved when the load impedance closely matches the conjugate of the internal impedance of the source. Using EIS for analysing an RC circuit on which the improved generators act as the capacitive element could be useful for

observing how the generators behave as electrical loads and might allow for the identification of an internal impedance model for these elements.

Since piezoelectric generators are often modelled as a predominantly capacitive element, the last 2 improved generators from table 4.5 were used as the capacitor C_L for the circuit shown in Figure 4-6. The equivalent impedance of the whole electrical load is shown in Equation 4.1.

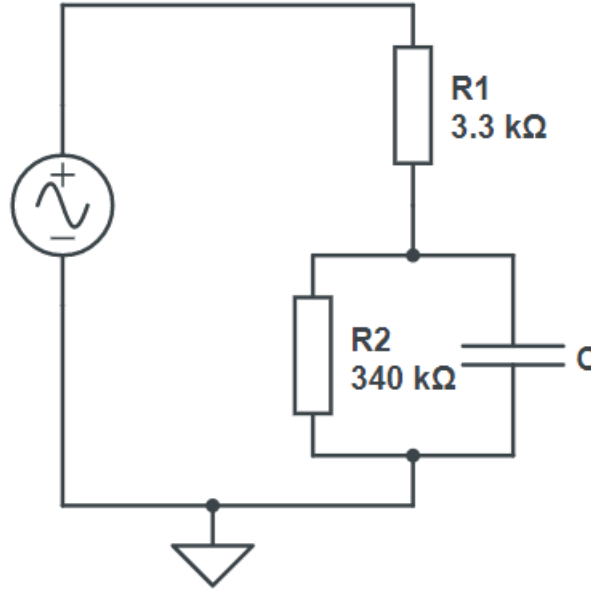


Figure 4-6: Test circuit used for evaluating the impedance and behaviour of the generators with 20 wt% PVDF in DMF/acetone cores. The generator substituted the capacitor C.

Equation 4.1

$$\left(3.3k + \frac{\frac{340k}{\omega^2 C^2}}{(340k)^2 + \frac{1}{\omega^2 C^2}} \right) + \frac{1}{j} \left(\frac{(340k)^2}{(340k)^2 + \frac{1}{\omega^2 C^2}} \right) \left(\frac{1}{\omega C} \right)$$

At $\omega = 0$, the capacitive element acts as an open circuit, resulting in the equivalent impedance to be 343.3 kΩ and having no reactive component. When $\omega = \infty$, the reactive component is once again 0. For the real component, the frequency-dependent value is also 0, thus resulting in the equivalent impedance being the 3.3 kΩ resistor. If the generators behave as capacitive elements, then a plot mapping the real and reactive components of the equivalent impedance obtained from a frequency sweep would result in a semicircle that intersects the real axis at 3.3 and 343.3 kΩ.

EIS spanning a frequency range from 1 Hz to 200 kHz (30 data points per decade) was carried out; with two recordings for each sample. The generators used for this experiment were those with core materials labelled as A_1 and A_2. The resulting data were processed using Matlab, and an equivalent capacitance value was estimated for both samples. Figure 4-7 shows a Nyquist plot with the recorded data points and a curve obtained when substituting an ideal capacitance of 54.4 pF instead of a generator. The estimated capacitance value for both generators was similar, indicating that the properties of the bulk material dominate over any effects that the individual morphological differences at the micro and nanoscale could be having in regards to the capacitive behaviour of the sample, specifically for situations in which the size of the sample is many orders of magnitude larger than the individual features of each fibre.

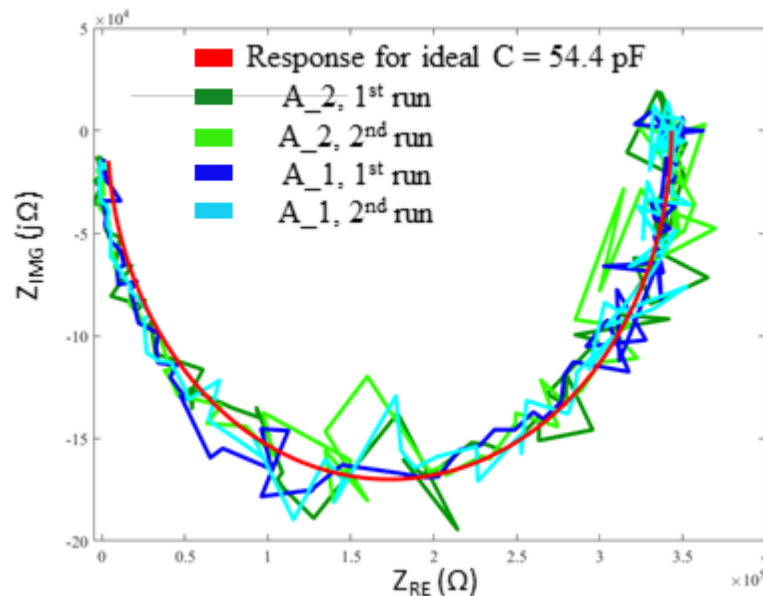


Figure 4-7: Nyquist plot of the EIS test for the circuit shown in Figure 4.8, substituting the capacitor C with the improved generators. The generators had cores obtained from samples A_2 and A_1. The responses for both trials for each generator resemble the general semi-circular shape of the ideal response.

While it was possible to confirm that a piezoelectric generator with an electrospun PVDF fibrous core does behave as it would be expected for such devices, the test circuit configuration does not provide a complete picture of the individual characteristics of the generator itself. Practical applications of piezoelectric generators predominantly involve low-frequency mechanical impacts, extending from 0.1 Hz up to 100 Hz at most. The data points acquired for this frequency range in the EIS scan reflect how the equivalent impedance of the capacitor at low frequencies is simply many orders of magnitude greater than that of the 340 k Ω resistor, thus resulting in those data points being close to the 340 k Ω and j0 k Ω region.

This only reveals that the equivalent impedance behaviour of the generator for that frequency range is that of a very large resistor, indicating that maximum power transfer at low frequencies can be extracted if the harvesting circuit has an equivalent input impedance of similar magnitude. However, the exact value is yet to be determined.

4.3 Interim summary

The experimental work presented in this chapter presents an overview of the various steps involved in the optimisation process of an electrospun solution. The effects of selecting flow rates, working distances, voltages, polymer concentration, solvent system composition, and special operating conditions such as that of using a nitrogen gas flow for reducing the effective relative humidity at the tip of the needle electrode were observed throughout this chapter. According to the observations made, PVDF solutions with compound solvent systems, exposed to relative humidity values in the vicinity of 35%, working distances over 15 cm, and voltage levels adjusted until a stable Taylor cone is formed had the potential for the electrospinning of fibre mats with a decreased amount of beads and agglomerations.

The best electrospun fibre mats obtained from these experiments demonstrated the potential to be used as the active core of mechanical energy harvesters. While the electrical response was consistently similar over the course of a few testing rounds, generator design and construction should prioritise the protection of the active material since it is vulnerable to abrasion and can be easily and irreversibly be damaged by mechanical impacts. Future implementations of generators for these types of active cores would benefit greatly from encapsulation in a flexible matrix.

The behaviour of the improved generators as an electrical load in the electrochemical impedance spectroscopy test circuit was matched to that of a non-ideal capacitor, which is in accordance with the equivalent models that have been proposed for these devices. The EIS tests helped to identify the favourable characteristics of the electrical loads that would allow for maximising the output power of the generators.

The experimental work presented in this chapter provided a broad set of observations that allowed for the identification of favourable conditions and parameters that would become critical for the fabrication of fibrous materials better suited for the intended applications. Design flaws and other issues identified when electrospinning the materials, fabricating the generators and testing their response were also of great importance, making it possible to more effective alternatives and implementations which would result in vast improvements for the project.

4.4 References

- 1 Peng, M., Dong, B., Zou, D.: 'Three dimensional photovoltaic fibers for wearable energy harvesting and conversion' *J. Energy Chem.*, 2018, **27**, (3), p. 611–621.
- 2 Li, H., Koh, C.S.L., Lee, Y.H., *et al.*: 'A wearable solar-thermal-pyroelectric harvester: Achieving high power output using modified rGO-PEI and polarized PVDF' *Nano Energy*, 2020, **73**, p. 104723.
- 3 Lu, Z., Zhang, H., Mao, C., Li, C.M.: 'Silk fabric-based wearable thermoelectric generator for energy harvesting from the human body' *Appl. Energy*, 2016, **164**, p. 57–63.
- 4 Chowdhury, A.R., Jaksik, J., Hussain, I., *et al.*: 'Multicomponent nanostructured materials and interfaces for efficient piezoelectricity' *Nano-Structures & Nano-Objects*, 2019, **17**, p. 148–184.
- 5 Kim, H.C., Fthenakis, V.: 'Life Cycle Energy and Climate Change Implications of Nanotechnologies' *J. Ind. Ecol.*, 2013, **17**, (4), p. 528–541.
- 6 Mullen, E., Morris, M.A.: 'Green Nanofabrication Opportunities in the Semiconductor Industry: A Life Cycle Perspective' *Nanomaterials*, 2021, **11**, (5), p. 1085.
- 7 Pandhi, S., Mahato, D.K., Kumar, A.: 'Overview of Green Nanofabrication Technologies for Food Quality and Safety Applications' *Food Rev. Int.*, 2021, p. 1–21.
- 8 Agarwal, S., Greiner, A., Wendorff, J.H.: 'Functional materials by electrospinning of polymers' *Prog. Polym. Sci.*, 2013, **38**, (6), p. 963–991.
- 9 Vempati, S., Ranjith, K.S., Topuz, F., Biyikli, N., Uyar, T.: 'Electrospinning Combined with Atomic Layer Deposition to Generate Applied Nanomaterials: A Review' *ACS Appl. Nano Mater.*, 2020, **3**, (7), p. 6186–6209.
- 10 Park, J.-S.: 'Electrospinning and its applications' *Adv. Nat. Sci. Nanosci. Nanotechnol.*, 2011, **1**, (4), p. 43002.
- 11 Wendorff, J.H., Agarwal, S., Greiner, A.: 'Electrospinning: Materials, Processing, and Applications' (Wiley, 2012)
- 12 Patra, S.N., Easteal, A.J., Bhattacharyya, D.: 'Parametric study of manufacturing poly(lactic) acid nanofibrous mat by electrospinning' *J. Mater. Sci.*, 2009, **44**, (2), p. 647–654.
- 13 Tan, S.-H., Inai, R., Kotaki, M., Ramakrishna, S.: 'Systematic parameter study for ultra-

- fine fiber fabrication via electrospinning process' *Polymer (Guildf)*, 2005, **46**, (16), p. 6128–6134.
- 14 Cozza, E.S., Monticelli, O., Marsano, E., Cebe, P.: 'On the electrospinning of PVDF: influence of the experimental conditions on the nanofiber properties' *Polym. Int.*, 2013, **62**, (1), p. 41–48.
 - 15 Liu, C., Zhang, W., Sun, J., *et al.*: 'Piezoelectric nanogenerator based on a flexible carbon-fiber/ZnO–ZnSe bilayer structure wire' *Appl. Surf. Sci.*, 2014, **322**, p. 95–100.
 - 16 Li, X., Lin, Z.H., Cheng, G., *et al.*: '3D fiber-based hybrid nanogenerator for energy harvesting and as a self-powered pressure sensor' *ACS Nano*, 2014, **8**, (10), p. 10674–10681.
 - 17 Ji, S.H., Cho, Y.-S., Yun, J.S.: 'Wearable Core-Shell Piezoelectric Nanofiber Yarns for Body Movement Energy Harvesting' *Nanomater.* 2019, Vol. 9, Page 555, 2019, **9**, (4), p. 555.
 - 18 Yang, T., Pan, H., Tian, G., *et al.*: 'Hierarchically structured PVDF/ZnO core-shell nanofibers for self-powered physiological monitoring electronics' *Nano Energy*, 2020, **72**, p. 104706.
 - 19 Fuh, Y.K., Wang, B.S., Tsai, C.-Y.: 'Self-Powered Pressure Sensor with fully encapsulated 3D printed wavy substrate and highly-aligned piezoelectric fibers array' *Sci. Rep.*, 2017, **7**, (1), p. 6759.
 - 20 Vong, M., Diaz Sanchez, F.J., Keirouz, A., Nuansing, W., Radacsi, N.: 'Ultrafast fabrication of Nanofiber-based 3D Macrostructures by 3D electrospinning' *Mater. Des.*, 2021, **208**, p. 109916.
 - 21 Santangelo, S.: 'Electrospun Nanomaterials for Energy Applications: Recent Advances' *Appl. Sci.* 2019, Vol. 9, Page 1049, 2019, **9**, (6), p. 1049.
 - 22 Obaid, M., Mohamed, H.O., Yasin, A.S., *et al.*: 'A novel strategy for enhancing the electrospun PVDF support layer of thin-film composite forward osmosis membranes' *RSC Adv.*, 2016, **6**, (104), p. 102762–102772.
 - 23 Costa, L.M.M., Bretas, R.E.S., Gregorio, R., Costa, L.M.M., Bretas, R.E.S., Gregorio, R.: 'Effect of Solution Concentration on the Electrospray/Electrospinning Transition and on the Crystalline Phase of PVDF' *Mater. Sci. Appl.*, 2010, **1**, (4), p. 247–252.
 - 24 Jacobs, V., Anandjiwala, R.D., Maaza, M.: 'The influence of electrospinning parameters on the structural morphology and diameter of electrospun nanofibers' *J. Appl. Polym.*

- Sci.*, 2010, **115**, (5), p. 3130–3136.
- 25 Lin, T., Wang, H., Wang, H., Wang, X.: 'The charge effect of cationic surfactants on the elimination of fibre beads in the electrospinning of polystyrene' *Nanotechnology*, 2004, **15**, (9), p. 1375–1381.
- 26 Pelipenko, J., Kristl, J., Janković, B., Baumgartner, S., Kocbek, P.: 'The impact of relative humidity during electrospinning on the morphology and mechanical properties of nanofibers' *Int. J. Pharm.*, 2013, **456**, (1), p. 125–134.

Chapter 5

3D sponge-like PVDF micro and nanofibrous structures for mechanical energy harvesting.

5.1 Introduction

The work presented in the previous chapter allowed for the identification of a range of electrospinning conditions and parameters that would result in the formation of electrospun PVDF fibres. However, the morphology of the resulting product had plenty of room for improvement. The experimental work presented in this chapter uses the previous results as a starting point and aims to find methods for improving the morphology and the properties of the electrospun products.

Aiming to find alternatives for enhancing the properties of the electrospun PVDF fibres, the initial step consisted of evaluating the role of additives such as other polymers and salts in the properties of the resulting products. The quality and morphology of the resulting products was observed to change dramatically, with both types of additives contributing to the transition from flat fibrous mats to thick, cloud-like 3D structures. Using PVDF-TrFE, a copolymer of PVDF, yielded similar results when similar additives and electrospinning conditions were employed.

A group of thick, non-woven fabric-like PVDF/PEO and PVDF-TrFE/PEO electrospun products were used as active cores for prototype mechanical energy harvesters. The properties of the devices such as output voltage and current as a function of resistive load, estimates of the output power, and performance under controlled and real-world conditions were explored in order to evaluate the potential that these materials have for mechanical energy harvesting.

The experimental work shown in this illustrates shows how the project progressed into a more advanced application of the manufactured materials, and outlines a novel method for electrospinning 3D PVDF structures.

5.2 Results and discussion

5.2.1 Electrospun materials morphology

The main objective was to identify methods that would allow us to fabricate electrospun 3D PVDF fibre structures. Based on the findings from previous collaborative work which describes the role that additives such as acids and salts have on the formation of 3D structures for various electrospun polymers [1], and the work that has been detailed in the previous chapter, lithium chloride salts were proposed as one of the additives to be employed in the experiments. Another advantage of using lithium chloride is that the presence of the β -phase configuration on electrospun PVDF, which has enhanced piezoelectric activity, is known to increase when processed from polymer solutions enriched with salts [2]. Two electrospinning setups were used for assessing the scalability and throughput of the process: the nozzle-based setup and a high-throughput nozzle-free system with a rotating collector mounted inside an isolated environmental chamber [3]. A heat gun was mounted externally to allow for chamber temperature control for the nozzle-free setup. Figure 5-1 shows a schematic diagram of both devices.

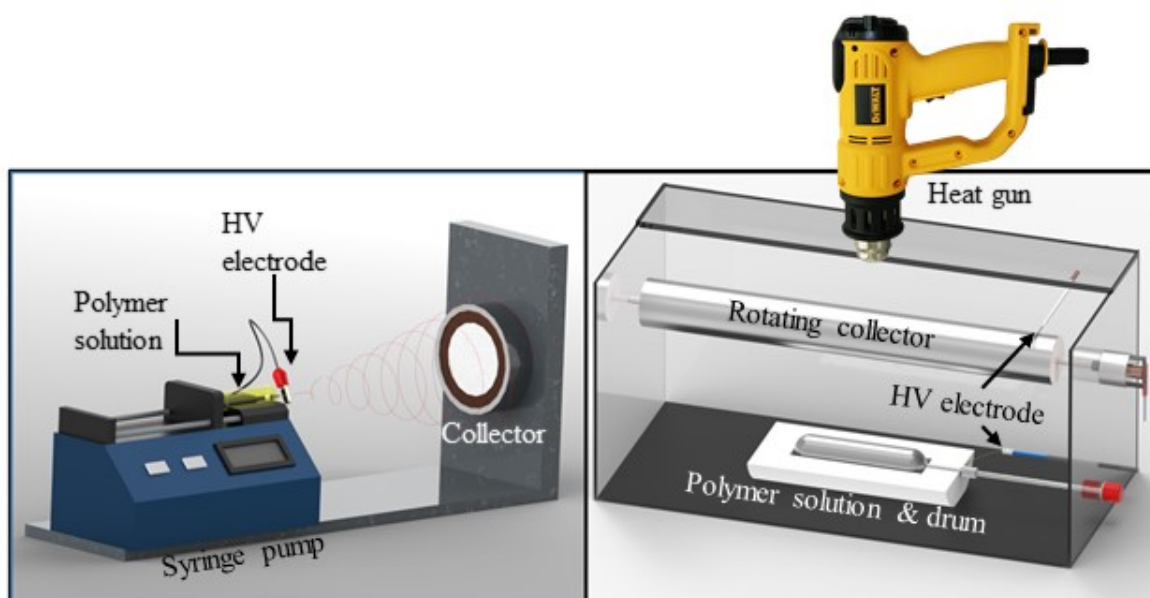


Figure 5-1: Electrospinning setups used for the fabrication of the active core material for piezoelectric generators. Left, nozzle-based setup. Right, nozzle-free setup.

The first challenge was to optimize the solution in order to obtain a reliable base on which to test the effects of the addition of LiCl salts. The starting point for these experiments was using

the solutions that had been tested in the previous chapter and reading about studies on which bead-less PVDF fibres had been successfully electrospun. For improving the morphology of the obtained fibres, the solution was adjusted, now including polyethylene oxide (PEO) and water in addition to DMF and PVDF [4]. The use of a DMF and water solvent/non-solvent system is known to allow the user to heavily modify fibre surface morphology [5]. The use of these additional elements stabilized the resulting fibre morphology on a larger scale, contributing to the elimination of beads, and the production of fibres with very uniform diameters. However, it also cause the fibres to have crater riddled surfaces. This effect occurs due to the interacting polymers in their solvent/non-solvent system as the solution is ejected from the nozzle/drum. A 10 wt% PVDF/PEO in DMF/water solution with a 50:3 ratio for both polymers and solvents were used for fabricating electrospun fibre mats with the nozzle-based setup. The conditions are summarised in Table 5.1.

Table 5-1: Electrospinning parameters used for fabricating 10 wt% PVDF/PEO fibre mats using the nozzle-based setup. T=22 °C, RH% = 42

Solution	FR ($\mu\text{l min}^{-1}$)	Voltage (kV)	WD (cm)
10 wt% PVDF/PEO in DMF/water	7	17	30
(50:3 polymer and solvent ratio)	15	22	35

SEM images of the resulting fibres showed that their morphology had improved dramatically. Figure 5-2 shows the images obtained for the two electrospun samples. For the sample that was obtained from electrospinning the solution with a flow rate of $7 \mu\text{l min}^{-1}$, the average fibre diameter was $928 \pm 194 \text{ nm}$. This figure increased to $1.498 \pm 242 \mu\text{m}$ for the fibres obtained with a flow rate of $15 \mu\text{l min}^{-1}$. In comparison with the fibres that had been obtained from the 20 wt% PVDF in DMF solutions, these had very uniform diameter for every single strand and beads were virtually non-existent. Another remarkable finding was how doubling up the flow rate resulted in the average diameter for the fibres increasing almost 1.61 times the one observed for a lower flow rate of $7 \mu\text{l min}^{-1}$. In the previous chapter, it was observed how varying WD and voltage allowed the electrospun product to transition from being predominantly composed of agglomerates to a greater presence of fibres. However, the results discussed in the previous chapter deal with the coarse aspect of the influence that working parameters have on the morphology of the resulting fibres. In contrast, the resulting fibre mats shown in figure 5.2 illustrate the finer details that can be adjusted by slight changes in the electrospinning parameters.

The same solution was electrospun with the same electrospinning setup but under a different set of conditions in order to observe and confirm the observations obtained from the previous

trials. For this series of experiments, the working distance was kept at 35 cm. Table 5-2 summarises the conditions used for each experiment. The Taylor cone forming at the needle tip had been observed to be very stable in the previous set of experiments for a broad range of voltages for both working distances of 30 and 35 cm, ranging from as low as 11 kV up to 22 kV. Thus, trying out different voltages for constant flow rates and WDs could potentially allow for the identification of the most favourable conditions for the formation of the PVDF/PEO fibres. SEM images of the resulting fibre mats are shown in Figure 5-3.

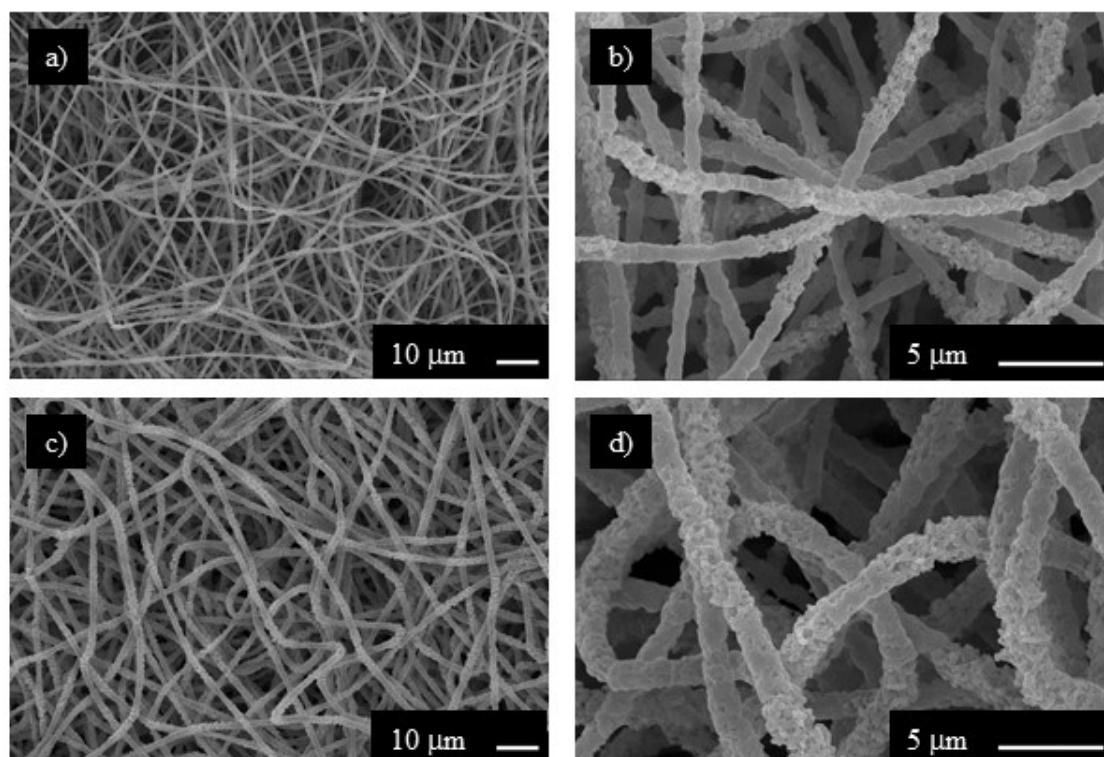


Figure 5-2: SEM images of the fibre mats obtained from electrospinning 10 wt% PVDF/PEO in DMF/water (50:3 ratios for both solvents and polymers) solutions. $T=22\text{ }^{\circ}\text{C}$, $\text{RH}\% = 42$. (a) Fibres obtained with the following conditions: $7\text{ }\mu\text{L min}^{-1}$ FR, 17 kV, 30 cm WD. (b) Same as (a), magnified image. (c) Fibres obtained with the following conditions: $15\text{ }\mu\text{L min}^{-1}$ FR, 22 kV, 35 cm WD. (d) Same as (c), magnified image.

Table 5-2: Electrospinning parameters used for fabricating 10 wt% PVDF/PEO fibre mats using the nozzle-based setup. $T=21.8\text{ }^{\circ}\text{C}$, WD 35 cm.

Solution	Sample	FR ($\mu\text{L min}^{-1}$)	Voltage (kV)	RH%
10 wt% PVDF/PEO in DMF/Water	A	7	17	35
	B	7	14	33
	C	7	11	33

(50:3 ratio for both solvents and polymers)	D	15	20	33
	E	25	20	33
	F	25	15	31

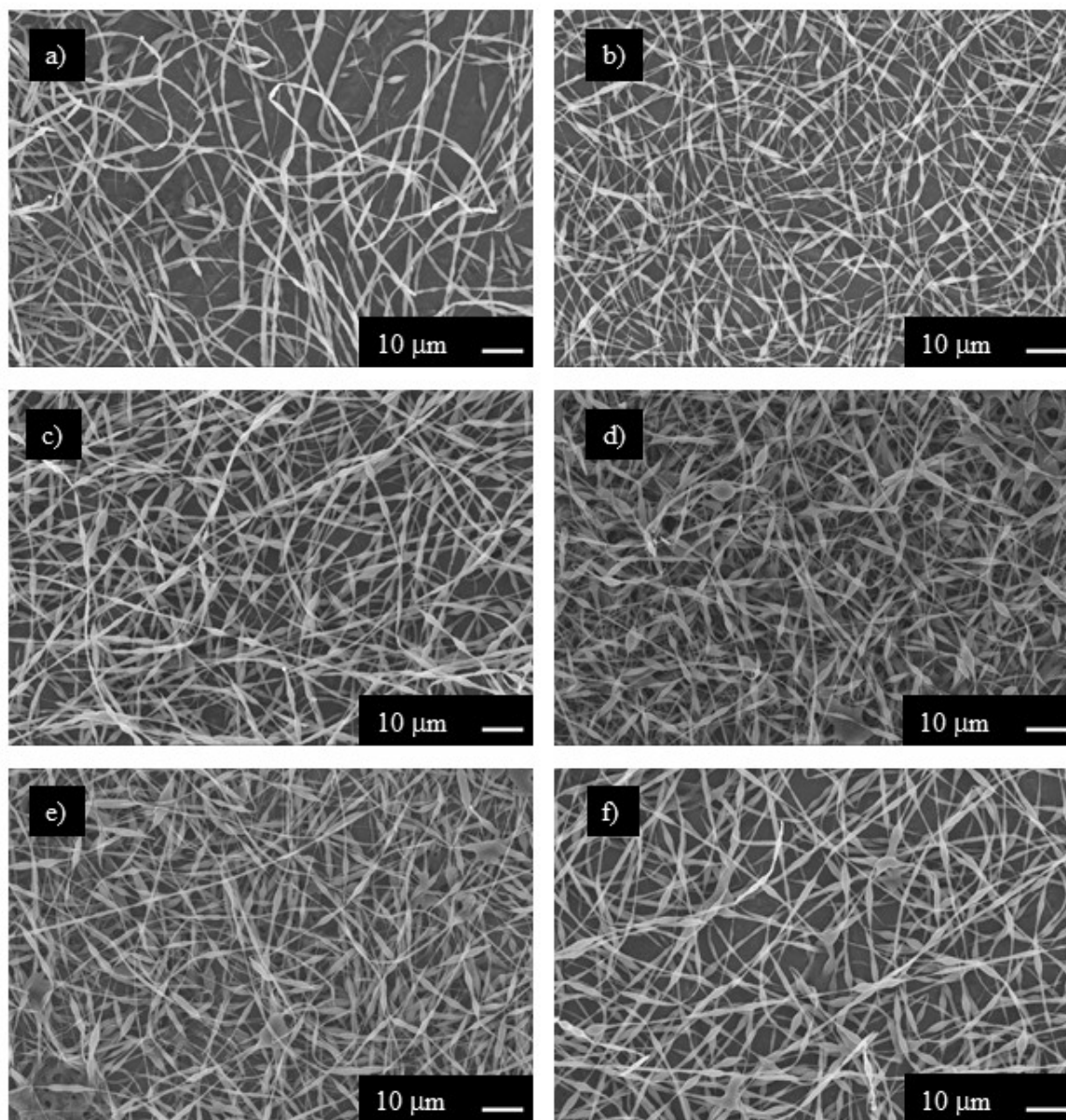


Figure 5-3: SEM images of the fibre mats obtained from electrospinning 10 wt% PVDF/PEO in DMF/water (50:3 ratios for both solvents and polymers) solutions. Temperature and WD were kept constant at 21.8 °C and 35 cm respectively. Fibres obtained with the following conditions: (a) 7 $\mu\text{l min}^{-1}$ FR, 17 kV, 35% RH. (b) 7 $\mu\text{l min}^{-1}$ FR, 14 kV, 33% RH. (c) 7 $\mu\text{l min}^{-1}$ FR, 11 kV, 33% RH. (d) 15 $\mu\text{l min}^{-1}$ FR, 20 kV, 33% RH. (e) 25 $\mu\text{l min}^{-1}$ FR, 20 kV, 33% RH. (f) 25 $\mu\text{l min}^{-1}$ FR, 15 kV, 31% RH.

The SEM images from figure 5.3 show that all fibres had thicker regions scattered along the length of each individual fibre. This dumbbell-like morphology can be explained by the lower voltage for some cases and the increased flow rate used for some of the others [6]. The fibres shown in figure 5-3a, b and c had the same FR of $7 \mu\text{l min}^{-1}$, but had voltages of 17, 14 and 11 kV respectively. The fibres shown in 5-3a appear to be thinner than those in either b or c, with the dumbbell shape being less pronounced. For the sample shown in 5-3 d, which was electrospun at $15 \mu\text{l min}^{-1}$ and a voltage of 20 kV, and for those shown in 5-3 e and f, for which the FR was $25 \mu\text{l min}^{-1}$, the difference in the diameter of the thicker sections to the thin ones appears to be larger. These were all measured for each of the samples shown in figure 5-3. The results are shown in Table 5-3.

Table 5-3: Average fibre diameter measured for the thick and thin regions for the electrospun 10 wt% PVDF/PEO in DMF/water (50:3 solvent and polymer ratio) fibre mats. The ratio of the averages is included.

Sample	Thick regions		Thin regions		Thin region average to thick region average ratio
	Average (μm)	SD (μm)	Average (μm)	SD (μm)	
A	1.14	0.196	0.834	0.172	0.73
B	1.378	0.293	0.787	0.174	0.57
C	1.639	0.342	0.929	0.198	0.57
D	1.65	0.50	0.833	0.252	0.50
E	1.547	0.451	0.909	0.288	0.59
F	1.81	0.366	0.984	0.257	0.54

The thin-to-thick region ratios shown in table 5-3 indicate that electrospinning parameters which include a lower FR and higher voltage values allow for the fabrication of more uniform PVDF/PEO fibres. Taking the results observed for sample A for this trial ($7 \mu\text{l min}^{-1}$ FR, 17 kV, 35% RH, 35 cm WD) and comparing them with those shown in figure 5-2a ($7 \mu\text{l min}^{-1}$ FR, 17 kV, 42% RH, 30 cm WD), it is possible to appreciate the effect that voltage and RH% had on the morphology of the resulting fibres. Since the WD was 5 cm shorter for one of the experiments, the influence of the 17 kV applied was stronger for that experiment, which resulted in a more uniform product. As shown from the rest of the experiments in this trial, higher FRs coupled with lower voltages resulted in beaded fibres. The results obtained are congruent with what has been explored in general for other polymer solutions [6].

The more favourable conditions for electrospinning bead-free PVDF/PEO fibre mats had been identified. The next step was to use additives with the solutions in order to promote the transition from flat fibre mats to 3D structures, and for enhancing the piezoelectric properties of the material. The 10 wt% PVDF/PEO in DMF/water (50:3 ratio for both polymers and solvents) solution was enhanced with 0.75 or 1.0 wt% LiCl. Additionally, a 12 wt% variant was added to the experimental efforts. The 12 and 10 wt% solutions with added 0.75 wt% LiCl were used in both the nozzle-free and nozzle-based electrosp spinners. Initial trials in the nozzle-based electrosp spinner required further adjustment of the WD, FR, and voltage conditions since the addition of LiCl had resulted in an increased solution conductivity and had made the solutions susceptible to gelating and precipitating.

On one hand, the high electric field needed for electrospinning is known to facilitate the transition of other PVDF crystal phases into the β -phase. The increased solution conductivity could thus be allowing for the resulting products to have an increased β -phase content. Additionally, the addition of LiCl influenced charge distribution on the fibres as they were being ejected and then deposited on the rotating collector. A higher number of free ions in the solution facilitated the 3D build-up process by increasing the strength of local repulsion and attraction events between individual fibres, indicating a greater influence of the electric field on the solution. The enhanced susceptibility of the solution to the electric field is equivalent to ramping up the working voltage of the electrospinning setup, thus facilitating the transition of other domains to the β -phase while also affecting the shape of the final product as it deposits on the collector. On the other hand, the addition of LiCl causes the solution to gelate, which may compromise the integrity of the resulting structures [7]. If the solutions were left at room temperature for more than a couple of hours after having added the LiCl, these would slowly become a gel-like substance that was not compatible with the process of electrospinning. Placing these solutions in a hot magnetic stirring plate would reverse this process, allowing the solution to be used for electrospinning once again.

When attempting to electrospin the 10 wt% solutions with 1 wt% added LiCl, the solution would slowly gelate as the process carried on, which resulted in the nozzle-based often being clogged. However, the product obtained resembled a 3D fibrous structure. One of the earliest samples is shown in Figure 5-4. The one parameter that had changed the most at this stage was WD, since no Taylor cone had been observed for distances greater than 15 cm when using the solutions with added LiCl. The nozzle-based setup allows for a maximum of 25 kV to be used; this would limit the ranges of WDs that would work in this experiment since aiming for a greater WD would require the voltage to be ramped up for the formation of a stable Taylor

cone, and this voltage value might be well beyond the 25 kV limit. The parameters used in this experiment were $12 \mu\text{l min}^{-1}$ FR, 16 kV, 8 cm WD. The ambient conditions recorded were a temperature of 16.8°C and 61% RH.



Figure 5-4: 3D structure obtained from electrospinning a 10 wt% PVDF/PEO in DMF/water (50:3 ratios) with 1 wt% added LiCl solution. The parameters used for this experiment were: $12 \mu\text{l min}^{-1}$ FR, 16 kV, 61% RH and an 8 cm WD.

The resulting PVDF/PEO fibre product transitioned from a flat mat into a 3D structure for both salt concentrations. The resulting 3D structures obtained from operating the nozzle-based device for 10 minutes resembled cotton balls or clouds, weighing on average 57.5 mg, having a thickness of 1.2 cm and an area of 5 cm^2 . Figure 5-5 shows a macroscopic image of the resulting 3D structures.

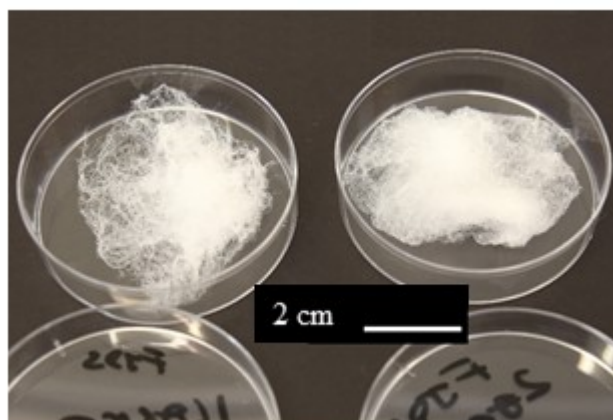


Figure 5-5: Cloud-like structures obtained from electrospinning PVDF/PEO in DMF/water (50:3 ratio) solutions. On the left, samples obtained when adding 0.75 wt% LiCl. On the right, 1 wt% added LiCl.

Figure 5-6 shows SEM images obtained for the sample that had 0.75 wt% added LiCl. The SEM images reveal that the morphology of the fibres was not negatively affected by the LiCl, and no bead formation occurred. The average fibre diameter for the sample enriched with 0.75 wt% LiCl was 819 ± 193 nm.

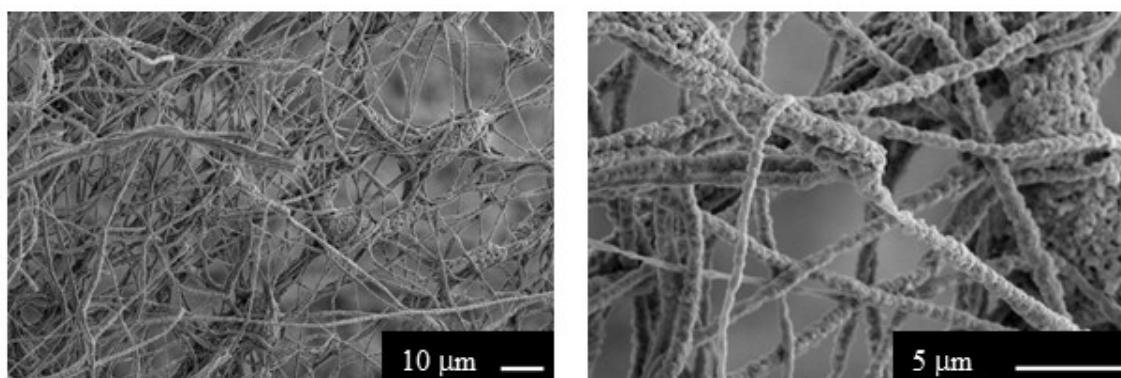


Figure 5-6: SEM images of the 3D cloud-like structures obtained from electrospinning the 10 wt% PVDF/PEO in DMF/water (50:3 ratios) with added 0.75 wt% LiCl.

The same solutions were used with the nozzle-free setup. The product obtained from operating the nozzle-free setup for 15 minutes resembled a sponge-like mat, weighing on average 2.8 g, being 28 cm wide, 19 cm long, with thicknesses ranging from over 0.4 to 0.72 mm. Figure 5.7 shows a macroscopic view of the product width, length and thickness for a 12 wt% PVDF/PEO in DMF/water with added 0.75 wt% LiCl sample. SEM images for these samples are shown in Figure 5-8. Compared to the fibres obtained from the nozzle-based setup, these had comparatively higher average diameters. These are listed in Table 5-4. As observed in this table, higher polymer concentration and higher salt content were observed as

conditions that favoured the formation of thicker fibres. This is also true for other commonly used polymers.

Table 5-4: Average fibre diameter for the samples obtained from the nozzle-free electrospinner.

Solution	Average fibre diameter (μm)	SD (μm)
10 wt% PVDF/PEO, 0.75 wt% LiCl	1.173	0.256
10 wt% PVDF/PEO, 1 wt% LiCl	1.635	0.307
12 wt% PVDF/PEO, 0.75 wt% LiCl	1.236	0.351
12 wt% PVDF/PEO, 1 wt% LiCl	1.926	0.41

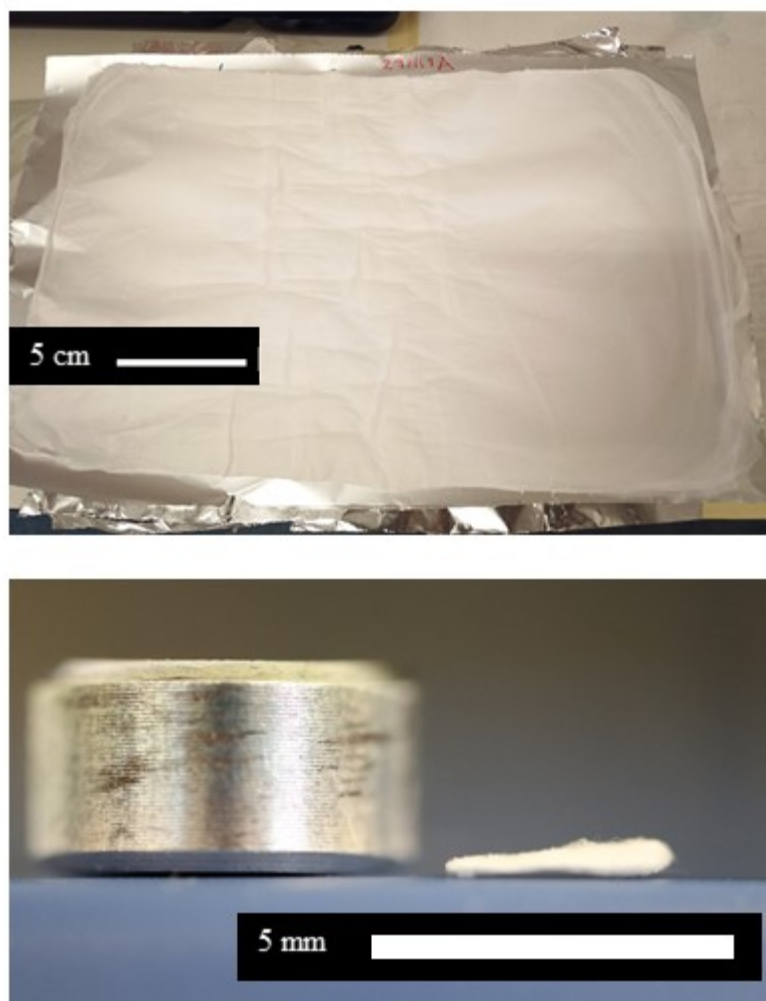


Figure 5-7: Thick sponge-like sample obtained from electrospinning a 12 wt% PVDF/PEO in DMF/water with added 0.75 wt% LiCl solution.

Electrospinning in similar conditions as those used previously for the PVDF/PEO solution with the nozzle-free device was carried out with solutions containing PVDF-TrFE instead of PVDF.

The PVDF-TrFE to PEO and DMF to water ratios were kept as 50:3, and identical working voltage and ambient conditions were used for the experiment. The final product resembles that from figure 5-7, and 3D build-up was observed to start immediately after initiating electrospinning. Table 5-5 lists the thicknesses of all the PVDF/PEO and PVDF-TrFE/PEO thick sponge-like mats obtained from this setup.

XRD analysis was carried out on the PVDF/PEO samples to evaluate changes in the crystalline phase composition of the sample. The results, shown in Figure 5-9, showed slight differences when compared with a reference pristine PVDF pattern [8]. The blue curve is that one obtained from the 1 wt% LiCl 12 wt% PVDF/PEO electrospun sample. The black curve corresponds to that one obtained from the 0.75 wt% LiCl 12 wt% PVDF/PEO sample. However, the differences are not clear enough to assure that the β -phase content in the samples has become significantly greater than that of pristine PVDF because of the addition of the salts. However, the addition of the salts did result in the electrospun product transitioning from flat fibre mats into 3D structures, something that could be advantageous for implementing mechanical energy harvesters as discussed in chapter 2, section 2.2.4.

Table 5-5: Thickness measurements of the electrospun thick sponge-like product obtained with the nozzle-free setup. All samples were obtained after electrospinning for 15 minutes.

Polymer concentration	Added LiCl (wt%)	Thickness (mm)
10 wt% PVDF/PEO	<i>0.75</i>	<i>0.474</i>
10 wt% PVDF/PEO	<i>1.0</i>	<i>0.550</i>
12 wt% PVDF/PEO	<i>0.75</i>	<i>0.689</i>
12 wt% PVDF/PEO	<i>1.0</i>	<i>0.723</i>
12 wt% PVDF-TrFE/PEO	<i>0.75</i>	<i>0.731</i>

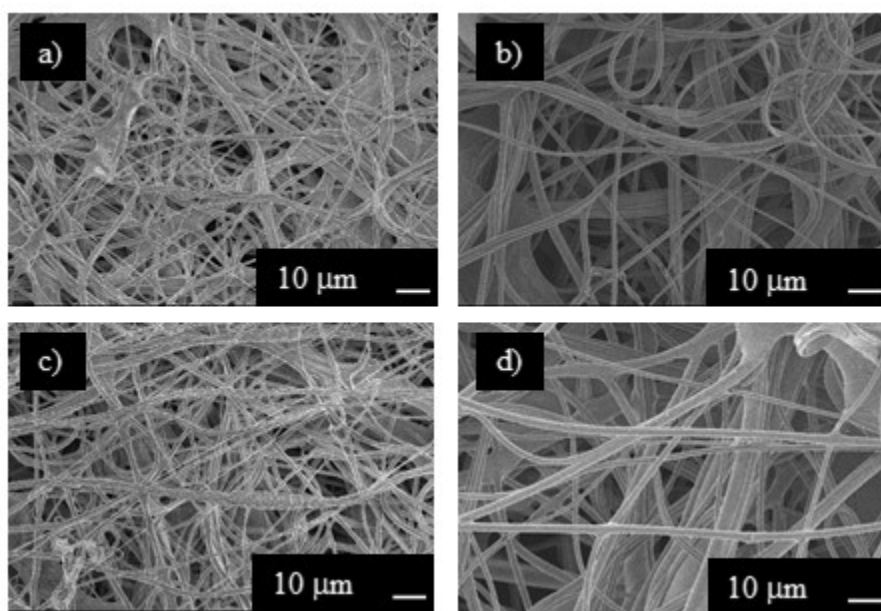


Figure 5-8: SEM images for the thick sponge-like PVDF/PEO fibre mats. (a) 10 wt% polymer concentration, 0.75 wt% LiCl. (b) 10 wt% polymer concentration, 1 wt% LiCl. (c) 12 wt% polymer concentration, 0.75 wt% LiCl. (d) 12 wt% polymer concentration, 1 wt% LiCl

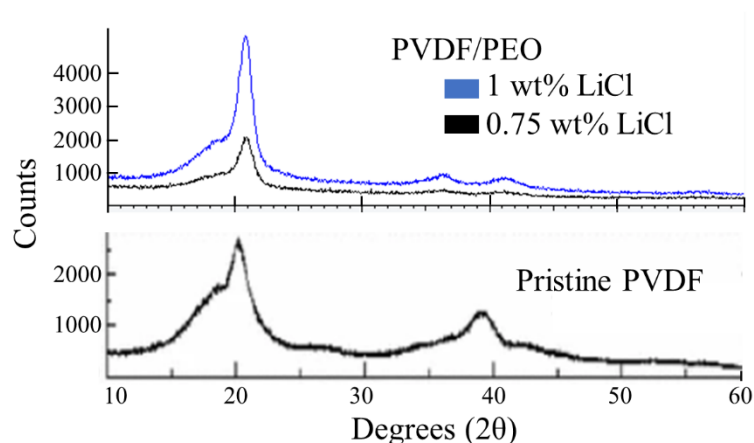


Figure 5-9: XRD pattern obtained from scanning two PVDF/PEO sponge like samples, each one with different added salt concentrations of 0.75 wt% (black) and 1 wt% (blue). Pristine PVDF pattern was adapted from [8].

The formation of 3D structures could be partially explained by the effect that adding salts has on the solution's properties. The addition of salts caused the conductivity of the solutions to increase. Solutions containing only PVDF or PVDF/PEO and their respective solvents had conductivity values between 2 and 4 $\mu\text{S cm}^{-1}$, while those with added salts had 1000 times

those figures. These are shown in Table 5-6. Increasing solution conductivity is one of many factors that facilitate the formation of Taylor cones on the surface of the drum immersed in the solution bath [9].

Table 5-6: Measured solution conductivity changes under different polymer and added LiCl salt concentrations.

Solution characteristics	Solution conductivity ($\mu\text{S cm}^{-1}$)
15 wt% PVDF in DMF	3.56
20 wt% PVDF in DMF	3.61
10 wt% PVDF/PEO in DMF/Water	3.05
10 wt% PVDF/PEO in DMF/Water/Acetone	2.35
10 wt% PVDF-TrFE/PEO in DMF/Water, 0.75 wt% added LiCl	3240
12 wt% PVDF-TrFE/PEO in DMF/Water, 0.75 wt% added LiCl	3070
12 wt% PVDF-TrFE/PEO in DMF/Water, 1 wt% added LiCl	3580

The presence of PEO might also play a fundamental role in the formation of 3D structures. Electrospinning a solution with only PVDF-TrFE, DMF and 0.75 wt% LiCl yielded a flat product. Adding PEO, water, and adjusting both the polymer and solvent ratio to 100:3 for both resulted in an observable initiation of 3D build-up when initiating electrospinning, although this was weak and yielded only a very thin layer of fibres. Increasing the PEO and water content so that the ratios were 50:3 resulted in an almost immediate fibre build-up on the collector after initiating electrospinning, indicating that PEO also plays a critical role in facilitating the 3D build-up process.

Temperature control during the electrospinning process was critical for facilitating the transition from a flat end-product to the sponge-like mats and improving the quality of the 3D structures. Keeping the chamber temperature at 33 °C and preheating the drum and solution bath to that target temperature ensured that the solution would not gelate during electrospinning.

5.2.2 Electrospun 3D structures as active cores for the generators

The electrospun products obtained from the previous experiments were used for assembling piezoelectric generators. For comparison purposes, the materials used as active cores were PVDF flat mats, thick sponge-like PVDF/PEO, and PVDF-TrFE/PEO fibre mats. The generator design consists of 1 cm² square shaped strips fitted with copper foil electrodes, all encapsulated in PDMS. The electrodes were placed at opposite ends along the length of the active material. PDMS encapsulation allows for the fabrication of soft, flexible generators, and protects the active core material from severe wear and tear damage. The generator assembly method is illustrated in Figure 5-10. Evaluating the response of the generators over a broad range of resistive loads allows for the characterization of essential parameters required for assessing their performance. The output voltages and currents observed when the samples were subjected to a series of continuous mechanical impacts were recorded for varying resistive loads (10, 100 k, 1.6 M and 15.1 M Ω). The forces exerted on the generators were monitored with a force sensitive resistor (FSR).

The experimental trial was carried out for three generator families grouped by active core material. These were PVDF flat mat, PVDF/PEO thick fibre mats or PVDF-TrFE/PEO thick fibre mat core generators. Several recordings spanning two seconds per generator family were taken for each resistive load value. The intended testing impact frequency was 4 Hz. Table 5-7 summarizes the key output figures obtained for the best performing generator of each core material family when the resistive load was 15.1 M Ω .

Table 5-7: Electrical response of the best performing generators per core material family when subjected to continuous mechanical impacts. Recordings obtained for the maximum electrical load (15.1 M Ω). Average impact force recorded for each sample is also shown.

Best performing samples		15.1 M Ω resistive load		
Core		PVDF	PVDF/PEO	PVDF-TrFE/PEO
V_{PP} (V)		6.42 \pm 1.01	22.65 \pm 2.55	38.28 \pm 3.26
I_{PP} (μ A)		0.43 \pm 0.07	1.54 \pm 0.17	2.57 \pm 0.22
Impact force (N)		0.1 \pm 0.04	0.17 \pm 0.06	0.25 \pm 0.05
Instantaneous output power (μ W cm $^{-2}$)		1.35 \pm 0.7	13.8 \pm 2.5	45.5 \pm 8.82

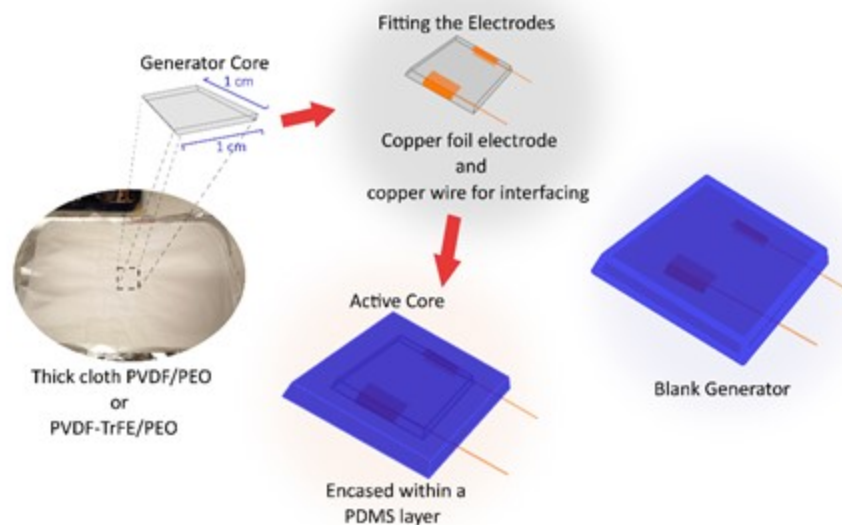


Figure 5-10: Schematic diagram showing the method used for assembling the generators used for evaluating the electrical response of various PVDF fibrous mats.

The I_{SC} of the generators was obtained from recording the I_{PP} observed when the resistive load was 10 Ω . The generators with a PVDF flat mat core had an I_{PP} of 290 ± 40 nA on average. For generators belonging to the PVDF/PEO and PVDF-TrFE/PEO core families, this average figure increased to 1.32 ± 0.38 and 1.95 ± 0.5 μ A, respectively. Increasing the resistive load resulted in the output voltage increasing as the current started to decrease. For all generators, the output V_{PP} for the 15.1 M Ω load increased dramatically. The best performing flat PVDF core generator had a V_{PP} figure of 6.4 ± 1.0 V. For the PVDF/PEO core generator, this figure

was 19.25 ± 1.42 V. The PVDF-TrFE/PEO core generator achieved up to 38.28 ± 3.26 V. Figure 5-11a shows a group of bar plots showing the average output V_{PP} for each generator when driving 100 k Ω , 1.6 M Ω and 15.1 M Ω resistive loads. Figure 5-11b shows a V_{PP} vs I_{PP} plot that includes all the data points captured only for the recordings taken when the resistive load was 15.1 M Ω . This figure shows a clear gap between the flat mat cores and the sponge-like mat cores, with the PVDF-TrFE having a stronger response. Figure 5-12a shows a detailed view of the output voltage waveform obtained from the PVDF/PEO generator, and figure 5-12b shows the same for the PVDF-TrFE/PEO generator. A detailed table containing the average key figures obtained per family for a broader range of resistive loads is shown in Table 5-8.

Table 5-8: Average electrical response parameters of the generators as a response to repeated mechanical impacts per resistive load for all three generator core families. The average forces recorded at impact are included for the higher resistive loads.

Core material	PVDF	PVDF/PEO	PVDF-TrFE/PEO
10 Ω resistive load			
I_{SC} (μA)	0.29 ± 0.04	1.32 ± 0.38	1.95 ± 0.53
100 kΩ resistive load			
V_{PP} (V)	0.035 ± 0.005	0.135 ± 0.039	0.203 ± 0.047
I_{PP} (μA)	0.34 ± 0.05	1.39 ± 0.4	2.05 ± 0.46
Instantaneous output power (μW cm⁻²)	0.0064 ± 0.0021	0.11 ± 0.07	0.21 ± 0.09
Impact force (N)	0.125 ± 0.069	0.268 ± 0.142	0.38 ± 0.257
1.6 MΩ resistive load			
V_{PP} (V)	0.65 ± 0.13	2.18 ± 0.56	3.2 ± 0.8
I_{PP} (μA)	0.39 ± 0.07	1.4 ± 0.36	2.02 ± 0.5
Instantaneous output power (μW cm⁻²)	0.065 ± 0.006	1.73 ± 0.99	3.42 ± 1.61
Impact force (N)	0.118 ± 0.047	0.278 ± 0.127	0.35 ± 0.2
15.1 MΩ resistive load			
V_{PP} (V)	5.76 ± 1.2	18.53 ± 4.49	29.5 ± 6.8
I_{PP} (μA)	0.37 ± 0.085	1.26 ± 0.3	1.99 ± 0.45

Instantaneous			
output power ($\mu\text{W cm}^{-2}$)	1.03 ± 0.51	12.36 ± 6.14	31.83 ± 14.75
Impact force (N)	0.15 ± 0.07	0.262 ± 0.12	$0.35. \pm 0.21$

Instantaneous output power was calculated by multiplying the individual maximum single-ended voltage and its corresponding single-ended current value for each mechanical impact. For all generators, the peak output power was observed to occur at higher resistive loads. As described in Table 5-7, the average instantaneous output power figures on the 15.1 M Ω load, approach the tens of μW for the best performing PVDF/PEO and PVDF-TrFE/PEO core samples. Remembering that all generators were designed as having an active area equivalent to 1 cm^2 , all the instantaneous power values are given as $\mu\text{W cm}^{-2}$. The instantaneous power value calculated for the best performing flat PVDF generator was $1.35 \pm 0.7 \mu\text{W cm}^{-2}$. In comparison, the best performing PVDF/PEO generator yielded $17.9 \pm 3.7 \mu\text{W cm}^{-2}$, corresponding to 13.3 times that observed for the PVDF generator. The best performing PVDF-TrFE/PEO generator achieved 34 times the value observed for the flat PVDF generator, having yielded $45.5 \pm 8.82 \mu\text{W cm}^{-2}$.

The observed response of the fabricated generators shows that both sponge-like PVDF/PEO and PVDF-TrFE/PEO cores perform better than flat PVDF mat cores in terms of output V_{PP} , I_{PP} , and instantaneous output power. The greatest increase was observed when the generators were driving the 15.1 M Ω load. The electrical output characteristics of any power source encompass a range that begins with the short circuit point, on which the load resistance is theoretically zero, thus resulting in the output current being at its maximum possible value while the output voltage is zero. On the other end of the spectrum, there is the open circuit voltage point, on which the load resistance is infinite, causing output current to be zero, and maximizing the output voltage. Since the output power is nothing more than the current and voltage product, these points represent the lowest possible power outputs. The maximum occurs somewhere in between; to be precise, it occurs at the resistive load value that is identical to the internal equivalent resistance of the driving source. Since the output power kept increasing with increasing resistive load values, there must exist a higher resistive load value for which the PVDF/PEO and PVDF-TrFE/PEO generators can source an output power figure of greater magnitude. This implies that, for instance, it is perfectly possible to use specialized impedance matching instrumentation for optimizing load conditions and extracting the maximum power deliverable by the generators.

Given that the electrical outputs of piezoelectric energy harvesters are AC signals, additional instrumentation is required for converting it to a DC signal and for its storage. To evaluate the response of the best performing thick sponge-like cores in the context of an AC to DC conversion and storage stage, the generators were connected to a full bridge rectifier with a capacitive load, valued either 1, 4.7 or 10 μF . The voltage charging curves were observed as the generators received repeated mechanical impacts over a period of 100 seconds per recording. Mechanical impact frequency was set to 4 Hz. Figure 5-11c shows the charging curves recorded for each capacitor by the different generators. The charging curve for the 1 μF capacitor starts plateauing at 3.7 V well before reaching the 100-second mark when using the PVDF-TrFE/PEO core generator, indicating that maximum charge was almost achieved. The PVDF/PEO generator did not manage to reach a similar stage, appearing to plateau at 2.5 V. For the 4.7 and 10 μF capacitors, the charging curves show no indication of reaching a state where the voltage starts to plateau. However, these curves demonstrate that the PVDF-TrFE core generator can supply greater amounts of charge to the capacitors and achieve full charge in a short time window for smaller capacitive loads.

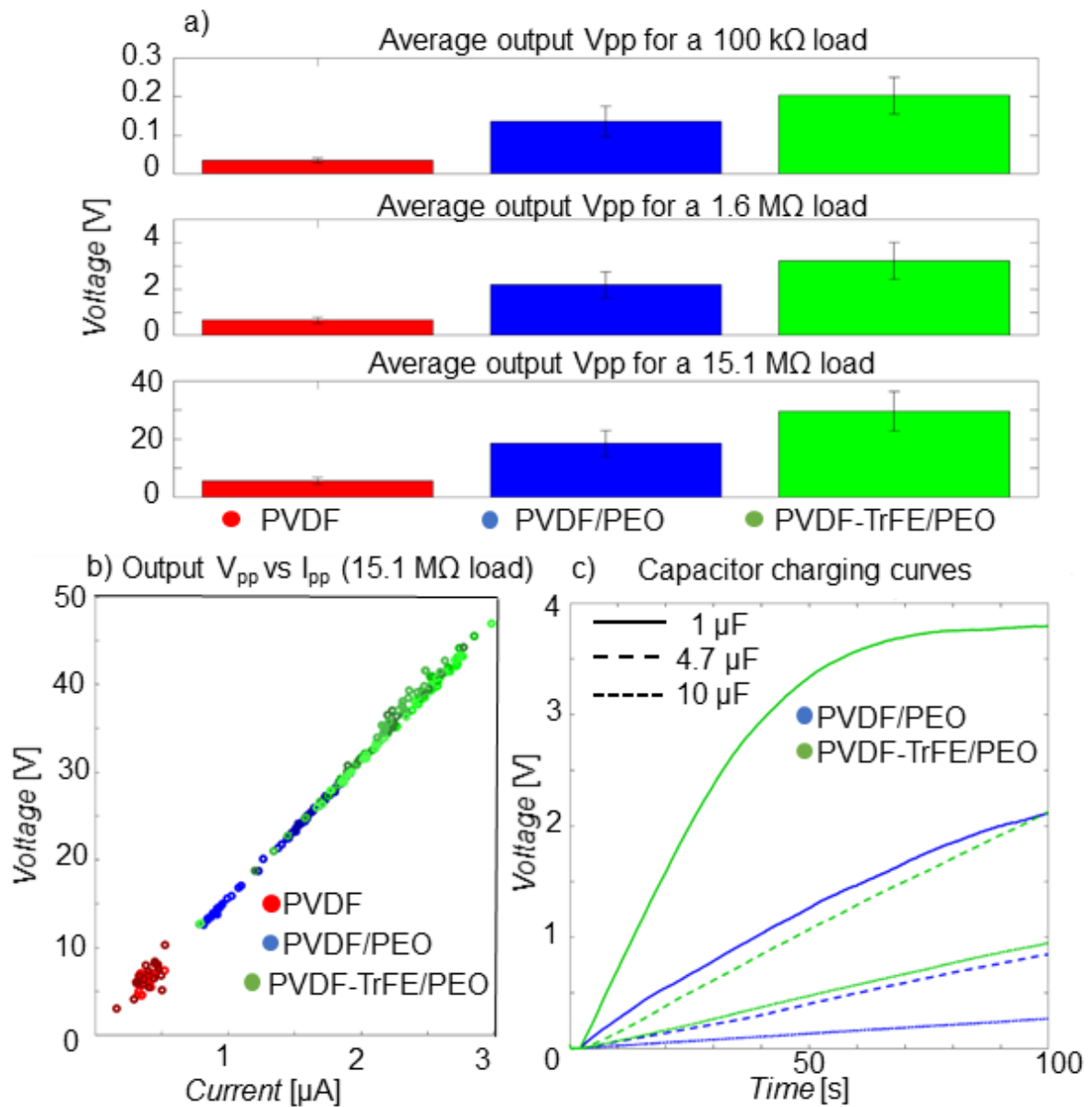


Figure 5-11: The output voltage and current figures obtained when recording the electrical response of 3 different types of generators when subjected to a 4 Hz mechanical impact. PVDF flat mat cores are shown in red. PVDF/PEO core are shown in blue and those with a PVDF-TrFE core are shown in green. (a) Bar plots showing the average V_{pp} for the three generator families when connected to 100 k, 1.6 M and 15.1 M Ω resistive loads. (b) V_{pp} vs I_{pp} scatter plot of all the recorded impacts, colour coded for a 15.1 M Ω resistive load. (c) Capacitor charging curves for the best performing PVDF/PEO and PVDF-TrFE/PEO generators. Three different capacitors were connected as the loads of a full-wave bridge rectifier driven by the generators.

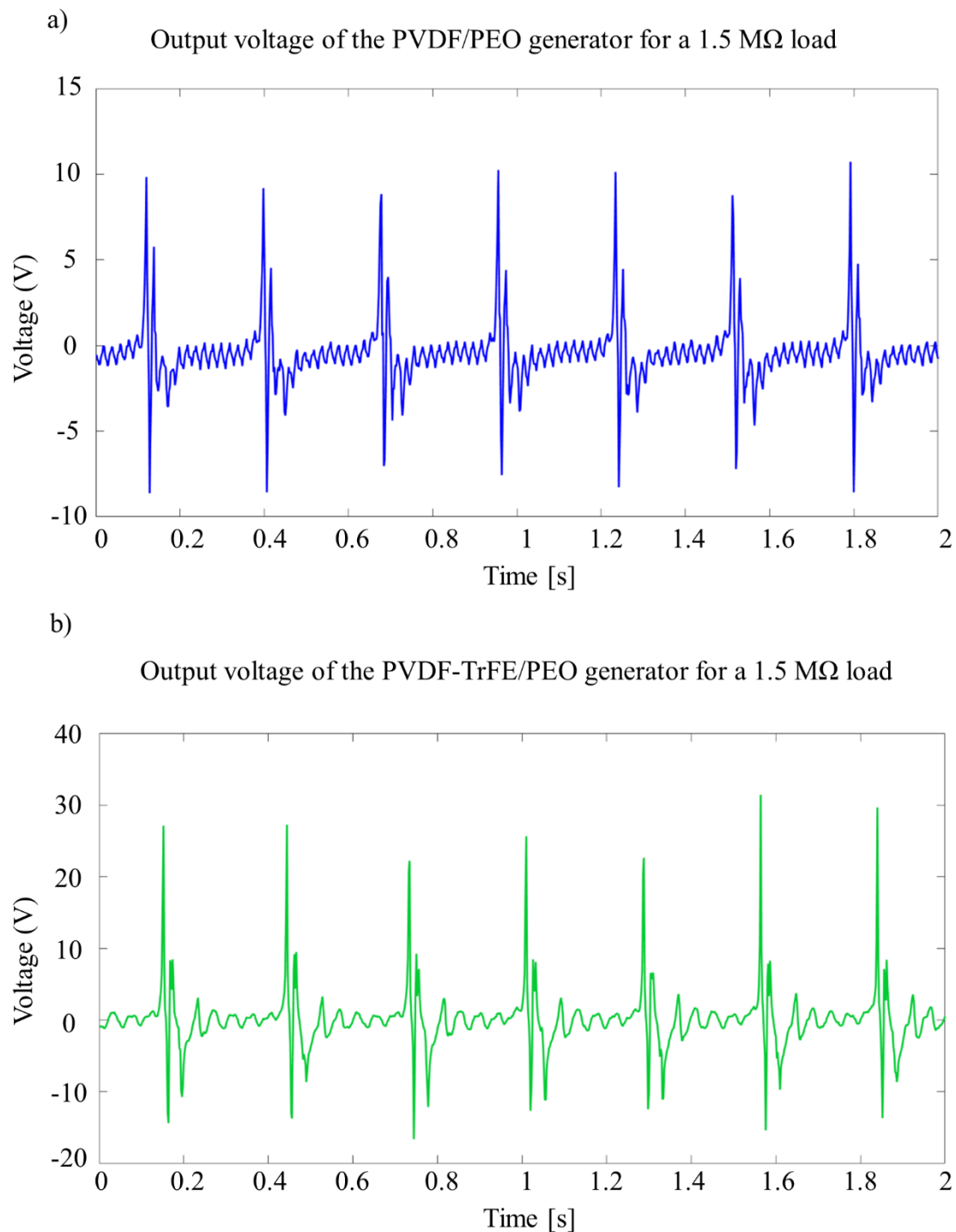


Figure 5-12: Detailed view of the output voltage signals recorded when subjecting generators to repeated mechanical impacts with a frequency of 4 Hz and when the resistive load of the system was $1.5 \text{ M}\Omega$. (a) Response for the PVDF/PEO generator. (b) Response for the PVDF-TrFE/PEO generator.

5.2.3 Extended cyclic mechanical impact test

The best-performing generator from the PVDF/PEO and PVDF-TrFE/PEO groups were subjected to 500 seconds of continuous mechanical impacts for evaluating response degradation due to wear and tear. The most through degradation or wear and tear testing usually involves exposing the generators to impact frequencies over 5 Hz for periods of up to 36 hours [10, 11]. However, several studies use relatively lower time period and impact frequency settings to observe and assess the degradation of the durability of their generators. Some common proposed figures aim for a time period of 1000 seconds of continuous impacts, while others aim for at least 1000 continuous impacts. For instance, selecting settings such as impact frequencies of 0.5 Hz for a period of 100 minutes would yield around 3000 impact events in total [12–15]. Taking into account the limitations of the cyclic mechanical impact device, which can in theory operate for long periods of time but may drift away from the sample after several hundreds of impacts have been delivered, a time window of 500 seconds and an impact frequency of 4 Hz were selected. These settings would allow for the recording of at most 2000 impacts, which would allow for assessing the durability of the samples in similar conditions to those outlined in other studies.

A blank generator consisting of a pair of PDMS encapsulated copper foil electrodes of similar area and placement to those from the other generators but with no an active core was tested under similar conditions. The addition of the blank generator allowed for the evaluation of the nature and magnitude of any residual signals that may arise from the interaction between the copper electrodes and the PDMS, thus revealing the magnitude of the signal arising exclusively from the mechanical deformation of the active core. The signal recorded from testing the blank generator was subtracted from the raw signal obtained from the active cores. As in the previous experiment, the impact frequency was 4 Hz. The recordings corresponded only to the output V_{pp} when the resistive load was 15.1 M Ω . Figure 5-13a shows the recorded raw signal, its average value calculated for all the registered V_{pp} values, and the individual V_{pp} values for each impact. As seen in this figure, the electrical response did not decay even after the generators sustained more than 1800 consecutive impacts, indicating stability and resistance to wear and tear. Figure 5-13b and 5-13c map the V_{pp} values after data processing and its corresponding impact force for the PVDF/PEO and PVDF-TrFE/PEO generators, respectively. Figure 5-13d and 5-13e show histograms of their respective output V_{pp} . Table 5-9 summarizes the key information of this experiment.

Table 5-9: Summary of the data gathered from recordings obtained from the best performing generators under continuous mechanical impacts (observed testing frequency was 3.6 Hz)

	PVDF/PEO core	PVDF-TrFE/PEO core
Number of detected impacts	1856	1850
Average Raw Vpp (V)	24.29±3.17	68.32±6.40
Average Vpp attributed to the active core (V)	21.29±3.17	65.32±6.4
Average impact force (N)	1.04±0.24	1.68±0.45

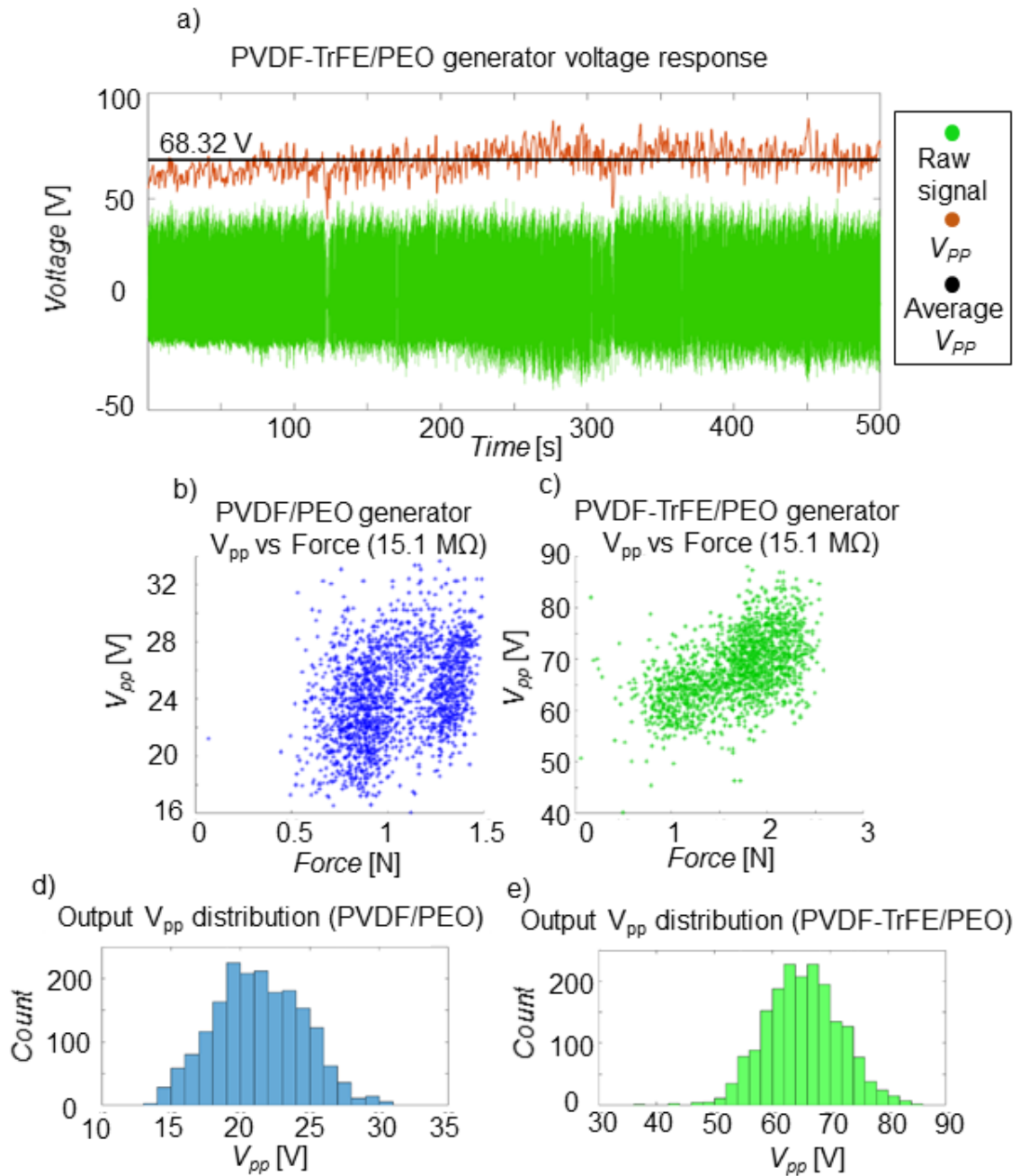


Figure 5-13: Response of the best performing PVDF/PEO and PVDF-TrFE/PEO generators under a constant mechanical impacts (4Hz) over a window of 500 seconds. Over 1800 impact points were recorded for each generator. (a) Signal obtained from a blank generator (no core). (b) Recorded raw V_{pp} signal for the PVDF-TrFE/PEO generator, formed by the superposition of the response by the core material and that purely attributed to the electrode-PDMS interface. All the following sub-figures reflect only the part of the signal attributed to the core material. (c) Scatter plot of the V_{pp} values vs the estimated impact force for the PVDF/PEO generator and a 15.1 M Ω load. (d) Scatter plot of the V_{pp} values vs the estimated impact force for the PVDF-TrFE/PEO generator and a 15.1

MΩ load. (e) Histogram showing the distribution of V_{pp} for all 1800+ data points for the PVDF/PEO generator. (f) Same as (e), but for the PVDF-TrFE/PEO generator.

5.2.4 Testing under real world conditions with a live test subject

An additional experiment was carried out to explore the output of the generator in conditions that would be more easily found in a real-life situation. A 63 kg test subject was asked to wear a flip flop that was fitted with a compound generator on its heel. The generator consisted of thirteen 1 cm^2 units connected in parallel and arranged in a diamond pattern. Figure 5-14 shows the modified flip flop and the generator design. The generator was connected to a full bridge rectifier which had a $1\text{ }\mu\text{F}$ or $4.7\text{ }\mu\text{F}$ capacitive load. A single pole double throw switch was used to allow for the capacitor to be toggled between charging mode and demonstration mode, which consisted of powering up an array of 40 LEDs in parallel. The test subject was instructed to march at different speeds for 100 seconds, having to step on the generator 50, 70, 95 or 115 times per minute for each trial. Figure 5-14b shows the implemented circuit and the lit up LEDs. Figure 5-13c and 5-13d show the charging curves observed for the 1 and $4.7\text{ }\mu\text{F}$ capacitive loads for the four different step frequencies. The resulting curves show that the $1\text{ }\mu\text{F}$ capacitor was charged to a much higher voltage than that observed for the one valued at $4.7\text{ }\mu\text{F}$, 15.31 V and 2.47 V , respectively, for the 115 steps per minute curves. No curve is shown to reach a state of plateauing during the 100 s time window, indicating that the capacitor can be further charged to a much higher value.

The capacitors used for the charging experiment shown in figure 5-13 were metalized polyester film capacitors instead of the electrolytic type used in the experiment shown in figure 5-11c. The differences in the maximum voltage achieved were expected to be relatively large because of a few different properties of these capacitors. The insulation resistance for the chosen polyester film capacitors is around $1000\text{ M}\Omega$, thus, being around four orders of magnitude larger than that of an electrolytic capacitor, which is around $1\text{ M}\Omega$. Thus, when connected to the polyester film capacitor, the effective load resistance seen by the generator increases. In the case of the circuit with the polyester film capacitor, the equivalent resistance seen by the generator is that of the capacitor's insulation resistance. As shown in table 5-7 and 5-8, increasing the resistive load results in a net increase in output power, at least until the maximum instantaneous output power is reached. Therefore, having an equivalent load resistance in the $1000\text{ M}\Omega$ range very likely results in the generator sourcing increased net output power. For the case of the electrolytic capacitor, the insulation resistance of this component is closer to the $1\text{ M}\Omega$ range, thus the generator can source less output power.

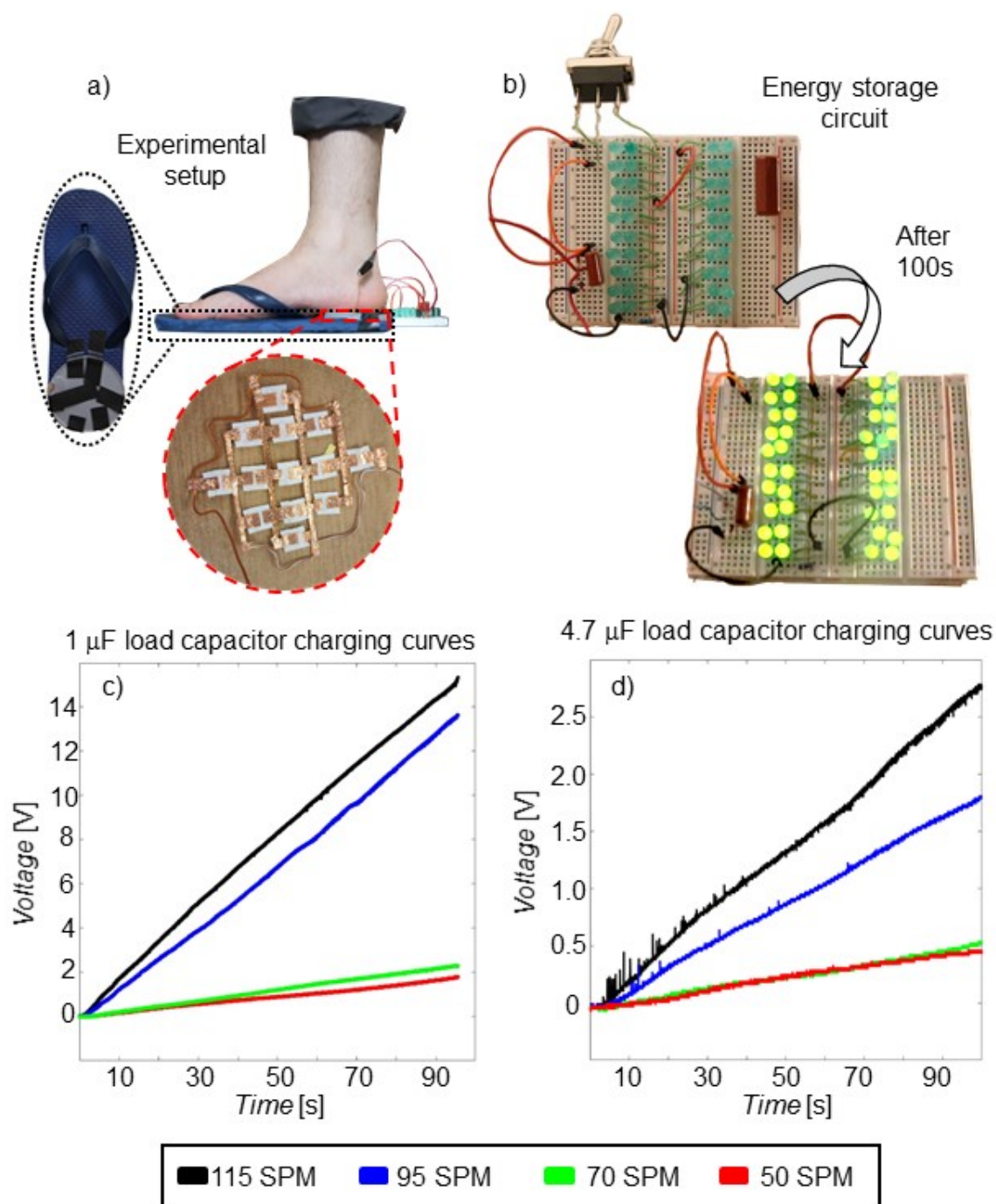


Figure 5-14: Experimental setup used to evaluate the performance of a compound PVDF-TrFE/PEO generator. A user was asked to step on the generator at 4 different steps per minute rates (SPM) for a period of 100 seconds. The generator was connected to a full wave rectifier with a 1 or 4.7 μF capacitive load. A switch allowed for the user to light up 40 LEDs in parallel after the 100 second charging period. (a) Bottom-up view of the testing scheme. A compound generator with 13 active PVDF-TrFE/PEO subunits was placed on the heel portion of a flip-flop. (b) Circuit used for rectifying the output signal of the

generator and for showing the harvested energy in action. (c) Charging curves obtained for the 1 μF load.

(d) Charging curves obtained for the 4.7 μF load.

5.3 Interim summary

The fabricated flexible, sponge-like, 3D structures offer several unique opportunities for developing mechanical energy harvesters. The proposed generator design achieved instantaneous output power figures that surpass those of other state-of-the-art PVDF-based generators. Table 5-10 lists the power output of these devices for comparison purposes. However, the output figures obtained with the PVDF/PEO and PVDF-TrFE/PEO materials can potentially be further improved by redesigning the electrodes.

Table 5-10: Output power figures of a broad spectrum of state-of-the-art fibre based energy harvesters with PVDF-based cores and those obtained from the generators presented in this chapter. The devices presented range from those relying on membranes and electrospun fibre mats to those which use complex composite materials.

Core material	Output power figure ($\mu\text{W cm}^{-2}$)	Reference
Electrospun PVDF nanofibres decorated with zinc oxide nanowires	0.078	[16]
Thin-film PVDF-TrFE	4.5	[17]
Composite PVDF and barium titanate	5.3	[18]
Sponge-like mesoporous PVDF	20	[19]
Patterned EHD pulling PVDF-TrFE	5	[20]
Electrospun porous PVDF-TrFE fibres	5.7	[21]
Composite PVDF-ZnO layered generator	16	[22]
Randomly oriented PVDF fibre generators	0.74	[23]
PVDF nanofibre generator with a ZnO/rGO nanofiller	74.6	[24]
Electrospun 3D PVDF-TrFE/PEO	45.5	This work

Under optimal conditions, electrospinning allowed for the successful fabrication of various types of 3D structures that can be used as the active core material of mechanical energy harvesters, and their electrical response was shown to be greater than that observed from various different types of polymer-based generators, even for those involving composites with ZnO, graphene oxide, and ceramics; the PVDF-TrFE/PEO structures achieved an estimated instantaneous peak power density figure of $45.5 \mu\text{W cm}^{-2}$ when subjected to a 0.25 N impact force. The fabricated 3D sponge-like structures show great promise as the core materials of portable generators.

5.4 References

- 1 Vong, M., Diaz Sanchez, F.J., Keirouz, A., Nuansing, W., Radacsi, N.: 'Ultrafast fabrication of Nanofiber-based 3D Macrostructures by 3D electrospinning' *Mater. Des.*, 2021, **208**, p. 109916.
- 2 Dhakras, D., Borkar, V., Ogale, S., Jog, J.: 'Enhanced piezoresponse of electrospun PVDF mats with a touch of nickel chloride hexahydrate salt' *Nanoscale*, 2012, **4**, (3), p. 752.
- 3 Waqas, M., Keirouz, A., Sanira Putri, M.K., *et al.*: 'Design and development of a nozzle-free electrospinning device for the high-throughput production of biomaterial nanofibers' *Med. Eng. Phys.*, 2021, **92**, p. 80–87.
- 4 Yang, Y., Centrone, A., Chen, L., Simeon, F., Alan Hatton, T., Rutledge, G.C.: 'Highly porous electrospun polyvinylidene fluoride (PVDF)-based carbon fiber' *Carbon N. Y.*, 2011, **49**, (11), p. 3395–3403.
- 5 Yazgan, G., Dmitriev, R.I., Tyagi, V., *et al.*: 'Steering surface topographies of electrospun fibers: Understanding the mechanisms' *Sci. Rep.*, 2017, **7**, (1).
- 6 Zuo, W., Zhu, M., Yang, W., Yu, H., Chen, Y., Zhang, Y.: 'Experimental study on relationship between jet instability and formation of beaded fibers during electrospinning' *Polym. Eng. Sci.*, 2005, **45**, (5), p. 704–709.
- 7 Lin, D.-J., Chang, C.-L., Huang, F.-M., Cheng, L.-P.: 'Effect of salt additive on the formation of microporous poly(vinylidene fluoride) membranes by phase inversion from LiClO₄/Water/DMF/PVDF system' *Polymer (Guildf)*, 2003, **44**, (2), p. 413–422.
- 8 Indolia, A.P., Gaur, M.S.: 'Investigation of structural and thermal characteristics of PVDF/ZnO nanocomposites' *J. Therm. Anal. Calorim.*, 2013, **113**, (2), p. 821–830.
- 9 Angammana, C.J., Jayaram, S.H.: 'Analysis of the effects of solution conductivity on electrospinning process and fiber morphology' *IEEE Trans. Ind. Appl.*, 2011, **47**, (3), p. 1109–1117.
- 10 Anwar, S., Hassanpour Amiri, M., Jiang, S., Abolhasani, M.M., Rocha, P.R.F., Asadi, K.: 'Piezoelectric Nylon-11 Fibers for Electronic Textiles, Energy Harvesting and Sensing' *Adv. Funct. Mater.*, 2021, **31**, (4), p. 2004326.
- 11 Lu, X., Qu, H., Skorobogatiy, M.: 'Piezoelectric Micro- and Nanostructured Fibers Fabricated from Thermoplastic Nanocomposites Using a Fiber Drawing Technique:

- Comparative Study and Potential Applications' *ACS Nano*, 2017, **11**, (2), p. 2103–2114.
- 12 Chang, C., Tran, V.H., Wang, J., Fuh, Y.-K., Lin, L.: 'Direct-Write Piezoelectric Polymeric Nanogenerator with High Energy Conversion Efficiency' *Nano Lett.*, 2010, **10**, (2), p. 726–731.
 - 13 Veeramuthu, L., Cho, C.-J., Venkatesan, M., *et al.*: 'Muscle Fibers Inspired Electrospun Nanostructures Reinforced Conductive Fibers for Smart Wearable Optoelectronics and Energy Generators' *Nano Energy*, 2022, p. 107592.
 - 14 Sun, Y., Liu, Y., Zheng, Y., *et al.*: 'Enhanced Energy Harvesting Ability of ZnO/PAN Hybrid Piezoelectric Nanogenerators' *ACS Appl. Mater. Interfaces*, 2020, **12**, (49), p. 54936–54945.
 - 15 Su, Y., Li, W., Yuan, L., *et al.*: 'Piezoelectric fiber composites with polydopamine interfacial layer for self-powered wearable biomonitoring' *Nano Energy*, 2021, **89**, p. 106321.
 - 16 Kim, M., Wu, Y., Kan, E., Fan, J.: 'Breathable and Flexible Piezoelectric ZnO@PVDF Fibrous Nanogenerator for Wearable Applications' *Polymers (Basel)*, 2018, **10**, (7), p. 745.
 - 17 Pi, Z., Zhang, J., Wen, C., Zhang, Z. bin, Wu, D.: 'Flexible piezoelectric nanogenerator made of poly(vinylidene fluoride-co-trifluoroethylene) (PVDF-TrFE) thin film' *Nano Energy*, 2014, **7**, p. 33–41.
 - 18 Hu, P., Yan, L., Zhao, C., Zhang, Y., Niu, J.: 'Double-layer structured PVDF nanocomposite film designed for flexible nanogenerator exhibiting enhanced piezoelectric output and mechanical property' *Compos. Sci. Technol.*, 2018, **168**, p. 327–335.
 - 19 Mao, Y., Zhao, P., McConohy, G., Yang, H., Tong, Y., Wang, X.: 'Sponge-Like Piezoelectric Polymer Films for Scalable and Integratable Nanogenerators and Self-Powered Electronic Systems' *Adv. Energy Mater.*, 2014, **4**, (7), p. 1301624.
 - 20 Chen, X., Tian, H., Li, X., *et al.*: 'A high performance P(VDF-TrFE) nanogenerator with self-connected and vertically integrated fibers by patterned EHD pulling' *Nanoscale*, 2015, **7**, (27), p. 11536–11544.
 - 21 Abolhasani, M.M., Naebe, M., Hassanpour Amiri, M., *et al.*: 'Hierarchically Structured Porous Piezoelectric Polymer Nanofibers for Energy Harvesting' *Adv. Sci.*, 2020, **7**, (13), p. 2000517.

- 22 Lee, M., Chen, C.-Y., Wang, S., *et al.*: 'A Hybrid Piezoelectric Structure for Wearable Nanogenerators' *Adv. Mater.*, 2012, **24**, (13), p. 1759–1764.
- 23 Zaarour, B., Zhu, L., Huang, C., Jin, X.: 'Enhanced piezoelectric properties of randomly oriented and aligned electrospun PVDF fibers by regulating the surface morphology' *J. Appl. Polym. Sci.*, 2019, **136**, (6), p. 47049.
- 24 Azimi, S., Golabchi, A., Nekookar, A., *et al.*: 'Self-powered cardiac pacemaker by piezoelectric polymer nanogenerator implant' *Nano Energy*, 2021, **83**, p. 105781.

Chapter 6

Electrode-core interface optimisation for enhanced mechanical energy harvester performance

6.1 Introduction

The electrospun PVDF-TrFE/PEO and PVDF/PEO structures can be successfully used as the active core material for mechanical energy harvesters. However, as experimental work in the previous chapter was carried out for assessing their response, certain aspects on which the design of the generators could be improved were starting to become apparent.

For instance, electrode placement and layout for the 1 cm² active area generator units had been decided based on the assumption that the selected configuration would be the best fitting for a randomly oriented network of electrospun fibres. Considering that the sponge-like fibrous structures exist as a stack of randomly oriented fibrous layers, there is a possibility that a better electrode placement and layout would allow for greater electrical outputs to be obtained from these devices. Another assumption was that the adhesive of copper foil that had been selected as the electrode material provided a good enough interface between the active core and the electrode material. However, there is also the possibility that additional treatment on the surfaces that are in contact with the electrode would result in a greater electrical output.

The experimental work outlined in this chapter addresses these concerns, exploring different generator layouts, surface treating materials, and electrode materials which would allow for the improvement of the output power figures obtained in the previous chapter.

6.2 Results and discussion

6.2.1 Effect of electrode placement and active core surface modifications on generator response

Electrospun PVDF fibre mats are typically used for designing piezoelectric generators for which the electrical output arises due to compression/decompression or bending/releasing action. The high electric field used for electrospinning causes the material to be poled along the length of the fibres; in other words, the dipoles are oriented in parallel to the direction of fibre growth. Electrode placement affects the output of the generators because it determines whether the applied mechanical stress direction is parallel or perpendicular to the poling axis, which would relate to the piezoelectric charge constants d_{33} or d_{31} respectively. For both PVDF-TrFE and PVDF, d_{33} has a greater magnitude, indicating that stress applied along the poling axis generates a net higher polarisation [1–3]. Assuming that the nonwoven fibrous PVDF-TrFE/PEO structures used as the active core material in previous experiments could be modelled as a layered stack of fibres, it is very likely that there is no clear net dipole orientation for each layer since the deposition of each individual fibre on the surface of the rotating drum electrode is random. However, as indicated in the previous chapter, there is an observable output when the devices are subjected to a mechanical stimulus. This suggests that the working mechanism of the energy harvesters is not purely piezoelectric but also significantly triboelectric.

It is also possible that, rather than having a net random polarisation in the electrospun layers of the active material, there is a minor alignment that may have originated from having the material being exposed to the strong electric field during electrospinning as it deposited and remained in the rotating collector. Perhaps the electric field aligned a few dipoles in a direction perpendicular to the surface of the fibrous sheet being produced. While the mechanisms that explain the generation of the output signal are not clear, the role that the generator design, electrode placement, and electrode material selection was further analysed. Initially, two different electrode layouts were considered when designing the mechanical energy harvesters. These are shown in Figure 6-1.

The first proposed layout had each electrode covering the active core material predominantly on one of the sides with a 1 cm^2 area each, extending over the edge, and clamping on the opposite side. Since the electrode design resembles a letter L, this design will be referred to as having L-shaped electrodes. The second generator design, which was employed in the work presented in the previous chapter, has the electrodes placed perpendicularly to the fibrous layers, with each clamping on the sides of the active core material. These are referred

to as the generators with regular electrodes. Generators with a 1 cm² active core (12 wt% PVDF-TrFE, 1 wt% added LiCl) were assembled following each of the electrode layout designs shown in Figure 6-1.

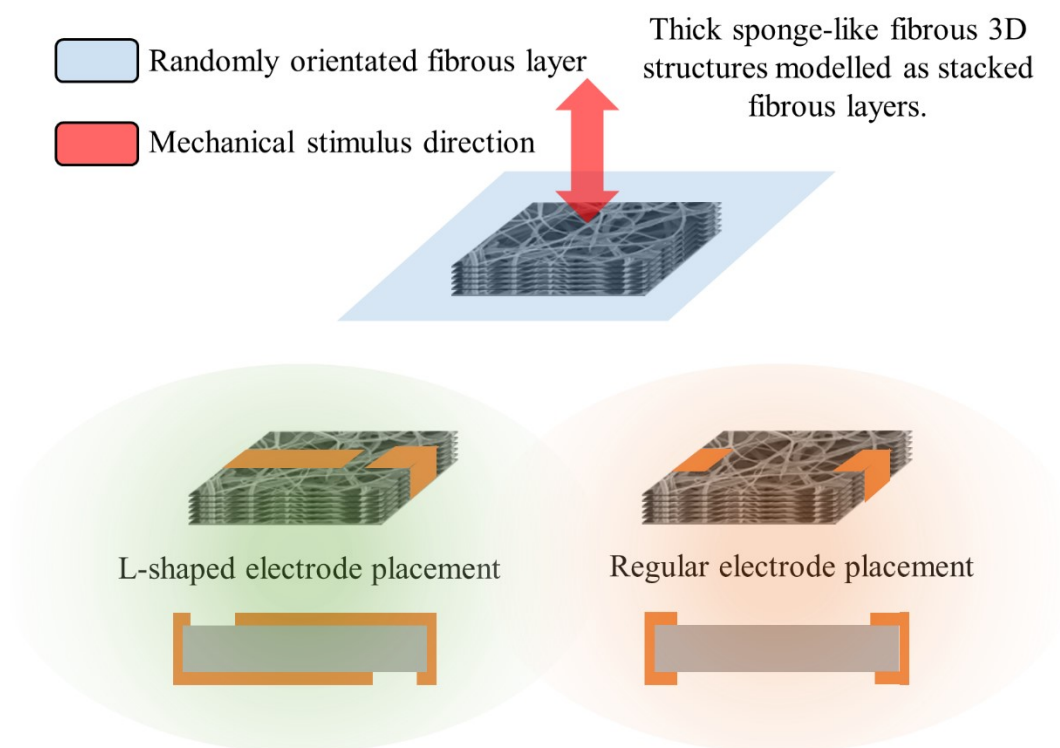


Figure 6-1: Top: Thick sponge-like fibrous PVDF-TrFE/PEO non-woven mats were modelled as stacked fibrous layers. Left: L-shaped electrode placement. Right: Electrode placement used in the

The electrical response of these generators to a mechanical stimulus was evaluated with the cyclic mechanical impact device. This time, instead of using the cubic impact head, a model of a human heel was attached to the device. Using this other striking part would allow for evaluating the response of the generators to different mechanical excitation conditions. Electrical response recordings spanning 100 seconds were captured for each sample. The true impact frequency was 3.4 Hz, the equivalent electrical load used was 15.1 MΩ. Table 6-1 summarises the output V_{PP} figures observed for both samples.

Table 6-1: Output V_{PP} figures obtained when regular and L-shaped electrode generators were subjected to 100 seconds of continuous mechanical impacts.

Electrode placement	Average V_{PP} (V)	Number of recorded impacts
L-shaped	4.54 ± 0.77	340
Regular	11.04 ± 1.64	340

The results revealed that the generators with the regular-shaped electrodes had outperformed those with the L-shaped electrodes by a factor of 2.43. The electrode position relative to the plane of dipole orientation does not completely explain the difference observed in the output V_{PP} figures. It is possible that the net total electrode-core contact area changed because of variation in electrode size when cutting the copper foil, for example. While the generator design with regular electrode placement allowed for greater output signals to be obtained for the same type of core material and mechanical stimuli, the results indicate that adjusting the electrode layout would allow for an even greater response.

Another method that could be used to improve the response of the generators is related to the interface between the copper foil and the surface of the active core materials. The adhesive backing of the copper foil that was used as the primary electrode material is the only interface between the electrodes and the active core. While this interfacing material has allowed for the successful implementation of the generators, treating the active core surface before attaching the adhesive copper foil would result in a better coupling since certain glues and coatings can reduce the energy that is lost internally by reducing the effective contact resistance of the electrode and core junction [4]. A group of PVDF-TrFE/PEO generators with regular electrode placement but cores that had been treated with different substances was built to test this proposition. Conductive silver paint and a 15 nm layer of sputtered gold were used as the materials for improving the active core to electrode interface. The two generators with a modified interface and an unmodified generator were exposed to 100 seconds of cyclic mechanical impacts delivered at a true frequency of 3.4 Hz, using the 3D printed heel model as the striking head. The equivalent resistive load of the system was once again 15.1 M Ω . The average V_{PP} figures recorded for each type of generator are shown in Table 6-2.

Table 6-2: Output V_{PP} figures obtained when generators with different interface surface modifications were subjected to 100 seconds of continuous mechanical impacts.

Surface modification	Average V_{PP} (V)	Number of recorded impacts
No modification	11.04 ± 1.64	340

Silver paint	13.97 ± 1.93	341
15nm gold layer	13.02 ± 1.91	341

The two generators with modified surfaces achieved higher average V_{PP} readings, indicating that the interface between the active core and the electrodes can be further improved. The observed results could be attributed to a reduction of the effective contact resistance at the interface. For both the 15 nm layer of sputtered gold and the silver paint, it is possible that the acrylate functional groups of the adhesive layer on the copper foil interact more strongly with the gold and the acrylic resin of the silver paint than they do with the PVDF-TrFE/PEO fibres [5]. However, there is another possible explanation for the observed increase in the output V_{PP} values. The copper foil electrodes on their own are only in contact with the surface of the active core. Given that this material is a complex 3D fibrous network, perhaps there are several individual fibres that exist deep within the sample and are not in contact with the electrodes, thus resulting in their output signals being lost. Both the sputtered gold layer and silver paint, may have penetrated slightly into the fibrous network while they were being applied to the active core, resulting in an increased number of individual fibres that had direct contact with the electrode or were now close enough for charge transfer to occur.

Focusing on the idea that surface modifications allow for more energy to be transferred to the load, the next step was to evaluate if the observed increase in V_{PP} observed in the previous experiment can truly be attributed to the surface modifications. One-way ANOVA and post hoc tests were used to identify if a significant difference exists between the values observed for the unmodified surface and those with modified interfaces. One condition for ANOVA analysis is that the data to be analysed must be normally distributed. Histograms showing the distribution of the standardised V_{PP} values for each of the generators are shown in Figure 6-2.

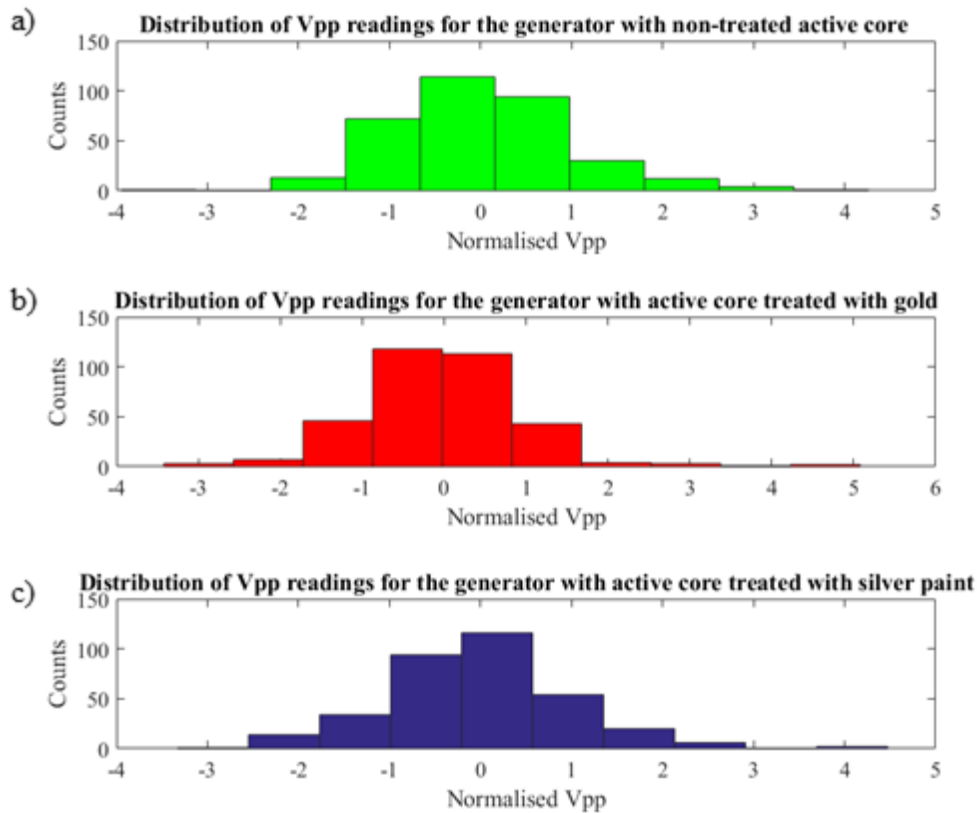


Figure 6-2: Histograms showing the distribution of the standardised output V_{pp} values recorded for each of the tested generators. (a) Generator with a non-treated active core. (b) Generator with active core treated with a layer of gold. (c) Generator with an active core treated with silver paint.

While visual inspection of the histograms appear suggest that the data is normally distributed, confirmation of the datasets conforming to a normal distribution can be visually assessed by comparing the empirical cumulative distribution function plots for the generators with that from a normally distributed reference dataset. This is shown in Figure 6-3. The curves obtained for each generator closely match that which was obtained from the reference dataset, confirming that the data from the recordings is normally distributed. One way ANOVA analysis was thus performed on the data, with the null hypothesis being that surface modification of the active core has no effect on the output signals of the generators. The results obtained from running the test are shown in Table 6-3. Box plots obtained from the non-standardised datasets are shown in Figure 6-4.

Table 6-3: Results of running a one way ANOVA on the data recorded for the generators with different active core surface modifications.

Source	SS	df	MS	F
Groups	1.53E+03	2	7.63E+02	2.28E+02
Error	3411.216	1019	3.347612	
Total	4936.82	1021		

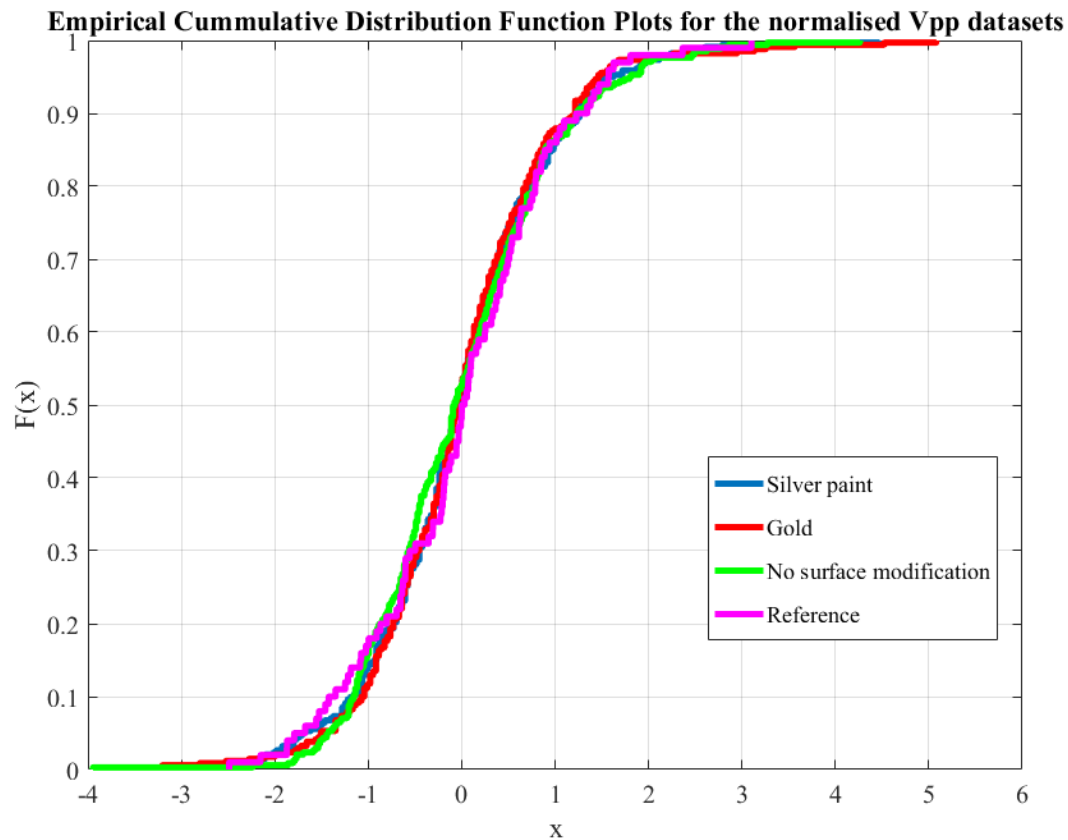


Figure 6-3: Empirical cumulative distribution function plots of the normalised responses obtained from the generators with different surface modifications. The response of the three generator variants approaches the reference curve that corresponds to a normally distributed dataset.

The results obtained indicate that the surface modifications have a statistically significant influence in the output signals obtained from these generators; in other words, modifying the surface of the active core material that would be in contact with the electrodes causes differences in their output V_{PP} values. A Tukey's HSD test was carried out to see if the differences observed between each type of generator are significant. This would help to confirm that the response observed for the generator with a gold layer are different from that obtained from the generator with the silver paint. The results of this test, shown in table 6-4, show that the mean values observed for the three groups are different from each other, indicating that the output signals of depend on their type of surface modifications and each type of surface modification has an independent effect on the output response.

Table 6-4: Results of running a Tukey's HSD test on the data recorded for the three different generators. Group 1 corresponds to the generator with a core treated with silver paint. Group 2 represents the generator treated with gold. Group 3 is that for the generator that had no active core surface treatment.

Groups compared	Lower limit	Difference between group means	Upper limit	p-value
1-2	0.470246	0.969946	1.469645	9.66E-10
1-3	2.446484	2.946183	3.445882	9.56E-10
2-3	1.476538	1.976237	2.475937	9.56E-10

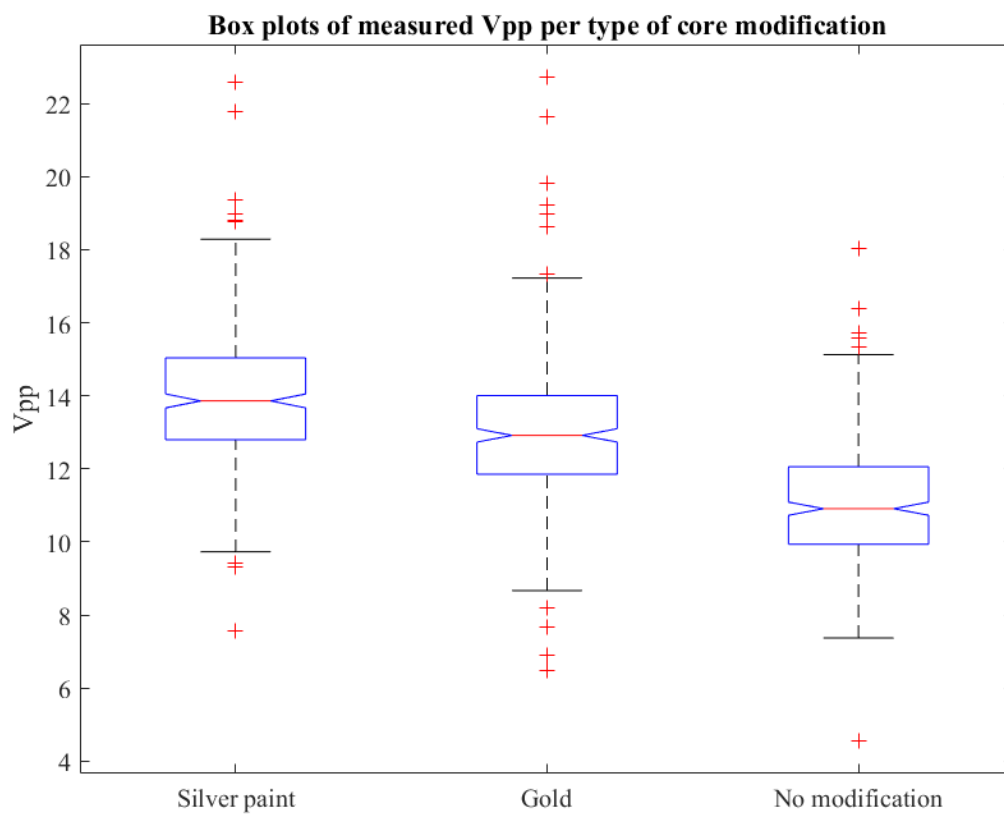


Figure 6-4: Box plots for the data recorded when subjecting the three generators with different active core material surface treatments to cyclic mechanical impacts.

Electrode placement is critical for the electrical performance of the generators. Choosing a configuration that is well adapted to characteristics of the material and takes into consideration aspects such as dipole orientation of the active core material can potentially allow for the fabrication of generators with greater output signal characteristics. Modifying the surface of the core material that would be in contact with the electrodes was also shown to have a positive impact on the output response, allowing for greater power to be delivered to the loads connected to the generators. Another possible mechanism for improving the electrical

response of the generators was identified while the experiments presented on this section where being conducted; using a different electrode design which interacts not only with the surface of the active core material but with the innermost layers of this structure might allow for the harvesting of more power. This will be explored in the following section.

6.2.2 Conductive thread and fabric electrodes

The similarity of the thick sponge-like PVDF/PEO structures to non-woven fabrics raised the possibility of using conductive fabrics and threads as the electrode materials. Perhaps sewing conductive fabrics to the active material would not only allow for securing the electrode to the surface of the core but would also interact with the inner fibrous network deep within the surface of the active material.

PVDF-TrFE/PEO (12 wt%, 1 wt% LiCl) generators with 1 cm² active core and sewn conductive fabric electrodes were prepared using similar designs as those employed in the previous chapter. The active cores surfaces were not treated. The samples were subjected to 100 seconds of cyclical mechanical impacts administered at a frequency of 3.4 Hz. The striking head used for this experiment was also the 3D printed heel model. Table 6-5 summarises the data recorded for this generator, and lists the summarised data recorded for the generator with no modifications and the one with modified surfaces that performed the best for comparison purposes. A histogram for the recorded V_{PP} values for the generator with conductive fabric electrodes is shown in Figure 6-5.

Table 6-5: Output V_{PP} figures obtained when generators with different interface modifications or electrodes were subjected to 100 seconds of continuous mechanical impacts.

Generator type	V_{PP} (V)	Number of recorded impacts
No modification	11.04 ± 1.64	340
Silver paint on active core surface	13.97 ± 1.93	341
Conductive fabric electrode	19.41 ± 1.69	340

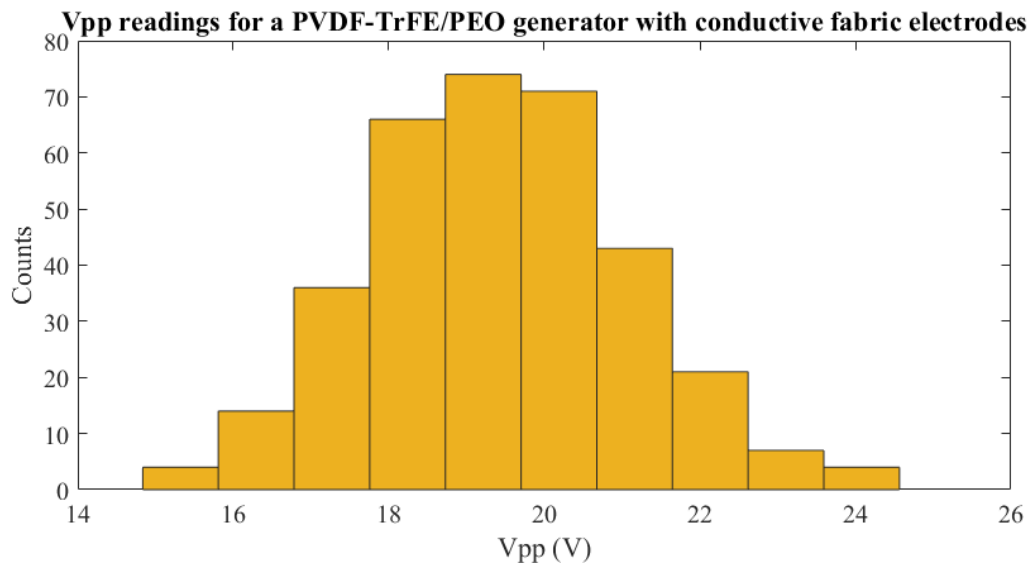


Figure 6-5: Histogram showing the recorded V_{PP} values for the PVDF-TrFE/PEO generator with conductive fabric electrodes.

As shown in table 6-5, the average V_{PP} values for the generator with conductive fabric electrodes improved by a factor of 1.76 and 1.4 times when compared to the unmodified generators and those with active core surface modifications respectively. The results strongly suggested that by gaining access to the inner layers of the active core fibrous structure would result in the potential to obtain an enhanced electrical output from the generators. The promising voltage figures obtained from this test encouraged further exploration of the electrical output for this generator type.

The first additional test replicated the experimental conditions used for evaluating generator output current and voltage for a variable resistive load. Cyclic mechanical impacts at a frequency of 3.6 Hz were applied to the sample, and recordings spanning two seconds for the conductive fabric generator were taken when the resistive loads were 10, 1.6M and 15 M Ω . The cubic striking head was used for this experiment. The results for this test are shown in Table 6-6. Table 6-7 compares the data obtained for this generator and compares it to the best performing generators used in the previous chapter. Figure 6-6 shows a detailed view of the output voltage signals obtained from the generator with conductive fabric electrodes when the load was 15 M Ω .

Table 6-6: Summary of the output characteristics of the generator with conductive fabric electrodes and the impact forces recorded when powering up various resistive loads.

Resistive load (Ω)	I_{SC} or I_{PP} (μA)	V_{PP} (V)	Instantaneous output power ($\mu W\ cm^{-2}$)	Impact force (N)
--------------------------------	----------------------------------	--------------	---	---------------------

10	2.88 ± 0.37	---	---	---
1.6 M	3.17 ± 0.25	5.17 ± 0.45	16.5 ± 2.61	1.8 ± 0.46
15.1 M	2.75 ± 0.46	43.09 ± 7.7	121.8 ± 18.7	1.8 ± 0.69

Table 6-7: Summary of the output characteristics and recorded impact forces for the best performing unmodified PVDF, PVDF/PEO and PVDF/TrFE/PEO active core, copper foil electrode generators and for the PVDF-TrFE/PEO generator with conductive fabric electrodes.

Best performing samples				
15.1 MΩ resistive load				
Core type	PVDF	PVDF/PEO	PVDF-TrFE/PEO	PVDF-TrFE/PEO, conductive fabric electrodes
V_{PP} (V)	6.42 ± 1.01	22.65 ± 2.55	38.28 ± 3.26	43.09 ± 7.7
I_{PP} (μA)	0.43 ± 0.07	1.54 ± 0.17	2.57 ± 0.22	2.75 ± 0.46
Impact force (N)	0.1 ± 0.04	0.17 ± 0.06	0.25 ± 0.05	1.8 ± 0.69
Instantaneous output power (μW cm⁻²)	1.35 ± 0.7	13.8 ± 2.5	45.5 ± 8.82	121.8 ± 18.7

The data obtained from this experiment showed that substituting the copper foil electrode materials with the conductive fabrics resulted in an improvement of all the electrical output figures, with the instantaneous output power for the generators with conductive fabric electrodes achieving 2.68 times that observed for the original equivalent with copper foil electrodes when the resistive load was 15.1 MΩ.

The instantaneous output power figures shown in table 6-8 provide a simplified overview of the actual power than can be delivered by the generators. While it shows what occurs at only one instant during testing, this figure does not provide much insight into the effective amount of power being generated while the sample is exposed to the cyclic mechanical impacts. A more informative figure for the output power of the generators can be obtained by multiplying RMS estimates for the voltage and current signals recorded for each sample. The RMS value

for one pair of the voltage and current waveforms captured for each type of generator (PVDF, PVDF/PEO, PVDF-TrFE/PEO and PVDF-TrFE/PEO with conductive fabric electrodes) were calculated and then multiplied times each other. This provides an approximation of the average power, which can be easily compared to DC power references. The resulting values are shown in Table 6-8. Figure 6-7 shows the waveforms obtained when multiplying the voltage and current signals for each generator type, showing the individual instantaneous output power peaks for each type.

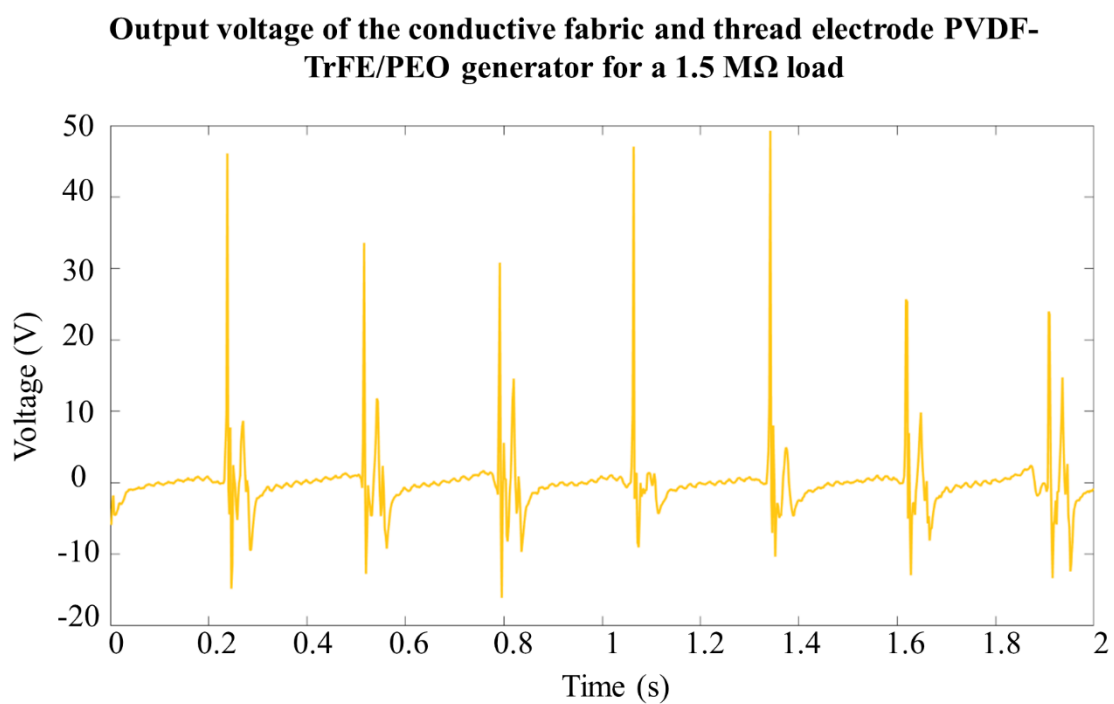


Figure 6-6: Output voltage waveform obtained when subjecting the PVDF-TrFE-PEO generator with conductive fabric and thread electrodes to a mechanical stimulus imparted at a frequency of 3.6 Hz and with a 15 M Ω resistive load.

Table 6-8: RMS values calculated for pairs of voltage and current signals recorded for each type of generator. The average power is then calculated by multiplying V_{RMS} and I_{RMS} .

Generator type	V_{RMS} (V)	I_{RMS} (nA)	P_{AVG} (nW) per 1 cm^2 active area
PVDF	0.598 ± 0.02	38.7 ± 1.5	23.2 ± 1.8
PVDF/PEO	2.61 ± 0.27	175.9 ± 18.0	460.3 ± 94.0
PVDF-TrFE/PEO	3.72 ± 0.08	249.7 ± 5.8	928.7 ± 42.8
PVDF-TrFE/PEO with conductive fabric electrodes	4.22 ± 0.37	270.3 ± 20.5	1141 ± 188.7

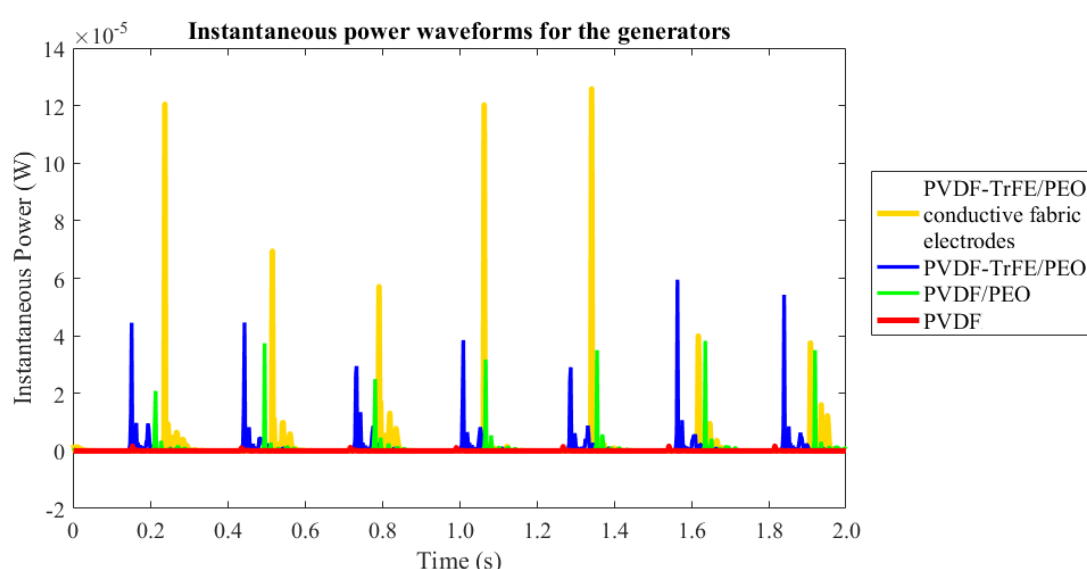


Figure 6-7: Power waveforms obtained when multiplying the voltage and current recorded for each type of generator under the following experimental conditions: 15.1 M Ω resistive load, 3.64 Hz impact frequency, multiple recordings lasting 2 seconds were obtained for each generator. The cubic striking head was used in this experimental trial.

The values obtained from these calculations reflect the average power that would be provided by the generators if the mechanical impact frequency, sample position, and other parameters remained constant over a long time. While the P_{AVG} figures are considerably lower than the instantaneous output power figures shown in Table 6-8, they can be easily used to assess if the generators are well suited specific applications. For instance, consider a Bluetooth low-power wireless transmission device. The device cycles through a series of different operational modes depending on the task being addressed. Active transmission and reception of data packets consume 20 mA. The device is able to go into sleep mode, for which only a few critical processes will be active, wake-up mode, and stand-by mode. These modes consume lower

amounts of power, with each having requiring currents of 0.4, 0.9 and 240 μA respectively [6, 7]. These characteristics are listed for a 3 V supply. These voltage and current figures can be used to estimate the DC power required to keep the system working on each mode. The required power for each mode is shown in Table 6-9, as well as the active area of each type of generator that would be required to power these up based on the P_{AVG} figures from table 6-8.

Table 6-9: Estimated PVDF based active core generator area required for powering up a low-power wireless transmission module in one of several available modes.

Operational mode of the wireless transmitter	Generator area required (cm^2)				
	Required power (μW)	PVDF	PVDF/PEO	PVDFTrFE/PEO	PVDF-TrFE/PEO and conductive fabric electrodes
Tx/Rx	60k	2.586 M	130.4 k	64.6 k	52.58 k
Stand-by	720	31 k	1.56 k	775.3	631
Wake-up	2.7	116.4	5.86	2.91	2.37
Sleep	1.2	51.7	2.6	1.29	1.05

The results shown in table 6-10 indicate that the generators are well suited as independent power sources for the device when it operated in sleep or wake-up mode. The other two modes would require generators with an active area that would not be suitable for a portable device; for instance, a 2.29 m wide and 2.29 m long PVDF-TrFE/PEO generator with conductive fabric electrodes would be required for powering up the wireless transmitter in Tx/Rx mode. Additionally, this would only be possible if such a generator was being subjected to cyclic mechanical impacts delivered at a frequency of 3.64 Hz. However, wireless transmitter modules are typically operated in sleep mode, transitioning only to stand-by or active mode when specific conditions such as a signal being monitored by an ADC port increasing over a threshold value or a timer expiring. The device will only transition to the active Tx/Rx state for a small percentage of the time it will be operating for, and thus can be at least partially powered up by these generators if an energy storage element is added to the mix. While it is unlikely that the PVDF-TrFE/PEO generator with conductive fabric electrodes would be capable to power up this wireless system in Tx/Rx mode on its own, it can still become part of a secondary power system that would help extend the battery life of a primary power cell.

The generator with conductive fabric electrodes was tested under the experimental conditions that had been used previously for charging the 1, 4.7 and 10 μF capacitors. Given that the instantaneous output power figures and P_{AVG} had been shown to be higher than for the generators with copper foil electrodes, faster capacitor charging and a higher plateauing voltage were expected. The results of the capacitor charging experiments are shown in Figure 6-8, including the plots that had been obtained for the generators tested in the previous chapter.

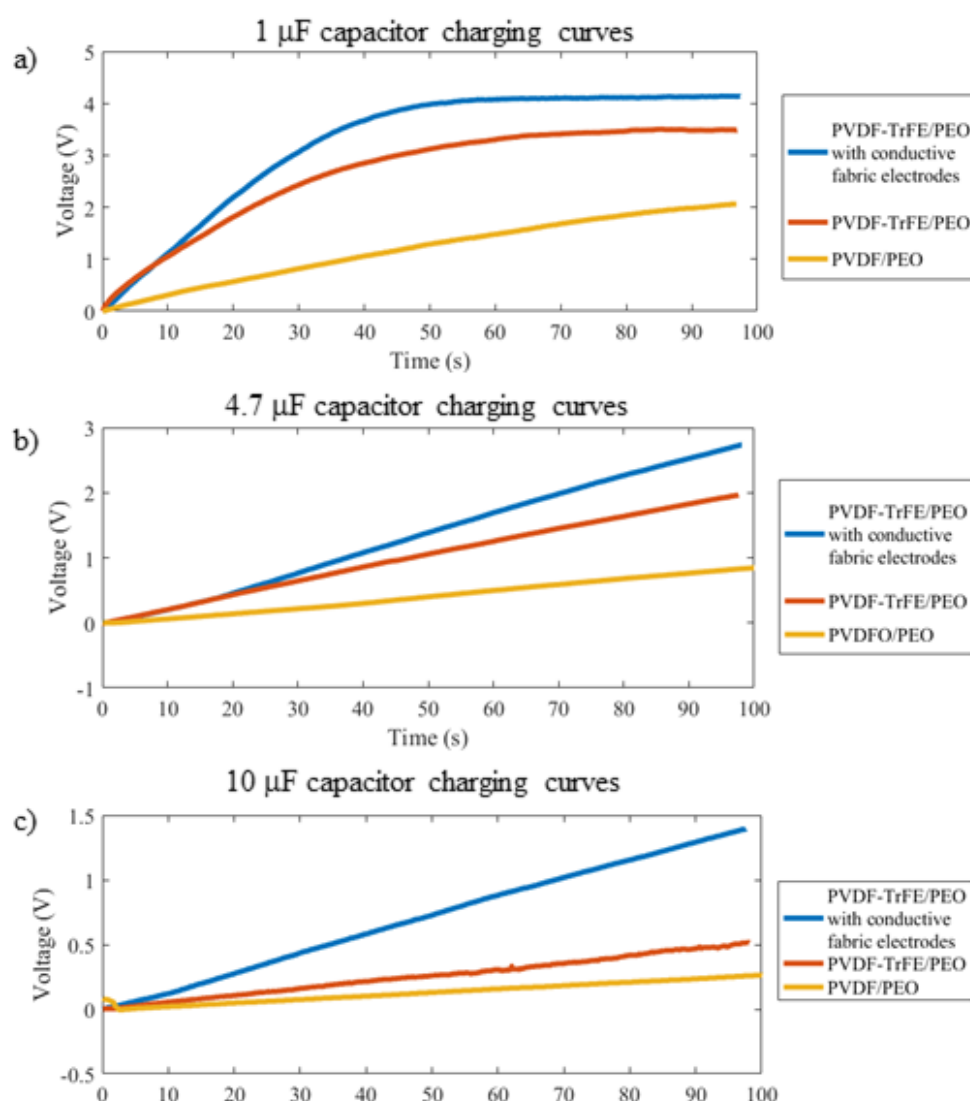


Figure 6-8: Capacitor charging curves obtained from the generators used in the previous experiments.

The charging curves confirm that the generators with conductive fabric electrodes achieved a higher final charge voltage and reached the plateauing state after 50 seconds, reaching a voltage of 4.13 V. For the larger capacitive loads, the curves do not approach the plateauing state but do achieve higher voltage levels at the end of the recordings. These results are strong indicators that using conductive thread and fabric as the electrode materials are

beneficial for the performance of the generators, resulting in a net improvement of the power that can be delivered to the loads.

6.3 Interim summary

Using the thick sponge-like electrospun PVDF structures as the active core material for mechanical energy harvesters requires careful consideration of the layout of the device and the selection of the materials used in their construction. While the properties of the active core are fundamental, being of great importance for determining the electrical output performance of the device, selecting the optimal interfacing approach is critical to ensure that the system is being used to its full potential.

Selecting the electrode placement based on the properties of the core material allowed for an almost 2.5-fold increase in the observed output signals of the generators, increasing from an average 4.54 ± 0.77 V to 11.04 ± 1.64 V_{PP}. Treating specific regions on the surface of the active core material with conductive substances resulted in a net improvement as well, allowing the average output V_{PP} to increase up to 13.97 ± 1.93 V. Observing the results that surface treatments had on the performance of the generators led to the idea that interfacing with the inner regions of the fibrous active core would further enhance the output. Further experiments demonstrated that using conductive fabric electrodes and conductive threads which interact with the inner layers of the material allow for a dramatic increase in the output signals of the generators, with the average V_{PP} values now being 19.41 ± 1.69 V. Not only did the output V_{PP} increase, but the power sourced by the generator did so as well. In terms of instantaneous power, the generator with conductive fabric electrodes achieved a power density of 121.8 ± 18.7 $\mu\text{W cm}^{-2}$ which was 2.67 times that of the variant with copper foil electrodes. In terms of P_{AVG}, the generator with fabric electrodes achieved a power density of 1.141 ± 0.19 $\mu\text{W cm}^{-2}$, which was still greater than that estimated for the 928.7 ± 0.04 nW cm⁻² estimated for the variant with copper foil electrodes.

The work presented in this chapter outlines only some of the methods that can be used for further improving the performance of the energy harvesters. The approaches taken in this chapter allowed for a net improvement of the output signal characteristics of the generators, but future work and exploration of alternative methods might allow for further refining the potential of the 3D PVDF fibrous materials as elements for energy harvesting.

6.4 References

- 1 Shao, H., Wang, H., Fang, J.: 'Piezoelectric energy conversion performance of electrospun nanofibers' (IOP Publishing, 2019), p. 4–42
- 2 Yan, Y., Kim, W.G., Ma, X., *et al.*: 'Nanogenerators facilitated piezoelectric and flexoelectric characterizations for bioinspired energy harvesting materials' *Nano Energy*, 2021, **81**, p. 105607.
- 3 Roji, A.M.M., Jiji, G., Raj, A.B.T.: 'A retrospect on the role of piezoelectric nanogenerators in the development of the green world' *RSC Adv.*, 2017, **7**, (53), p. 33642–33670.
- 4 Zhao, Y., Liu, D., Yan, Z., *et al.*: 'Preparation and characterization of the Ag₂Se flexible films tuned by PVP for wearable thermoelectric generator' *J. Mater. Sci. Mater. Electron.*, 2021, **32**, (15), p. 20295–20305.
- 5 Tsurumi, N., Masago, N., Baba, T., Murata, H., Tsuji, Y., Yoshizawa, K.: 'A Study of Adhesion Interface about Die Bonding Structure with Conductive Silver Paste', in '2018 IEEE CPMT Symposium Japan (ICSJ)' (2018), p. 45–48
- 6 Kamath, S., Lindh, J.: 'Measuring Bluetooth® Low Energy Power Consumption' *Texas Instruments*, 2012, p. 1–24.
- 7 'CC2540 data sheet, product information and support | TI.com', <https://www.ti.com/product/CC2540?keyMatch=CC2540&tisearch=search-everything&usecase=GPN>

Chapter 7

Conclusions & Recommendations for future work

7.1 Conclusions

The work carried out throughout this project focused on the fabrication of electrospun piezoelectric polymer based structures that would then be used to create energy harvesting devices. Recalling the information provided previously (Chapter 1, section 2), the specific goals of this thesis were the following:

- Electrospinning piezoelectric polymer fibrous structures
 - Focusing on the manufacturing of biocompatible active materials that are compatible with wearable device design approaches.
- Characterisation of the resulting fibrous structures
 - Observe which conditions allow for the fabrication of the most promising structures.
- Use the fabricated fibrous product to design and implement a mechanical energy harvester.
- Demonstrate the properties of the fabricated materials and designed generators by evaluating their electrical response.
 - Evaluate effects of using different electrode designs and materials.
 - Characterise the electrical response of the generators under different testing conditions.
- If any improvements to the designs or material fabrication methods are found, implement them and re-evaluate the electrical responses.

The experimental work was initially dedicated to the identification of favourable conditions for the electrospinning of PVDF (Chapter 4). Observing the effects that the working parameters of the experimental setup, the ambient conditions, and the composition of the solvents and polymer content of the solutions had on the morphology of the fibres allowed for the identification of the favourable conditions that would yield fibres with a reduced amount of breaks and beads. A preliminary analysis of the sample that had been deemed to have the

best quality as the core material of a generator showed promise. These experimental trials served as the foundation of the project, laying the groundwork required to try new approaches for obtaining enhanced materials and eventually led to the fabrication of the novel 3D structures. Additionally, it allowed for the creation of improved generator designs, which were capable of better harnessing the potential of the enhanced materials as a key component of mechanical energy harvesters. (Chapter 5 and 6).

However, the mechanisms explaining the working principle of the generators that were designed and built was not properly identified. The results obtained from the experiments outlined in chapter 5 and the early analysis carried out in chapter 6 suggested that the observed polarisation and thus the output signals were most likely originating from both the piezoelectric and triboelectric effect, and not only because of the piezoelectric effect. The initial assumption that using a blank generator consisting of the copper foil used as an electrode attached to wires and encapsulated in PDMS would allow for the identification of the portion of the signal arising from the triboelectric effect was flawed, since the role of the increased contact area that the core material had with the PDMS would be unaccounted for in a completely blank generator. For this reason, the goal of creating piezoelectric generators was not completely achieved. However, the experimental work culminated in the fabrication of mechanical energy harvesters based on a combination of the triboelectric and piezoelectric effect instead, and it was still possible to further improve on the output signals being generated by proposing alternative designs and using other electrode and interfacing materials.

The findings reported throughout this document as well as the challenges that were identified but remained unaddressed offer only a glimpse of what can be achieved when novel electrospun structures are used to build energy harvesters. The project evolved through several stages, initially being focused on the materials aspect, and eventually progressing to an application-oriented evaluation of their electrical properties. The interdisciplinary work presented in this thesis opens up new pathways for exploration in regards to the field of materials science, electrical and electronics engineering.

The following sections will discuss in depth the concluding remarks pertaining to the materials science aspect of the project, the work related to the application of the fabricated structures, and the limitations and constraints associated with the project.

7.1.1 Conclusions related to the fabrication of electrospun PVDF active core materials.

This stage of the project focused initially on electrospinning polymer solutions, starting with the optimisation of the solution and the identification of the working parameters and ambient

conditions that would result in quality fibrous products for the nozzle-based setup. The first set of experiments involved using 20 wt% PVDF in DMF and acetone (4:1 solvent ratio) polymer solutions, keeping the working distance at 20 cm while varying the voltage and flow rate. At first, a voltage of 12 kV and a flow rate of $7 \mu\text{L}\cdot\text{min}^{-1}$ were used. It was observed that increasing the voltage to 14.5 kV influenced the presence of beads in the electrospun product, with the higher voltage level having reduced the amount of beads observed in the SEM images taken for each sample. The following trial kept the 14.5 kV, but this time the flow rate was reduced to $5 \mu\text{L}\cdot\text{min}^{-1}$. This did not have an apparent influence on the morphology of the fibres. Fibre diameters for these trials were $388 \pm 128 \text{ nm}$, $447 \pm 161 \text{ nm}$ and $405 \pm 139 \text{ nm}$ respectively.

Aiming to improve the quality of the product, a special nozzle that allows nitrogen gas to be pumped around the nozzle was used to reduce the RH% on the vicinity of the needle tip. A 20 wt% PVDF in DMF solution was electrospun with this nozzle, keeping a constant flow rate ($7 \mu\text{L}\cdot\text{min}^{-1}$) and voltage (18 kV) while varying the working distance from 20 cm to 15 cm. The product obtained from these experiments had a higher bead content. An additional trial involved keeping the flow rate constant at $15 \mu\text{L}\cdot\text{min}^{-1}$, changing the working distance from 10 to 25 cm in 5 cm increments, and adjusting the voltage to levels that were high enough to form a stable Taylor cone. A final trial involved adjusting the polymer concentration to 15 wt%, using a higher flow rate of $25 \mu\text{L}\cdot\text{min}^{-1}$, 21 kV, and working distance of 20 or 15 cm. The results obtained from all the previous experimental trials allowed for the identification of the experimental conditions that were most favourable for the fabrication of electrospun PVDF fibres. A working distance of 15 cm, voltage just high enough to observe a stable Taylor cone on the needle tip, and a flow rate lower or equal to $15 \mu\text{L}\cdot\text{min}^{-1}$ allowed for the fabrication of more uniform fibres with a lower presence of beads. Additionally, using a lower polymer concentration (15 wt%) or a solvent system of DMF and acetone also had a favourable effect on the product.

The next step was to use a more complex polymer and solvent system; a solution consisting of a combination of PVDF and PEO in a solvent system of DMF and water (50:3 ratio for both polymers and solvent). This combination resulted in a dramatic improvement of the quality of the fibres; the average diameters recorded for two different trials were $928 \pm 194 \text{ nm}$ and $1.498 \pm 242 \mu\text{m}$. The first figure was obtained from fibres that were elctrospun with a flow rate of $7 \mu\text{L}\cdot\text{min}^{-1}$, 17 kV and a working distance of 30cm. The other figure corresponds to a flow rate of $15 \mu\text{L}\cdot\text{min}^{-1}$, 22 kV and a working distance of 35 cm. No beads were present in any of the samples. The electrospinning parameters were once again optimised for this solution, with conditions such as a lower flow rate, higher voltages, and higher working distances being identified as favourable for both 10 wt% and 12 wt% PVDF/PEO solutions.

Once products with more uniform, bead-free fibres were obtained, LiCl was added to the polymer solutions. The most important result of this phase of the project was also observed after having added this salt; electrospinning a 10 wt% PVDF/PEO solution with added 1 wt% LiCl resulted in the formation of 3D fibrous structures. After 10 minutes of electrospinning, these structures had an area of 5 cm², a thickness of 1.2 cm, and weighed 57.5 mg. At the time, the fabrication of 3D PVDF structures had only been achieved with extruder-based methods; this was a result that had not been reported previously in the literature. Additionally, when using these solutions with the needleless electrospinning setup, a thick, sponge-like fibrous non-woven fabric was obtained. This method yielded a 28 cm wide, 19 cm long sheet with a thickness from 0.4 to 0.72 mm and a weight of 2.8 g after only 15 minutes of electrospinning. Replacing PVDF with PVDF-TrFE yielded similar results. Thus, the electrospinning of 3D PVDF and PVDF-TrFE structures was achieved with both the classical electrospinning method and with a high throughput method.

The effects that added LiCl had on the morphology of the fibres and how these may also occur when different salts are used as additives encouraged one additional experimental trial. Zinc nitrate was also tested as an additive to the solutions. While the resulting fibrous product did show a limited degree of 3D build-up for added salt concentrations of 1 and 5 wt%, the product was not as sturdy as that obtained when using LiCl. Further information regarding these results can be found in Appendix B.

The identification of the ideal conditions for electrospinning a combination of polymers can be complicated. While the conditions found to be favourable for one combination of polymers can also work if one of them is changed for a similar one (for instance, what was observed when PVDF was replaced with PVDF-TrFE), the addition of minute amounts of additives can alter the solution to a degree for which these favourable conditions no longer work. However, fine-tuning of the working parameters is what makes it possible to fabricate products with unique properties tailored for a particular application. In the case of the studies conducted in this thesis, this process resulted in polymer-based 3D structures in forms that can be effectively integrated into portable devices.

7.1.2 Conclusions related to the mechanical energy harvesters.

The potential of the fibrous products and structures obtained throughout this study as active materials were evaluated by using them as cores for different energy harvester designs. The earliest version of the generators were built with 1 cm² sections of the electrospun fibre mats obtained from the 20 wt% PVDF in DMF solutions. While it was possible to observe an electrical response in the oscilloscope when connecting the probe to the terminals of these

early designs, several issues were affecting the performance of the devices. First and foremost, the layered design, which consisted of the flat PVDF fibre mat sandwiched between aluminium or copper electrodes and sealed with insulating tape, was flawed in regards to the choice of wiring and the vulnerability of the design to mechanical impacts. The first wiring choice were 23 AWG bare copper wire pieces, which were found to rub against the fibrous core and destroy it just after a few mechanical impacts had been exerted on the generator. Replacing the copper wire with copper foil solved this issue, but the active core was still being damaged after a few rounds of mechanical testing, with the response decaying rapidly until it was non-existent. In spite of the generators being fragile and considering how the fibrous mats used for this iteration had some imperfections, the responses recorded showed promise, indicating that addressing these issues would help with the durability of the generators.

The design and implementation of generators was attempted once more after obtaining the thick sponge-like and cloud-like 3D PVDF/PEO and PVDF-TrFE/PEO structures. The products obtained up to this point would be tested against each other to discover which would have the most favourable response. Layered generators with adhesive copper foil electrodes and modified electrode placement were built, using PVDF fibre mats, PVDF/PEO and PVDF-TrFE/PEO thick-sponge like structures as the active core material. PDMS was used as an encapsulation material to ensure that the active core would not break down when subjected to continuous mechanical impacts. Additionally, this PDMS layer would seal the core and electrodes from the environment and provide insulation for the devices.

A custom-made mechanical testing device consisting of a slider and crank mechanism was designed and built. This device, capable of delivering repeated mechanical impacts at a user-designated frequency, was used to test the electrical output of the generators. An initial evaluation compared the output current and voltage of the generators when these were connected to different load resistors, ranging from 10 Ω to 15.1 M Ω , and exposed to a series of mechanical impacts (3.65 Hz impact frequency). The impact head of the device was a 1 cm³ cube. The average output V_{PP} obtained for all generator types increased with increasing resistive load. These values were 5.76 ± 1.2 V, 18.53 ± 4.49 V and 29.5 ± 6.8 for the PVDF, PVDF/PEO and PVDF-TrFE/PEO generators respectively when the resistive load of the system was 15.1 M Ω . The average output I_{PP} values decreased as the resistive load increased. These values were 0.37 ± 0.085 μ A, 1.26 ± 0.3 μ A and 1.99 ± 0.45 μ A for the PVDF, PVDF/PEO and PVDF-TrFE/PEO generators respectively, for a 15.1 M Ω load. The maximum instantaneous output power for all generators was calculated for the signals obtained at this resistive load value. These were 1.35 ± 0.7 μ W, 13.8 ± 2.5 μ W and 45.5 ± 8.82 μ W for the best performing PVDF, PVDF/PEO and PVDF-TrFE/PEO generators respectively. These figures were found to be comparable and in some cases superior to other similar state-of-the-

art generators. Further analysis of these generators involved rectifying the output and charging capacitors of different values. The PVDF-TrFE/PEO generator managed to almost fully charge a 1 μF capacitor in under 100 seconds, with the recorded voltage value being close to 3.7 V.

The following step was to evaluate the response of the best performing PVDF/PEO and PVDF-TrFE/PEO generators over 500 seconds of continuous mechanical impacts to test the stability of their electrical response. Since the impact frequency was once again close to 3.65 Hz, these tests probed the response for around 1850 continuous impacts. The results obtained showed that the response of the generators did not decay even after sustaining a high number of mechanical impacts, with the average V_{PP} being 21.29 ± 3.17 V and 65.32 ± 6.4 V for the generators with PVDF/PEO and PVDF-TrFE/PEO cores respectively.

A compound generator consisting of 13 basic units in parallel (each unit is a 1 cm^2 piece of active core material) was assembled and tested in real world conditions. A user was asked to wear a flip-flop fitted with the compound generator and told to march at four different speeds, ranging from a gentle stroll (50 SPM) to a very vigorous jog (115 SPM). The generator was connected to a rectifier, with the aim of the experiment being to observe the charging of the capacitors over a period of 100 seconds. These trials involved using a different type of capacitor that is better suited for energy harvesting applications since their insulation resistance value is many orders of magnitude higher than that of the electrolytic capacitors used in the previous experimental trial. The results for this experiment showed that the faster marching speeds resulted in the capacitors charging up to higher voltages. However, even when the load was a 1 μF capacitor and the user marched at the fastest speed, it was not possible completely to charge the capacitor in under 100 seconds. The voltage recorded on the capacitor approached 15 V and the curve still had a linear profile, which strongly indicated that a longer charging time would result in the capacitor charging up to higher voltages. Using a 4.7 μF capacitor as the load resulted in the voltage reaching around 3 V at the end of the charging period when the user had marched at 115 SPM. The stored energy was used to light up an arrangement of 40 green LEDs in parallel to demonstrate that energy had been harvested in the process.

The original generator design was not without its flaws; the next step was to improve on the aspects that had been identified as upgradeable. Thinking of the thick sponge-like fibrous core structures as stacked layers of fibrous mats led to the idea that using adhesive copper foil as the electrode material had resulted in the inner fibrous layers within the core not being in contact with the electrodes, thus causing a fraction of the energy being harvested to be lost. Additionally, it was possible that the adhesive of the copper foil was not the most effective material to use as an interface between the active core and the electrodes.

Additional PVDF-TrFE/PEO core generators were assembled with an additional surface treatment step right before the adhesive copper foil was placed on the active core material. Conductive silver paint or a 15 nm gold layer were used as the surface treatment materials. The new generators were compared to the original PVDF-TrFE/PEO iteration by analysing their output V_{PP} when being exposed to repeated mechanical impacts for a period of 100 seconds. This time, however, instead of using the same cube-shaped striking head that had been employed before, a realistic heel model that was obtained from 3D scanner was fitted to the device. This would allow for the observation of the response of the generators under a different mechanical impact profile. The results obtained from this experiment showed that there was a slight but significant increase in the V_{PP} of the generators with surface modifications. The values recorded were 11.04 ± 1.64 , 13.97 ± 1.93 and 13.02 ± 1.91 V for the generators with no surface modification, conductive silver paint, and a 15 nm gold layer respectively. This increase in the output V_{PP} can be attributed to the treatment effectively reducing the contact resistance at the core-to-electrode interface.

To assess whether using electrode materials that could access the fibrous layers within the sponge-like core would result in an increased electrical output, additional PVDF-TrFE/PEO generators with the same layout but different electrode materials were assembled. The electrode material selected for these was conductive fabric and conductive thread. The use of the conductive thread to sew the conductive fabric directly onto the active material would in theory allow the electrode to extend deep into the sample with each individual stitch. This generator was subjected to the same testing conditions used previously and the output V_{PP} value for it was compared to that of the original generator and the one with conductive silver paint. The output V_{PP} for the generator with conductive fabric and thread electrodes was 19.41 ± 1.69 V, showing that this technique managed to improve the performance of the generator dramatically, by a factor of 1.76 and 1.4 when compared to the unmodified generator and the one treated with the silver paint.

The next experimental trial aimed to compare the generator with conductive fabric electrodes to the best performing PVDF, PVDF/PEO and PVDF-TrFE/PEO, offering a more complete overview of the performance of this new iteration. The cubic-shaped striking head was fitted to the cyclic mechanical impact device, and the generator with conductive fabric electrodes was tested under the same conditions as it had been done previously with the other three generators. The results showed that the V_{PP} and I_{PP} for the generator with conductive fabric electrodes when the resistive load was $15.1 \text{ M}\Omega$ had increased slightly, with these values being 43.09 ± 7.7 V and $2.75 \pm 0.46 \text{ }\mu\text{A}$ respectively. In terms of instantaneous output power, the best performing conductive fabric generator achieved $121.8 \pm 18.7 \text{ }\mu\text{W}$. Thus, it was theorised that using electrode materials and assembling methods that ensured access to the

inner fibrous network of the active core may potentially increase the electrical output figures of the generators. While the instantaneous output power figure is typically used to describe the capabilities of an energy harvester, the average power figure can be extrapolated to practical situations more easily. P_{AVG} represents the outputs of these generators in terms of DC elements, being directly comparable with the constant power consumed by electronic devices such as integrated circuits, sensing systems, and others. The P_{AVG} values calculated for the PVDF, PVDF/PEO, PVDF-TrFE/PEO and PVDF-TrFE/PEO with conductive fabric electrodes were $23.2 \pm 1.8 \text{ nW}$, $460.3 \pm 94.0 \text{ nW}$, $928.7 \pm 42.8 \text{ nW}$, and $1.14 \pm 0.19 \text{ } \mu\text{W}$ respectively. A few comparisons were made to provide some context for these figures. Considering how one specific wireless transmission module consumes $2.7 \text{ } \mu\text{W}$ when operating in a low-power mode, the generator area required to provide this amount of power would be 116.4 cm^2 , 5.86 cm^2 , 2.91 cm^2 and 2.37 cm^2 by core type respectively.

Overall, the process of building different generator prototypes allowed for the continuous improvement of the designs, resulting in a better understanding of how the 3D thick sponge-like materials behave when used as part of an energy harvester. The process allowed for the identification of the characteristics that should be taken into account to ensure that the core material is being used to its full potential. The results obtained in this thesis have addressed the original aims and objectives of the project, and provide a starting point for future research activities relating to the use of 3D electrospun materials for portable energy harvesting applications. However, there exist several points that require further study and clarification.

7.1.3 Limitations of the work presented in this thesis

Perhaps the greatest limitation of the work presented in this thesis was the lack of a more effective strategy for assessing whether the observed outputs obtained from the generators were a product of both the piezoelectric and triboelectric effects and to identify the contribution that each had to the observed outputs. An exploration of these characteristics would have altered the course of the experimental work outlined in chapter 6; having a clearer picture of the behaviour of the core materials and their interaction with the electrodes and encapsulation materials would have allowed for a more effective identification of beneficial generator designs and geometries, which in turn would have resulted in the design of better performing generators.

Other limitations were related to the availability of equipment and accessories, as well as those arising from the pandemic. Most of the research activities outlined in this document were carried out in the nanomaterials laboratory. The electrospinning setups available in this laboratory allowed for the successful fabrication of the 3D PVDF fibrous materials. However,

both the nozzle-based and the nozzle-free setup lacked a few accessories and features that would have potentially allowed for a more efficient and exhaustive electrospinning experience. For instance, the nozzle-based setup had an accessory that could be used to electrospin core-shell nanofibers, but this accessory had been missing for a very long time. The RPM controller for the nozzle-free electrospinner works very well, but the device itself appears not to be able to withstand speeds over 1000 RPM for a prolonged time. When operating at high RPM, the device begins to shake and if left running for a long time had been reported to cause heavy mechanical stress on the walls of the electrospinning chamber. The opportunity to conduct a few experiments when operating the device at high RPMs would have allowed to evaluate if electrospinning the 3D structures under these conditions would have resulted in thick structures composed of mostly aligned fibres.

Another limitation at times was the availability of an oscilloscope and mechanical testing devices. There is no oscilloscope available in the nanomaterials laboratory; thus, it was necessary to borrow one from other laboratories. This would work out fine most of the time, but often resulted in the interruption of my experimental work when the owners of the device requested to get it back. The devices available for testing the mechanical properties of the products created in the nanomaterials laboratory were mostly related to slow actuation rather than the fast impact frequency desired for characterising the response of the generators. This was addressed by collaborating with another student and creating our own custom-made device.

Measuring the impact force being exerted on the generators by the cyclic mechanical impact device proved to be challenging. Using the FSR and comparing the readings to calibration curves provided by the manufacturer of the sensor allowed to measure these forces on a very basic level. However, a more meaningful exploration of the role that the impact force plays relative to the output of the generators would require equipment that is more sophisticated.

The effect of the previous limitations was further exacerbated by the COVID-19 pandemic. Laboratory closures and the restrictive working policies enforced once people were being allowed back into the buildings resulted in the experimental work presented in this thesis slowing down severely.

A final experimental trial had been planned to evaluate how the best performing generators, both original and modified, would perform when used to power up a simulated wearable device. A Würth Elektronik energy harvesting kit was purchased with the intention of using the included evaluation board to program a simplified sensing system. The evaluation board has an EFM32 microprocessor and has been built with the most efficient passive components available in the market; in other words, it is tailored specifically for these kind of applications.

Although this experiment was not carried out due to time constraints, it is something of interest that would have complemented greatly the results obtained in this thesis, and can always be addressed in future work.

7.2 Thesis contributions

The main original contributions of the work presented in this thesis relate to the fabrication of novel 3D forms of PVDF and PVDF-TrFE fibrous structures by electrospinning and their use as active cores for mechanical energy harvesters. The contributions of the work presented in this document are outlined below.

- Fabrication of electrospun 3D PVDF/PEO and PVDF-TrFE/PEO structures.
 - The process of electrospinning solution optimisation and employing the nozzle-free and nozzle-based electrospinning setups allowed for the identification of the favourable conditions required for inducing a form change in the electrospun product. The addition of the LiCl salts mediated a transition from 2D fibrous mats to 3D fibrous structures. The 3D structures ranged from thick, sponge-like variants to cloud-like structures.
- Mechanical energy harvesters with thick sponge-like PVDF/PEO and PVDF-TrFE/PEO cores.
 - The 3D structures that resembled thick sponge-like materials were used to assemble a variety of mechanical energy harvesters. The basic design consisted of an active area of 1 cm², copper foil electrodes and PDMS as the encapsulating material. The best performing generator, which had a PVDF-TrFE/PEO core, achieved an instantaneous output power of $45.5 \pm 8.82 \mu\text{W}$, a figure that compares favourably or surpasses those of other state-of-the-art generators based on similar materials. However, it was unclear if the objective of enhancing the β -phase content of the fabricated materials had been achieved. The XRD scans obtained from the PVDF/PEO samples were not taken at a scan rate that would allow for the clear distinction between the crystalline domains present in the sample when compared to the reference pristine PVDF curve; thus, it is not possible to say with confidence that the β -phase content of the electrospun fibres was enhanced at all. Additionally, the generated output power was not proven to be unequivocally because of the piezoelectric effect. A more rigorous approach for assessing the portion of the signals that arise from the triboelectric effect is required. For these reasons, the generators were subsequently referred to as mechanical energy harvesters, indicating that both the piezoelectric and triboelectric effects play a role in generating the output signals.
- PVDF-TrFE/PEO core generator with conductive fabric and thread as electrode materials.

- Using the generators mentioned previously as a starting point, a few different electrode materials were used for assessing how these would change the electrical outputs of the devices. Generators built with conductive thread and fabric electrodes instead of adhesive copper foil allowed for the instantaneous output power to increase to $121.8 \pm 18.7 \mu\text{W}$. The average power figure was calculated as well, resulting in a value of $1.14 \mu\text{W}$. This figure can be interpreted as the generator being able to source this constant amount of output power over time.
- Cyclic mechanical impact device.
 - A custom-built device for testing the electrical properties of the generators was designed and built in collaboration with one of my fellow PhD students, Michael Chung. The device can strike a sample at a programmable frequency of up to 9.42 Hz in optimal conditions. In relation to the mechanical parts, I was responsible of designing and printing some of the parts and accessories of the device, focusing on sample holders, another striking head, and the fixture that would house the force sensitive resistor. The code, electronics and interfacing was also my responsibility.

7.3 Recommendations for future work

The work carried out in this thesis allowed me to experiment with several fabrication methods, generator designs and substances for improving the response of the piezoelectric materials obtained in these studies. While this work was going on, several improvements were identified, some of which were addressed in previous chapters. However, some of the aspects that were identified posed greater challenges and would require more extensive work. The following propositions represent the main lines of work that could be of interest for further investigation.

PVDF based electrospun 3D structures:

1. The use of the nozzle-free electrospinning setup resulted in an up-scaled production of the PVDF/PEO and PVDF-TrFE/PEO fibrous structures. The rotating collector was only used at relatively low speeds, which resulted in the electrospun structures to be a collection of randomly oriented fibres. If the RPM setting had been ramped up to over 2000, the resulting material would have consisted of a collection of aligned fibres instead. However, the effect that the rapid rotation of the collector would have on the 3D build-up of the material would need to be reviewed. This setting could potentially allow for the fabrication of highly aligned PVDF structures, which have been shown to have a higher electrical properties when tested against randomly oriented fibrous structures [1, 2].

Generator design

1. The use of gold and conductive silver paint for treating the surface of the thick sponge-like PVDF-TrFE/PEO fibrous cores that would be in contact with the copper foil electrodes resulted in a slight yet significant improvement of the electrical output of the generators. These findings strongly suggest that improving the interface between the electrode and the surface of the active core material can be used to reliably increase the electrical output characteristics of the devices. One method that could be used to achieve this would involve using the conductive polymer poly(3,4-ethylenedioxythiophene) polystyrene sulfonate (PEDOT:PSS). This polymer, which is widely regarded in the field of polymer science as a very promising alternative for the creation of flexible electronics due to its high conductivity, could be used to coat the regions of the active core that would be in contact with an electrode [3–5]. A layer of PEDOT:PSS can be effectively deposited on the surface of PVDF fibrous structures by using functionalisation methods such as plasma treatment, which allow for more efficient charge transfer due to the strong chemical bonds which attach the coating to the surface of the core material.

2. The output V_{PP} of generators with thick sponge-like PVDF-TrFE/PEO fibrous structures was observed to increase by a factor of 1.75 times when the sticky copper foil electrodes were replaced with conductive fabric and thread. The observed increase was attributed to the conductive fabric electrodes gaining access to the inner layers of the fibrous core material by having the conductive thread penetrating into the fibrous structures as the electrode were being sewn. One method that could potentially result in an increased amount of contact points between the electrode material and the fibrous layers within the cores would be the fabrication of structures such as copper dendrites on the electrodes. This idea was inspired by the formation of lithium dendrites on batteries [6]. Methods such as electrodeposition could be used for creating micrometric copper wires branching out of a seeded electrode surface, although the viability of this idea would depend on how damaging the solutions involved in the electrodeposition of copper are to the PVDF-TrFE structures [7–9]. PVDF is typically used as a coating material in the industry due to its chemically inert nature; thus, the risk of the cores being damaged is relatively low [10–12].
3. The implementation of generators using the cloud-like 3D PVDF/PEO structures was found to be challenging in regards to the type of electrodes that would better adapt to the core material. The use of conductive fabrics and threads was problematic due to the difficulty of sewing the electrodes to the sample without deforming the material. Trying with the copper foil and using conductive glue for facilitating the bonding process, a prototype 3D PVDF generator was built, using clear PDMS as the encapsulation material to allow for the observation of the state of the sample after having been exposed to the curing process. The resulting generator did not appear to have been negatively affected by the vacuuming process used to extract air bubbles from the PDMS before curing, with the electrodes not having been brought too close together in the process. This prototype is shown in Figure 7-1. This very basic generator assembly method could be further improved upon.
4. The thick sponge-like PVDF-TrFE/PEO structures resembled non-woven fabrics, with some of the samples being very similar to felt textiles often employed for making clothes and accessories. The compound generators with 13 units in parallel presented in chapter 5 were originally assembled with copper foil and copper tape as the electrode and interconnect materials, which might have affected the flexibility of the generator since the copper tape and foil are not as pliable as the core material itself. Considering a smart textile design approach, a similar compound generator was assembled using only conductive thread and fabrics, and a regular cotton fabric as a substrate. The prototype is shown in Figure 7-2. This type of designs might result in

purely fabric-based generators that could be more easily integrated to smart shirts and similar wearables.

5. Identifying and designing an adequate control experiment for identifying the contribution that the triboelectric effect had to the overall electrical response of the generators would be beneficial for better understanding the potential of the materials as cores for mechanical energy harvesters. One alternative would be making a generator for which the core material has been replaced for a different electrospun 3D polymer with a similar layered structure. This would be useful to compare the response from the PVDF-TrFE/PEO and PVDF/PEO generators against that from a non-active core generator with similar surface area. Another alternative would be to acquire a commercially available PVDF membrane or foam that has not been poled, which would allow for observing the response arising from the interaction between the PDMS and the PVDF core, although how fitting the model is would be dependent on the characteristics of the purchased material.

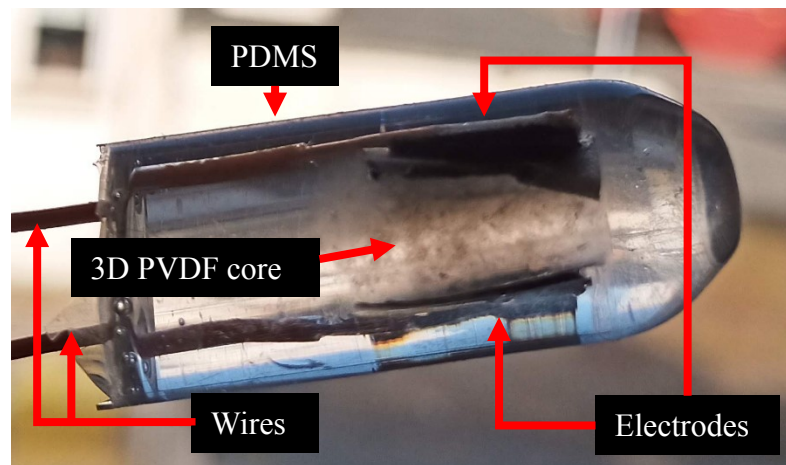


Figure 7-1: True 3D PVDF/PEO generator. This prototype uses the cloud-like sample as the active core material. The vacuuming process did not affect the positioning of the electrodes and core material.

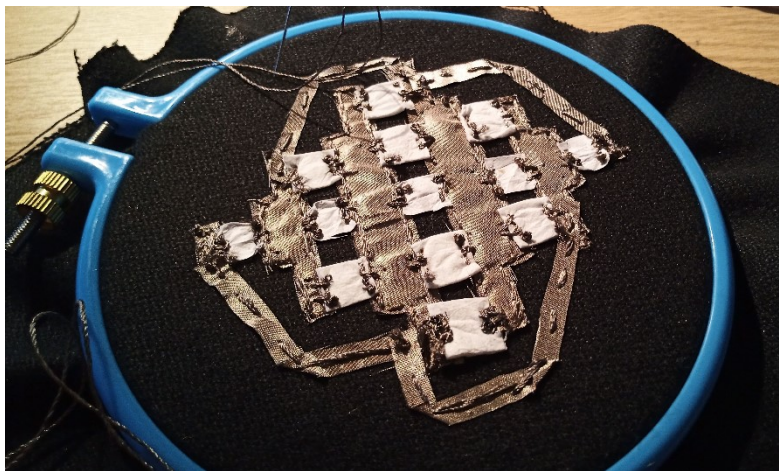


Figure 7-2: Prototype fabric only compound generator. The 1 cm^2 PVDF-TrFE core units are sewn into a cotton fabric substrate using conductive thread. Conductive fabrics are used to connect all the 13 core units in parallel.

7.4 References


- 1 Zaarour, B., Zhu, L., Huang, C., Jin, X.: 'Enhanced piezoelectric properties of randomly oriented and aligned electrospun PVDF fibers by regulating the surface morphology' *J. Appl. Polym. Sci.*, 2019, **136**, (6), p. 47049.
- 2 Wu, C.M., Chou, M.H., Zeng, W.Y.: 'Piezoelectric Response of Aligned Electrospun Polyvinylidene Fluoride/Carbon Nanotube Nanofibrous Membranes' *Nanomater.* 2018, Vol. 8, Page 420, 2018, **8**, (6), p. 420.
- 3 Kayser, L. V, Lipomi, D.J.: 'Stretchable Conductive Polymers and Composites Based on PEDOT and PEDOT:PSS' *Adv. Mater.*, 2019, **31**, (10), p. 1806133.
- 4 Rachel Feig, V., Tran, H., Lee, M., *et al.*: 'An Electrochemical Gelation Method for Patterning Conductive PEDOT:PSS Hydrogels' *Adv. Mater.*, 2019, **31**, (39), p. 1902869.
- 5 Wang, G., Xia, H., Sun, X.C., *et al.*: 'Actuator and generator based on moisture-responsive PEDOT: PSS/PVDF composite film' *Sensors Actuators B Chem.*, 2018, **255**, p. 1415–1421.
- 6 Cao, D., Sun, X., Li, Q., Natan, A., Xiang, P., Zhu, H.: 'Lithium Dendrite in All-Solid-State Batteries: Growth Mechanisms, Suppression Strategies, and Characterizations' *Matter*, 2020, **3**, (1), p. 57–94.
- 7 Shao, W., Zangari, G.: 'Dendritic Growth and Morphology Selection in Copper Electrodeposition from Acidic Sulfate Solutions Containing Chlorides' *J. Phys. Chem. C*, 2009, **113**, (23), p. 10097–10102.
- 8 Mezine, Z., Kadri, A., Hamadou, L., Benbrahim, N., Chaouchi, A.: 'Electrodeposition of copper oxides (Cu_xO_y) from acetate bath' *J. Electroanal. Chem.*, 2018, **817**, p. 36–47.
- 9 Nikolić, N.D., Popov, K.I., Pavlović, L.J., Pavlović, M.G.: 'Morphologies of copper deposits obtained by the electrodeposition at high overpotentials' *Surf. Coatings Technol.*, 2006, **201**, (3–4), p. 560–566.
- 10 Sharma, P.P., Yadav, V., Gahlot, S., *et al.*: 'Acid resistant PVDF-co-HFP based copolymer proton exchange membrane for electro-chemical application' *J. Memb. Sci.*, 2019, **573**, p. 485–492.
- 11 Mertens, M., Van Goethem, C., Thijs, M., Koeckelberghs, G., Vankelecom, I.F.J.: 'Crosslinked PVDF-membranes for solvent resistant nanofiltration' *J. Memb. Sci.*, 2018,


566, p. 223–230.

- 12 Kang, G. dong, Cao, Y. ming: 'Application and modification of poly(vinylidene fluoride) (PVDF) membranes – A review' *J. Memb. Sci.*, 2014, **463**, p. 145–165.

Appendix A

Publications







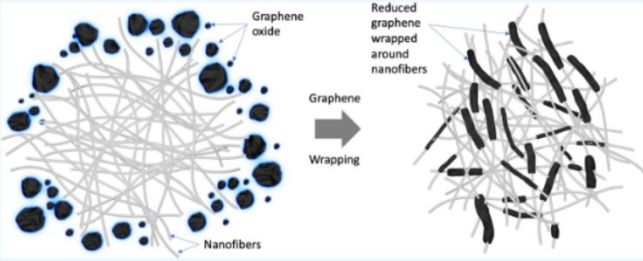
<http://pubs.acs.org/journal/acsodf> Article

Graphene Wrapping of Electrospun Nanofibers for Enhanced Electrochemical Sensing

Andreas Tsiamis, Francisco Diaz Sanchez, Niklas Hartikainen, Michael Chung, Srinjoy Mitra, Ying Chin Lim, Huey Ling Tan, and Norbert Radacsi*

 Cite This: *ACS Omega* 2021, 6, 10568–10577  [Read Online](#)

[ACCESS](#) | [Metrics & More](#) | [Article Recommendations](#) | [Supporting Information](#)



ABSTRACT: This paper presents a scalable method of developing ultrasensitive electrochemical biosensors. This is achieved by maximizing sensor conductivity through graphene wrapping of carbonized electrospun nanofibers. The effectiveness of the graphene wrap was determined visually by scanning electron microscopy and chemically by Fourier transform infrared spectroscopy, Raman spectroscopy, and X-ray diffraction. The sensing performance of different electrode samples was electrochemically characterized using cyclic voltammetry and electrochemical impedance spectroscopy, with the graphene-wrapped carbonized nanofiber electrode showing significantly improved performance. The graphene-wrapped carbonized nanofibers exhibited a relative conductivity of ~14 times and an electroactive surface area of ~2 times greater compared to the bare screen-printed carbon electrode despite experiencing inhibitive effects from the carbon glue used to bind the samples to the electrode. The results indicate potential for a highly conductive, inert sensing platform.

1 INTRODUCTION

Access to health care is the key to functional people.

added via SCOTLANDS RURAL COLL on December 14, 2021 at 15:12:53 (UTC).
 pubs.acs.org/sharingguidelines for options on how to legitimately share published articles.

Medical Engineering and Physics 92 (2021) 80–87



Contents lists available at ScienceDirect

Medical Engineering and Physics

journal homepage: www.elsevier.com/locate/medengphy

Technical note

Design and development of a nozzle-free electrospinning device for the high-throughput production of biomaterial nanofibers



Muhammad Waqas^{a,*}, Antonios Keirouz^{a,*}, Maria Kana Sanira Putri^a, Faraz Fazal^{a,b}, Francisco Javier Diaz Sanchez^a, Dipa Ray^a, Vasileios Koutsos^a, Norbert Radacsi^{a,†}

^a School of Engineering, Institute for Materials and Processes, The University of Edinburgh, Robert Stevenson Road, Edinburgh, EH9 3FB, United Kingdom.

^b Department of Mechanical Engineering, University of Engineering and Technology, Lahore, (city campus) Pakistan.

ARTICLE INFO

Article history:

Received 26 October 2020

Revised 10 April 2021

Accepted 29 April 2021

Keywords:

Nozzle-free
electrospinning
cryo-electrospinning
nanofibers
high-throughput
biomaterials

ABSTRACT

This technical note provides a step-by-step guide for the design and construction of a temperature-controlled nozzle-free electrospinning device. The equipment uses a rotating mandrel partially immersed within a polymer solution to produce fibers in an upward motion by inducing the formation of multiple Taylor cones and subsequently multi-jetting out of an electrified open surface. Free-surface electrospinning can overcome limitations and drawbacks associated with single and multi-nozzle spinneret configurations, such as low yield, limited production capacity, nonuniform electric field distribution, and clogging. Most importantly, this lab-scaled high-throughput device can provide an alternative economical route for needleless electrospinning research, in contrast to the high costs associated with industrially available upscaling equipment. Among the device's technical specifications, a key feature is a cryo-collector mandrel, capable of collecting fibers in sub-zero temperatures, which can induce ultra-porous nanostructures, wider pores, and subsequent in-depth penetration of cells. A multi-channel gas chamber allows the conditioning of the atmosphere, temperature, and airflow, while the chamber's design averts user exposure to the high-voltage components. All the Computer-Aided Design (CAD) files and point-by-point assembly instructions, along with a list of the materials used, are provided.

© 2021 IPFM. Published by Elsevier Ltd. All rights reserved.

Medical Engineering and Physics 94 (2021) 52–60



Contents lists available at ScienceDirect

Medical Engineering and Physics

journal homepage: www.elsevier.com/locate/medengphy

Technical note

A modified 3D printer as a hybrid bioprinting-electrospinning system for use in vascular tissue engineering applications



Faraz Fazal^{a,b}, Francisco Javier Diaz Sanchez^a, Muhammad Waqas^a, Vasileios Koutsos^a, Anthony Callanan^c, Norbert Radacsi^{a,*}

^a School of Engineering, Institute for Materials and Processes, The University of Edinburgh, Robert Stevenson Road, Edinburgh, EH9 3FB, United Kingdom

^b Department of Mechanical Engineering, University of Engineering and Technology, Lahore, (new campus) Pakistan

^c School of Engineering, Institute for Bioengineering, The University of Edinburgh, The King's Buildings, Edinburgh, EH9 3JL, United Kingdom

ARTICLE INFO

Keywords:

Bioprinting
Electrospinning
3D printing
Vascular tissue engineering

ABSTRACT

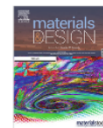
There is a high demand for small diameter vascular grafts having mechanical and biological properties similar to that of living tissues. Tissue-engineered vascular grafts using current methods have often failed due to the mismatch of mechanical properties between the implanted graft and living tissues. To address this limitation, a hybrid bioprinting-electrospinning system is developed for vascular tissue engineering applications. The setup is capable of producing layered structure from electrospun fibres and cell-laden hydrogel. A Creality3D Ender 3D printer has been modified into a hybrid setup having one bioprinting head and two electrospinning heads. Fortus 250mc and Flashforge Creator Pro 3D printers were used to print parts using acrylonitrile butadiene styrene (ABS) and polylactic acid (PLA) polymers. An Arduino mega 2560 and a Ramps 1.4 controller board were selected to control the functions of the hybrid bioprinting setup. The setup was tested successfully to print a tubular construct around a rotating needle.



Contents lists available at ScienceDirect

Materials & Design

journal homepage: www.elsevier.com/locate/matdes



Ultrafast fabrication of Nanofiber-based 3D Macrostructures by 3D electrospinning

Michel Vong^{a,*}, Francisco Javier Diaz Sanchez^a, Antonios Keirouz^a, Wiwat Nuansing^{b,c}, Norbert Radacsi^{a,*}

^aSchool of Engineering, Institute for Materials and Processes, The University of Edinburgh, Sanderson Building, King's Buildings, Edinburgh EH9 3FB, United Kingdom

^bSchool of Physics, Institute of Science, Suranaree University of Technology, Thailand

^cSUT CoE on Advanced Functional Materials (SUT-AFM), Suranaree University of Technology, Thailand

HIGHLIGHTS

- Various polymers and shapes can be built with the 3D electrospinning technology.
- The mechanism behind 3D build-up has been analyzed and characterized thoroughly.
- The shaping of 3D electrospun structures can be further enhanced with electrodes.
- The shelf-life and compressibility of the 3D structures have been characterized.
- The upscaling of 3D electrospinning, in term of size and quantity, has been achieved.

ARTICLE INFO

Article history:

Received 12 February 2021

Revised 10 June 2021

Accepted 16 June 2021

Available online 21 June 2021

Keywords:

3D electrospinning

Formation mechanism

Upscalability

Polystyrene

Polyacrylonitrile

Polyvinylpyrrolidone

ABSTRACT

Fabrication of macroscopic three-dimensional (3D) structures made of nanofibers of widely used polymers is reported. 3D structures have several benefits over conventional flat two-dimensional (2D) structures by the added dimension. The structures have been fabricated by the 3D electrospinning technology that can build 3D structures rapidly due to certain additives in the solution and appropriate process conditions. The process parameters of 3D electrospinning have been identified and investigated to better understand the formation mechanism of the 3D build-up for polystyrene (PS), polyacrylonitrile (PAN), and polyvinylpyrrolidone (PVP). Different types of electrodes were inserted in the electrospinning chamber to alter the electric field and have better control over the shape of the 3D structure. The upscalability of this technology was investigated by using a standard electrospinner and a nozzle-free electrospinning setup. It was possible to manufacture 3D structures with these devices, highlighting the versatility of this technology. 3D electrospinning opens the pathway for the facile fabrication of macroscopic 3D structure with microfibrillar features on a commercial scale.

© 2021 The Authors. Published by Elsevier Ltd. This is an open access article under the CC BY-NC-ND license (<http://creativecommons.org/licenses/by-nc-nd/4.0/>).



Article

Fabrication of Piezoelectric Electrospun Termite Nest-like 3D Scaffolds for Tissue Engineering

Thanapon Muenwacha ^{1,2}, Oratai Weerananatanapan ^{3,4}, Nuannoi Chudapongse ^{3,4},
Francisco Javier Diaz Sanchez ⁵, Santi Maensiri ^{1,4,6}, Norbert Radacsi ^{5,*} and Wiwat Nuansing ^{1,4,6,*}

¹ Institute of Science, School of Physics, Suranaree University of Technology, Nakhon Ratchasima 30000, Thailand; t.muenwacha@gmail.com (T.M.); santimaensiri@sg.sut.ac.th (S.M.)

² Thailand Center of Excellence in Physics (ThEP), Ministry of Higher Education, Science, Research and Innovation, Bangkok 10400, Thailand

³ Institute of Science, School of Preclinical Sciences, Suranaree University of Technology, Nakhon Ratchasima 30000, Thailand; oratai@sut.ac.th (O.W.); nuannoi@sut.ac.th (N.C.)

⁴ Center of Excellence on Advanced Functional Materials (CoE-AFM), Suranaree University of Technology, Nakhon Ratchasima 30000, Thailand

⁵ Institute for Materials and Processes, School of Engineering, The University of Edinburgh, Robert Stevenson Road, Edinburgh EH9 3FB, UK; s1673949@sms.ed.ac.uk

⁶ Research Network NANOTEC—SUT on Advanced Nanomaterials and Characterization, Suranaree University of Technology, Nakhon Ratchasima 30000, Thailand

* Correspondence: N.Radacsi@ed.ac.uk (N.R.); w.nuansing@sg.sut.ac.th (W.N.); Tel.: +44-(0)-131-651-7112 (N.R.); +66-(0)-6254-55630 (W.N.)



Citation: Muenwacha, T.; Weerananatanapan, O.; Chudapongse, N.; Diaz Sanchez, F.J.; Maensiri, S.; Radacsi, N.; Nuansing, W. Fabrication of Piezoelectric Electrospun Termite Nest-like 3D Scaffolds for Tissue Engineering. *Materials* **2021**, *14*, 7684. <https://doi.org/10.3390/ma14247684>

Academic Editors: Tsz Ho Kwo, Xiangjia Li and Yang Yang

Received: 3 November 2021

Accepted: 8 December 2021

Published: 13 December 2021

Abstract: A high piezoelectric coefficient polymer and biomaterial for bone tissue engineering—poly(vinylidene fluoride-co-hexafluoropropylene) (PVDF-HFP)—has been successfully fabricated into 3D scaffolds using the wet electrospinning method. Three-dimensional (3D) scaffolds have significant advantages for tissue engineering applications. Electrospinning is an advanced method and can fabricate 3D scaffolds. However, it has some limitations and is difficult to fabricate nanofibers into 3D shapes because of the low controllability of porosity and internal pore shape. The PVDF-HFP powders were dissolved in a mixture of acetone and dimethylformamide with a ratio of 1:1 at various concentrations of 10, 13, 15, 17, and 20 wt%. However, only the solutions at 15 and 17 wt% with optimized electrospinning parameters can be fabricated into biomimetic 3D shapes. The produced PVDF-HFP 3D scaffolds are in the cm size range and mimic the structure of the natural nests of termites of the genus *Apicotermes*. In addition, the 3D nanofiber-based structure can also generate more electrical signals than the conventional 2D ones, as the third dimension provides more compression. The cell interaction with the 3D nanofibers scaffold was investigated. The in vitro results demonstrated that the NIH 3T3 cells could attach and migrate in the 3D structures. While conventional electrospinning yields 2D (flat) structures, our bio-inspired electrospun termite nest-like 3D scaffolds are better suited for tissue engineering applications since they can potentially mimic



Nano Energy
Volume 98, July 2022, 107286



Sponge-like piezoelectric micro- and nanofiber structures for mechanical energy harvesting

Francisco Javier Diaz Sanchez ^a, Michael Chung ^a, Muhammad Waqas ^a, Vasileios Koutsos ^a, Stewart Smith ^b, Norbert Radacsi ^a

^a School of Engineering, Institute for Materials and Processes, The University of Edinburgh, King's Buildings, Robert Stevenson Road, EH9 3FB, UK

^b School of Engineering, Institute for Bioengineering, The University of Edinburgh, Faraday Building, King's Buildings, Colin Maclaurin Road, Edinburgh EH9 3DW, UK

Received 19 October 2021, Revised 31 March 2022, Accepted 12 April 2022, Available online 15 April 2022, Version of Record 21 April 2022.



Appendix B

Morphological effects of using other salt additives for electrospinning PVDF/PEO

The work presented in this thesis mostly relates to the fabrication of electrospun materials and their performance as the core of mechanical energy harvesters. The use of zinc oxide nanowires grown on the surface of substrates and active materials, as well as its use for the decoration of electrospun nanofibres, for the enhancement of the piezoelectric response of the material has been thoroughly documented in the literature [1–4]. The work presented in this section deals with a series of experiments conducted for evaluating if variations of the electrospun materials obtained in the previous chapters are compatible with the hydrothermal method for the fabrication of ZnO nanowires.

The main objective of these experiments was to observe if the use of other salts such as zinc nitrate and zinc acetate instead of LiCl would result in the formation of 3D electrospun structures or in the initiation of 3D build-up. If this was found to occur, the feasibility of using the hydrothermal growth method to decorate the resulting fibres with ZnO would be evaluated.

The experiments conducted on this chapter show additional methods that can be used to further improve the piezoelectric properties of the electrospun structures showcased in the previous chapters, showing that the improvement of the materials obtained as the cores of piezoelectric energy harvesters can be achieved with different approaches.

As discussed in chapter 5, the use of LiCl as an additive had allowed for the fabrication of 3D PVDF/PEO structures with morphologies that ranged from thick sponge-like mats to 3D cloud-like structures. The goal of the following experiments was to test two additional salts, zinc nitrate and zinc acetate, as additives for the 10 wt% PVDF/PEO in DMF/water solutions (50:3 ratio for both the polymers and the solvents) to observe whether these would also promote the transition from flat mats to 3D structures. PVDF/PEO stock solution enhanced with 0.5, 1 and 5 wt% zinc nitrate and zinc acetate was electrospun using the nozzle-based setup (please refer to Chapter 3, section 3.4.1) with the conditions outlined in Table B-1.

Table B-1: Electrospinning conditions used for the fabrication of electrospun PVDF/PEO fibrous structures or mats with added zinc nitrate or zinc acetate.

Additive	Quantity	Voltage (kV)	FR ($\mu\text{L}\cdot\text{min}^{-1}$)	WD (cm)	Temperature ($^{\circ}\text{C}$)	RH%	Observations
Zinc nitrate	0.5 wt%	18	12	10	21	42	2D mat
	1 wt%	16	12	8	17	61	3D build-up
	5 wt%	20	16	12	16.8	60	2D mat, 3D build-up.
Zinc acetate	0.5 wt%	18	7	16	16.7	61	2D mat
	1 wt%	20	25	12	16.7	61	2D mat
	5 wt%	18	25	12	16.8	61	Slight 3D build-up

For those with zinc nitrate, gelation was apparent starting at 1 wt%, with the needle tip requiring frequent cleaning for the trials involving both the higher wt% solutions, causing the frequent interruption of the experiment. In the case of the solutions with added zinc acetate, no gelation was observed for any of them during electrospinning. In regards to 3D build-up, the solutions with added zinc acetate did not yield more than 2D flat mats for the lower added salt concentrations. The solution with added 5 wt% did show structures for which the initiation of the 3D build-up process was observed. Over the course of 10 minutes after initiating electrospinning, a few very fine threads started forming on the surface of the collector, as shown in Figure B-1a. These strands were attracted to the nozzle-based, grew longer, often collided with each other and coalesced into thicker threads. After 5 more minutes, several strands had started to attach to each other, forming an even thicker and longer strand, shown in figure B-1b. The experiment had to be interrupted since the growing strand was now too close to the nozzle-based, resulting in an electric arc becoming visible between the nozzle and the tip of the strand. For the solution with added zinc nitrate, the initiation of the 3D build-up process was observed to occur immediately after initiating electrospinning for the solution with added 1wt% of this salt. The resulting product did not resemble those that had been observed for the solutions with added LiCl; a wispy fibre mat had formed instead of a cloud-like structure. The resulting fibre mat is shown in figure B-1c. For the solution with added 5 wt% zinc nitrate, a thick strand product very similar to that observed when electrospinning the 5 wt% zinc acetate solution was obtained, although the formation of this one occurred over the course of very frequent experiment interruption and nozzle cleaning steps.

The solutions with added zinc acetate content had the advantage of not showing signs of gelation even for added salt content as high as 5 wt%. When electrospinning this group of solutions, the experiment would not need to be interrupted to clean the nozzle, potentially allowing for the fabrication of materials without the risk of any polymer solution droplets depositing on the surface of the fibre mats every time that the process is interrupted and restarted. However, the formation of fibrous structures that indicated the start of the 3D build-up process was only observed for the solution with the highest zinc acetate content, and was not as fast as for the solutions that had LiCl or zinc nitrate. For this reason, only the products obtained from solutions with zinc nitrate were considered for the next stage.

SEM images of the fibres obtained from electrospinning the 10 wt% PVDF/PEO in DMF/water solution with 1 wt% added zinc nitrate revealed that the resulting product consisted mostly of groups of fibres that had formed thick yarn-like structures and a few individual fibres. The average individual fibre diameter was 708 ± 182 nm, and their surface resembled the crater-like appearance that had been observed for the fibres that had been obtained previously for the stock solution, indicating that the addition of zinc nitrate to the solution had no negative influence in the morphology of the surface in the sense of causing beads or breaks in the fibres. Figure B-2 shows two captures of the same region with different focus settings.

The use of zinc nitrate and zinc acetate as additives allowed for the formation of electrospun structures that transitioned from flat mats to 3D structures when concentrations higher than 1 wt% relative to the base solution had been employed. However, the amount of zinc salts required to replicate or surpass the 3D build-up observed when using solutions with added LiCl is higher; using 5 wt% zinc nitrate or zinc acetate results in a 3D build-up rate that comes close but is not completely similar to that observed when using 0.75 wt% of added LiCl. While the formation of 3D structures was observed, the greater amounts of zinc nitrate and zinc acetate required for generating a strong build-up response and the tendency of these solutions to start showing signs of gelation for concentration as low as 1 wt% are disadvantageous. For instance, additional mechanisms and instrumentation for generating and maintaining the temperature conditions necessary to keep the solutions from gelating would complicate the fabrication process. Thus, for the electrospinning setups employed in this project, the use of zinc nitrate and zinc acetate as additives for the electrospinning of PVDF does not provide any advantageous properties over the use of LiCl.



Figure B-1: (a) Product obtained from electrospinning a 10 wt% PVDF/PEO in DMF/water solution with 5 wt% added zinc acetate. (b) Yarn obtained from electrospinning the solution from (a) for 5 additional minutes. (c) Wispy fibre mat obtained from electrospinning a 10 wt% PVDF/PEO in DMF/water solution with 1 wt% added zinc nitrate.

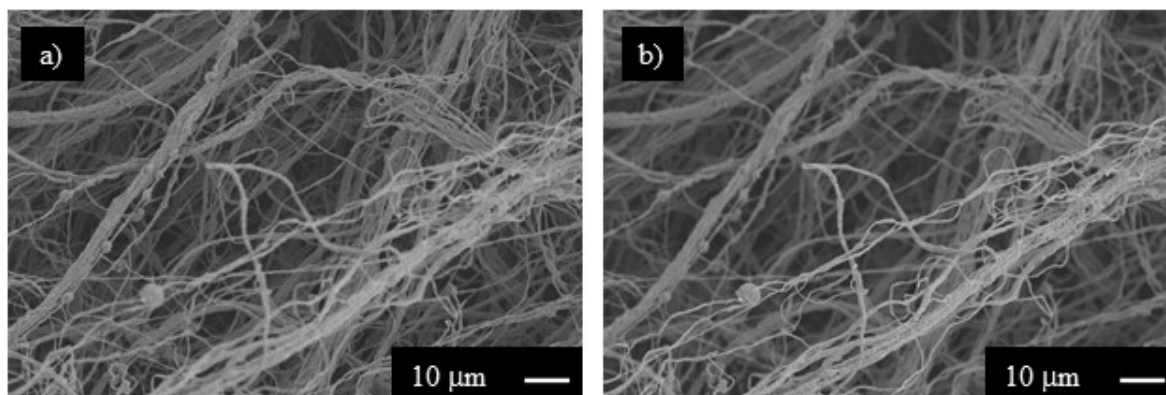


Figure B-2: SEM images of the wispy PVDF/PEO mat with added 1 wt% zinc nitrate. Both images show the same region, but focus was adjusted to clearly show the fibres on the background or those on top.

Employing zinc salts in the previous experiment inspired one additional idea. Zinc nitrate and acetate are often used as reagents for the hydrothermal growth of zinc oxide (ZnO) structures. ZnO nanostructures grown on the surface of electrospun PVDF fibres have been proven to increase the V_{OC} of the material when used as a mechanical energy harvester. The use of ZnO nanostructures for the fabrication of sensing surfaces, microelectromechanical systems, and the enhancement of the piezoelectric properties of other systems has been thoroughly documented [1, 2, 5–7]. The following experiment was done to evaluate if the electrospun structures obtained when using 1 wt% zinc nitrate as an additive can be decorated with ZnO nano or microstructures.

A few samples of the structure obtained when using 1 wt% zinc nitrate were selected. Four individual sample holders with the sample and an additional control sample, which consisted of 10 wt% PVDF/PEO fibres with 0.75 wt% added LiCl, were prepared. These were placed on carbon tape that had been placed on individual SEM stubs. 100 mL stock solutions for ZnO crystal growth comprised of 100 mL DI water, 50 mM HMTA, and 50 mM zinc nitrate were prepared at room temperature and left stirring at 400 RPM until the liquid had turned clear. The solution was then set on a heated stirring plate, and the samples were placed within the solution once the temperature had reached 90° C. Each one of the sample holders would be extracted from the solution at different times, allowing for the observation of the crystal growth process at 30 minutes, 1, 2 and 4 hours after initiating the experiment. The control sample was exposed to the solution for 4 hours. SEM was used to observe the surface of the fibres for all 5 samples. The images obtained for the control sample are shown in Figure B-3.

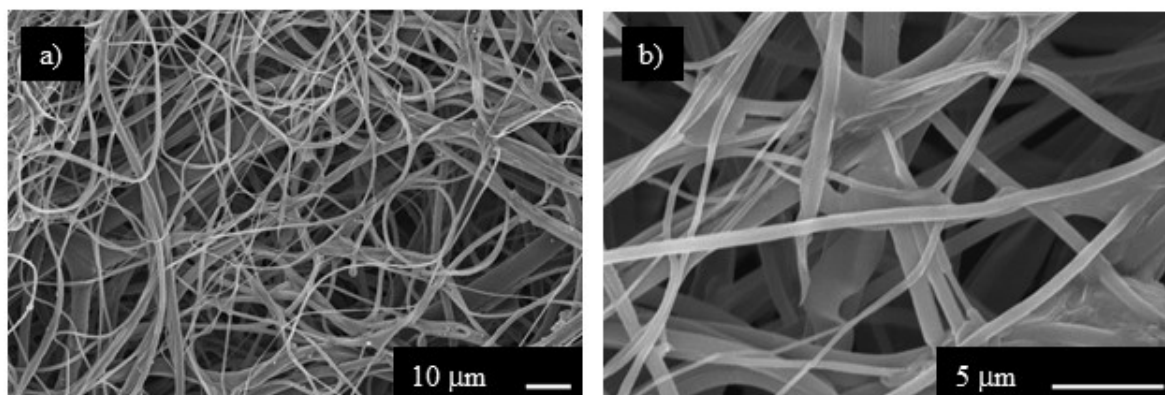


Figure B-3: Images showing PVDF/PEO with 1 wt% added LiCl fibrous structures that were exposed to ZnO hydrothermal growth conditions for 4 hours.

Microstructure growth on the sample with added zinc nitrate was revealed not to occur evenly. 30 minutes of initiating the hydrothermal growth process, SEM images revealed a few structures of unidentified composition had formed on the surface of the most external fibres for the corresponding sample. These SEM images are shown in Figure B-4.

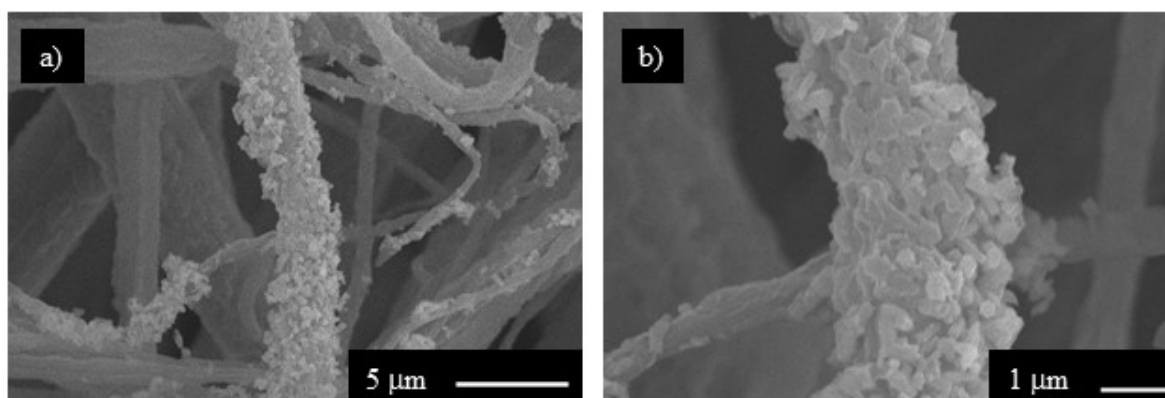


Figure B-4: Images showing unidentified microstructures growth on PVDF/PEO fibres with 1 wt% added zinc nitrate after 30 minutes of exposure to hydrothermal growth conditions. A few microstructures can be observed scattered on the surface of the fibres.

SEM images for the sample that had been exposed to the hydrothermal growth conditions for 1 hour show that the microstructures had now started to grow on the surface of the fibres. The images corresponding to the sample exposed for 1 hour are shown in Figure B-5.

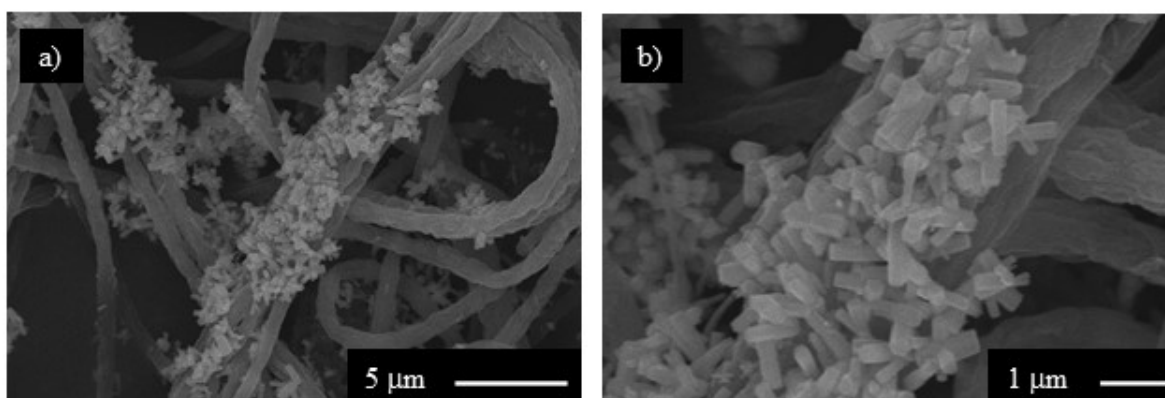


Figure B-5: Images showing an unidentified microstructure growth on PVDF/PEO fibres with 1 wt% added zinc nitrate after 1 hour of exposure to hydrothermal growth conditions. Longer microstructures are visible on the surface of the fibres on top and for those within the fibrous network.

The SEM images for the sample that had been exposed for 2 hours, shown in Figure B-6, revealed that small, medium and large formations now covered most of the surface of the fibres. Regions with no crystals still existed, but not as extended as those that had been observed on the samples exposed for 30 minutes or 1 hour.

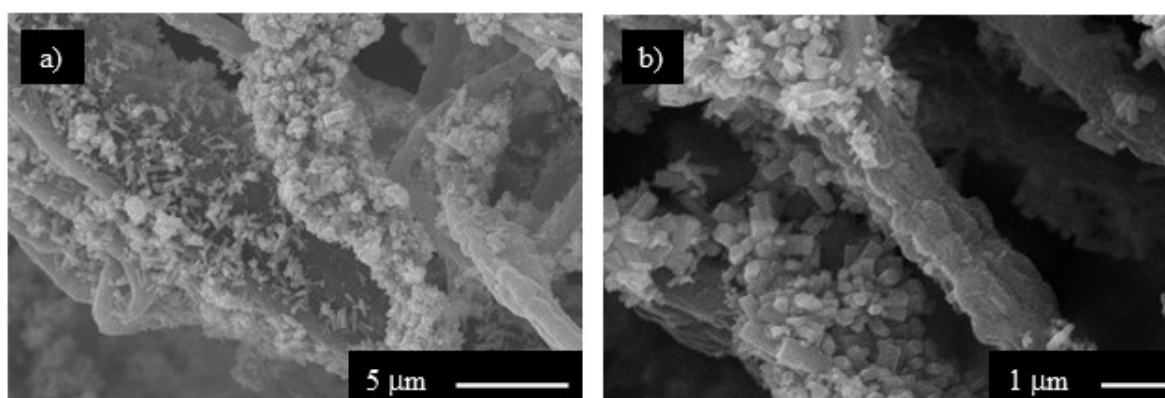


Figure B-6: Images showing microstructure growth on PVDF/PEO fibres with 1 wt% added zinc nitrate after 2 hours of exposure to hydrothermal growth conditions. The surface of the fibres is being covered by the microstructures, although the process is not uniform. Nascent structures are visible in some of the regions that have almost no presence of ZnO microstructures.

After 4 hours of exposure to hydrothermal growth conditions, most of each individual fibre surface had been covered by the unidentified crystals. As seen in the SEM images for this sample, shown in Figure B-7, individual fibres deep within the sample had been covered in crystals, with the coverage being virtually complete judging by the absence of visible fibre

surfaces. The SEM image with the highest magnification shows that the individual structures had varying width and lengths.

Microstructures had been observed to grow on the 1 wt% zinc nitrate samples; whether this unidentified material is ZnO or a different one altogether remains to be determined. In the case of the control sample, which consisted of the electrospun sample with added LiCl, no unidentified microstructures had been observed on the surface of the fibres. However, this does not necessarily mean that the method employed for placing the samples in the solution had an impact in the absence of visible structures.

The morphology of the products obtained from this experimental trial, which had a diameter of 708 ± 182 nm, was comparable with those that had been obtained from electrospinning the 10 wt% PVDF/PEO in DMF/water solutions without other additives, for which the average fibre diameter had been 928 ± 194 nm when comparing only individual fibres. However, the fibrous structures obtained from the solutions with added zinc nitrate are formed by combinations of individual fibres and groups of these in the form of thick yarn-like arrangements. Additionally, in contrast with the thick fibrous structures obtained from the solutions with added LiCl, the products of the experiments outlined in this section were wispy fibre mats for which 3D build-up did occur, but not to the same degree observed for other solutions. The resulting structures were found to be frail, unravelling easily even when handled with care.

References

- 1 Yang, T., Pan, H., Tian, G., *et al.*: 'Hierarchically structured PVDF/ZnO core-shell nanofibers for self-powered physiological monitoring electronics' *Nano Energy*, 2020, **72**, p. 104706.
- 2 Kim, M., Wu, Y., Kan, E., Fan, J.: 'Breathable and Flexible Piezoelectric ZnO@PVDF Fibrous Nanogenerator for Wearable Applications' *Polymers (Basel)*, 2018, **10**, (7), p. 745.
- 3 Filippin, A.N., Sanchez-Valencia, J.R., Garcia-Casas, X., *et al.*: '3D core-multishell piezoelectric nanogenerators' *Nano Energy*, 2019, **58**, p. 476–483.
- 4 Zhang, Z., Chen, Y., Guo, J.: 'ZnO nanorods patterned-textile using a novel hydrothermal method for sandwich structured-piezoelectric nanogenerator for human energy harvesting' *Phys. E Low-dimensional Syst. Nanostructures*, 2019, **105**, p. 212–218.
- 5 Mahmud, A., Khan, A.A., Voss, P., Das, T., Abdel-Rahman, E., Ban, D.: 'A High Performance and Consolidated Piezoelectric Energy Harvester Based on 1D/2D Hybrid

- Zinc Oxide Nanostructures' *Adv. Mater. Interfaces*, 2018, **5**, (23), p. 1801167.
- 6 Kapat, K., Shubhra, Q.T.H., Zhou, M., Leeuwenburgh, S.: 'Piezoelectric Nano-Biomaterials for Biomedicine and Tissue Regeneration' *Adv. Funct. Mater.*, 2020, **30**, (44), p. 1909045.
 - 7 Fortunato, M., Chandraiahgari, C.R., De Bellis, G., *et al.*: 'Piezoelectric thin films of ZnO-nanorods/nanowalls grown by chemical bath deposition' *IEEE Trans. Nanotechnol.*, 2018, **17**, (2), p. 311–319.